IntechOpen

Mitigation of Ionospheric Threats to GNSS: an Appraisal of the Scientific and Technological Outputs of the TRANSMIT Project

Edited by Riccardo Notarpietro, Fabio Dovis,
Giorgiana De Franceschi and Marcio Aquino

MITIGATION OF IONOSPHERIC THREATS TO GNSS: AN APPRAISAL OF THE SCIENTIFIC AND TECHNOLOGICAL OUTPUTS OF THE TRANSMIT PROJECT

Edited by **Riccardo Notarpietro, Fabio Dovis, Giorgiana De Franceschi and Marcio Aquino**

Mitigation of Ionospheric Threats to GNSS: an Appraisal of the Scientific and Technological Outputs of the TRANSMIT Project
http://dx.doi.org/10.5772/58550
Edited by Riccardo Notarpietro, Fabio Dovis, Giorgiana De Franceschi and Marcio Aquino

© The Editor(s) and the Author(s) 2014
The moral rights of the and the author(s) have been asserted.
All rights to the book as a whole are reserved by INTECH. The book as a whole (compilation) cannot be reproduced, distributed or used for commercial or non-commercial purposes without INTECH's written permission.
Enquiries concerning the use of the book should be directed to INTECH rights and permissions department (permissions@intechopen.com).
Violations are liable to prosecution under the governing Copyright Law.

Individual chapters of this publication are distributed under the terms of the Creative Commons Attribution 3.0 Unported License which permits commercial use, distribution and reproduction of the individual chapters, provided the original author(s) and source publication are appropriately acknowledged. If so indicated, certain images may not be included under the Creative Commons license. In such cases users will need to obtain permission from the license holder to reproduce the material. More details and guidelines concerning content reuse and adaptation can be foundat http://www.intechopen.com/copyright-policy.html.

Notice
Statements and opinions expressed in the chapters are these of the individual contributors and not necessarily those of the editors or publisher. No responsibility is accepted for the accuracy of information contained in the published chapters. The publisher assumes no responsibility for any damage or injury to persons or property arising out of the use of any materials, instructions, methods or ideas contained in the book.

First published in Croatia, 2014 by INTECH d.o.o.
eBook (PDF) Published by IN TECH d.o.o.
Place and year of publication of eBook (PDF): Rijeka, 2019.
IntechOpen is the global imprint of IN TECH d.o.o.
Printed in Croatia

Legal deposit, Croatia: National and University Library in Zagreb

Additional hard and PDF copies can be obtained from orders@intechopen.com

Mitigation of Ionospheric Threats to GNSS: an Appraisal of the Scientific and Technological Outputs of the TRANSMIT Project
Edited by Riccardo Notarpietro, Fabio Dovis, Giorgiana De Franceschi and Marcio Aquino
p. cm.
ISBN 978-953-51-1642-4
eBook (PDF) ISBN 978-953-51-5050-3

Meet the editors

Riccardo Notarpietro is assistant professor since 2006 at the Politecnico di Torino. He received his Ph.D. in 2001 with a thesis on the atmosphere remote sensing exploiting GPS measurements from space and from ground. His fields of activities included also electromagnetic wave propagation, radarmeteorology, and more recently, GNSS-Reflectometry. He has been Visiting Scientist at EUMETSAT and DMI for GNSS Radio Occultation data analysis. He is actually working at EUMETSAT, providing scientific support to the development of the Radio Occultation payload and ground segment for the Second Generation of the Eumetsat Polar System (EPS-SG) program.

Fabio Dovis is currently assistant professor at Politecnico di Torino, working at the Dept. of Electronics and Telecommunications as a member of the Navigation Signal Analysis and Simulation (NavSAS) group. His research interests cover the design of GPS and Galileo receivers and advanced signal processing for interference and multipath detection and mitigation. He has a relevant experience in European projects in GNSS as well as cooperation with industries and research centers. He is member of the Galileo/EGNOS Mission Evolution Advisory Group of the European Commission.

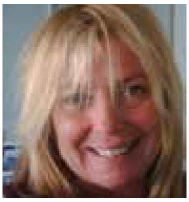

Dr. Giorgiana De Franceschi (Female) is Director of research at Istituto Nazionale di Geofisica e Vulcanologia (INGV). She was the director of the Upper Atmosphere Physics group from January 2002 to June 2007. She is principal investigator of research projects in the frame of PNRA (Programma Nazionale di Ricerche in Antartide, the Italian National Program for the Antarctic Research) since 1997 and member of the PNRA national Committee in the frame of Geodesy and Observatories sector since 1999. Since 2007 she is the leader of the SCAR expert group GRAPE (GNSS Research and Application for Polar Environment, www.grape.scar.org). Her main research interests are the temporal/spatial modelling and investigation of the high and low latitude ionosphere in different time-scales based on a multi-instrument approach (GNSS receivers, ionosondes, riometers, and HF radars).

Dr Marcio Aquino is the TRANSMIT project coordinator. He is a principal research fellow at the Nottingham Geospatial Institute (NGI) of the University of Nottingham. In the last 14 years he has concentrated on research related to ionospheric effects on GNSS. He is currently the PI and main contributor to several UK and EU funded projects at the NGI. Marcio recent work on ionospheric effects on GNSS includes higher order effects and system vulnerability to ionospheric scintillation and relevant countermeasures. He was the technical leader of the CIGALA project (2010/2012) and the NGI PI on MImOSA (Monitoring the Ionosphere Over South America), a competence survey funded by ESA (2013), he is coordinator of the ongoing CALIBRA project (FP7, 2012/2015) and the NGI PI for the MISW project (FP7, 2014/2017). In the last 7 years he has co-authored more than 50 publications in international journals and conference proceedings and has been the leader of ionospheric research at the NGI.

Contents

Preface

The European Community has predicted an annual global market for Global Navigation Satellite Systems (GNSS) of 300bn € by 2020. Europe is currently developing its own GNSS system Galileo that will become operational over the next few years. The main threat to the reliable and safe operation of GNSS is the variable propagation conditions encountered by GNSS signals as they pass through the Earth's upper atmosphere (the ionosphere). At a COST 296 workshop held in 2008, the establishment of a sophisticated Ionospheric Perturbation Detection and Monitoring (IPDM) network (http://ipdm.nottingham.ac.uk/) was proposed by European experts, and supported by the European Space Agency (ESA), as the way forward to deliver the state of the art to protect a range of essential technological systems vulnerable to Ionospheric threats. In a bid to initiate research and training of scientists in Europe for the development of the IPDM network, the TRANSMIT project (www.transmit-ionopshere.net) was conceived and later funded by the European Commission through their FP7 PEOPLE Programme, in the form of a Marie Curie Initial Training Network (ITN). Marie Curie ITNs aim to improve the career perspectives of researchers who are in the first five years of their research career in both public and private sectors. TRANSMIT is a 4 year project of this kind, started in February 2011 and led by the University of Nottingham, in the UK. It is a coordinated programme of academic and industrial training focusing on atmospheric phenomena that can significantly impair a wide range of systems and applications that are at the core of several activities embedded in our daily life. This is an area of immediate interest to the European society.

TRANSMIT comprises a consortium of leading universities and research centres in Europe, with associated partners from top European industry stakeholders, as well as industry and academia from Brazil and Canada. Research in TRANSMIT initiated in September 2011 with the recruitment of 14 Marie Curie Fellows (13 Early Stage Researchers and one Experienced Researcher) with two more Experienced Researches recruited in 2012 and 2013, to take up a number of coordinated projects aiming to develop real time integrated tools to mitigate ionospheric threats in particular to GNSS and related applications. The project fully exploits the existing specialized European science base and takes advantage of insight from European industry and end users in order to prove the IPDM network concept and setup its prototype.

The final TRANSMIT product that glues the different fellows' projects together is a prototype of the proposed IPDM network. A first taste of what this prototype aims to achieve was provided during the prestigious International Beacon Satellite Symposium 2013 held in July in Bath, UK. Referring to the project's research philosophy shown in Figure 1, the research feeds from real world scientific and industrial problems, generates initial solutions that are then tested, validated and fine-tuned against the originating problems and finally lead to the end product, i.e. the prototype that demonstrates the IPDM network and service.

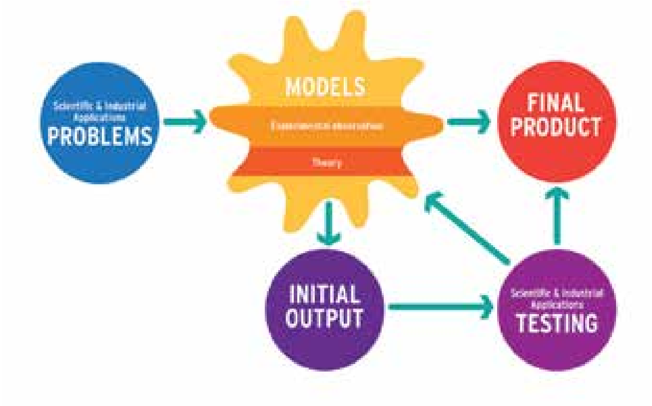

Figure 1. The TRANSMIT project's research philosophy

Figure 2 shows a high level representation of the overall project structure and how its Work Packages (WPs) interact. WP 1, 2 and 3 form what we call the 'modelling area' of the project and will output predicted scintillation indices/parameters, improved background ionospheric models, scintillation forecasts, scintillation climatology and optimised data treatment strategies. Concurrently, WP4 represents what we call the 'tools area' and addresses directly the needs of our industrial partners, with outputs of a more direct use to GNSS based applications, such as scintillation and interference resilient receiver tracking models, real time and post mission line of sight tracking errors, improved positioning algorithms and corrections for augmentation systems - all these tailored for legacy and new GNSS signals. It is clear that the outputs of the models developed in WP 1, 2 and 3 can either be made directly available to users or serve as input to WP4 in order to support the tools that will enable a more application-led demonstration of the project results. Therefore the prototype will address both users interested in model outputs and application related tools.

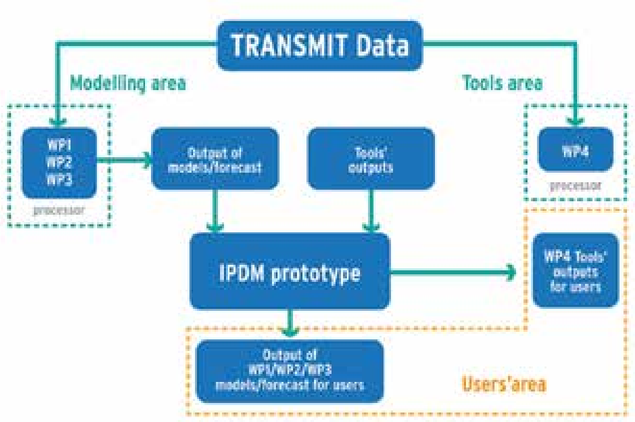

Figure 2. The TRANSMIT project's structure

This book is concerned with the TRANSMIT 2014 Workshop "Appraisal of Scientific and Technological Output" that took place in Torino 19-20 Feb 2014, where a full update on the status of the prototype development and the next steps leading to its full implementation were provided. In the TRANSMIT Final Event that will take place in the framework of the 11th European Space Weather Week (ESWW - Liege, Belgium, 17-21 November 2014 (http://www.stce.be/esww11/abstract.php), we will report the final results of the project and will invite the community to share their ideas and bring their very welcome contribution to this important area of research.

The TRANSMIT prototype demonstrator will be a web based interface aiming to showcase the project research outcomes in a user friendly manner, through a series of model outputs and tools that could serve as the blueprint for a future service to assist users and industry to mitigate the effects of ionospheric threats to GNSS. The prototype demonstrator will consist of 'processors' (referred to as 'TRANSMIT processors') addressing a selection of research topics within the project. Such topics, which follow the prototype development logic, constituted the sessions of the TRANSMIT 2014 Workshop and define the different parts of this book.

Part 1: Introduction

This part introduces the TRANSMIT prototype idea and its implementation. The scope of this first part is to put the TRANSMIT project in a context considering a wider perspective of scientific and industrial work on the ionosphere and GNSS. Chapters are provided by **Eleftherios Plakidis, Vincenzo Romano, Luca Spogli and Giorgiana De Franceschi** (*"Data Management Strategy for GNSS Services: the TRANSMIT Project case"*) and **Hirohato Sato, Nikolai Hlubek and Marcio Aquino** (*"The Concept of the TRANSMIT Prototype: Network Based Service for Mitigation of Ionospheric Threat on GNSS"*)

Part 2: Robust Receiver Architectures for GPS and Galileo

This second part focuses on the impact of ionosphere activity on signal tracking and on signal processing as well as on the more general topic related to interference mitigation. Chapters for this second part are provided by **Melania Susi, Marcus Andreotti and Marcio Aquino** (*"Kalman Filter Based PLL Robust against Ionospheric Scintillation"*), **Rodrigo Romero and Fabio Dovis** (*"Towards Analysing the Effect of Interference in GNSS Scintillation Monitoring"*) and **Marko Vuckovic and Samo Stanic** (*"Computation of Scintillation Indices for the Galileo E1 Signals Using a Software Receiver"*).

Part 3: Improved Positioning

Contributions on mitigation of GNSS positioning errors on related applications and services due to ionospheric activity and perturbations are the main topic of this third part. Chapters are provided by **Peter Kieft, Marcio Aquino and Alan Dodson** (*"Using Ordinary Kriging for the Creation of Scintillation Maps"*), by **Marija Cokrlic** (*"Challenges of Real-time Monitoring of Ionospheric Perturbations and TEC Fluctuations with GPS Single Station"*) and **Kinga Wezka** (*"The Reliability Evaluation of GNSS Observations in the Presence of Ionospheric Perturbation"*). A further contribution is provided by **Luca Spogli, Vincenzo Romano, Giorgiana De Franceschi, Lucilla Alfonsi, Eleftherios Plakidis, Claudio Cesaroni, Marcio Aquino, Alan Dodson, Joao Francisco Galera Monico, Bruno Vani** (*"A Filtering Method Developed to Improve GNSS Receiver Data Quality in the CALIBRA Project"*).

Part 4: Scintillations, TEC Modelling and forecast, TEC comparisons

This fourth part focuses on the scientific and theoretical aspects of modelling and predicting ionospheric perturbations, including scintillation, as well as on results related to TEC modelling comparisons. Chapters are provided by **Shishir Priyadarshi and Andrzej W. Wernik** (*"B-spline Model of Ionospheric Scintillation for High Latitude Using In-situ Satellite Data"*), by **Oksana Grynyshyna-Poliuga, Iwona Stanislawska and Anna Swiatek** (*"Regional Ionosphere Mapping with Kriging and B-spline Methods"*), **Dorde Stevanović** (*"Statistical Case Study of High and Low Latitude Ionospheric Scintillation"*) and **Pavel Najman and Tomislav Kos** (*"Performance Analysis of Empirical Ionosphere Models by Comparison with CODE Vertical TEC Maps"*). This part includes a contribution external to the project, provided by **Ayman M. Mahrous, O. A. Abuelezz, Amr M. Abdallah and R. Fleury** (*"Comparison between the Ne-Quick Model and VTEC Estimation by GPS Measurements Over Egypt"*).

Part 5: Electron Density Characterization

This final part mainly deals with the characterization of electron density distributions exploiting imaging algorithms and other techniques, like those based on the inversion of GNSS Radio Occultation observations. Contributions are provided by **T. Panicciari, Nathan D. Smith, Federica Da Dalt, Cathryn N. Mitchell and Gary S. Bust** (*"Multi-resolution Tomography of Ionospheric Electron Density"*), **Federico Da Dalt, C. Benton, Tommaso Panicciari, Nathan D. Smith and Cathryn N. Mitchell** (*"ANIMo: A New Ionospheric Model"*) and **Mubasshir Shaikh, Riccardo Notarpietro and Bruno Nava** (*"Implementation of Ionospheric Asymmetry Index in the TRANSMIT Prototype"*).

Acknowledgements

TRANSMIT is funded by the Research Executive Agency within the 7th Framework Program of the European Commission, People Program, Initial Training Network, Marie Curie Actions - GA no. 264476. The project is grateful to the following TRANSMIT Level 2 academic and industrial partners who helped steer the project and hosted the TRANSMIT fellows through various placements:

The Editors gratefully acknowledge TRANSMIT, funded by the Research Executive Agency within the 7th Framework Program of the European Commission, People Program, Initial Training Network, Marie Curie Actions - GA no. 264476. The following TRANSMIT Level 2 academic and industrial partners were particularly active and helped steer the project and hosted the TRANSMIT fellows through various placements:

EISCAT(European Incoherent Scatter Scientific Association), Sweden

Fugro N.V, The Netherlands

ICTP (International Center for Thoretical Physics), Italy

ISC-CNR (Institute for Complex Systems- Consiglio Nazionale delle Ricerche), Italy

Septentrio satellite navigation, Belgium Spirent Communications plc, United Kingdom

NovAtel Inc., Canada

Thales Alenia Italy

University of New Brunswick, Canada

UNESP - Universidade Estadual Paulista – Presidente Prudente, Brazil

Thanks are also due to all the reviewers who assisted with the making of this proceedings book. In particular we would like to acknowledge:

Marcio AQUINO (University of Nottingham – United Kingdom)

Yannick BÉNIGUEL (IEEA - France)

Alan DODSON (University of Nottingham – United Kingdom)

Fabio DOVIS (Politecnico of Turin - Italy)

Giorgiana DE FRANCESCHI (Istituto Nazionale di Geofisica e Vulcanologia INGV – Italy)

Roman GALAS (Technical University of Berlin – Germany)

Nicolai HLUBEK (German Aerospace Center – Germany)

Norbert JAKOWSKI (German Aerospace Center – Germany)

Tomislav KOS (University of Zagreb – Croatia)

Cathryn MITCHELL (University of Bath – United Kingdom)

Riccardo NOTARPIETRO (Politecnico of Turin – Italy)

Vincenzo ROMANO (Istituto Nazionale di Geofisica e Vulcanologia INGV – Italy)

Iwona STANISŁAWSKA (Space Research Centre - Polish Academy of Science – Poland)

Samo STANIC (University of Nova Gorica – Slovenia)

Andrzej W. WERNIK (Space Research Centre - Polish Academy of Science – Poland).

Riccardo Notarpietro
Politecnico di Torino – Department of Electronics and Telecommunications

Fabio Dovis
Politecnico di Torino – Department of Electronics and Telecommunications

Giorgiana De Franceschi
Upper Atmosphere Physics

Istituto Nazionale di Geofisica e Vulcanologia

Marcio Aquino
Nottingham Geospatial Institute, The University of Nottingham

Chapter 1

Data Management Strategy for GNSS Services — The TRANSMIT Project Case

Eleftherios Plakidis, Vincenzo Romano,
Luca Spogli and Giorgiana De Franceschi

Additional information is available at the end of the chapter

http://dx.doi.org/10.5772/58767

1. Introduction

TRANSMIT project is a Marie Curie Initial Training Network (ITN), funded under the EU FP7 framework [1]. The programme vision is to act as the enabler of the IPDM network [2] which will deliver the state-of-the-art to protect the range of essential systems vulnerable to ionospheric threats.

TRANSMIT's primary mission is to provide Europe with the next generation of researchers, equipping them with skills, through a multi-disciplinary, inter-sectorial, comprehensive, coordinated, industry-led training programme. The training offered, should enable the new researchers to understand in depth, the threats that ionosphere poses on modern technological systems, and more importantly on GNSS Precise Point Positioning (PPP) value chain [3], and respond to the needs of various stakeholders for robust counter-measures to deal with these threats. The secondary mission of TRANSMIT project is to develop real-time integrated state-of-the-art tools to mitigate the ionospheric threats, and make these tool available and accessible to the various stakeholders, via the "*TRANSMIT Prototype*.

In this chapter we concentrate on the definition of the "*data management strategy*" or in simpler terms a plan for data management. In theory, data management (hereinafter DM) is defined as a function that includes "*the planning and execution of policies, practices and projects*", with aim of "*acquiring, controlling, protecting, delivering and enhancing the value of data and information assets*" [4].

DM is typically organized into ten basic components or functions, each consisting of a family of activities that belong to one of four groups [4]; planning activities (P) that set strategic and tactical course for other DM activities, development activities (D), undertaken within the system development lifecycle, creating data deliverables through analysis, design, building, testing, preparation and deployment, control activities (C) or supervisory activities performed on an on-going basis and, finally, operational activities (O) to include service and support activities performed on an on-going basis.

At the heart of any data related activity is Data Governance (DG). DG is the core function of DM that guides how all other functions are performed and it can be defined as "*the exercise of authority and control over the management of data assets*" [4]. DG consists of two groups of activities, namely planning and controlling. There are seven planning activities that comprise the DG function, and are typically implemented sequentially. The first two are relevant to our discussion, which are to understand the data/information needs, i.e. of the IPDM prototype, and based on these needs **to** *develop a data management strategy*. Moreover, the execution of the DG planning activities, and thus the definition of data strategy, should be driven by both business and IT strategies [4]. In Figure 1, we present a novel framework that captures this dependency by depicting the different components of the overall TRANSMIT project's strategy and the relationship between them. This novel framework is based on a proper combination of the framework for IT, Business and Data strategies', described in [4], with the IT, IS (Information System) and Business Strategies' framework in [5].

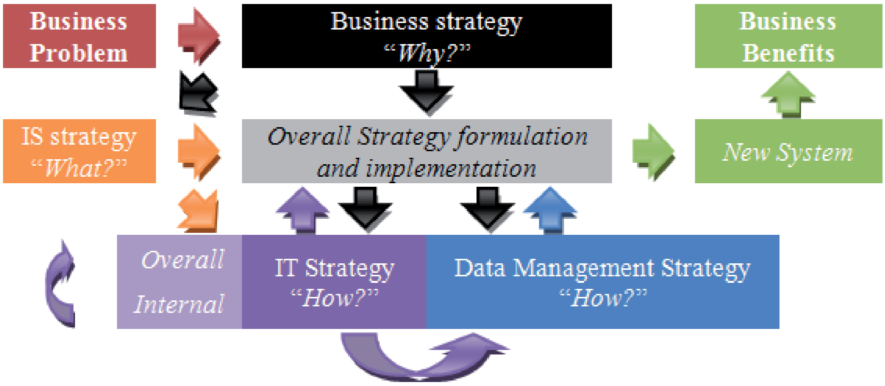

Figure 1. TRANSMIT project overall strategy approach

In sections 2, 3, 4 the TRANSMIT Business and IT/S strategies are described since are required inputs for the definition of data strategy. Finally, in section 5 we formulate the TRANSMIT data strategy, and provide in the closing section the state of art regarding the implementation status of this strategy.

2. Business strategy overview

The TRANSMIT business strategy presented in this section focuses on four themes which are the identification of the relevant business area and process, assessment of the business problem, a solution strategy and expected competitive advantage from the TRANSIT project, that can be further exploited by the future IPDM system, based on that strategy. The selection of appropriate business services (see section III) to support the given business problem is determined by the chosen business strategy and also drive the DG planning activities by providing the required data/information needs for which the data strategy is being developed.

The TRANSMIT project focuses on GNSS precise positioning business area. From a business perspective, PPP is a business process that outputs positions with high accuracy anywhere on the globe using a single GNSS receiver. To achieve that, a GNSS receiver on PPP mode relies on typical GNSS observables as well as input data products, i.e. precise orbits and clocks, provided by external entities, such as the International GNSS Service (IGS) [6]. More detailed information about PPP, can be found in [7] and [8].

In both single-(L1) and dual-frequency (L1+L2) PPP modes, and after the permanent removal of Service Availability (SA), the ionosphere has become the largest source of error that can potentially degrade the quality of the estimated user position. More specifically, and as described in [9], ionospheric scintillation, which is produced by ionospheric irregularities, affects GNSS signals in two ways, broadly classified as refraction and diffraction. A more thorough treatment of the effects of ionosphere on wideband GNSS signals can be found in [10].

At the application level, the refractive effect manifests as a group delay and phase advancement of the GNSS signal. A slower group delay velocity produces ranging errors while a faster phase velocity causes unexpected phase shifts. If the phase shifts are rapid enough, they can challenge the tracking loops in the receivers. In dual-frequency mode, the linear combination of observations and the formation of the so-called ionospheric-free observable, eliminates the biggest part, almost 99%, of this kind of ranging-error, however for very precise positioning, the remaining, higher-order terms need to be considered and compensated [11]. For the case of a single-frequency PPP mode, this ionospheric delay is typically corrected using available ionospheric models such as the Klobuchar, IRI and NeQuick ones [12], [13].

As far as the diffraction effect of the ionosphere is concerned, the situation is more complicated and influences the GNSS service availability. Compensation of the effect cannot be achieved, but only mitigation is possible. It should be stressed that in situations of severe diffraction, a total loss of signal at the receiver site can be caused, which make any mitigation technique useless. In these cases prompt warning of forthcoming strong signal scintillations, can provide valuable time to businesses to alter their service delivery strategy, e.g. switching from GNSS to other means of providing precise positioning.

There are different ways that TRANSMIT project could support GNSS service providers in dealing with the ionosphere as a potential risk. Here we refer to the lesson learned by collaborating with FUGRO Intersite B.V. [14], one of the biggest GNSS service providers which carries activities worldwide, focused on four key areas, namely Geotechnical, Survey, Subsea Services and Geoscience, and targeting markets such as the oil and gas, building and infrastructure, mining, renewable energy and other public and private sectors.

One of its main requirements towards the TRANMSIT project can be phrased as "*a business continuity planning (BCP) under severe scintillation regime*". This practically means the development of a plan which begins by firstly assessing Fugro's exposure to ionospheric threats, then requires the provision of effective prevention and recovery from them, while maintaining competitive advantage and value system integrity. An ionospheric risk management initiative should be part of such BCP, and as far as the TRANSMIT is concerned the chosen strategy was to mitigate ionospheric scintillation, targeting the PPP value chain, both at the hardware (receiver tracking) and software (stochastic model) levels, by incorporating into the process unique business services, enabled by the research conducted in two different fronts, as will be further discussed in the Information System strategy. Whether or not a full BCP will be finally realized by the TRANSMIT consortium is a decision which has not be made at the time of writing of this article.

To ensure the sustainability of the TRANSMIT endeavor, a clear differentiation of the TRANSMIT approach with respect to competitors have to be foreseen. In Figure 2, the *primary* strategic direction [15] that was chosen is the "customer intimacy" or "customer focus". This practically means that the business improvements offered in the form of services or products are tailored to the needs and processes of individual customers (i.e. Fugro) by solving their business problem. Product leadership, which implies continuous and rapid introduction of new products and services, was difficult to be achieved given the complexity of the business problem, the existing competition, such as NASA, ESA and NOAA just to name a few, and the nature of TRANSMIT project. In the next two sections however we will see how the operational excellence can be targeted/supported by the IS, IT and Data strategies, as a *secondary* improvement dimension, which in principle requires improvement/optimization of business performance.

Figure 2. TRANSMIT overall strategy orientations in order to create added value to the end-user and achieve a competitive advantage, based on the three dimensions defined in [15].

3. IS strategy

In broad terms, information systems (IS) strategy defines what kind of system is necessary to cover the business needs for the foreseeable future. It is based on proper analysis of the business, its environment and the general business strategy [16]. In this section we focus and outline some key features of the required TRANSMIT IS, and we outline the application portfolio [17] which contains the currently developing business services.

TRANSMIT IS will be realised as an *"internet-based, web-enabled, distributed system"* with the aim of providing *"decision support about selected ionospheric-related risks for the PPP business processes"*. The above definition captures many features of the system, is compatible with the business needs, i.e. BCP, and for more details on decision support systems (DSSs) the reader is directed to reference [18].

As far as the TRANSMIT IS is concerned the functionality has been split into 4 layers following the multi-tier architectural paradigm. The data and presentation layers consist of one tier each while the business layer consists of various tiers, deployed on the premises of the Institutions partners of the TRANSMIT project [1].

The TRANSMIT IS will act as the demonstrator of the capabilities (business services) developed from the research base of the programme. The "prototype" term implies that the system will be intentionally incomplete, i.e. will capture only the essential features of IPDM [2], and is to be modified, supplemented, or supplanted [19] in order to realize the desired future state. For its development various methodologies exist [20], however the one that represents more adequately the philosophy of TRANSMIT project, is the evolutionary [20] presentation [21] prototyping. This iterative methodology allows flexibility in the software development process so that it can adapt to changing requirements, and also convince end-users of the feasibility of the system, as shown schematically in Figure 3 below. TRANSMIT IS prototype is based on a consortium that brings together some of the biggest GNSS Rx manufactures and precise positioning service providers, to act as the end-users (e.g. Fugro) as well as leading research institutes and universities around the Europe to lead the system development and provide the different services as well as the initial system and user requirements.

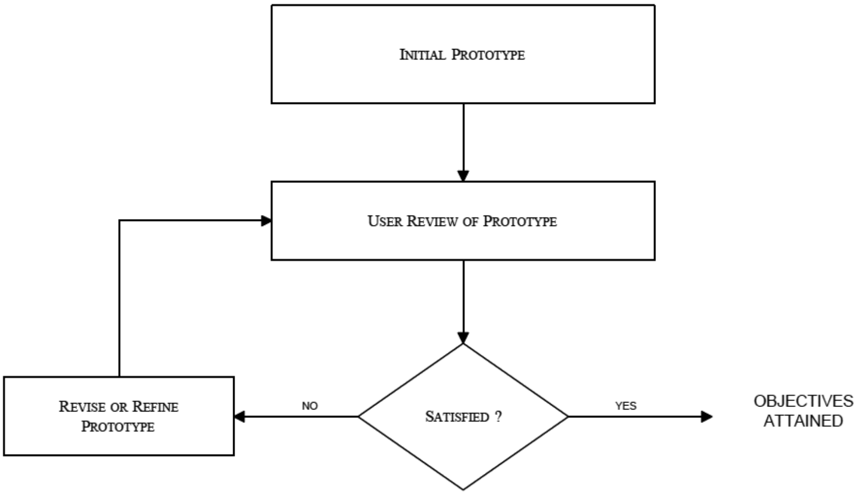

Figure 3. IPDM prototype system development methodology

For what concerns the application portfolio, i.e. business services, hereafter few examples are given as current services developed as part of the TRANSMIT IS with potential value in PPP business area for the end customers (e.g. Fugro). The first service aims to deliver improved estimation, after interference cleansing, and prediction of amplitude scintillation parameter, S4. The second concentrates on providing improved ionospheric delay estimation for different geomagnetic conditions. These services generally needs support and contributions from the TRANSMIT partners in terms of data (e.g. measurements from various ground-based and space-borne instruments, such as GNSS, ionosondes, and radio occultation) and modeling (e.g. advanced 3D tomographic techniques, forecasting, etc.

4. IT strategy overview

The IT strategy for TRANSMIT is split into two sections as shown in Figure 1: internal and overall. The internal is responsibility of the TRANSMIT partners participating to the TRANSMIT IS via a service [22]. The overall is defined by the developers of the prototype presentation layer. It is beyond the scope of this article to expand further on the overall IT strategy, however SOA (Service Oriented Architecture) is briefly recalled as one of the best practices that are used within the IT strategy and is known to generate real business value. Moreover SOA supports the so-called "*Workflow Systems*" (WSs) which allows for "*...building of software applications from a number of loosely coupled, heterogeneous, distributed services...*" [23] which is the case of TRANSMIT IS needs.

SOA represents a paradigm shift in applications design, which includes decomposing business functions and application features into a set of independent but cooperative subsystems or services. This helps businesses to gain flexibility, reuse, and interoperability [24], which in turn implies reduction of operational costs, acceleration of the development of new application by leveraging shared service capabilities, minimization of operating errors and reduction of risks and disruptions to business [25]. Finally, SOA can demonstrate business value and at the same time assess/fine-tune performance and model/modify processes through Key Performance Indicators (KPIs) [26].

No matter what the overall IT is going to be, SOA philosophy can be still applied for the development of various data services within the data layer. However it should be stressed that the development of the presentation and business layers dictated by the overall IT strategy, influences the developed of the data system which will realize the data layer, since it can pose unique requirements on the data system or require the design of new data services.

5. Results

The strategy adopted for data management in the frame of TRANSMIT is broad in scope to allow flexibility given the evolutionary prototyping development methodology of the TRANSMIT IS (see Figure 3). Such choice will also benefit the IPDM prototype development by providing the capacity to the data layer to accommodate further business and application layers needs in terms of data management services. We begin this section by discussing the data and information needs of the TRANSMIT IS which capture the state of the IPDM prototype at the time of writing of this article. These needs should be frequently re-evaluated and the data strategy should be kept up-to-date.

The initial survey conducted shows that the prototype system relies on a variety of proprietary data files in ASCII & Binary format, originating mainly from GPS and Radio occultation satellites as well as other Space-borne instruments. The input and output products have either spatial (e.g. global TEC maps) or temporal dimensions (e.g. complex GPS RF-data) or in some cases both (global TEC maps, predicted over time). Regarding the complex GPS data per se, the size of data files can generate a huge bottleneck, if data movement is scheduled during the operation of the distributed system. Finally, outputs from theoretical models, implemented in different programming languages, have to be also provided (such as the ionospheric models IRI and NeQuick2, just to name a few).

Based on the above needs we have developed a general **data management strategy** that includes, among the others [4]:

- A compelling vision for DM.
- The mission and long-term directional goals of DM.
- Strategy statement.
- Short-term SMART (Specific Measurable Actionable Realistic Time-bound) DM objectives.

The TRANSMIT DM vision and mission is to realize an intelligent DM system that will offer benefits to the enterprise and its customers and leverage existing IT/DM activities. The main mission of the DM function is to meet and exceed the data/information needs of all stakeholders in terms of data/information **availability, security and quality**. To pursuit our vision and fulfill our mission, our strategy is to establish the following data management initiatives:

- Data Architecture (DA) function
- Data Development (DD) function
- Data Operations (DO) function
- Content Management (CM) function
- Meta-data Management (MdM) function
- Data Security Management (DSM) function
- Data Quality Management (DQM) function

Finally, the short-term SMART DM objectives are listed below for each of the above-mentioned function.

Data Architecture (DA) objectives

- Define the "data model"

- Analyze and align with “business models”
- Define data technology architecture
- Define meta-data architecture

Data Development (DD) objectives

- Analyze information requirements
- Develop conceptual, logical and physical data models
- Design physical databases
- Design information products
- Design access services
- Implement development/test database changes
- Create test data
- Migrate and convert data
- Build and test information products
- Build and test data access services
- Validate information requirements
- Prepare for data deployment

Data Operations (DO) objectives

- Implement and control database environments
- Obtain externally sourced data
- Plan for data recovery
- Backup and recover data
- Set database performance service levels
- Monitor and tune database performance
- Plan for data retention
- Archive, retain and purge data
- Support specialized databases

Content Management (CM) objectives

- Implement management systems for acquisition, storage, access and security controls of unstructured data
- Backup and dispose unstructured data

- Retain and dispose unstructured data

Data Security Management (DSM) objectives

- Understand data security needs and regulatory requirements
- Define data security policy
- Define data security standards, controls and procedures
- Manage users, passwords and group memberships
- Manage data access views and permissions
- Monitor user authentication and access behavior

Meta-data Management (MdM) objectives

- Implement a managed meta-data environment
- Create and maintain meta-data
- Integrate meta-data
- Manage meta-data repositories
- Distribute and deliver meta-data
- Query meta-data

Data Quality Management (DQM) objectives

- Define data quality requirements
- Define data quality metrics
- Define data quality business rules
- Test and validate data quality requirements
- Set and evaluate data quality service levels
- Design, implement and monitor operational data quality procedures

6. Final remarks

In this paper we introduce the data management strategy formulated for the TRANSMIT project case. We hope that we achieved to clearly underline the overall requirements for both the IS/IT and data/information, and proposed feasible strategies to be implemented in TRANSMIT prototype in order to support the future GNSS services. To achieve the technical goals of TRANSMIT project, it is needed a flexible, secure, reliable, data system layer to be aligned with the business strategy and generate added value via operational excellence. The current development effort regarding the data system development is on the realization of meta-data repository, as well as on archiving of the necessary test-data, to be later on loaded on the database management system and become accessible from application developers. The data security function, has been implemented and its user interface can be accessed via [28]. Finally, data access services have been developed and tested for different application regimes.

Acknowledgements

Eleftherios Plakidis is one of the three Experience Researchers in TRANSMIT project [1]. The authors would like to thank Dr. Kees de Jong, and the rest personnel of Fugro Intersite B.V., for their valuable suggestions during Eleftherios Plakidis placement at the company's offices and the insights they offered regarding the business needs of the company of ionospheric related services. This interaction contributed very constructively towards steering the business strategy of the TRANSMIT programme into the right direction.

Author details

Eleftherios Plakidis, Vincenzo Romano, Luca Spogli and Giorgiana De Franceschi

Istituto Nazionale di Geofisica e Vulcanologia, Rome, Italy

References

[1] Training Research and Applications Network to Support the Mitigation of Ionospheric Threats – TRANSMIT. Retrieved January 05, 2014 from http://www.transmit-ionosphere.net/

[2] Ionospheric Perturbation Detection and Monitoring. Retrieved January 05, 2014 from http://ipdm.nottingham.ac.uk/

[3] K. Enßlin, "Enabling the GNSS downstream value chain," Retrieved January 05, 2014 from http://www.dlr.de/Portaldata/28/Resources/dokumente/RN/satnav/Treffen12-EuroTeleServ.pdf

[4] M. Mosley and M. Brackett, Eds., The DAMA guide to the data management body of knowledge (DAMA-DMBOK Guide). Bradley Beach, NJ: Technics Publications, LLC, 2010.

[5] A. Bytheway, Information management body of knowledge (IMBOK). Cape Town: Cape Technikon, 2004.

[6] International GNSS Service. Retrieved January 05, 2014 from: http://igscb.jpl.nasa.gov/

[7] Y. Gao, "What is precise point positioning (PPP), and what are its requirements, advantages, and challenges?," Inside GNSS, November / December, 2006. Retrieved January 05, 2014 from http://www.insidegnss.com/auto/NovDec06GNSSSolutions.pdf

[8] H. Marel, and P. Baker, "Single-versus dual-frequency precise point positioning," Inside GNSS, July / August, 2012. Retrieved January 05, 2014 from http://www.insidegnss.com/auto/julyaug12-Solutions.pdf

[9] P.M. Kintner, T. Humphereys, and J. Hinks, "GNSS and ionospheric scintillation: how to survive the next solar maximum," Inside GNSS, July / August, 2009. Retrieved January 05, 2014 from http://www.insidegnss.com/auto/julyaug09-kintner.pdf

[10] G.X. Gao, S. Datta-Barua, T. Walter, and P. Enge, "Ionosphere effects for wideband GNSS signals," ION Annual Meeting, Cambridge, Massachusetts, 2007.

[11] M.M. Hoque and N. Jakowski, "Ionospheric Propagation effects on GNSS signals and new correction approaches," Global Navigation Satellite Systems: Signal, Theory and Applications, Prof. Shuanggen Jin (Ed.), ISBN: 978-953-307-843-4, InTech, 2012.

[12] J. Vukovic and T. Kos, "Ionospheric time-delay models for GNSS," ELMAR Proceedings, pp.191-194, September 14-16, 2011.

[13] A. Angrisano, S. Gaglione, C. Gioia, M. Massaro, U. Robustelli, and R. Santamaria, "Ionospheric models comparison for single-frequency GNSS positioning," European Navigation Conference, 2011.

[14] Fugro world Wide. Retrieved January 05, 2014 from www.fugro.com

[15] M. Treacy and F. Wiersma. The Discipline of Market Leaders. Reading, MA: Addison-Wesley, 1995.

[16] A. Sharp and P. McDermott, Workflow modeling: tools for process improvement and applications development 2nd Ed. Norwood, MA: Artech House, 2008.

[17] J. Ward and P. Griffiths. Strategic Planning for Information Systems, 3rd Ed. Chichester, England: John Wiley & Sons Ltd, 2002.

[18] F. Burstein and C.W. Holsapple, Handbook on Decision Support Systems. Berlin: Springer Verlag, 2008.

[19] J. D. Nauman and M. Jesnins, "Prototyping: The new paradigm for systems development," MIS Quarterly, vol. 6, n. 3, Management Information Systems Research Center, University of Minnesota, 1982, pp. 29–44.

[20] M. Carr and J. Verner, "Prototyping and software development approaches" Retrieved January 05, 2014 from http://www.cb.cityu.edu.hk/is/getFile.cfm?id=55

[21] R. Budde, K. Kautz, K. Kuhlenkamp and H. Zullighoven, "What is prototyping?," Information Technology & People, vol. 6, n. 2-4, 1992, pp.89-95

[22] V. Romano et al., "eSWua: a tool to manage and access GNSS ionospheric data from mid-to-high latitudes", Annals of Geophysics, v.56, n.2, p. R0223, June 2013.

[23] Barker, A. and van Hemert, J., (2008), "Scientific Workflow: A Survey and Research Directions", In Wyrzykowski, R. and et al., editors, Seventh International Conference on Parallel Processing and Applied Mathematics, Revised Selected Papers, volume 4967 of LNCS, pages 746–753. Springer.

[24] HP Viewpoint Paper, "SOA Management – a must for operational excellence", 2009. Retrieved January 05, 2014 from h20195.www2.hp.com/V2/GetPDF.aspx %2F4AA2-9325ENW.pdf

[25] IBM, "Pursuing operational excellence in IT", 2008. Retrieved January 05, 2014 from https://www.ibm.com/services/us/cio/pdf/ciw03019usen.pdf

[26] Software AG Business White Paper, "What is the business value of SOA? Show it with KPIs", 2010. Retrieved January 05, 2014 from http://www.softwareag.com/jp/Images/SAG_SOA-KPI_WP_Oct10-web_tcm87-56981.pdf

[27] GEIA-HB-859, "Implementation Guide for Data Management", Government Electronics and Information Technology Association, 2006. http://www.dlr.de/Portaldata/28/Resources/dokumente/RN/satnav/Treffen12-EuroTeleServ.pdf

[28] TRANSMIT Data System INGV. Retrieved January 05, 2014 from http://transmit.rm.ingv.it/index.php

Chapter 2

The Concept of the TRANSMIT Prototype –Network Based Service for Mitigation of Ionospheric Threats to GNSS

Hiroatsu Sato, Nikolai Hlubek and Marcio Aquino

Additional information is available at the end of the chapter

http://dx.doi.org/10.5772/58770

1. Introduction

Global Navigation Satellite Systems (GNSS) are a crucial component in countless modern systems, e.g. in telecommunication, navigation, remote sensing and precision timing. The main threat to the reliable and safe operation of GNSS is the variable propagation conditions encountered by GNSS signals as they pass through the Earth's upper atmosphere (the ionosphere).

The ionospheric plasma can be perturbed by severe space weather conditions due to varying solar and geomagnetic activities. These perturbations come at a wide range of spatial and temporal scales as observed by ground based and space-borne instruments. The perturbations lead to formation of irregularities and disturbances in the ionosphere which can strongly affect the performance of GNSS positioning, by degrading its accuracy, reliability and availability. The scintillation phenomenon characterized by sudden signal fluctuations, for example, may cause GNSS operational outages.

Therefore it is important to assess the threat that space weather can pose to GNSS as well as estimate the strongest possible influence of the ionosphere. Enhanced research activities in this field are desired for the mitigation of the ionospheric impact on GNSS.

The European Commission FP7 funded project Training Research and Applications Network to Support the Mitigation of Ionospheric Threats (TRANSMIT) focuses on bringing together young researchers to undertake the aforementioned challenges for ionospheric impacts on GNSS. The research sub-projects under TRANSMIT aim to provide awareness of current ionospheric threats and improved solutions for the mitigation of ionospheric impacts for users of GNSS and related services and applications.

To highlight the research results of the TRANSMIT project, a prototype of a service is being designed and implemented for access via the internet. The TRASNMIT prototype can be considered as a milestone for the establishment of a Pan-European network for Ionospheric Perturbation Detection and Monitoring (IPDM) in the upcoming years (Jakowski et al., 2008).

In this paper we present an overview of the prototype service and the integration of the research results from TRANSMIT's sub-projects. The concept of data network over the project's partner institutions will be illustrated for optimal operation of the final product.

2. The TRANSMIT prototype

The TRANSMIT prototype is a web-based demonstrator and consists of three processors (called TRANSMIT processors) addressing six applications. The processors have been developed by the TRANSMIT research fellows exploiting the varied expertise in the project's partner institutions. TRANSMIT processors are designed to be able to exchange their outcomes and use them as inputs to other related applications via the prototype network. The design of data flow in the prototype system is characterized as a cross-institutional network approach. The main concept of the prototype network is to clearly divide the functions of the partner institutions. The user portal and demonstration, data archive and processor applications are hosted by different institutions distributed over Europe. The data flow design in the TRANSMIT prototype service is shown in Figure 1. The demonstration portal, denoted as institution C in the middle of the figure, receives queries sent by the users. The user queries can be parameter input or selection of particular ionospheric event that will be used in the processor applications.

Once the users define parameters and store them in the prototype portal, the prototype data transfer is triggered by requesting processing on the selected processor. The transfer of the parameters is forwarded directly to the processor hosting institutes denoted as B. The processor parses the parameters and determines whether it computes locally or requests the necessary data from the data archive hosting institute A. The processing time until the delivery of results of the applications varies among the processors. The variation of computation time will be estimated from less than one minute to a few hours. When a user selects a quick processing application, the results can be displayed on the prototype portal directly after the processing. Other processors with longer processing time require post-sending service. In this case the results will be accessible, for example, by implementing an email notification function.

Figure 1 also implies an advantage of this data transfer design for future application and project. The element blocks that form the network system for database and applications (A and B) can be renewable and replaceable. The new data archive, new processor hosting institutes or redesigned output from the existing processor will be easily integrated to be a part of the prototype system. For the TRANSMIT project, this flexibility would provide the young researchers opportunity to present their most recent result to the scientific and industrial community related to GNSS services. This functionality will be a key component in the

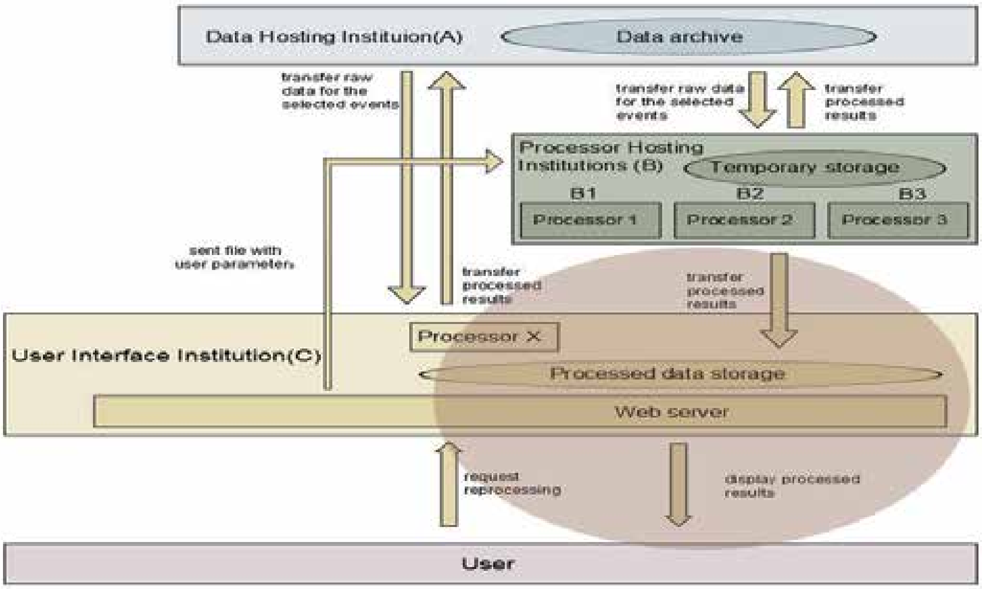

Figure 1. Schematic diagram of TRANSMIT prototype network and the modelled data flow

fundamental data management design for professional services involving multiple research organization such as the IPDM network.

3. TRANSMIT prototype processors

3.1. Processor 1: Scintillation index prediction by a Spline model

Small scale irregularities in the ionospheric plasma may cause fluctuations of the signal strength of radio waves e.g., GNSS signals. The S4 Index is a measure to describe the amount of amplitude variation in the received GNSS signals. This index is calculated by the standard deviation of the signal power received on the ground normalized to the average signal power. The S4 index is considered to reflect on the influence of radio wave scattering by electrons on the received signals. Therefore it is important to predict event of scintillation in terms of electron density in the Ionosphere. There have been numerous efforts made to model scintillation mechanisms, including measurement based statistical method and theoretical model using phase screening approach (Rino, 1979). The first TRANSMIT processor aims at developing an S4 index (and TEC value) prediction model over the European high to middle latitude regions. The advantage of this modelling is to combine the ground based measurements with in-situ (directly observed) plasma parameters by spacecraft orbiting over the concerned region. In this version of the model, the Dynamic Explorer 2 (DE2) satellite is selected as in-situ reference. The DE2 data provides local information of plasma parameters in the ionosphere including electron density and its fluctuation levels.

The developed model will be expressed with an analytical cubic B-Spline function that is derived from time, position, season and solar activity levels (Kp and solar flux value F10.7) as input parameters. The contribution from satellite measurements comes through a phase screening model to calculate S4. A correction method in propagation geometry is introduced for these regions (Priyadarshi & Wernik, 2013). Combining these inputs of ionospheric plasma parameters, the spline model gives a map of the predicted S4 values in geographical coordinates. This model will be compared to the observed S4 values from the receivers from arctic and middle latitudes. The measurement of scintillation is provided by stations from Spitsbergen, northern Norway, to Warsaw in Poland. The results will be visualized by 2D color-coded mapping of S4 or turbulence strength parameters. An example under a quiet geomagnetic condition is shown in Figure 2. The horizontal and vertical axes for the plot have been chosen to be magnetic local time and invariant latitude of the spacecraft. This comparison of the model and observation will give a convincing conclusion of modelling the scintillation over the European region. An advantage of using this model is that it may predict scintillation values which has good match with corresponding local plasma density even in the area that is not covered by the spacecraft. Thus the TRANSMIT processor 1 provides users a trustable tool to visualize scintillation estimate from the concerned solar activity level and geomagnetic conditions.

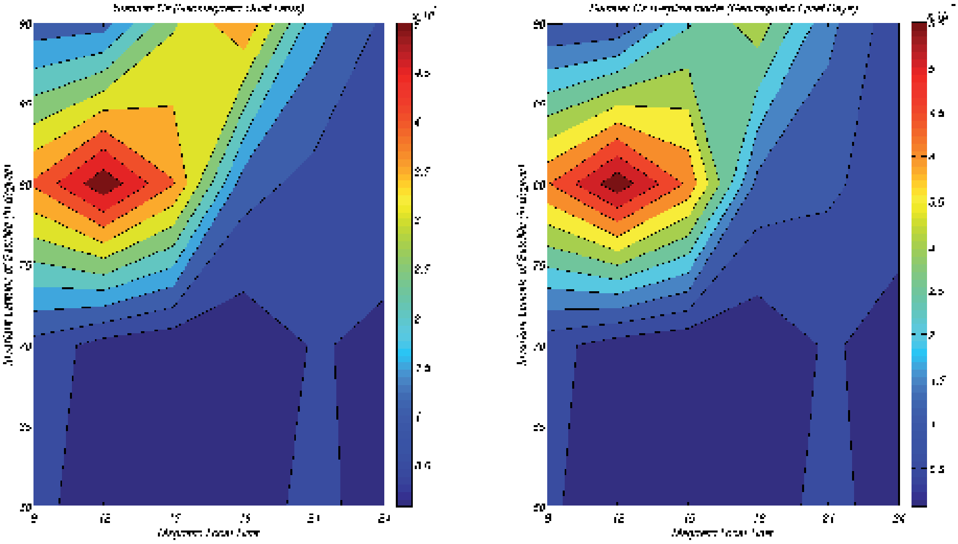

Figure 2. Example output from processor 1. Observation (left) and B spline model (right) result for turbulence strength parameters in quiet condition.

3.2. Processor 2: Improved tracking architecture and positioning error mitigation

As described in section 1, the radio signals from GNSS satellite can experience unexpected fluctuations in amplitude and phase when traveling through ionospheric irregularities. These unfavourable conditions may lead to errors in positioning application services. This can be a critical issue especially in absolute GNSS positioning solutions such as Precise Point Positioning (PPP), where a high level of accuracy is expected from the estimated coordinates. While the first TRANSMIT processor aims to model the S4 scintillation index from observed plasma parameters, the second processor investigates and mitigates the effects of ionospheric disturbances at receiver and positioning level. The focus is on the following research topics: i) investigate the effect of mitigation techniques on the accuracy of positioning applications. ii) design a robust receiver architecture that will be able to cope with different scintillation and radio frequency interference scenarios..

The effect of the application of the mitigation technique in the positioning accuracy of a GNSS receiver is shown in Figure 3. The variation in the receiver position accuracy computed with an improved stochastic model based mitigation technique is plotted during a scintillation event day. Here the three components of the positioning error in north, east and height are coloured in blue, green and red respectively. A couple of scintillation events have been observed on this day. The performance of the mitigation implementation is proven to be able to reduce the positioning error from the ground truth in comparison with the conventional results, i.e. when no mitigation technique is applied. The convergence time of the positioning error during the scintillation event is improved by this mitigation technique. This would be particularly evident for the height component when compared to non-mitigated results.

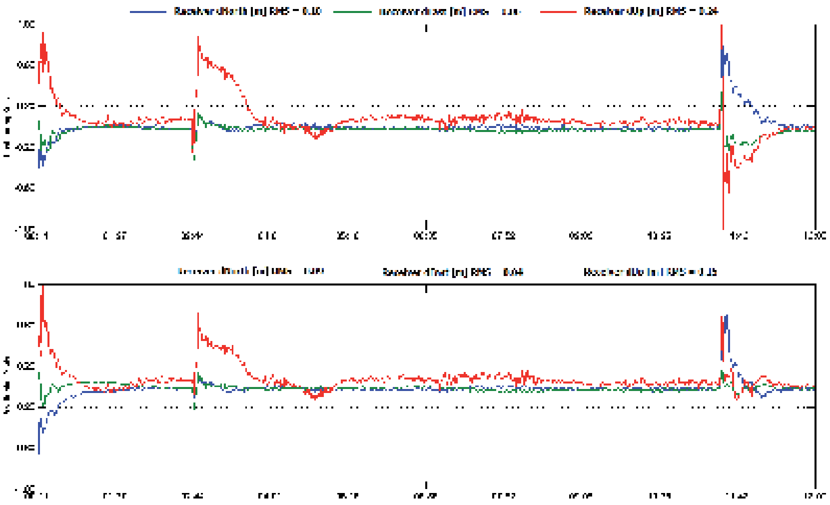

Figure 3. (top) The variation of PPP positioning error computed by TRANSMIT processor 2 without mitigation technique. (bottom) The same as the top but the mitigation technique is applied.

Processor 2 also deals with the design and implementation of a robust GNSS tracking architecture under different scintillation and radio frequency interference scenarios. It will output the performance of the receiver tracking scheme as well as characterization of the scintillation level according to the user's scenario specification. The designed scheme of the robust receiver features an adaptive Kalman filter based Phase Locked Loop (PLL) for GPS and Galileo signals. The software receiver implemented with this scheme is able to evaluate scintillation levels and use them to adapt the PLL loop filter. The parameters for scintillation detection are derived from the carrier phase spectrum with a dedicated algorithm. The algorithm has been examined by using real data from the receivers set in middle latitude regions. In simulation, the performance of the proposed architecture can be tested with different scenarios: scintillation and a combination of scintillation and various levels of other types of interference. Results of the comparison between our tracking scheme and a traditional fixed bandwidth PLL will be demonstrated for both the GPS L1 and Galileo E1 signals. This comparative performance study is made in terms of the following output parameters: C/N0, phase lock indicator and phase jitter. The algorithm implemented in the software receiver has been validated using the Septentrio PolaRxS scintillation monitor receiver as benchmark.

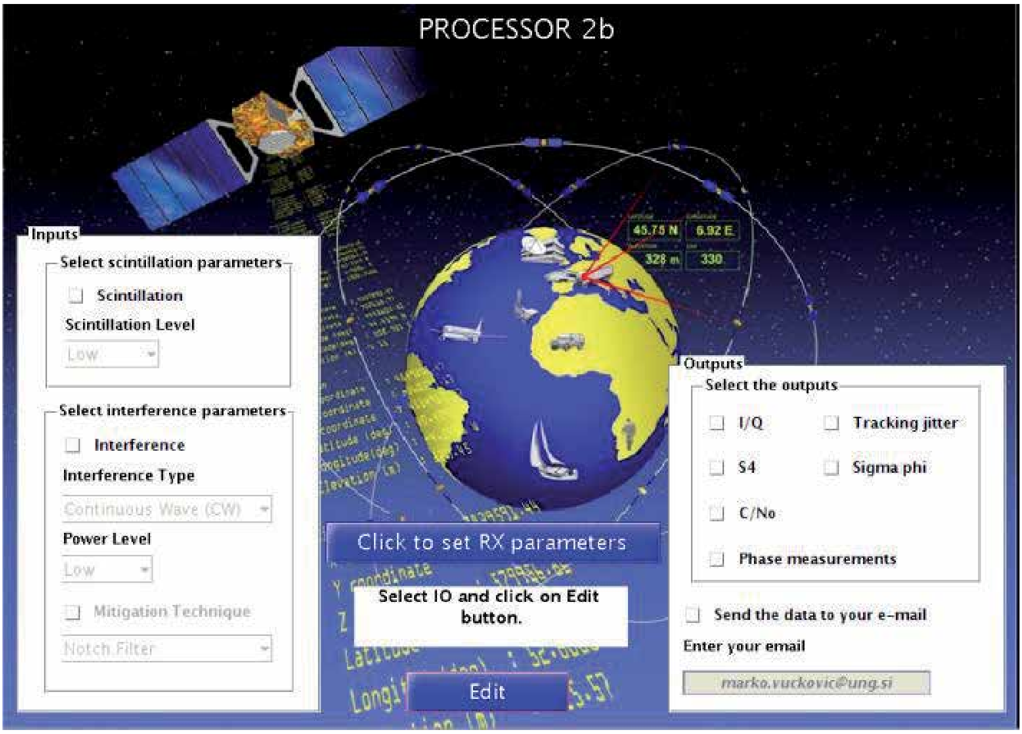

Inputs

Select scintillation parameters

☐ Scintillation

Scintillation Level: Low

Select interference parameters

☐ Interference

Interference Type: Continuous Wave (CW)

Power Level: Low

☐ Mitigation Technique

Notch Filter

Select IO and click on Edit button.

Outputs

Select the outputs

☐ I/Q ☐ Tracking jitter

☐ S4 ☐ Sigma phi

☐ C/No

☐ Phase measurements

☐ Send the data to your e-mail

Enter your email: marko.vuckovic@ung.si

Figure 4. A showcase interface for input and output parameters selection of TRANSMIT Processor 2 for robust receiver architecture.

On the graphical interface of TRANSMIT processor 2, the user can determine their specific scenarios, which will be used to affect the receiver performance. Figure 4 shows an example interface for showcasing the results. Once the scenario is defined, the processor will provide the related outputs in Matlab format, defining the performance of the receiver tracking scheme and characterizing the scintillation level. The PLL application is designed to provide pseudorange and phase measurements. These improved pseudo-range and phase measurements will be used as input in the PPP application.

3.3. Processor 3: Ionospheric models and applications

Prediction of potential scintillation event and other threats from our space environment has a crucial role for GNSS users in practical applications. Therefore modelling the ionosphere is an important approach for mitigation of ionoshperic threats. The purpose of the third TRANSMIT processor is to provide a new insight on existing ionospheric models. The starting point of this approach is to develop a new TEC prediction model with a data assimilation technique. Next, we make a comparative study of some widely used models, including our developed model, with a measurement database of global network of GNSS stations. Finally, as an application of the modeling approach, this processor demonstrates the error caused by the assumption residing in a common modeling method in Radio Occultation remote sensing for ionospheric research. The three applications forming the processor are designed to exchange outputs and inputs (See element B in the Figure 1).

The TEC model developed in TRANSMIT processor 3 employs computerized ionospheric tomography (CIT) and integrated Slant TEC measurements to estimate ionospheric electron density (Mitchell & Spencer, 2003). The main additions to the work by previous authors are a regularization technique using wavelet and physics based models. This approach will solve the major undermined problems in ionoshepric reconstruction that lack of data is the source of instability in numerical results. It is expected that this method can improve the imaging quality of the tomography as well as enabling short-term ionospehric forecasting

The second output of TRANSMIT processor 3 is a world map of the most suitable ionospheric model that fits observational data. To make a reasonable observation-based recommendation among the selected models, we use the CODE (Center for Orbit Determination in Europe) as the reference database. From this international GNSS service database, TRANSMIT processor 3 takes electron density data input from more than 200 stations (Hugentobler et. al., 2008). For the prototype service, we have selected the following four ionospheric models: Klobuchar model (Klobuchar, 1987), International Reference Ionosphere 2012 (IRI2012, http://iri.gsfc.nasa.gov), NeQuick2 (Nava et. al., 2008) and Neustrelitz TEC Model (NTCM, Jakowski et. al., 2010).The result of the comparison will be displayed in the form of global maps indicating the best fit model for a given user input of month of year, hour of day and observed solar radio flux (SF). At the current stage of development, computation of data from year 2010 to 2012 is ready to use for output.

Ionospheric models can be used as a reference to create electron density maps for Radio-Occultation (RO) remote sensing. The observational "real" and modeled ionosphere often show asymmetrical configuration of plasmas. For the standard inversion technique for RO, however, it is often assumed that the distribution of electrons is spherically symmetric in the ionosphere, which can be an effective and trustable assumption when the horizontal gradient of electron density is not significant. Such a condition can be satisfied typically in low solar activity conditions and a non-disturbed ionosphere. This assumption, however, may cause an untruthful retrieval of electron density when the spatial variation of plasma concentration is not negligible (Shaikh, et. al., 2014). In this case, the ionosphere is not spherical and should be treated as an asymmetrical distribution of plasma. The error that can be caused by this assumption will be demonstrated as the third output of TRANSMIT processor 3. Figure 5 illustrates the process for this application. The user of the processor can select specific geographical locations (star symbols) in the global map to view a plot showing expected electron density retrieval from the used models. The computed errors caused by the symmetry assumption are displayed against the aforementioned background models.

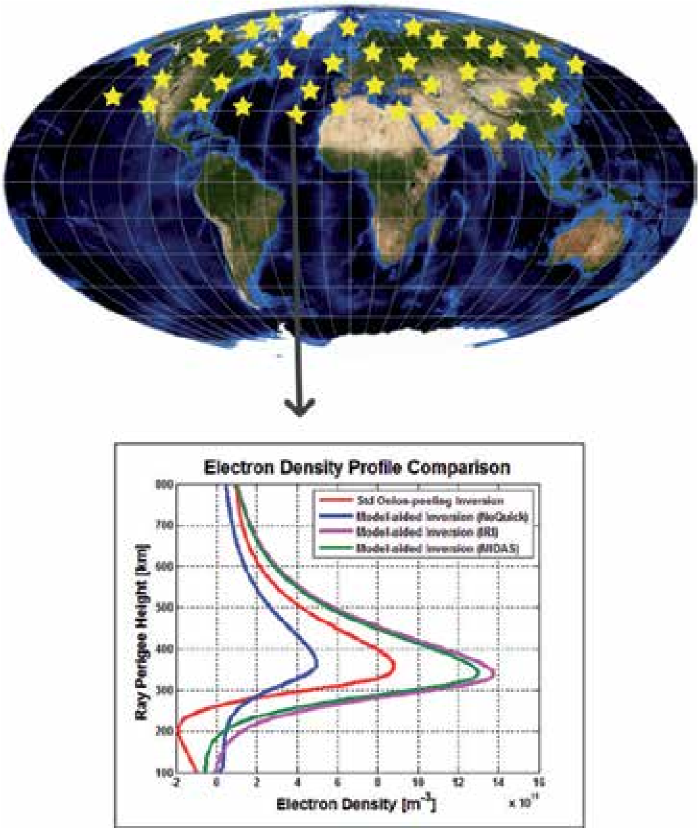

Figure 5. The procedure of location selection (star symbol) and electron density retrieval in the Processor 3 output.

4. Conclusions and future work

We presented the concept of the TRANSMIT prototype network and its application output from the processors for mitigation of ionospheric effects on GNSS. The processors in the prototype service will provide users awareness of current threats from the ionosphere. The data flow in the proposed cross institutional network design gives the TRASNMIT prototype simplicity and flexibility to present research result to the users. TRANSMIT prototype outputs are diverse and involve different scientific and engineering disciplines. The design of the final product should include an optimal interface for users with various interests related to GNSS based services. The processing time and the delivery method will need to be carefully estimated for each processor application result. A post-sending service such as email notification, for example, must be considered for time consuming processing applications. Establishment of data transfer within multiple institutions needs to be done under a coordinated and integrated scheme. When these challenges are overcome, the prototype service can be regarded as a milestone to evaluate the proposed IPDM network model in the real world. The TRANSMIT prototype has also other types of challenges as it has a cross disciplinary nature. The original purpose of the project is expected to be best achieved when scientists and engineers involved work together beyond their ordinary disciplines.

Author details

Hiroatsu Sato[1], Nikolai Hlubek[1] and Marcio Aquino[2]

1 Institute of Communications and Navigation, German Aerospace Center (DLR) Neustrelitz, Germany

2 Nottingham Geospatial Institute, the University of Nottingham, Nottingham, UK

References

[1] Hugentobler, U. Meindl, M. Beutler, H.G. Bock, R. Dach, A. Jäggi, C. Urschl, L. Mervart, M. Rothacher, S. Schaer, E. Brockmann, D. Ineichen, A. Wiget, U. Wild, G. Weber, H. Habrich, C. B. (2008). *CODE IGS Analysis Center Technical Report 2003/2004*.

[2] Jakowski, N., Aquino, M., Beniguel, Y., Bourdillon, A., De Franceschi, G., & Luntama, J.-P. (2008). On the establishment of a European "Ionospheric Perturbation Detection and Monitoring (IPDM) – Network". Nottingham: Ionospheric Scintillation: Scientific aspects, Space Weather application and Services,.

[3] Jakowski, N., Mayer, C., & Hoque, M. M. (2010). TEC MODELS AND THEIR USE IN IONOSPHERE MONITORING. *TEC Models and Their Use in Ionosphere Monitoring*. Barcelon: Beacon Satellite Symposium 2010.

[4] Klobuchar, J. (1987). Ionospheric Time-Delay Algorithms for Single-Frequency GPS Users. *IEEE Transactions on Aerospace and Electronic Systems*, 325– 331.

[5] Mitchell, C. N., & Spencer, P. S. J. (2003, December 25). A three-dimensional time-dependent algorithm for ionospheric imaging using GPS. *Annals of Geophysics*. doi: 10.4401/ag-4373

[6] Nava, B., Coïsson, P., & Radicella, S. M. (2008). A new version of the NeQuick ionosphere electron density model. *Journal of Atmospheric and Solar-Terrestrial Physics*, *70*(15), 1856–1862. doi:10.1016/j.jastp.2008.01.015

[7] Priyadarshi, S., & Wernik, A. W. (2013). Variation of the ionospheric scintillation index with elevation angle of the transmitter. *Acta Geophysica*, *61*(5), 1279–1288. doi: 10.2478/s11600-013-0123-3

[8] Shaikh, M. M., Notarpietro, R., & Nava, B. (2014). The impact of spherical symmetry assumption on radio occultation data inversion in the ionosphere: An assessment study. *Advances in Space Research*, *53*(4), 599–608. doi:10.1016/j.asr.2013.10.025

Chapter 3

Kalman Filter Based PLL Robust Against Ionospheric Scintillation

Melania Susi, Marcus Andreotti and Marcio Aquino

Additional information is available at the end of the chapter

http://dx.doi.org/10.5772/58769

1. Introduction

Global Navigation Satellite Systems (GNSS) are playing a key role in modern society finding applications in several crucial sectors. Strategic areas of applications include vehicular and personal navigation, aircraft and maritime navigation, location based and rescue services. However, despite its worldwide success and diffusion, GNSS is still a sensitive system vulnerable to failure and disruptions. This is of particular concern for user of safety of life services demanding high reliability, availability and continuity. The disruptions potentially threatening GNSS are usually classified as intentional and unintentional. Intentional disruptions, such as jamming, spoofing, are produced to deliberately impair GNSS receiver operation. Unintentional disruptions can be man-made interference, for example originating from satellite communications, TV broadcasting and Ultra Wide Band (UWB) communications, and natural interference, due to space weather events. One of the main natural threats to the reliability and availability of GNSS is represented by the non-stationary propagation conditions experienced by Radio Frequency (RF) signals inside the ionosphere. In particular small scale ionospheric irregular structures may refract and diffract GNSS signals producing random and fast variations in their amplitude and phase [1]. Amplitude scintillation manifests itself as instantaneous increases and decreases of the transionospheric signal intensity. This phenomenon, when severe, can lead to deep signal fading and, consequently, induce the signal to noise ratio to drop below the receiver tracking threshold. Moreover, phase scintillation could increase the Doppler shift so to render it larger than the phase lock loop bandwidth. As a consequence cycle slips or even a loss of lock could occur. Even if this phenomenon usually does not affect all satellites in view at the same time, involving only a portion of the sky, it may be able to degrade the final solution accuracy. Moreover if the healthy satellite links are not enough to provide a solution, outages in the GNSS operation could be experienced. A way to mitigate scintillation effects on GNSS is to increase the robustness of GNSS receivers, and in particular of the carrier tracking stage that is the receiver part most vulnerable to scintillation effects. In particular, the literature has shown that Kalman Filter (KF) based tracking schemes represent good candidates to replace traditional Phase Locked Loop (PLL) tracking algorithms in presence of scintillation [2], [3]. The main advantage of KF PLLs is the possibility to automatically optimize the loop filter, minimizing the phase mean square error. However, the effectiveness of KF based tracking algorithms is dependent on the use of a correct state space dynamic model to predict the parameters to be estimated, and on the monitoring of the actual measurement noise. Consequently, in presence of variable conditions, as in the case of scintillation, the initially assumed model could not be valid anymore, leading to a filter divergence. In this paper first of all the design and the implementation of a classical adaptive KF based PLL with variable measurement noise is detailed. In this scheme the measurement noise is a function of the carrier to noise ratio (C/N$_0$) which is computed in real time. Then, a second adaptive KF based PLL is proposed. The latter scheme tunes the covariance matrix, the measurement noise and the KF gains according to the working conditions, i.e. the detected level of scintillation. The weighting of the KF gain represents the element of novelty with respect to the architecture previously presented by the authors [4]. First tests carried out by using both simulated and real data affected by scintillation, respectively at high and equatorial latitudes, are presented herein. The remainder of this paper is organized as follows. Section 2 provides a general overview about scintillation effects on the tracking loop of a GNSS receiver. Section 3 describes the design and the implementation of the KF based algorithms examined herein. Section 4 details the methodology and the experimental set up exploited for the assessment of the above algorithms. Moreover, initial results are discussed. Finally, Section 5 draws some conclusions

2. Ionospheric scintillation

Ionospheric scintillation is determined by regions of enhanced or depleted [1] electron density affecting the propagation of Radio Frequency (RF) signals. The characteristics and the occurrence of these irregularities show a stochastic dependence on both spatial and temporal parameters, such as the local time, the season, the magnetic activity, the solar activity, and the geographical region of occurrence. Indeed, ionospheric scintillation is predominant at high latitude and equatorial regions. However the different ionospheric morphology of these two regions is responsible for different scintillation characteristics. While at high latitudes scintillation manifests itself as strong phase fluctuations and weak amplitude variations in the signal, at equatorial regions scintillation can show both significant phase fluctuations and amplitude fades. A GNSS signal affected by scintillation at the receiver input can be modelled as follows [4]

$$s(t) = A^{*}\delta A^{*}C(t)^{*}D(t)cos(2\pi f_{IF} + \phi + \phi_0 + \phi_i) + n(t) \tag{1}$$

Where

- A is the nominal signal amplitude,
- δA is the amplitude signal variation due to scintillation,
- $C(t)$ is the Pseudo Random Noise (PRN) spreading code,
- $D(t)$ is the navigation data,
- f_{IF} is the intermediate frequency,
- φ_0 is the phase variation due to scintillation,
- φ_i is the phase variation due to any other source apart from scintillation,
- $n(t)$ is the additive Gaussian noise.

To measure the level of scintillation two indices are widely used, namely S4 and σ_ϕ. S4 quantifies the level of amplitude scintillation and is computed as the standard deviation of the receiver power normalized by its mean value. σ_ϕ measures the phase scintillation and is obtained evaluating the standard deviation (in radians) of the detrended carrier phase, averaged over a specific temporal window, of 1minute of data. According to the temporal duration of the window used to perform the average, different versions of σ_ϕ can be defined. The widely used 60 seconds version of σ_ϕ is indicated as Phi60 [5]. The scintillation effects on the tracking loop of a GNSS receiver consist in an increase of thermal noise due to a decrease of C/N_0 and an increase of the phase error. The Power Spectral Density (PSD) of the phase error due to scintillation can be modelled as in [6] by an inverse power law given by the following

$$S_{\delta\varphi}(f) = \frac{T}{\left(f_0^2 + f^2\right)^{\frac{p}{2}}} \tag{2}$$

Where T is the spectral strength of the phase noise at 1 Hz and p is the spectral slope of the phase PSD, f is the frequency of phase fluctuations, f_0 is the frequency of the maximum irregularity size present into the ionosphere. Assuming that $f \gg f_0$ the (2) can be approximated by $S_{\delta\varphi}(f) = T f^{-p}$[6].

3. Designing a carrier tracking architecture robust under scintillation

The fast dynamics and the weak signals induced by scintillation can be particularly challenging for the PLL of a GNSS receiver. The latter has the purpose to compare the incoming carrier phase with its local replica and to minimize this error tuning the phase generated by the Numerical Controlled Oscillator (NCO). To increase the robustness of a GNSS receiver under scintillation, a careful selection of the PLL parameters is necessary. In order to follow the high dynamics induced by phase scintillation, short prediction integration time and wide carrier loop bandwidth should be preferred. On the other side, to minimize the noise induced by amplitude scintillation and to obtain accurate carrier phase measurements a long prediction integration time and a narrow carrier loop bandwidth should be selected. To cope with scintillation effects advanced tracking schemes have been proposed in the literature. For example FLL assisted PLL algorithms can be used with the purpose of exploiting the advantages of both tracking schemes [7]. In fact a FLL, although less accurate than the PLL, is less vulnerable to scintillation effects. Another possible approach consists in using the FLL as a backup solution in case of a loss of lock [8]. In order to select the optimum loop parameters an alternative strategy is to exploit adaptive tracking schemes which tune the loop filter bandwidth according to an optimization criteria depending on the estimated C/N_0 and signal dynamics [9]. Alternatively, the loop filter can be replaced with a KF [10] which allows selecting the optimum loop filters coefficients so to minimize the mean square error between the input signal and the replica generated by the NCO [2],[3]. However, in order to ensure the optimality of the KF, some assumptions should be fulfilled. First of all, the additive noise should be white and Gaussian, then the process noise covariance and the measurement noise should be known [11]. Indeed any mismodelling could lead to a solution degradation and, in the worst case scenario, to a filter divergence. In this section two KF based PLLs are proposed. Both schemes are based on the use a three state KF. The first architecture is a classical [2],[4] adaptive KF PLL with the measurement noise tuned according to the monitored C/N_0. This scheme will be indicated as AKF (Adaptive Kalman Filter) PLL in the rest of this paper. The second KF PLL scheme adapts in real time not only the measurement noise but also the covariance matrix and the weight of the KF gain, according to the detected scintillation phase variation level. This second scheme will be indicated with the acronym SAKF (Scintillation based Adaptive Kalman Filter) PLL. The latter is based on the algorithm presented in [4] but it includes also an algorithm to weight the KF gains, as detailed later on in this section. For both schemes the KF state vector, defining the parameters to be estimated, is composed of the following three terms

- $\delta\phi$, which is the difference between the input carrier and the phase of the local carrier provided by the NCO at the beginning of the integration period,
- δf, which is the difference between the Doppler shift of the input signal and the Doppler shift affecting the carrier provided by the NCO at the beginning of the integration period,
- δa, which is the difference between the frequency rates of the input signal and the carrier provided by the NCO at the beginning of the integration period.

Specifically, the proposed KF PLLs are based on the system model presented in [2] and it can be so described

$$\frac{d}{dt}\begin{bmatrix}\delta\varphi\\ \delta f\\ \delta a\end{bmatrix}=\begin{bmatrix}0 & 1 & 0\\ 0 & 0 & 1\\ 0 & 0 & 0\end{bmatrix}\begin{bmatrix}\delta\varphi\\ \delta f\\ \delta a\end{bmatrix}+\begin{bmatrix}1 & 0 & 0\\ 0 & 1 & 0\\ 0 & 0 & 1\end{bmatrix}\begin{bmatrix}w_{\delta\varphi}\\ w_{\delta f}\\ w_{\delta a}\end{bmatrix} \tag{3}$$

Where $w_{\delta\varphi}$, $w_{\delta f}$, and, $w_{\delta a}$ are the driving noise, respectively, of the phase, frequency, and the rate of the frequency variations. In order to define the process noise, the error covariance matrix **Q**, determined by the expected value of the noise vector, should be defined. The latter can be represented as a diagonal matrix whose elements are PSDs (S (•)) of the related process noise as in [10]

$$Q = \begin{bmatrix} S_{\delta\varphi} & 0 & 0 \\ 0 & S_{\delta f} & 0 \\ 0 & 0 & S_{\delta a} \end{bmatrix} \tag{4}$$

In the literature, KF based PLL architectures are traditionally designed assuming that the clock is the main contributor to the bias and the drift error sources and that, when the receiver is static, the frequency rate component error is only due to the dynamics along the Line Of Sight (LOS) between satellite and receiver [2],[3],[10]. Consequently, $S_{\delta\varphi}$ and $S_{\delta f}$ can be expressed using the standard expressions provided by the literature for the clock bias and drift spectrum noise [10] and defined as:

$$S_{\delta\varphi\text{-}clock} = (f_{L1})^2 \frac{h_0}{2} \tag{5}$$

$$S_{\delta f\text{-}clock} = (f_{L1})^2 2\pi^2 h_{-2} \tag{6}$$

The terms h_0 and h_{-2} are determined by the type of oscillator used by the receiver [10]. The AKF PLL presented herein is based on the traditional assumption that the main bias and drift contributions are due to the clock noise, and, consequently the related PSDs are given by (5) and (6). The SAKF PLL, however, takes into account both clock and scintillation error noise contributions so that $S_{\delta\varphi}$ and $S_{\delta f}$ are computed as the sum of the clock and the scintillation spectral noise as in the following

$$S_{\delta\varphi} = S_{\delta\varphi\text{-}clock} + S_{\delta\varphi\text{-}scintillation} \tag{7}$$

$$S_{\delta f} = S_{\delta f\text{-}clock} + S_{\delta f\text{-}scintillation} \tag{8}$$

In equations (7) and (8) the sum operation is valid since the clock and the scintillation noise are independent. Moreover, the phase error contributor due to scintillation is computed as $S_{\delta\varphi\text{-}scintillation}(f) = T f^{-p}$ by exploiting the approximation introduced in Section 2. Then, the frequency noise PSD is derived by the phase noise PSD as $S_{\delta f\text{-}scintillation} = f^2 S_{\delta\varphi}$ [7] where f represents the frequency of the maximum irregularity size inside the ionosphere. The value of f is set to 0.19 Hz, which is considered a typical value for this parameter [12]. Furthermore, the scintillation parameters p and T are computed by detrending the carrier phase obtained from the PLL and by evaluating respectively the slope and the strength of the carrier Fast Fourier Transform (FFT) computed at 1 Hz, as presented in [4]. For the work performed in this paper, the computation of the above parameters has been performed over a sliding window of 3000 samples corresponding to 3 seconds of GPS L1 C/A signal integrated every 1 ms. The general scheme of the proposed SAKF PLL is reported in Figure 1 where it is clear that the above scintillation parameters, computed by a dedicated block, are fed into the KF replacing the traditional PLL loop filter. In Figure 1 it can be seen that also C/N_0 is exploited to tune the KF. The use of C/N_0 as a KF tuning parameter is detailed further in this section.

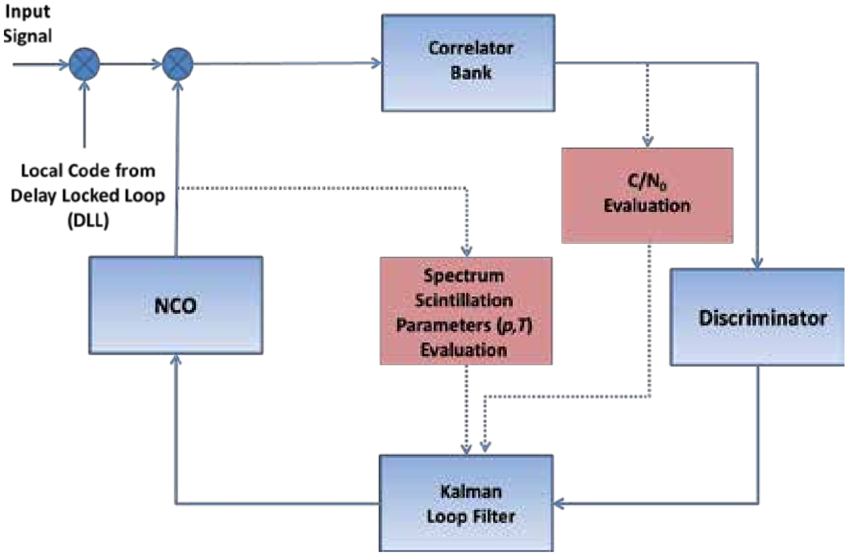

Figure 1. Scintillation based Adaptive KF PLL.

After defining the system dynamic model, the dynamic process measurements must be estimated [4]. This can be done using directly the correlator output as measurements. In this case the relationship between these measurements and the state vector is highly non-linear and, consequently, an extended iterative KF should be adopted [10]. Alternatively, the output of the discriminator can be used as measurement. Indeed the discriminator provides the estimates of the (aforementioned) parameters of interest from the correlator output. This second approach is adopted in this paper. Consequently, since an *atan* discriminator has been used, the measurement function is expressed as:

$$y = atan\left(\frac{Q}{I}\right) \tag{9}$$

With Q and I indicating the *in-quadrature* and *in-phase* components of the correlator output. Lastly, the observation noise variance can be obtained by computing the variance of the discriminator output which, for an *atan* discriminator, can be approximated [10] by

$$R = \frac{1}{2C/N_0 T_s}\left(1 + \frac{1}{2C/N_0 T_s}\right) \tag{10}$$

With Ts and C/N_0 indicating the time of integration and the carrier to noise ratio. From the system process and the measurement model, the KF predictor based PLL can be applied by computing the KF gain vector $\boldsymbol{K}$ as in [10] so to obtain the final update equation:

$$\frac{d}{dt}\begin{bmatrix}\delta\varphi^{'}\\ \delta f^{'}\\ \delta a^{'}\end{bmatrix}=\frac{d}{dt}\begin{bmatrix}\delta\varphi\\ \delta f\\ \delta a\end{bmatrix}+K\left(y^{'}-y\right) \tag{11}$$

Where the superscripts indicate the a posteriori state estimation. The KF gain values assume a fundamental role indicating how much the estimator should rely on the measurements [11]. The gain values can also be fixed a priori and selected in order to have a desired bandwidth as in [2]. The selection of a fixed gain vector is motivated by the reduction of the computational cost. However, the basic assumption of this approach is that the covariance matrix is not changing (assumption of steady state). It has been proved that a three state KF in steady state is equivalent to a third order loop [11]. Furthermore, in [2] it has been shown that, for different levels of scintillation, there is an optimum gain vector that optimizes the performance of the KF. Consequently, it can be advantageous to design an adaptive KF able to automatically tune the gains according to the scintillation level. With the above consideration in mind the SAKF PLL has been designed in order to have also variable gains changing according to the phase scintillation level. Specifically for the SAKF approach, the gain has been described as a function of Phi3. The latter has been computed as the standard deviation of the detrended carrier phase computed over 3 seconds (3000 samples of GPS L1 C/A signals that have been integrated over a period of 1 ms).

$$K^{'}=\alpha^{*}K(Phi3) \tag{12}$$

Where α is a constant value empirically determined and Phi3 is computed by a sliding window in order to get an update value at each time of integration. The above relationship does not directly include the effect of the signal intensity variation due to scintillation. However it should be considered that the KF gains are evaluated as function of R and, which in turn is computed from the signal's C/N_0. A more direct use of a KF gain weight directly depending on the intensity of the signal amplitude variations is currently under investigation.

4. Experimental set-up and sample results

This section describes the experimental set up and the methodology adopted to test the algorithms described in Section 3. Specifically, a first experiment, described in Section 4.A, has been conducted to assess the proposed tracking scheme by using simulated high latitude GPS L1 data affected by scintillation. Then, a second test, detailed in Section 4.B, has been carried out by exploiting real equatorial GPS L1 data affected by scintillation.

4.1. Test 1: High latitude scintillation scenario

The capabilities of a GSS8000 Spirent signal simulator available at the University of Nottingham have been exploited in conjunction with a physics based scintillation model, the SPLN

(St Petersburg, Leeds, Newcastle) [13], in order to recreate a high latitude scintillation scenario. The SPLN model requires as input the ionosphere background profile, in terms of electron density, obtained from the Nequick model [14], geomagnetic and solar activity indices, the spectral index, cross field outer scale and aspect ratios of irregularities, and the carrier frequency of the signal. These parameters were selected to recreate a severe high latitude scintillation scenario with the purpose to challenge as much as possible the carrier tracking schemes under test. Afterwards the model outputs, namely scintillation amplitude and phase variations, have been formatted in a user command (.ucd) file, a particular type of file which can be input to the Spirent signal simulator to modify its generated GPS L1 signal. Once the signal affected by high latitude scintillation was produced, the data was collected by using a Universal Software Radio Peripheral (USRP) N210 front end connected to the simulator. The USRP has been used in conjunction with a Low Noise Amplifier (LNA) and an external low noise OCXO (Oven Controlled Crystal Oscillator). Moreover, a Septentrio PolaRxS receiver, used as benchmark, has been also connected to the simulator along with the above front end through a signal splitter. In Figure 2, a picture of the test set up is shown. Specifically, we can see the interface of the Spirent simulator and the GNU Radio Software interface used to collect the data using the USRP N210.

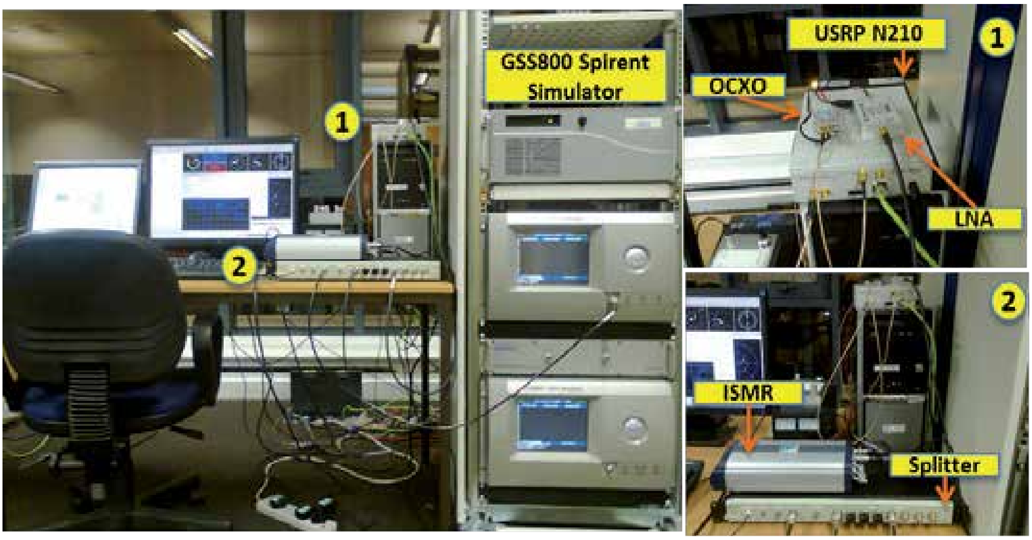

Figure 2. (Left) Experimental test set-up overview; (Right up) zoom of the USRP N210 connected to an external OCXO and to a LNA; (Right down) zoom of the splitter connecting the simulator output to a commercial ionospheric scintillation monitoring receiver (ISMR) and to the USRP N210.

Once captured, the collected data has been post-processed using a GNSS software receiver that included the implemented KF based tracking schemes described in Section 3 and a traditional third order PLL with fixed bandwidth of 15 Hz. The carrier tracking scheme has been set with integration time of 1 ms. Moreover, the spectral noise densities of the clock bias and drift in the KF based algorithms have been computed considering that an OCXO has been used for the data collection. In Figure 3, the S4 and Phi60 values recorded by the Septentrio receiver are shown for the simulated data set.

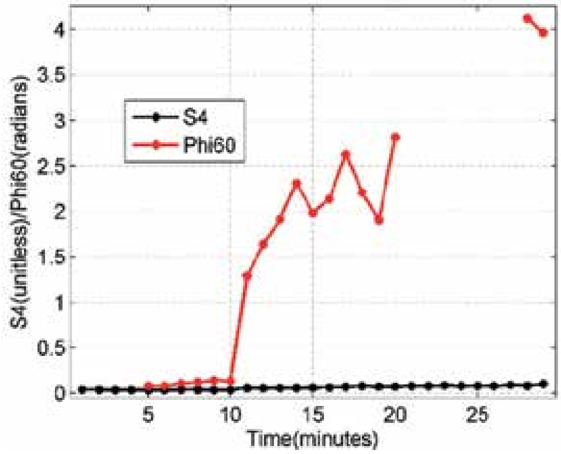

Figure 3. Scintillation parameters recorded by the Septentrio PolaRxS.

For Phi60 the first four minutes of data are missing since this time is required by the detrending filter to converge. As expected, the values of S4 are at noise level since high latitude scintillation is characterized by very weak amplitude fluctuations. On the other hand, for Phi60 very high values are observed, since, as previously underlined, intentionally an extreme scenario has been created in order to challenge the carrier tracking algorithms. In Figure 4 a comparison of the phase error obtained at the output of the discriminator for the three mentioned tracking schemes is reported.

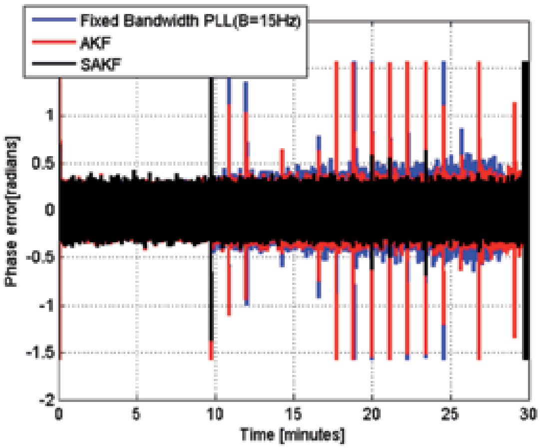

Figure 4. Phase error comparison

It can be observed that the SAKF shows the best performance in terms of noise reduction In Figure 5 the comparison between the phase jitter of the three different schemes is reported.

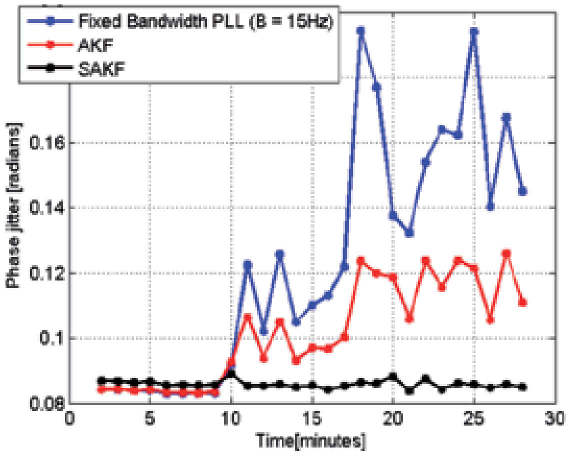

Figure 5. Phase jitter comparison

The phase jitter has been computed as the standard deviation of the phase error over temporal windows of 60 seconds. From this plot it is clear that the KF based schemes outperform the traditional PLL scheme.

4.2. Test 2: Equatorial scintillation scenario

A second test has been carried out by exploiting real equatorial data collected in Vietnam, Hanoi (21° 2' 0" N / 105° 51' 0" E) with a USRP N210 driven by a rubidium clock. Also in this case the data has been processed off-line using the three aforementioned tracking schemes. It should be noted that this time the KF algorithms have been tuned considering that a rubidium clock had been used for the data collection. A case of scintillation with moderate amplitude variation and high phase variation is taken into account for the assessment. The S4 and Phi60 values provided by the Septentrio PolaRxS for the considered satellite are shown in Figures 6.

Looking at the carrier Doppler in Figure 7 and at the phase jitter in Figure 8 we can see that the KF schemes allow reducing the noise if compared with the traditional PLL scheme and again the SAKF PLL achieves the best results.

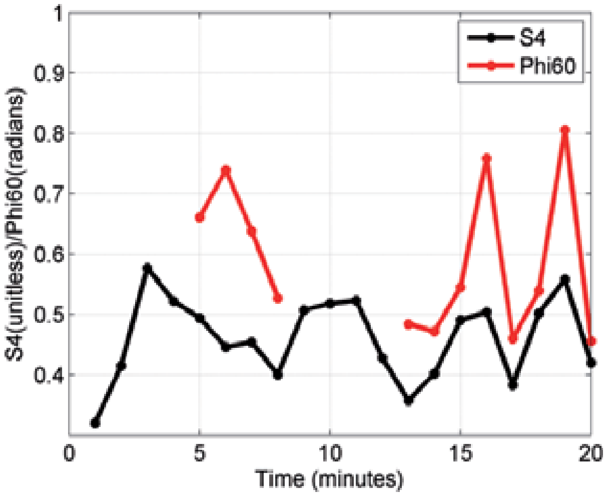

Figure 6. Scintillation parameters recorded by the Septentrio PolaRxS.

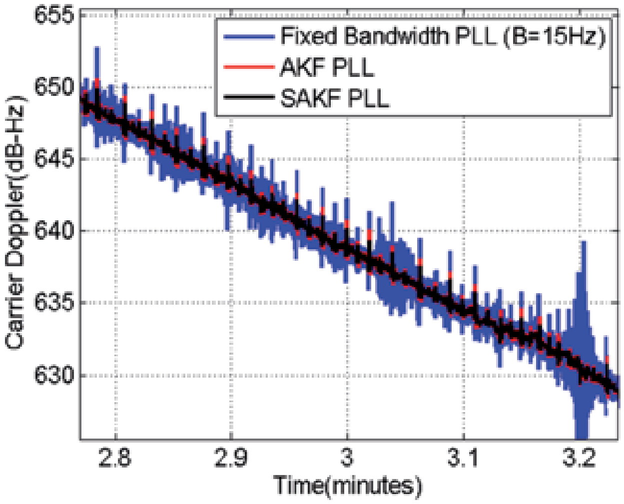

Figure 7. Carrier Doppler comparison.

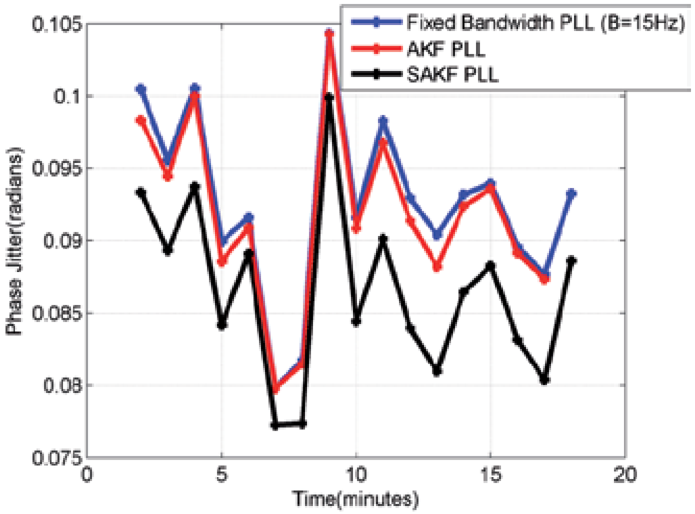

Figure 8. Phase jitter comparison.

5. Conclusions

This paper presented results that demonstrate that KF based PLLs achieve better performance than a traditional fixed bandwidth PLL when the tracked GNSS signal is affected by ionospheric scintillation. This paper also introduced and tested a novel adaptive KF tracking scheme. The novel PLL tracking scheme proposed here exploits widely used scintillation parameters to tune the covariance matrix and suitably weight the KF gains. First tests showed that the proposed tracking scheme enables a better performance by reducing the tracking noise and more closely following the signal dynamics during scintillation events. As future work, the algorithm presented herein will be assessed under a wider and more varied set of scintillation conditions. Moreover, further investigations are ongoing to modify the KF gain weight function in order to directly account also for the signal amplitude variation produced by scintillation.

Acknowledgements

The authors wish to thank Joaquim Fortuny (Joint Research Centre) for providing the real data affected by scintillation used in this work. The authors are also grateful to Rajesh Tiwari (Newcastle University) for providing the SPLN output used by to create the signal affected by high latitude scintillation. This research work is undertaken under the framework of the TRANSMIT ITN funded by the Research Executive Agency within the 7th Framework

Program of the European Commission, People Program, Initial Training Network, Marie Curie Actions.

Author details

Melania Susi[1], Marcus Andreotti[2] and Marcio Aquino[1]

1 University of Nottingham, UK

2 Novatel, Canada

References

[1] K. Yeh and C. H. Liu. Radio wave scintillations in the ionosphere, In *Proc.* of the IEEE, vol. 70, no.4, pp.324,360, April 1982

[2] C. Macabiau, V. Barreau, J.J. Valette, G. Artaud, and L. Ries. Kalman Filter Based Robust GNSS Signal Tracking Algorithm in Presence of Ionospheric Scintillations, in *Proc.* of ION GNSS 2012, Nashville, TN, September 2012

[3] M. Psiaki, T. Humphreys, A. C. Cerruti, S. Powell, and P. Kintner. Tracking L1 C/A and L2C signals through ionospheric scintillations, in *Proc.* of ION GNSS 2007.

[4] M. Susi, R. Romero, F. Dovis, M. Andreotti, and M. Aquino. Design of a Robust Receiver Architecture for Scintillation Monitoring, in *Proc.* of IEEE PLANS 2014, Monterey, California, May 2014

[5] A.J. Van Dierendonck, J. Klobuchar, and Q. Hua. Ionospheric Scintillation Monitoring Using Commercial Single Frequency C/A Code Receivers. In Proc.of ION GPS-93, Salt Lake City, UT, pp. 1333-1342, 1993.

[6] R.S. Conker, M.B. El-Arini, C.J. Hegarty, and T. Hsiao. Modelling the effects of ionospheric scintillation on GPS/satellite-based augmentationsystem availability. Radio Science 38 (1), 1001, doi: 10.1029/2000RS00260, 2003.

[7] Chiou T. Y, D. Gebre-Egziabher, T. Walter, and P. Enge. Model analysis on the performance for an inertial aided FLL-assisted PLL carrier tracking loop in the presence of ionospheric scintillation. In Proc. of the 2007 National Technical Meeting of The Institute of Navigation, pages 1276-1295, San Diego, CA, 2007.

[8] S. Fantinato, D. Rovelli, and P. Crosta. The switching carrier tracking loop under severe ionospheric scintillation. In *Proc.* Of the Satellite Navigation Technologies and European Workshop on GNSS Signals and Signal Processing, (NAVITEC), 2012 6th ESA Workshop on,pages 1-6, Noordwijk, The Netherlands.

[9] S. Skone, G. Lachapelle, D. Yao, W. Yu, and R. Watson. Investigating the Impact of Ionospheric Scintillation using a Software Receiver. In *Proc*. of ION GPS/GNSS, pages 1126-1137, Long Beach CA, September 2005.

[10] D. R. Salem, C. O'Driscoll, and G. Lachapelle. Methodology for comparing two carrier phase tracking techniques. GPS Solutions, vol. 16, pages 197–207, April 2012.

[11] R. G. Brown and P. Y. Hwang. Introduction to Random Signals and Applied Kalman Filtering, 3rd ed. USA: John Wiley&Sons, 1997

[12] B. Forte and S. M. Radicella. Problems in data treatment for ionospheric scintillation measurements. Radio Science, 37 (6), 1096, 2002.

[13] V. E. Gherm, N. Zernov, and H. J. Strangeways. Propagation model for transionospheric fluctuational paths of propagation: Simulator of the transionospheric channel. Radio Science, 40, 2005.

[14] S.M. Radicella and B. Nava. NeQuick model: Origin and evolution. Antennas Propagation and EM Theory (ISAPE), 2010 9th International Symposium, pages 422,425, Nov. 29-Dec. 2,2010.

Towards Analyzing the Effect of Interference Monitoring in GNSS Scintillation

Rodrigo Romero and Fabio Dovis

Additional information is available at the end of the chapter

http://dx.doi.org/10.5772/58768

1. Introduction

Electron concentration in the ionosphere affects GNSS (Global Navigation Satellite Systems) signals by introducing delays in their propagation. Such error can be corrected in part by making use of models of the background ionosphere when performing single frequency measurements, or entirely in the case of dual frequency measurements. In some cases electron density irregularities may appear that can disrupt further the propagation of the wave introducing fluctuations in amplitude and phase called scintillations [1].

How often GNSS signals are affected by scintillations depends on solar and geomagnetic activity, geographic location, season, local time and signal frequency. Amplitude scintillations cause signals to fade. Phase scintillations may induce a frequency shift in the signal carrier that in some cases can go beyond the Phase Lock Loop (PLL) bandwidth of the GNSS receiver. Both effects are very challenging for a receiver and may cause frequent cycle slips and losses of lock of the satellite signals during strong ionospheric events [2].

Ionospheric Scintillation Monitoring Receivers (ISMR) are specialized GNSS receivers able to track and monitor scintillations in order to collect data that can be used to model the phenomenon, study its affects at receiver level and possibly predict its occurrence in the future. Such receivers are able to measure the amount of scintillation affecting a satellite signal in both amplitude and phase by making use of correlation data from the tracking processing blocks. This is normally done by computing two indices: the S4 for amplitude scintillation and the phase deviation due to scintillations [3].

However, as more telecommunication systems are likely to work in frequency bands close to GNSS signals in the next years, monitoring of scintillation activity might be threatened by the presence of Radio Frequency Interference (RFI) in the operation area. It is of interest to study the effects these systems may have on the estimation of scintillation indices due to unintentional leakages of power out of their allocated bandwidth [4]. Robust tracking of GNSS signals under such conditions must be guaranteed and it must also be ensured as best as possible that the typical scintillation indices are not affected by the additional error source.

In this paper we deal with a specific environment of an ISMR where the monitoring of scintillation activity is threatened by the presence of interference. Section II offers some background on ionospheric scintillation measurements with GNSS receivers. Section III describes the interference scenarios. Section IV describes the set-up of a monitoring station deployed and installed in the city of Hanoi in Vietnam to collect real scintillating signals samples. Section V presents the results. Finally, conclusion and future work to be developed are summarized in Section VI.

2. Ionospheric scintillation measurements with GNSS receivers

The mathematical expression of the current GPS L1 C/A signal affected by scintillation can be written as:

$$S(t) = A\delta A(t) d_{L1}(t) c_{L1}(t) \sin\left(2\pi f_{L1} t + \varphi + \delta\varphi(t)\right) \tag{1}$$

Where A is the signal amplitude, δA (t) is the amplitude fluctuation due to scintillation, d (t) is the navigation data with a rate of 50Hz, c (t) is the PRN spreading code with period of 1ms, f_{L1} is the radiofrequency carrier, φ is the initial carrier phase and δφ (t) is the phase fluctuation due to scintillation. Scintillation is measured by 2 indices: S4 for amplitude scintillation and σφ (phase deviation) for phase scintillation. These are usually computed over an observation interval T_{obs}=60s, as described in [3].

The S4 index is the standard deviation of the Signal Intensity (SI) normalized by its mean value. It is calculated from the in-phase and quadrature-phase accumulation samples of the prompt correlator. The total S4 is calculated as:

$$S4_T = \sqrt{\frac{\langle SI^2\rangle - \langle SI\rangle^2}{\langle SI\rangle^2}} \tag{2}$$

Where <> represents the expected (or average) value over T_{obs}. If the carrier to noise density C/N_0 can be estimated during T_{obs}, it is possible to have an estimate of the S4 due to noise:

$$S4_n = \sqrt{\frac{100}{C/N_0}\left(1 + \frac{500}{19 * C/N_0}\right)} \tag{3}$$

The revised S4 without the noise contribution is obtained as:

$$S4 = \sqrt{S4_T^2 - S4_n^2} \tag{4}$$

The phase standard deviation index σφ is calculated as the standard deviation of the phase fluctuations due to scintillations, δφ (t) in (1). Such fluctuations correspond to the high-frequency portions of the carrier phase. Though it cannot be measured directly by the receiver, δφ (t) can be estimated by detrending the carrier phase measurements from the satellite signals. The method widely used for detrending is to pass raw 50Hz phase measurements through a sixth order high pass Butterworth digital filter with cut-off frequency of 0.1Hz.

3. Interference scenarios

Radio frequency interference is, among the different error sources that corrupt satellite navigation waveforms, a particularly harmful error since in some cases it cannot be mitigated by a simple correlation process. This is indeed a problem that may affect the detection of ionospheric scintillation when monitored by GNSS signals, and will be analyzed in several interference scenarios. The scintillating signal affect by interference is given by

$$S\_interf(t) = S(t) + i(t) \tag{5}$$

Where S (t) is a GNSS scintillating signal as defined in (1) and i (t) is the interference signal and can assume different forms depending on the system that generated it. Two types of interferences were generated and fed into the receiver along with the scintillating signal: A narrowband interference in the form of a Continuous Wave (CW) and a wideband interference in the form of a Chirp Signal (CS). Figure 1 shows the spectrum of an unperturbed GNSS signal along with the interfered versions.

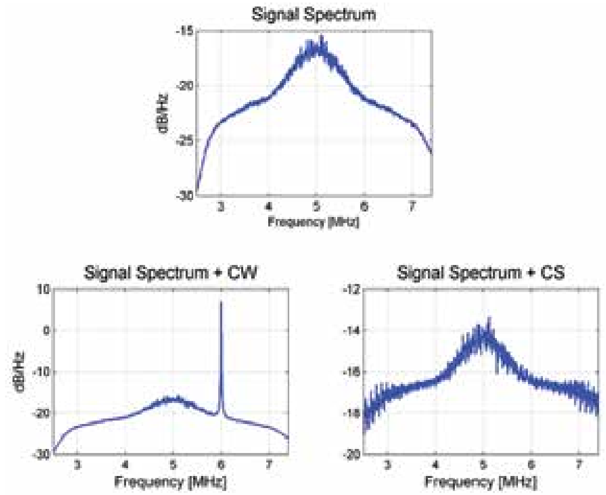

Figure 1. Spectra of Clean and Interfered Signals.

4. Scintillation data collection at Hanoi

A GNSS front-end based on a general purpose Universal Software Radio Peripheral (USRP) was installed in Hanoi, Vietnam (21° 2' 0" N / 105° 51' 0" E) for ionospheric scintillation data collection. The set up took place at the NAVIS Centre, Hanoi University of Science and Technology in collaboration with the European Joint Research Center based in Ispra, Italy and the NavSaS group of Politecnico di Torino / Istituto Superiore Mario Boella based in Turin, Italy. The installation consisted of an antenna AT1675-120W SEPCHOKE_MC with Spike Radome, an Ettus Research USRP Model N200 front-end with baseband low pass filter of 2MHz cut-off frequency, coupled with a 10MHz Rubidium reference oscillator, pc and hard drives as seen in Figure 2. Data were collected from February to September 2013 at 5 MSamples/sec in the L1/E1 band in a 20 minutes basis each day after sunset local time. A fully software receiver as presented in [5] and updated to process scintillating GPS signals was used to post-process the data coming from the USRP and calculate the scintillation indices.

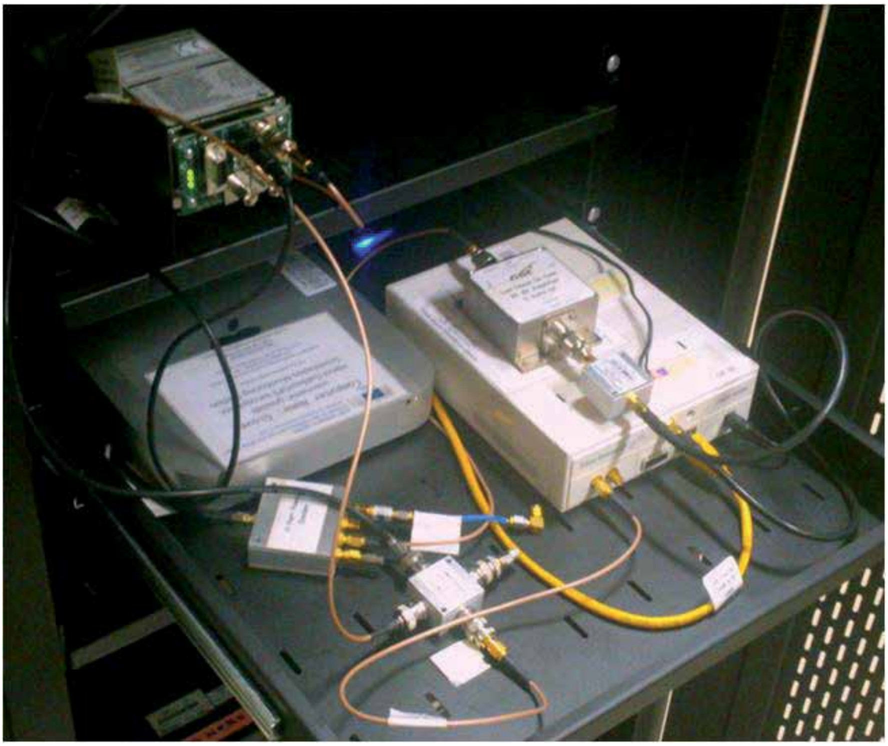

Figure 2. Hardware installed at Hanoi for collection of GNSS scintillating signals.

In parallel to the USRP data collections, a Septentrio PolaRx4 receiver was set up to continuously log regular observables such as C/N0, azimuth and elevation of available satellites from both GPS and Galileo. Through a replay process of the USRP logged data, scintillation indices are obtained from a Septentrio PolaRxS [6] for comparison purposes.

4.1. Scintillation observations

Figure 3 shows C/N_0 and correlator outputs for a GPS scintillating satellite, PRN23, acquired from a dataset during the 14 of March 2013, 1440UTC. As can be seen from the top plot, the so called focusing-defocusing effect of scintillation in the signal amplitude causes the power in the prompt correlator to fluctuate. The effect is also noticeable in the estimated C/N_0.

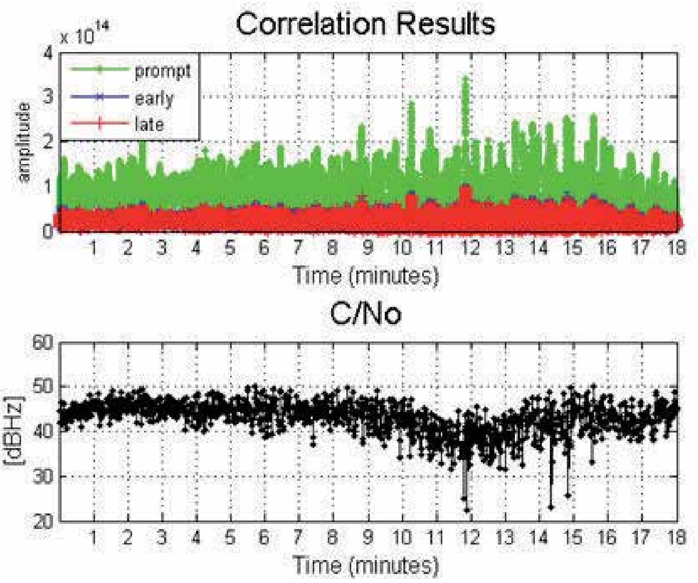

Figure 3. Correlation results (top) and estimated C/N0 (bottom) for GPS PRN23.

Figure 4 shows the estimated scintillation indices S4 and σφ (60s version) from the software receiver against the indices calculated by Septentrio's PolaRxS. For the software receiver, the tracking architecture consisted of a third order PLL with 12Hz bandwidth and integration time of 1ms. As can be seen there is a good agreement between the software receiver calculated indices with those from the PolaRxS, the latter used as a benchmark for our results. It is observed from the top plot of Figure 4 that the satellite was quite affected by scintillation, going from medium to very strong amplitude scintillation levels in the 18 minutes of processed data. To recall, S4 above 0.6 is considered strong in the literature.

The bottom plot of Figure 4 corresponds to the phase scintillation index σφ. There is no value shown for the index during the first four minutes of data processing due to the transient time of the detrending filter of the phase measurements. Severe scintillation activity may lead σφ in particular not being calculated at all if the satellite losses lock continuously.

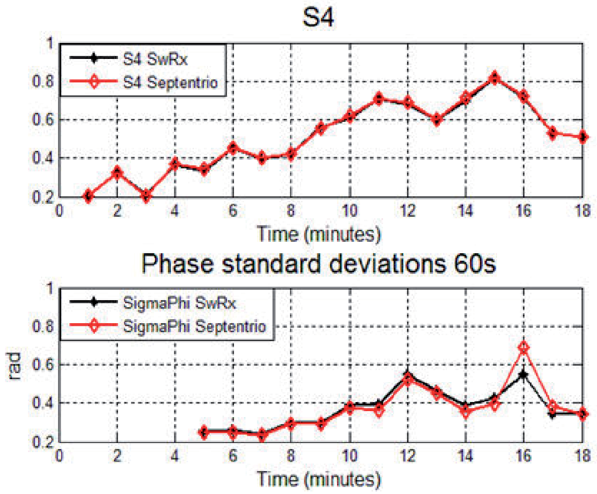

Figure 4. Software receiver computed S4 (top) and σφ (bottom) vs Septentrio PolaRxS for GPS PRN23

5. Results

The same dataset was contaminated by interference in order to observe its effect on the scintillation indices measurements. The operation was performed from minutes 5 to 14, as can be seen in Figure 5 for the comparison of the estimated C/N0 of one of PRN13 before and after the CW interference was injected. As observed in the figure, under interference GNSS receivers experience a drop in signal power and an increased variance in the signal amplitude.

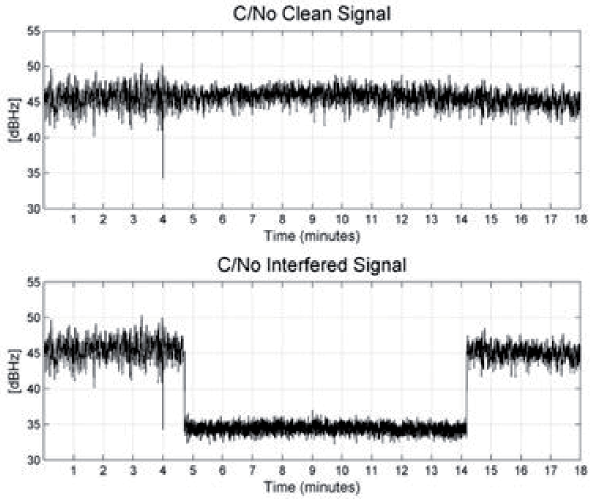

Figure 5. PRN11 C/N0 nominal case (top) vs. interfered case (bottom).

Figures 6 and 7 show the scintillation indices calculated under the effect of the CW and CS interferences for PRN11. As observed, the S4 index showed variations due to the interference, whereas the phase index remained largely unchanged. Given that the S4 index is calculated over the fluctuations of the signal intensity, it is indeed more vulnerable to additional error sources that also cause the signal power to fluctuate. However, how much the index will be affected if at all might ultimately depend on the relative power of the interference with respect to the signal, for how long it is active and the type of interference.

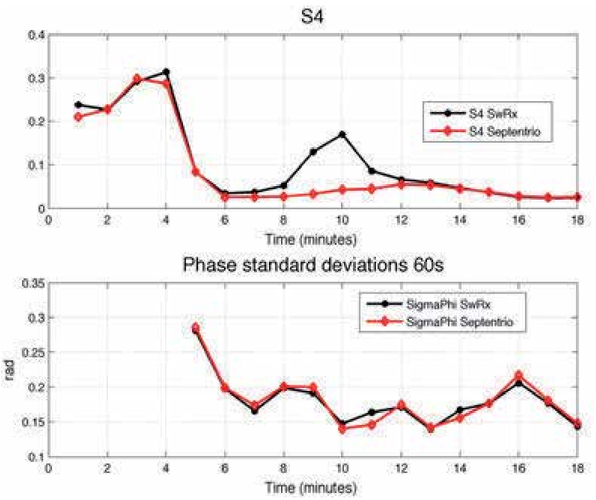

Figure 6. PRN11 S4 (top) and σφ (bottom) under CW interference.

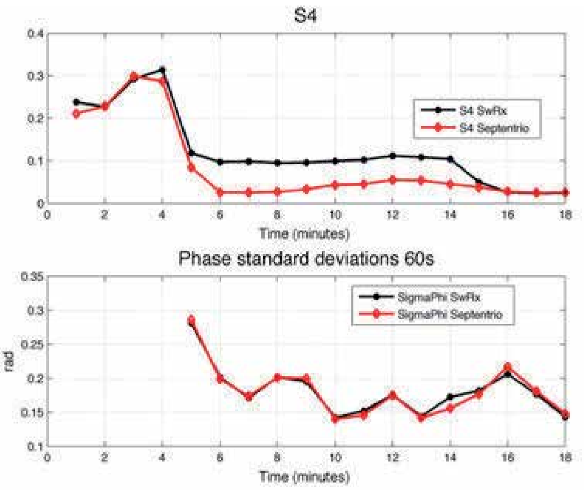

Figure 7. PRN11 S4 (top) and σφ (bottom) under CS interference.

To demonstrate, Figures 8 and 9 show the indices calculated for a different satellite, PRN13, in the same scenarios as before. It can be seen that indices for PRN13 barely changed. This is understandable as PRN13 presents a stronger level of scintillations than PRN11, so fluctuations introduced by the interference signals don't stand out as much as before.

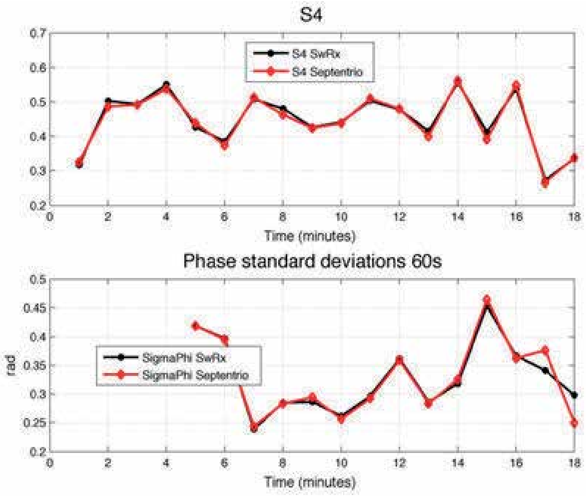

Figure 8. PRN13 S4 (top) and σφ (bottom) under CW interference.

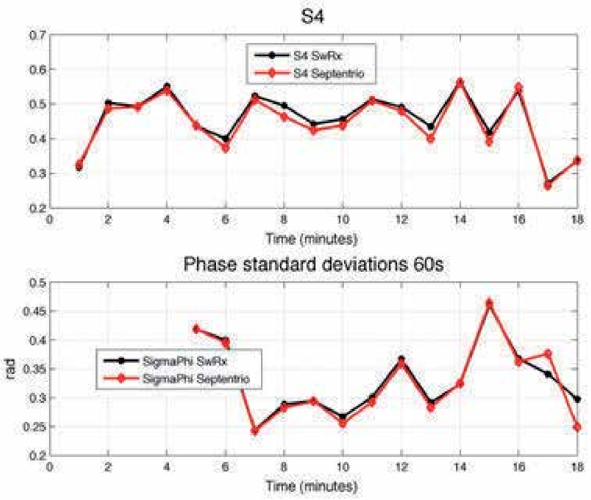

Figure 9. PRN13 S4 (top) and σφ (bottom) under CS interference.

In some cases, however, even if the effect of interference is not entirely reflected over the indices the combined effect of scintillation plus interference may prove too difficult for the receiver to track. This ultimately leads to a loss of lock of the satellite signal and a wrong estimation of the ionospheric scintillation, as shown in Figures 10 and 11 for PRN23, a satellite with strong scintillation. Compared to the previous case in Figures 4 and 5 where PRN23 was successfully tracked in its scintillation only scenario, it is noticeable now that at the point when scintillations are very high the receiver is not able to cope with both the scintillations and the added fluctuations introduced by the interference signal.

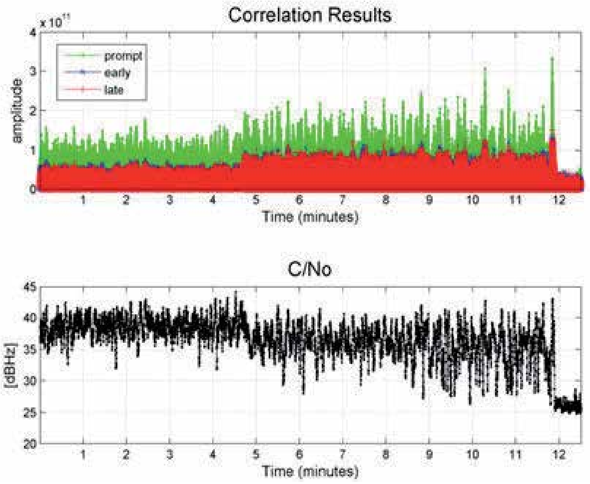

Figure 10. Correlation results (top) and estimated C/N0 (bottom) for GPS PRN23 under CW interference.

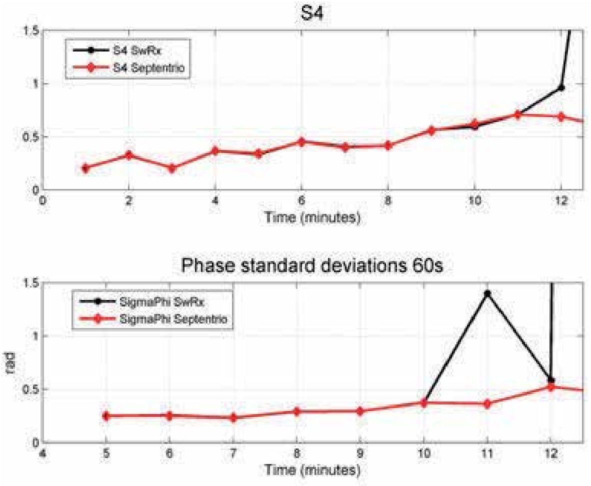

Figure 11. Software receiver computed S4 (top) and σ_φ (bottom) vs Septentrio PolaRxS for GPS PRN23 under CW interference.

6. Conclusion

A preliminary analysis of the effect of interference signals in the monitoring of ionospheric scintillation events was presented. Out of the two most common scintillation measurements with GNSS, the amplitude scintillation index S4 seems to be more susceptible to suffer variations due to the presence of external signals as compared to the phase deviation index. It was also shown that the combined effects of both scintillation and interference stresses the tracking blocks within the receiver to the point where losses of lock of the signals become more frequent. Nevertheless, the impact might ultimately depend on the level of scintillation of a given PRN and several characteristics of the interference itself: power, bandwidth and duration. Future work will continue to address the effect of interference on scintillation monitoring while taking into account the possibility to detect and mitigate the interference itself.

Acknowledgements

This research work is undertaken under the framework of the TRANSMIT ITN funded by the Research Executive Agency within the 7th Framework Program of the European Commission, People Program, Initial Training Network, Marie Curie Actions.

Author details

Rodrigo Romero* and Fabio Dovis

*Address all correspondence to: rodrigo.romero@polito.it

Department of Electronics and Telecommunications, Politecnico di Torino, Italy

References

[1] K. C. Yeh and C.-H. Liu. Radio wave scintillations in the ionosphere. In Proceedings of the IEEE, vol. 70, no. 4, 1982, pp. 324–360J.

[2] P. H. Doherty, S. Delay, C. Valladares, and J. Klobuchar. Ionospheric Scintillation Effects in the Equatorial and Auroral Regions. In Proceedings of the 13th International Technical Meeting of the Satellite Division of the Institute of Navigation (ION GPS 2000). Salt Lake City, UT. pp. 662–671.

[3] A. V. Dierendonck and Q. Klobuchar, "Ionospheric Scintillation Monitoring Using Commercial Single Frequency C/A Code Receivers," in Proc. ION GPS, 1993, pp. 1333–1342.

[4] B. Motella, M. Pini, and F. Dovis, "Investigation on the effect of strong out-of-band signals on global navigation satellite systems receivers," GPS Solutions, vol. 12, pp. 77–86, 2008.M. Young, The Technical Writer's Handbook. Mill Valley, CA: University Science, 1989.

[5] K. Borre. Software-defined GPS and Galileo receiver: A single-frequency approach. Boston: Birkhha©user. 2007.

[6] B. Bougard, J. Sleewaegen, L. Spogli, S. Veettil, S. & J. Galera. CIGALA: Challenging the Solar Maximum in Brazil with PolaRxS. In Proceedings of the 24th International Technical Meeting of The Satellite Division of the Institute of Navigation (ION GNSS 2011). Portland, OR, USA.2011. pp. 2572-2579.

Chapter 5

Computation of Scintillation Indices for the Galileo E1 Signals Using a Software Receiver

Marko Vuckovic and Samo Stanic

Additional information is available at the end of the chapter

http://dx.doi.org/10.5772/58783

1. Introduction

European Galileo system was designed to be inter-operable with the existing GPS and GLONASS systems with its Open Service (OS) targeted towards mass-market applications. The Galileo system provides signals in the so-called L frequency band. The frequency bands and central frequencies of E1 and E5a are common for both Galileo and GPS, i.e. E1/L1 has a center frequency at 1575.42 MHz and E5a/L5 has a central frequency at 1176.45 MHz, and thus GNSS receivers can seamlessly combine GPS and Galileo signals in their positioning and timing applications. Galileo will provide a variety of new, high accuracy services such as Commercial Service (CS), Safety of Life Service (SoL), Public Regulated Service (PRS) and Search and Rescue (SAR). In addition, a larger number of satellites will be available for the investigation of ionospheric threats and reception issues such as multi-path and interference. The use of new GNSS signals is expected to increase with the availability of the full Galileo constellation.

The ionosphere takes the upper part of the Earth's atmosphere which is ionized by solar radiation, extending from about 50 to near 1500-2000 km and completely encircling the Earth. Electron and ion densities in the ionosphere vary in complex manner with time, season, geographical location, solar and magnetic activity. The presence of small scale irregularities can disturb the radio frequency (RF) signals causing amplitude and phase fluctuations [1]. The amplitude fading or phase variations of RF signals (referred to as scintillations) can, among other effects, cause a receiver to lose lock to one or more signals broadcasted by the GNSS satellites. Very high scintillation activity levels may occur during solar maximum, in particular in the equatorial, polar and auroral regions [1].

One of the possibilities to investigate the influence of the scintillation on GNSS signals is using the so-called scintillation indices, S_4 and sigma phi (σ_Φ). They are used to estimate the fluctuations on the signal intensity and phase. This approach, which was adopted in this study, is given in the third section of this paper. The analysis was done using real Intermediate Frequency (IF) data collected by an experimental setup placed in Vietnam during a period of high solar activity. The IF data was fed into the MATLAB based software receiver capable of tracking the Galileo E1 signals after which the scintillation indices were estimated and compared with the results obtained by a professional Septentrio PolaRxS receiver.

2. Galileo signal structure

The Galileo OS system transmits GNSS signals in three frequency bands, E1, E5a/b and E6 (planned to be 1278.75 MHz since the signals in the E6 band have not yet been fully specified). A detailed description of the signals can be found in the Galileo OS Signal In Space Interface Control Document (SIS ICD) [2]. In its full constellation, the Galileo system will consist of 30 satellites (27 regular and 3 spare; but at the present only 4 satellites are available). New complex Galileo signals are not only stronger than the signals from GPS/GLONASS, but they also provide data free channels which should bring advantages in receiver processing for signal acquisition, code tracking, carrier tracking, and data demodulation.

2.1. Galileo OS E1 signal

The Galileo E1 OS band is located in the upper L-band with the frequency centered at 1575.42 MHz and a reference bandwidth of 24.552 MHz, the same as for GPS L1. The E1 signal uses the so called Composite Binary Offset Carrier CBOC, i.e. CBOC(6,1,1/11) modulation, defined as:

$$S_{E1}=\frac{1}{\sqrt{2}}e_{E1\text{-}B}(t)\left(\alpha sc_{E1\text{-}B,a}(t)-\beta sc_{E1\text{-}B,b}(t)\right)-\frac{1}{\sqrt{2}}e_{E1\text{-}C}(t)\left(\alpha sc_{E1\text{-}C,a}(t)-\beta sc_{E1\text{-}C,b}(t)\right). \tag{1}$$

The sub-carriers $sc_{E1\text{-}B}(t)$ and $sc_{E1\text{-}C}(t)$ are defined as:

$$sc_{E1\text{-}B}(t)=sng\left(sin\left(2\pi F_S t\right)\right), \tag{2}$$

$$sc_{E1\text{-}C}(t)=sng\left(sin\left(2\pi F_S t\right)\right), \tag{3}$$

where, Fs is a sub-carrier sampling rate frequency (1.023 MHz and 6.138 MHz for CBOC(6,1,1/11)), $\alpha=\sqrt{\frac{11}{10}}$ and $\beta=\sqrt{\frac{1}{10}}$ are parameters chosen in a way to combine the Power Spectrum Density (PSD) of two sub-carriers. The E1 signal consists of two channels: the in-phase I channel and the quadrature-phase Q channel. The I channel comprises both data and pilot channels taking into account orthogonality between them, i.e. the data channel sub-carrier is orthogonal to the pilot channel sub-carrier. The Q channel is reserved for the Public

Regulated Service (PRS). Ranging codes of the Galileo E1 signal are composed of primary and secondary codes by using the tiered code construction [2]. Primary codes for both data and pilot channels represent Pseudorandom Noise (PRN) codes with chip rate of 1.023 MHz and code length of 4092 chips, i.e. code length of 4 ms. The data channel is multiplied by the navigation data (NAV), while the pilot channel is multiplied by the secondary code instead of the NAV. The duration of the pilot channel is 100 ms. The secondary code is unique for all the satellites and has a length of 25 chips.

2.2. Galileo OS E5 signal

The Galileo E5a/b band is located in the lower L-band. The E5a frequency is centered at 1176.45 MHz (the same center frequency as GPS L5) and the E5b frequency is centered at 1207.14 MHz [2]. Both signals have a bandwidth of 20.46 MHz making the Galileo E5 OS the widest signal in the GNSS spectrum. If considered the entire E5 band an Alternative Binary Offset Carrier (AltBOC) modulation has to be taken into account. The AltBOC(15,10) is characterized by a very wide bandwidth and four complex channels modulated by four different PRNs, i.e. all four channels: E5aI, E5aQ, E5bI, E5bQ. E5aI and E5bI are data channels and they carry navigation messages, while EaQ and EbQ are pilot channels and they are data free. If the E5a/b signals are considered as separate frequency bands, the signals can be treated as Binary Phase Shift Keying (BPSK) signals. Since both E5a and E5b have two components (I and Q) the chip rate is 10.23 MHz for both data/pilot channels.

The ranging codes of the Galileo E5a/b signals are composed of primary and secondary codes. Duration of the primary codes are 1 ms and they can be generated as Linear Feedback Shift Register (LFSR) pseudo-noise sequence [2] or optimized pseudo-noise sequence also called 'memory codes'. On the other hand, the secondary codes are fixed sequences defined in hexadecimal form [2]. The data channels (E5aI and E5bI) have two unique secondary codes with a code length of 20 chips and 4 chips respectively. That means that the tiered code period for both data channels are respectively 20 ms for E5aI and 4 ms for codes E5bI. Different secondary codes are used for both pilot components for the all satellites. The code length for those codes is 100 chips and thus the pilot tiered code period is 100 ms.

3. Estimation of the scintillation indices

Estimation of the signal amplitude fluctuations induced by ionospheric irregularities can be done using the amplitude scintillation index S_4 [3]. The amplitude scintillation index is based on the signal intensity (SI) computation and it is given as:

$$S_4 = \sqrt{\frac{\langle SI^2 \rangle - \langle SI \rangle^2}{\langle SI \rangle^2}}, \tag{4}$$

where, <.> denotes an average value computed over a 60 second time interval and SI is taken to be the difference between the Narrow Band Power (NBP) and Wide Band Power (WBP) measure over the 20 ms time interval. According to [3], the NBP and WBP are given as:

$$NPB = \left(\sum_{i=1}^{M} I_i\right)^2 + \left(\sum_{i=1}^{M} Q_i\right)^2 \tag{5}$$

$$WBP = \left(\sum_{i=1}^{M} I_i + Q_i\right)^2 \tag{6}$$

I and Q represent the accumulated samples of the prompt correlator and period M is set to be 20 for Galileo OS E5a/b (it is the same as for GPS L1 C/A) and 5 for Galileo OS E1. To remove the errors originating from ionospheric effects, tropospheric effects and inaccuracies of satellite and user clocks, a detrending method has to be used [3]. For that purpose, the SI values are filtered by the 6th order low pass Butterworth filter, i.e. the SI is obtained by dividing the raw signal intensity by the filtered output:

$$SI = \frac{NBP\ \text{-}\ WBP}{(NBP\ \text{-}\ WBP)_{lpf}}\ . \tag{7}$$

To remove the ambient noise, the S_4 index given in Eq. (4) can be estimated as:

$$S_{4corr} = \sqrt{\frac{100}{\frac{S}{N_0}}\left[1 + \frac{500}{19\frac{S}{N_0}}\right]} \tag{8}$$

where, S/N_0 is the signal to noise density within the 60 seconds estimated as:

$$\frac{S}{N_0} = 10^{\frac{C}{10N_0}}\ , \tag{9}$$

and, C/N_0 is the carrier-to-noise ratio estimated from I and Q samples of the prompt correlator.

The phase fluctuation, on the other hand, is realized by σ_ϕ which represents the fluctuation of the carrier phase (φ). φ is the output of the carrier tracking loop and the phase scintillation indicator is given as:

$$\sigma_\phi = std(\varphi)\ , \tag{10}$$

where, ***std*** represents the standard deviation. The most common version of the sigma phi index is evaluated over 1 minute and it is indicated as Phi60 and it is used in this study. Finally, to avoid any false influence of the ionosphere scintillation activity, the process of detrending has to be used to remove all the fluctuations introduced by other factors (such as multipath, receiver noise, satellite clock errors and so on). The detrending method was done processing the carrier phase measurement through the 6th order high pass Butterworth filter with a cut off frequency of 0.1 Hz [3].

4. Results and discussion

The basic analysis of S_4 and Phi60 indices was performed using the real data affected by equatorial scintillation. To collect the IF data, a GNSS front-end based Universal Software Radio Peripheral (USRP) was used with an external 10 MHz rubidium clock as reference. The reason of using the rubidium clock lies in the fact that the Temperature-Controlled Crystal Oscillator (TCXO) integrated in the USRP is not suitable for scintillation monitoring process [3]. The system of an USRP model N200 front-end, an antenna AT1675-120W SEPCHOKE_MC with Spike Radome and a Septentrio PolaRxS receiver have been used as an experimental setup installed at the NAVIS centre, Hanoi University of Science and Technology, Vietnam in collaboration with the Joint Research Center (JRC) based in Ispra and NavSaS group of Politecnico di Torino based in Turin, Italy.

Data was collected from February till September 2013 in a period of 20 minutes basis each day in the E1/L1 band using 5 mega samples per second (MS/s), which is an optimal sampling rate for both GPS and Galileo E1 signals. The IF was zero since the USRP down-converts the signals and mixes them down to baseband [4]. The Septentrio PolaRxS receiver was used together with the USRP in order to collect the additional data, such as azimuth and elevation angles, as well as C/No of the satellites in view. Finally, the data obtained by the USRP front-end was played into the Septentrio PolaRxS receiver and the scintillation indices were estimated and used as a reference case in this study. The basic analysis of the scintillation indices has been done only for a limited data set, i.e. from March 14 2013 at 14:40 LT, where among GPS signals, two Galileo signals were available.

The CBOC is usually used in the conventional Galileo receivers but this requires higher sampling rates and more complex 4-level local replica [5]. To avoid this, the Galileo E1 signals have been treated as a Binary Offset Carrier (BOC), i.e. BOC(1,1). The acquisition and post-processing algorithm used for analysing the Galileo E1 signals are based on a modified version of MATLAB Borre's software receiver given in [6] and most commonly used tracking parameters are given in Tab. 1.

PLL filter order	Third-order
PLL bandwidth	10 MHz
PLL discriminator	Early minus late (E-L)
Integration time loop	4 ms

Table 1. PLL Loop tracking details

The block diagram shown in Fig. 1 represents a typically used tracking architecture in conventional GPS receivers and it is also used for Galileo. A third-order PLL loop was chosen to cope better with the fast fluctuations which can occur under scintillations. Both DLL and PLL loop discriminator values were filtered to reduce the noise and thus produce the correct estimate of the input value. According to this, a third-order loop filter was used [7]. After selecting the proper loop filter bandwidth and the integration time interval, the filtered values were used as an update for the Numerically Controlled Oscillator (NCO) to adjust the code frequency and carrier phase error.

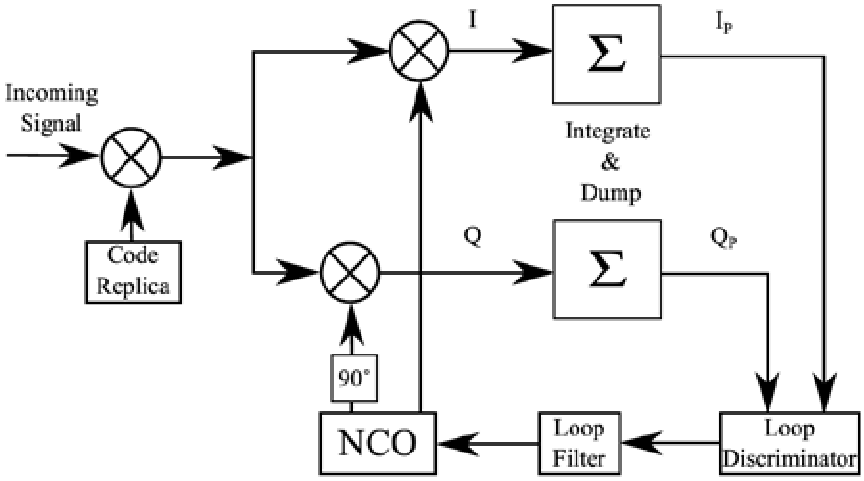

Figure 1. Carrier phase tracking loop

The same tracking parameters were used for both E1b and E1c channel. Third-order Phase Lock Loop (PLL)/ Delay Lock Loop (DLL) were chosen with bandwidths of 10 Hz and 5 Hz respectively. Integration time is 4 ms due to the duration of the primary codes. The carrier phase discriminator was set to be an atan(Q/I) [6] and the code discriminator was chosen to be a coherent early minus late power.

The data used in this study consists of both GPS L1 and Galileo E1 signals with different levels of scintillation. Fig. 2 shows S_4 values for four selected satellites, two GPS and two Galileo, estimated by the Septentrio receiver.

Accordingly, the Galileo E1 PRN 11 and PRN 12 as well as GPS PRN 19 were not affected but GPS PRN 23 shows a satellite link with a very high level of scintillations. Fig. 3 shows the Phi60 values for the same satellite links used for the S_4 estimated by the Septentrio receiver. As expected, higher values of the Phi60 are only for GPS PRN 23 due to the fact that for the equatorial scintillations the amplitude and phase scintillations are correlated [8].

In respect of the Galileo E1 satellites, the level of equatorial scintillations seems to be very low. Fig. 4 and Fig. 5 show the comparison of S_4 values obtained by the software receiver and values directly recorded by the Septentrio PolaRxS. In both figures the S_4 values for Galileo E1c PRN

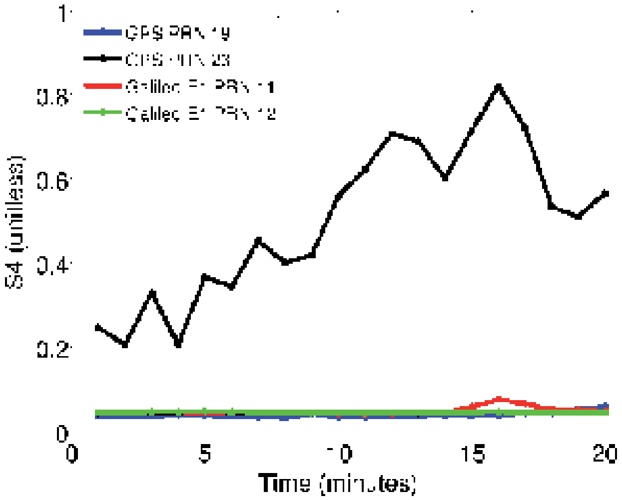

Figure 2. S_4 values obtained by the Septentrio PolaRxS receiver for GPS PRN 19 and PRN 23 and Galileo E1 PRN 11 and PRN 12 satellites. Higher S_4 values, up to 0.8, were observed only in GPS.

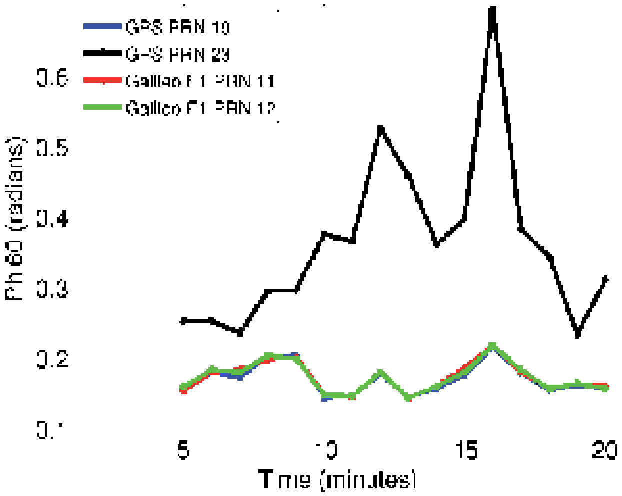

Figure 3. Phi60 index values obtained by the Septentrio PolaRxS receiver for GPS PRN 19 and 23 and Galileo E1 PRN 11 and 12 links. Higher values of Phi60, below 0.8 radians, were observed only for the GPS PRN 23. For the other satellites Phi60 was below 0.2 radians.

11 and PRN 12 signal almost overlap those obtained from the Septentrio receiver; however a significant deviation was observed for Galileo E1b.

Finally, a very good correlation was found between the estimated Phi60 values and those obtained by the Septentrio PolaRxS receiver as shown in Fig. 6 and Fig. 7.

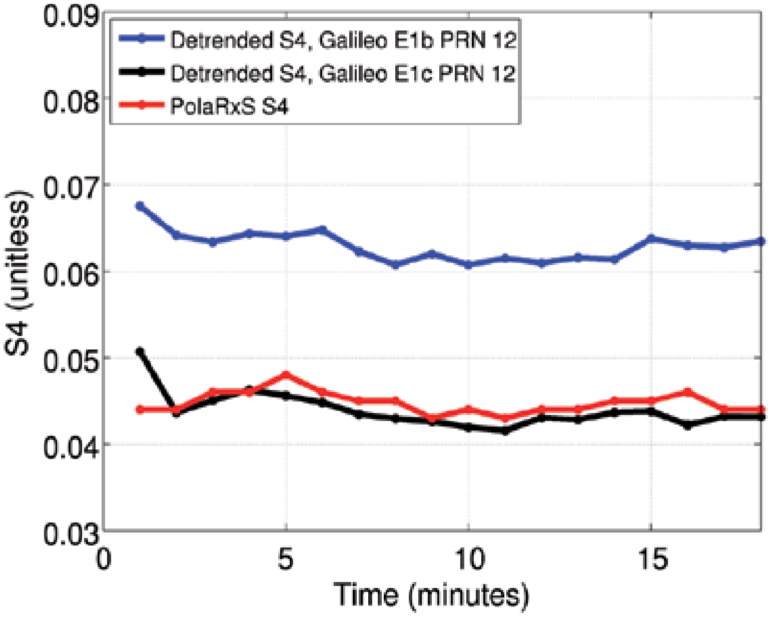

Figure 4. Comparison of S_4 values obtained by the Septentrio PolaRxS receiver and estimated values of Galileo E1b/c PRN 12 obtained by the software receiver.

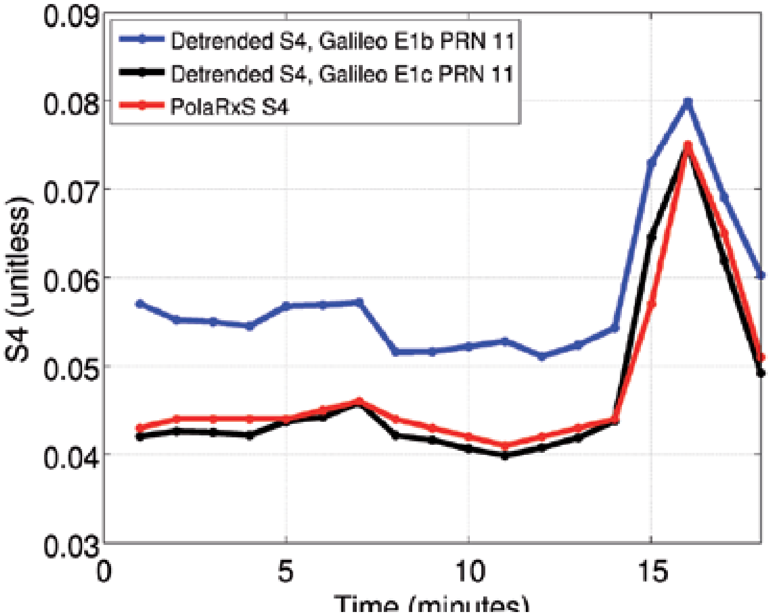

Figure 5. Comparison of S_4 values obtained by the Septentrio PolaRxS receiver and estimated values of Galileo E1b/c PRN 11 obtained by the software receiver.

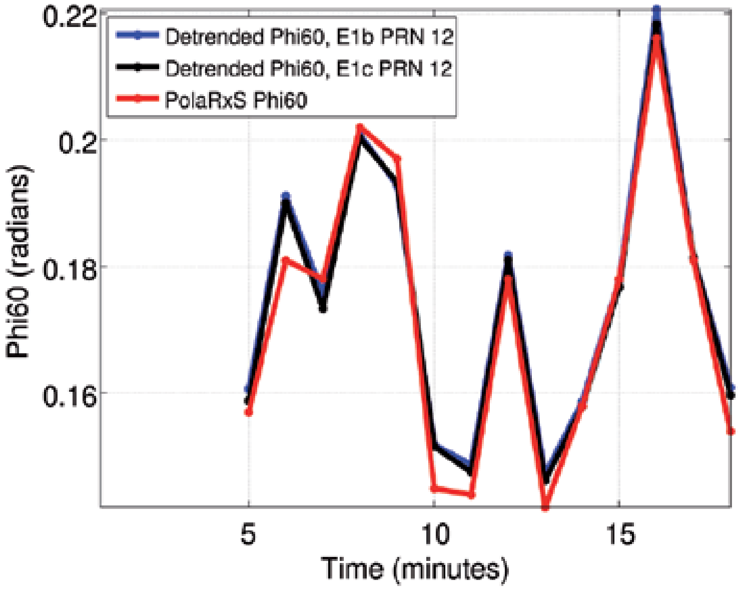

Figure 6. Comparison of Phi60 index obtained by the Septentrio PolaRxS receiver and estimated values of Galileo E1b/c PRN 12 obtained by the software receiver. Small deviations in Phi60 are due to temporal misalignment between the estimated and the Septentrio receiver values.

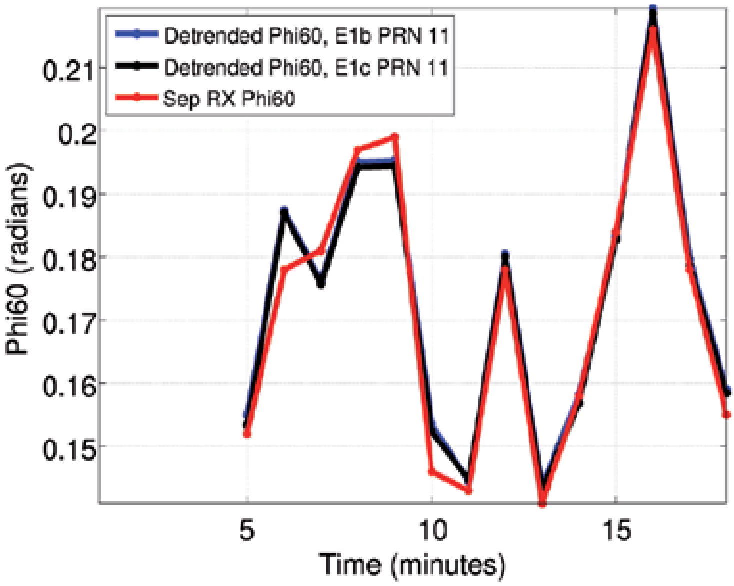

Figure 7. Comparison of Phi60 index obtained by the Septentrio PolaRxS receiver and the estimated values of Galileo E1b/c PRN 11 obtained by the software receiver. Small deviations in Phi60 are due to temporal misalignment between the estimated and the Septentrio values.

5. Conclusion

The research presented in this paper shows values of S_4 and Phi60 indices estimated for Galileo OS E1 signals for the equatorial region using a software receiver. The BOC tracking algorithm implemented into this software receiver, all together with standard third order PLL, showed good solution for this particular case study where Galileo signals seem not to be affected by equatorial scintillation. It was shown that for Galileo E1 signals the S_4 and Phi60 indices are not as high as those for GPS case estimated for this particular data set. The estimated indices by software receiver are verified by those obtained by a professional receiver and a very good correlation was found. However, the Phi60 values are almost overlapping meaning that the carrier phase was estimated properly and the detrending cut off frequency was chosen correctly.

Acknowledgements

The research work is undertaken in the scope of the TRANSMIT ITN (www.transmit-ionosphere.net), funded by the Research Executive Agency within the 7th Framework Program of the European Commission, People Program, Initial Training Network, Marie Curie Actions-GA no 264476.

Author details

Marko Vuckovic and Samo Stanic

*Address all correspondence to: marko.vuckovic@ung.si

Center for Atmospheric Research, University of Nova Gorica, Slovenia

References

[1] Groves K. M., Basu Su. And Sultan P. J.. Specification and forecasting of scintillations in communication/navigation links: current status and future plans. *Journal of Atmospheric and Solar-Terrestrial Physics*, Nov. 2002. 64: pp. 1745-1754.

[2] European GNSS (Galileo) Open Service Signal in Space Interface Control Document (SISICD). *Technical report*, Sep. 2010.

[3] Van Dierendonck A. J., Klobuchar J., And Hua Q.. Ionospheric Scintillation Monitoring Using Commercial Single Frequency C/A Code Receivers, in: *Proceedings of the 6th*

International Technical Meeting of the Satellite Division of The Institute of Navigation (ION GPS 1993). Sep. 22-24, 1993. Salt Lake City, UT. 1993. 1333-1342.

[4] Fähnle M.. Software-Defined Radio with GNU Radio and USRP/2 Hardware Front-end: Setup and FM/GSM Applications [Bachelor Thesis]. University of Applied Sciences Institute of Communication Technology Ulm, Germany: 2009. 92 p.

[5] Olivier J., Christophe M. And Emmanuel B.. Analysis of Galileo E1 OS unbiased BOC/CBOC tracking Techniques for Mass Market Applications, in: *Satellite Navigation Technologies and European Workshop on GNSS Signals and Signal Processing (NAVITEC), 2010 5th ESA Workshop on*. 8-10 Dec. Noordwaijk. IEEE. 2010. 1-8.

[6] Borre K., Akos M. D., Bertelsen N., Rinder P. And Jensen H. S.. *A Software-Defined GPS and Galileo Receiver: A Single-Frequency Approach*. Basel: Birkhäuser . 2007. 176 p.

[7] Kaplan E. And Hegarty C.. *Understanding GPS: Principles and Applications*. 2nd ed. Artech House, INC. 2006. 726 p.

[8] Bougard B., Sleewaegen J-M., Spogli L., Sreeja Vadakke Veettil, Galera Monico J.F.. CIGALA: Challenging the solar maximum in Brazil with PolaRxS, in: *Proceedings of the 24th International Technical Meeting of The Satellite Division of the Institute of Navigation (ION GNSS 2011)*. Sep. 20-23, 2001. Oregon Convention Center, Portland, Oregon. 2011. 2572-2579.

Chapter 6

Using Ordinary Kriging for the Creation of Scintillation Maps

Peter Kieft, Marcio Aquino and Alan Dodson

Additional information is available at the end of the chapter

http://dx.doi.org/10.5772/58781

1. Introduction

This paper introduces Ordinary Kriging as a method for the creation of maps of scintillation indices S_4 and σ_ϕ which could be used to provide the user information on the accuracy of specific receiver-satellite links. Sufficiently accurate scintillation maps, also providing an error estimate of the map values, could ultimately lead to their direct implementation in the positioning's stochastic model.

Small scale (in the order of a few hundred meters, time varying irregularities in electron density in the ionosphere can cause scattering and diffraction of the radio signals, passing through these irregularities [10].

Figure-1 provides a graph illustrating scintillation by looking at the incident wave plane (plane of equal phase) which is arriving at a layer with rapidly changing irregularities; the emerging wave front is no longer a plane due to scattering (signal hitting the structures and going off into multiple directions) and diffraction (part of a wave hitting a structure and going forward as a circular wave-front causing an interference pattern). The result for the observer is a signal which is rapidly changing in phase (phase scintillation) and intensity (amplitude scintillation) [2].

The morphology and climatology of scintillations have been studied extensively over the last half century. A brief summary of this is given in figure-2 [3], which shows a geographical overview of scintillation occurrences during periods of maximum and minimum solar activity.

From figure-2, we can see that the main areas of scintillation occurrence are in the equatorial zone (after sunset) and at high latitudes near the auroral oval (at night-time). During solar maximum conditions the scintillation effects are much more pronounced than during solar minimum conditions [3].

INTECH
open science | open minds

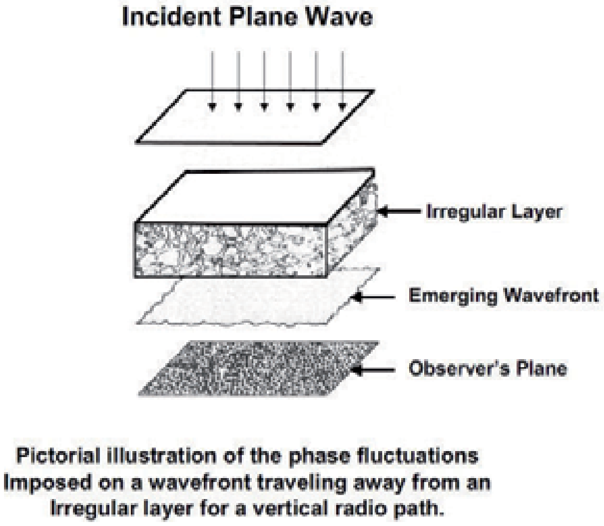

Figure 1. Scintillation Principle [2]

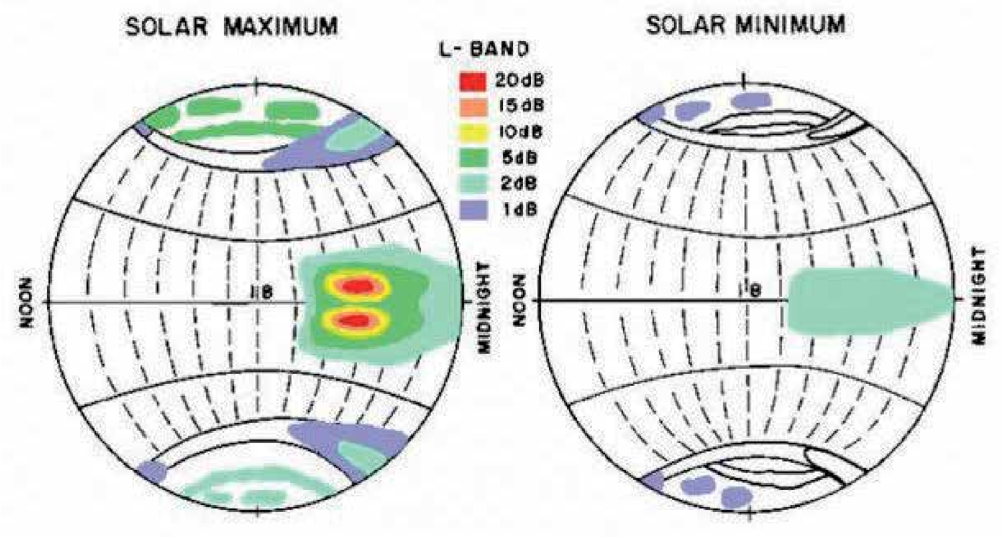

Figure 2. Scintillation Occurrence [3]

The effects of scintillations on the GPS receiver tracking ability, range from a complete loss of lock on the signal (satellite no longer available for positioning purposes), to degradation in the accuracy of the measured satellite – receiver range, which if not de-weighted in the stochastic positioning model, could degrade the accuracy of the computed position [1].

The creation of scintillation maps [11] using Ordinary Kriging is thus particularly valuable for areas with the highest frequency of scintillation occurrence (equatorial and high-latitude), where a positioning computation could be affected by multiple satellite-receiver links under scintillation.

2. Metrics of scintillation

The magnitude of scintillation occurrences (phase and amplitude) can be quantified through scintillation indices. Furthermore some parameters describing the effect of scintillation on the performance of receiver tracking loops, e.g. the Phase Locked Loop (PLL) can be obtained from the receivers' high rate phase and intensity data, if available to the user. These indices and receiver tracking performance parameters are the possible (combined) inputs for the scintillation maps and are normally only provided by scintillation monitoring receivers, which are specifically designed to maintain lock on the satellite even under high scintillation levels.

The following paragraphs provide an overview of the indices and receiver tracking parameters. The last paragraph concludes with a discussion on the preliminary choice for the map content.

2.1. Scintillation indices

According to [8] a simplified model for one particular signal as seen by the receiver can be expressed as (1):

$$r(t)=\sqrt{2P}s(t)\cos(\omega t+\phi)+n(t) \tag{1}$$

In which P is the received signal power (watts), ω is the carrier frequency (rad/s), s (t) is the normalised transmitted signal and n (t) is noise. Scintillation causes a perturbation on both the amplitude (δP) and phase (δϕ) and thus the signal under scintillation can be modelled as (2).

$$r(t)=\sqrt{2P\delta P}s(t)\cos(\omega t+\phi+\delta\phi)+n(t) \tag{2}$$

The following indices, S_4 (amplitude scintillation), σ_ϕ (phase scintillation) and SI (signal intensity), are frequently used to describe the severity of scintillation occurrence. A short description [8] is given here:

1. Signal Intensity (SI): Intensity of the received signal discarding noise. SI can be calculated from the difference between Narrow Band Power (NBP) and Wide Band Power (WBP) of the receiver measured over the same interval (within one bit of the navigation message-20 milliseconds). For the practical calculation of SI, see [12].
2. S_4 index: describing the severity of the amplitude fades caused by scintillation. The S4 index is defined as the standard deviation of the detrended power fluctuation δP, which has a Nakagami-m probability density function. For the practical calculation of S4, Total S4, see [12].

3. σ_ϕ index: describing the phase variations caused by scintillation. The σ_ϕ index is defined as the standard deviation of the de-trended phase. The de-trending is performed to remove slow variations due to e.g. satellite movement. The abbreviation $\sigma_{\phi 60}$ means that the standard deviation is taken over a sixty second period. For the practical calculation of σ_ϕ, see [12].

2.2. PLL and DLL tracking performance parameters

The influence of scintillation (amplitude and phase) can be observed in the receiver through various parameters. Amplitude scintillation has an effect on the Carrier-to-Noise density ratio (C/No) [13], which when calculated over a short timespan decreases with the amplitude fades observed in amplitude scintillation, see figure-3 [9]. Phase scintillation has an influence on the spectral parameters of the phase PSD (spectral slope) and T (spectral strength). Both are calculated from the de-trended phase spectrum [12].

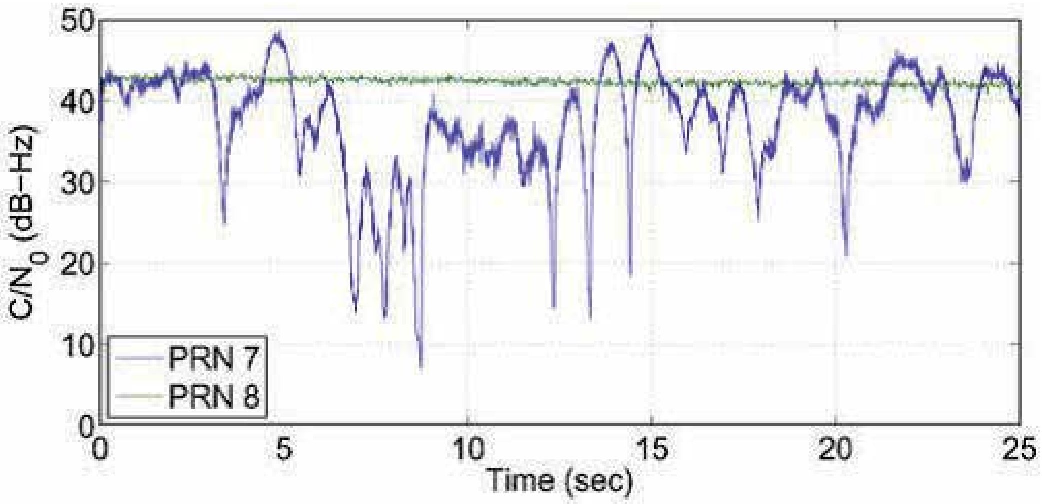

Figure 3. Amplitude Scintillation Effect on C/No [9]

The actual influence of amplitude and phase scintillation on the receiver tracking performance can be expressed by the tracking jitter variance (or its standard deviation) for the PLL and DLL. The tracking jitter variance may be directly estimated at receiver level or derived (in post processing) from the high rate data when combining this high rate data with the scintillation sensitive Conker model [4, 5]. As an example (3) shows the standard thermal noise formula for the DLL jitter variance without scintillation, whereas under amplitude scintillation the Conker model formulates the DLL jitter variance $\sigma^2_{\phi_T}$ (on GPS L1) as (4).

$$\sigma^2_{\phi_T} = \frac{B_n d\left(1 + \frac{1}{\eta (c/n_0)_{L\ 1\text{-}C/A}}\right)}{2(c/n_0)_{L\ 1\text{-}C/A}} \tag{3}$$

$$\sigma_{\phi_T}^2 = \frac{B_n d\left(1 + \frac{1}{\eta (c/n_0)_{L1\text{-}C/A}\left(1 - 2S_4^2\right)}\right)}{2(c/n_0)_{L1\text{-}C/A}\left(1 - S_4^2\right)} \tag{4}$$

The Conker model for phase scintillation (on L1) is given as (5), (6) and (7).

$$\sigma_{\phi_\varepsilon}^2 = \sigma_{\phi_S}^2 + \sigma_{\phi_T}^2 + \sigma_{\phi,osc}^2 \tag{5}$$

$$\sigma_{\phi_T}^2 = \frac{B_n\left(1 + \frac{1}{2\eta (c/n_0)_{L1\text{-}C/A}\left(1 - 2S_4^2\right)}\right)}{(c/n_0)_{L1\text{-}C/A}\left(1 - S_4^2\right)} \tag{6}$$

$$\sigma_{\phi_S}^2 = \frac{\pi T}{k f_n^{p-1} \sin\frac{[2k + 1 - p]\pi}{2k}} \tag{7}$$

Since scintillation monitor receivers (e.g. from Septentrio and NovAtel) are outputting their high rate data and/or scintillation indices files containing the spectral parameters (Septentrio), this data combined with the Conker model can be used to calculate the tracking jitter variance for the different GNSS signals (e.g. L1, L2, etc.). As can be seen in (4-7) the Conker model is dependent on the design of the receiver tracking implementation.

2.3. The preliminary choice for the map inputs

The preferred 'type' for the interpolated maps would be DLL and PLL tracking jitter maps, generated for all GNSS signal types. These could potentially (if the maps are accurate enough) be directly used as an input for the stochastic model of a receiver within the area of the map. As presented in the previous paragraph, the tracking jitter (variance) is a function of some obtainable receiver parameters (within the network). Unfortunately some of these parameters (e.g. p, T and C\No) are heavily receiver dependent. It will also require the map generation process to include a mapping function to verticalize the slant jitter values and vice versa. To demonstrate the ability of our Ordinary Kriging concept this paper presents S_4 and $\sigma_{\phi 60}$ (standard deviation over 60 seconds) maps, which avoid some of these complications.

3. Short introduction to Ordinary Kriging

The following paragraphs provide a short introduction to Ordinary Kriging which is used for the map interpolation [14].

3.1. Ordinary Kriging (OK)

In Ordinary Kriging a point is estimated as a weighted average from the points around it. It is an unbiased estimator because a constraint is set to the weights to sum up to one.

The Ordinary Kriging algorithm is given in (8). The weights (which sum up to one) are calculated from the underlying geospatial structure which can be found by means of an empirical variogram, described in the next section.

$$Z^{*}_{OK}\left(x_0\right)=\sum_{\alpha=1}^{n} w_\alpha Z\left(x_\alpha\right) \tag{8}$$

3.2. The Variogram and covariance function

The geospatial relationship (dissimilarity between points over distance / direction) within the area of interest can be described with an empirical Variogram. The inter-distances between the sample-points are calculated, see figure-4. The values making up the variogram are then calculated, through ordering the samples with inter-distances falling within a distance bin (h1, h2, etc.); see figure-5, calculating the value as an average of the square root of the difference in the samples γ (h) (9).

$$\gamma(h)=\frac{1}{2n}\sum_{\alpha=1}^{n}\left(Z(X_\alpha+h)-Z(X_\alpha)\right)^2 \tag{9}$$

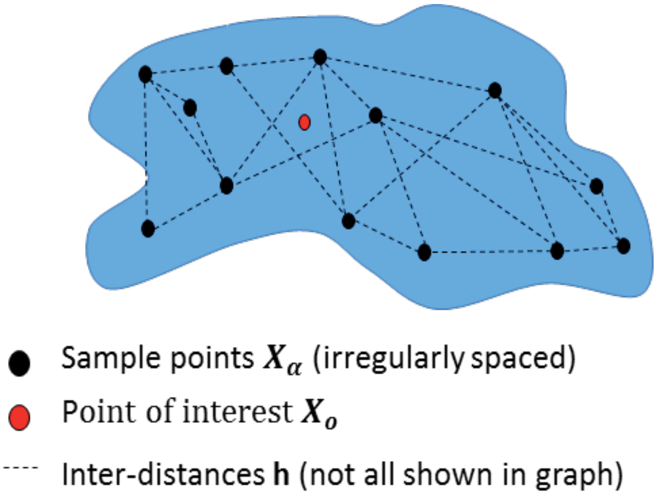

Figure 4. Sample points on the ionospheric shell and their inter-distances

The empirical variogram is subsequently replaced with a matching theoretical variogram (e.g. an exponential, Gaussian or spherical variogram model) to filter outliers and to make it practical to calculate the variogram values for different distances, necessary to be used in the Ordinary Kriging system.

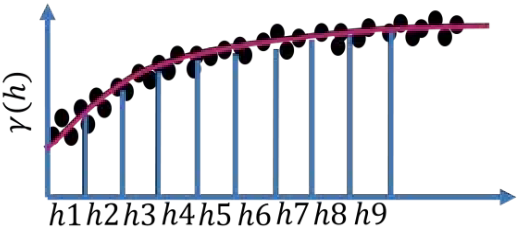

Figure 5. Empirical Variogram Calculation

The variogram can be described with the following characteristics; the nugget, the range and a possible sill, see figure-6. When the variogram has a sill (bounded variogram), it can be replaced with a covariance function through the relationship defined by (10).

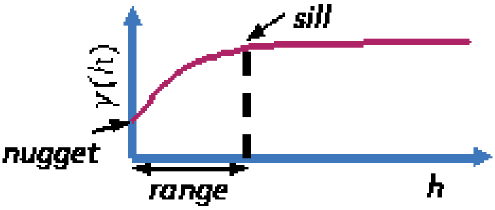

Figure 6. Variogram Characteristics

$$\gamma(h)=b-C(h) \tag{10}$$

When we also order the samples making up the empirical variogram by direction we are able to find a possible directional dependency (checking for anisotropy).

3.3. The Ordinary Kriging system

To calculate the weights in (8), an Ordinary Kriging system can be setup, which minimizes the estimation variance and constrains the weights to sum up to one (11).

$$\begin{bmatrix} \gamma(X_1-X_1) & \cdots & \gamma(X_1-X_n) & 1 \\ \vdots & \ddots & \vdots & \vdots \\ \gamma(X_n-X_1) & \cdots & \gamma(X_n-X_n) & 1 \\ 1 & \cdots & 1 & 0 \end{bmatrix} \begin{bmatrix} w_1^{OK} \\ \vdots \\ w_n^{OK} \\ \mu_{OK} \end{bmatrix} = \begin{bmatrix} \gamma(X_1-X_0) \\ \vdots \\ \gamma(X_n-X_0) \\ 1 \end{bmatrix} \tag{11}$$

The Ordinary Kriging system estimation variance is given by (12).

$$\sigma_{OK}^2 = \mu_{OK} - \gamma(X_0 - X_0) + \sum_{\alpha=1}^{n} w_\alpha^{OK} \gamma(X_\alpha - X_0) \tag{12}$$

Intrinsic Multivariate Correlation is the direct correlation between two or multiple variables, independent from their spatial correlation function. Additional variables having an intrinsic correlation structure with the variable of interest can be directly used as a secondary input, for the creation of the map. Additional variables which have a spatial correlation with the primary variable can also be incorporated through co-Kriging.

4. Ordinary Kriging applied to scintillation maps

4.1. The basic concept

The scintillation data is obtained from a network of stations. All sampled scintillation indices, for all stations and all satellites, with an elevation above the elevation mask are projected on the Scintillation Thin Shell (a model where all scintillations take place at the same height above the Earth's surface, with the height often taken as 350km). A comprehensive dataset (one year's worth of network data including all levels of ionospheric disturbances) is used to retrieve the underlying geospatial structure through the calculation of variogram (s). The overall variogram is calculated by combining the values calculated at each epoch or by combining an epoch with another epoch with a fixed time offset, to only take one variable (distance) into account for its calculation. Ordinary Kriging is applied to calculate values for all grid points in the map. Only sample points within the 'range' of the Variogram (neighbourhood) are taken into account to calculate the interpolation weights and perform the interpolation. Maps are created epoch by epoch for 24 hours during a day of interest, and can be shown as a film (evolving map during the day).

4.2. The limitations

The limitations of the basic concept described above are threefold; the ionospheric single shell assumption, the limited number of ionospheric data samples in an epoch, and a spatial correlation which is not constant within the area of interest (non-stationarity within the map).

The scintillation thin shell assumption (all scintillations take place at the same height above the Earth's surface) projects the scintillation occurrences at their respective IPPs (Ionospheric Pierce Point; the projection onto the thin shell model). The latitudinal and longitudinal position of these IPPs depends on the azimuth and elevation of the satellites, the used ellipsoid and the height of the thin shell model. However in reality these scintillation events are taking place mostly throughout the F-Region of the ionosphere (250 – 400km above the Earth's surface). Depending on the elevation (worse with lower elevation) the projection on the thin shell model will cause an error in the position of the scintillation occurrence. For the estimation of the geospatial correlation (creation of the variograms) this will not lead to significant errors as long as the variograms are based on a large enough dataset and the scintillation thin shell model uses a representative height for the scintillation occurrences (mean). However for the generated maps even a representative shell height will still leave a remaining inaccuracy on the position of the scintillation occurrences.

The use of one epoch of data samples leaves us a very limited sample-set to work with. If we assume 10 stations with on average 8 usable satellites (satellites above the elevation mask) we still only have 80 samples over a significantly large map area. Ordinary Kriging used as an interpolation method will statistically provide the best interpolation, but this does not mean that the interpolated values are correct. The more densely sampled the map is, the more accurate it can present the actual situation. Furthermore scintillations do not present a smooth phenomenon; they arise from small scale structures (a few hundred meters) and Ordinary Kriging interpolation therefore offers a more smoothed climatological (probabilistic) model of what is actually happening.

Our scintillation maps are generated every epoch, and the local time of the sampled data changes during the day, i.e. the Earth is turning underneath a sun fixed system. Since scintillation occurrences depend on local time and latitude, the spatial correlation will change during the day and will also vary for different latitude zones. Since scintillation activity is also dependent on solar activity, the geospatial correlation will also be different for quiet and active days.

4.3. Overcoming some of the limitations

The limitations discussed in paragraph 5.2 are:

1. The thin shell model
2. Limited amount of sample points and smoothing
3. The non-stationarity within the map

The thin shell model has to be applied to allow to make a two dimensional map of the scintillation occurrences. Furthermore from our measurements we are also not able to determine the height where the scintillations occur. However if we manage to choose a representative height (average height of scintillation occurrences) we can minimize the effects on the geo-statistical interpolation model and we can also minimize the average error introduced on the position of the scintillation occurrences.

The limited amount of sample points from just one epoch can be improved in two ways: the inclusion of previous epochs and through inclusion of secondary data with intrinsic correlation with the primary data. The inclusion of previous epochs can be achieved by projecting these epochs on where they would be after the Earth has rotated over the time difference with the current epoch. The de-correlation over time has then to be taken into account as well and is done by introducing a measurement error which increases with time. This method also allows a form of prediction.

The use of secondary parameters could be achieved from the inclusion of other non-scintillation monitoring stations, e.g. Rate of Change of TEC; which are correlated with scintillations.

The non-stationarity within the area of the map can be overcome with a method introduced in [6]. The map has to be split in different local time and latitudinal regions. For each of these regions a variogram is established for different disturbance levels. For each grid-point of the map a distance weighted 'localised variogram' is established from the surrounding regional variograms, see figure-7 and 8. The Kriging for the grid point proceeds as normal, including sample points which are within the range of this 'local variogram'.

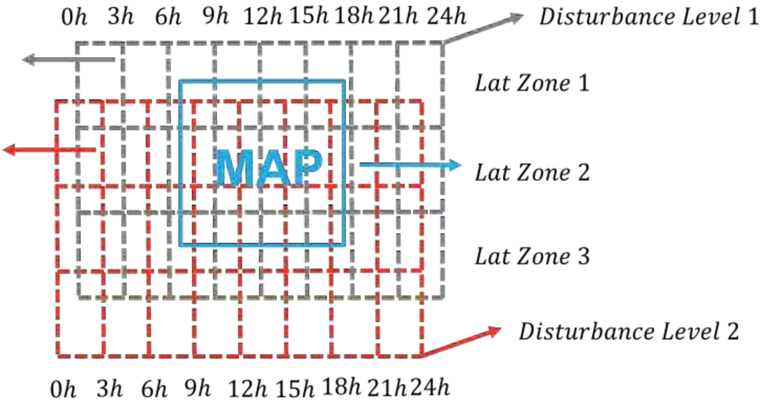

Figure 7. Division into zones

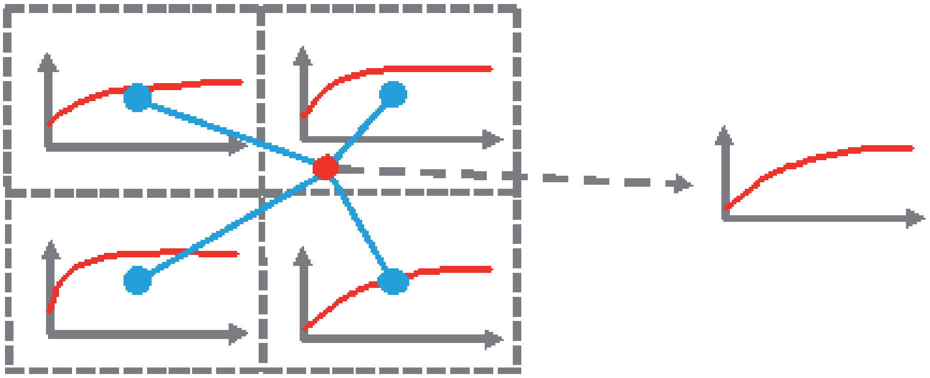

Figure 8. Distance weighted combined variogram

4.4. Validation of the results

Validation of the results is performed by leaving one network station (located approximately in the middle of the map) out of the map computation (sample points not used for the Ordinary Kriging interpolation). The measured scintillation data for this station is compared with the interpolated values from the map at the location of the stations IPPs.

For each scintillation index, the map will provide two values: the interpolated value and the error estimate for this interpolated value. The Kriging interpolation method is considered to be satisfactory when the following is observed:

- Overall the map value and the actual value are in agreement with each other.
- When the difference between the map value and the actual value is small, then the interpolation error estimate is small as well.
- When the difference between the map value and the actual value gets larger, then the interpolation error estimate gets larger as well.

5. Results and conclusions

5.1. The dataset

The variograms to establish the spatial and temporal correlation are generated from the complete 2012 archive of the CHAIN network [7], see figure-9.

Figure 9. The CHAIN Network [7]

On average this network consists of 8 to 10 active stations (depending on maintenance etc.). The dataset for the creation of the S4 and $\sigma_{\phi 60}$ maps is a small subset (one day, 9th of March 2012) of the 2012 dataset. The calculation is performed only with these stations (sparse network) and thus no secondary data has been used in the Kriging interpolation. An elevation mask of 20 degrees has been used for the generation of the maps.

5.2. Example Results

Figure-10 till 13 show some examples of the obtained geospatial correlation structure. The overall structure used consists of:

- Local hours: 0-6, 3-9, 6-12 etc.
- Latitude: 45-55, 55-65, etc.
- Kp: 0-2, 3-5, 6+

The figures clearly demonstrate the variability of the correlation structure in time (during the day), latitude and disturbance level.

Figure-14 and 15 show an example $\sigma_{\phi 60}$ map (one epoch) of the obtained geospatial correlation structure and its corresponding interpolation error map (Ordinary Kriging error). The maps will normally be calculated for each epoch during a complete day and can then be presented as a video file, showing the evolution of patches with higher scintillation. When they are used as an input for the stochastic model of a receiver's position computation they can be stored as a grid file similar to an IONEX (Ionosphere map exchange format) file.

Figure-16 and 17 show a comparison between the obtained map values and the actual values from station TALC which is left out from the map calculations. The map values show compliance with the trend in the actual $\sigma_{\phi 60}$ values and often follow the shape of the peaks, but do not manage to follow the extreme values (smoothing). In areas which are lacking enough (representative) observations they do not manage to follow the shape at all.

5.3. Conclusions and future work

The Ordinary Kriging algorithm seems a promising method to produce scintillation maps. When comparing the map with the directly obtained values it manages to follow the general trend and often follows the same pattern of rise and decline in the observed scintillation. As the Kriging interpolation algorithm has a smoothing effect, it does not manage to follow the extreme values. However one could take this smoothing effect into account when using the maps.

When the map values do not follow the observed pattern, it is due to a lack of (representative) data in the area of interest. The method to improve on this (including secondary data) has been discussed and will be part of the future work on this topic.

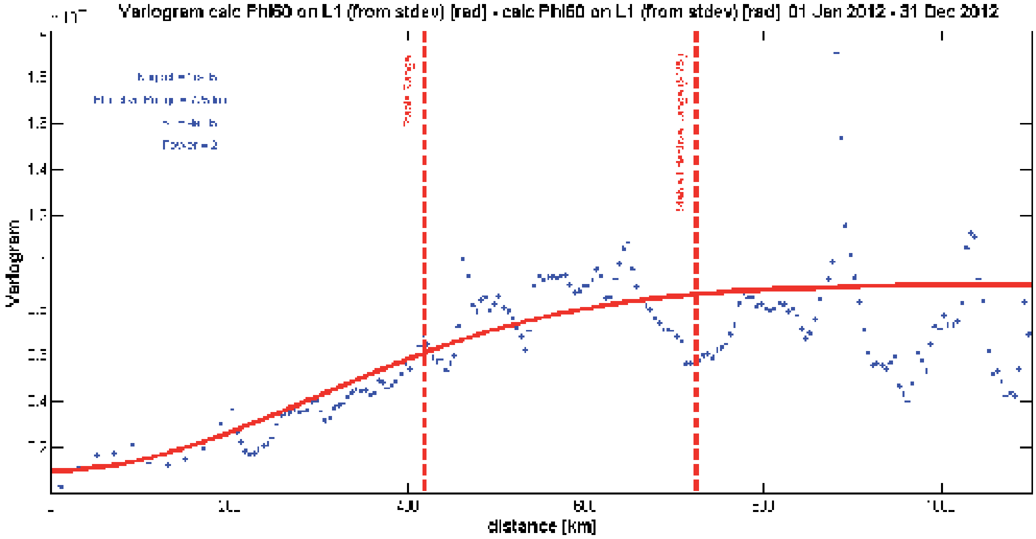

Figure 10. Local Time: 0-6, Lat.: 45-55, Kp: 0-2, Nugget 0.1e-4, Range 725km, Sill 0.9e-4, Power 2.0

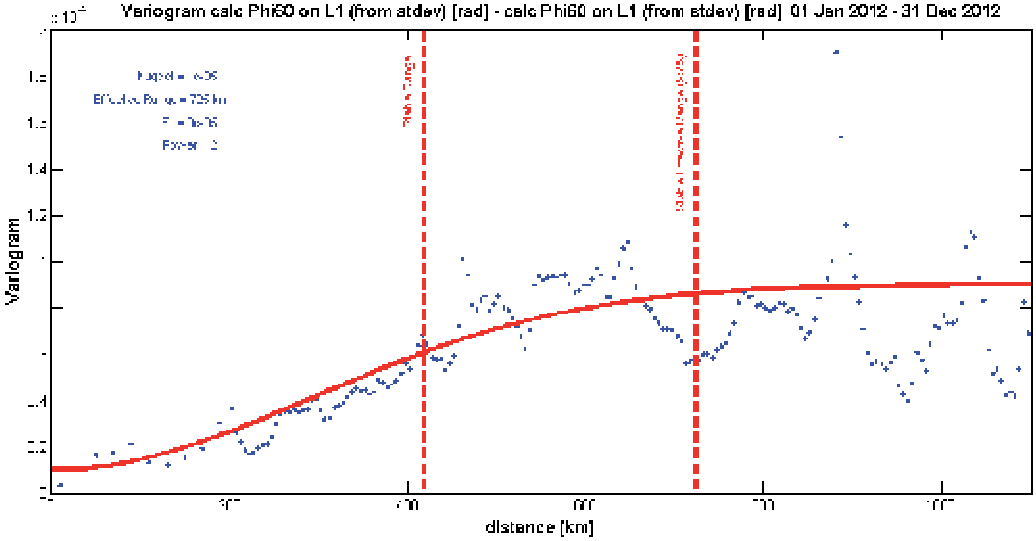

Figure 11. Local Time: 3-9, Lat.: 45-55, Kp: 0-2, Nugget 0.1e-4, Range 725km, Sill 0.9e-4, Power 2.0

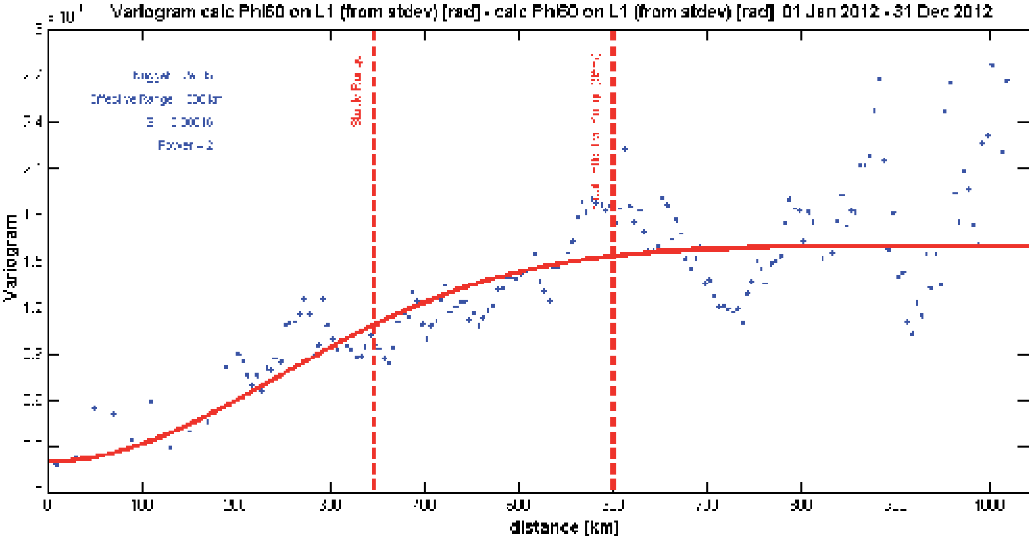

Figure 12. Local Time: 0-6, Lat.: 45-55, Kp: 3-5, Nugget 0.2e-4, Range 600km, Sill 1.6e-4, Power 2.0

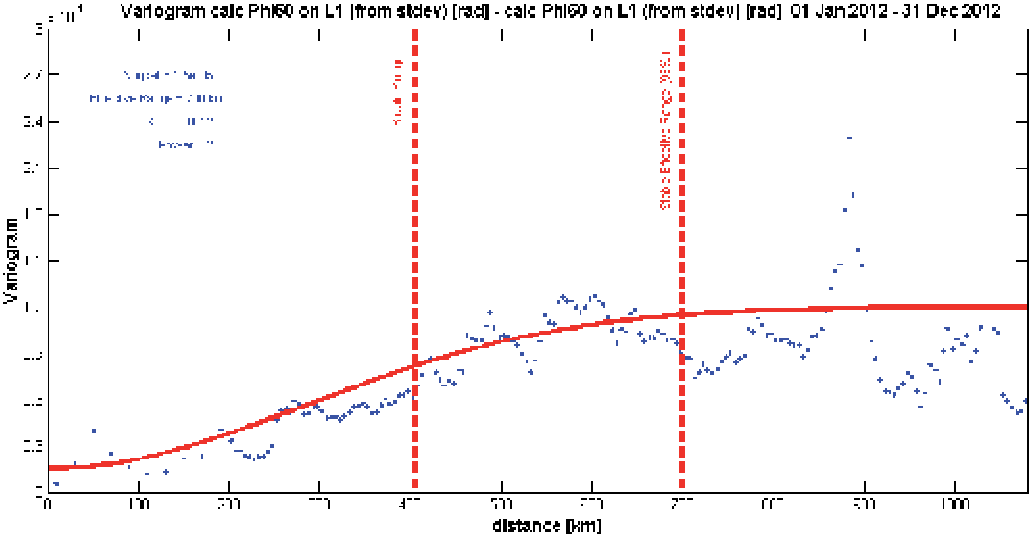

Figure 13. Local Time: 0-6, Lat.: 45-55, Kp: 3-5, Nugget 0.15e-4, Range 600km, Sill 1.2e-4, Power 2.0

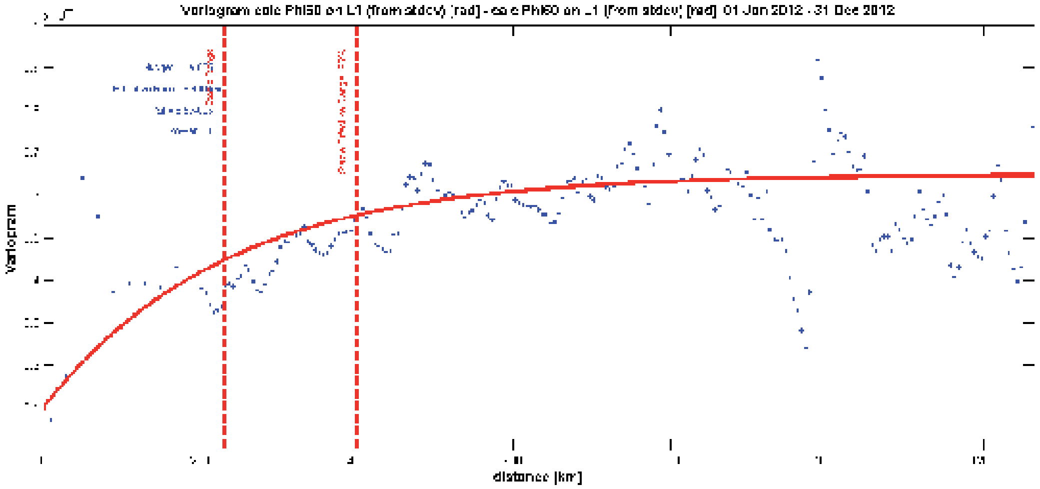

Figure 14. Local Time: 0-6, Lat.: 55-65, Kp: 0-2, Nugget 0.1e-4, Range 400km, Sill 0.65e-4, Power 1.0

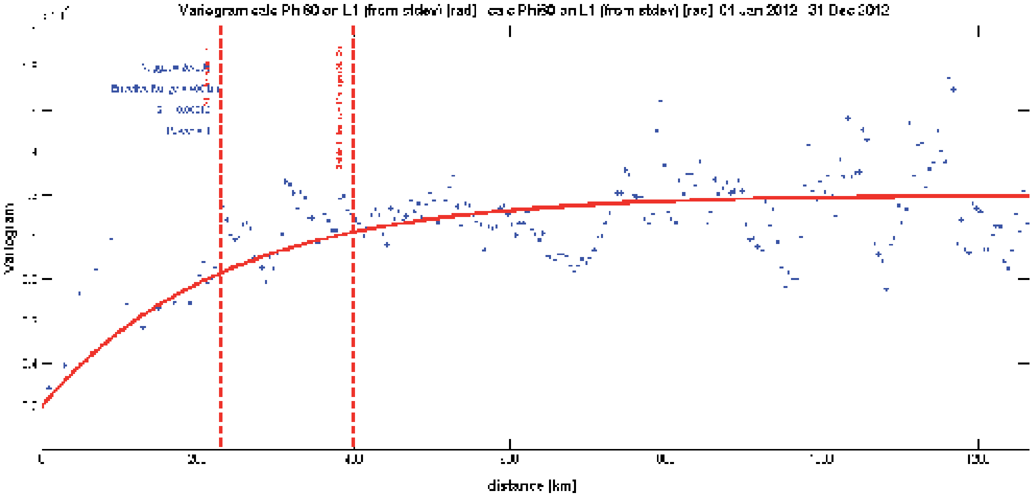

Figure 15. Local Time: 0-6, Lat.: 55-65, Kp: 3-5, Nugget 0.2e-4, Range 400km, Sill 1.2e-4, Power 1.0

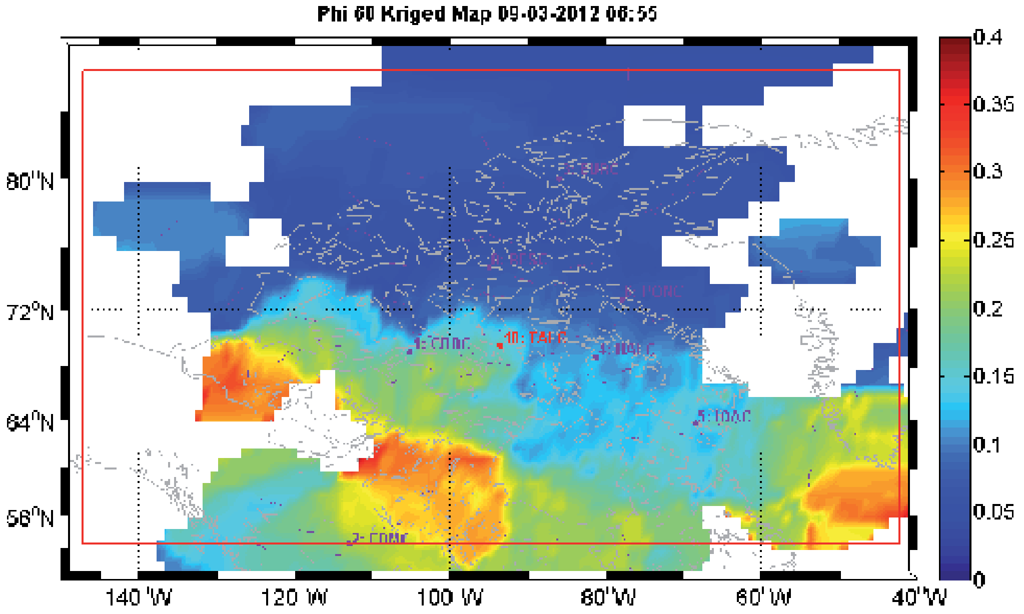

Figure 16. Phi60 map 9th of March 2012

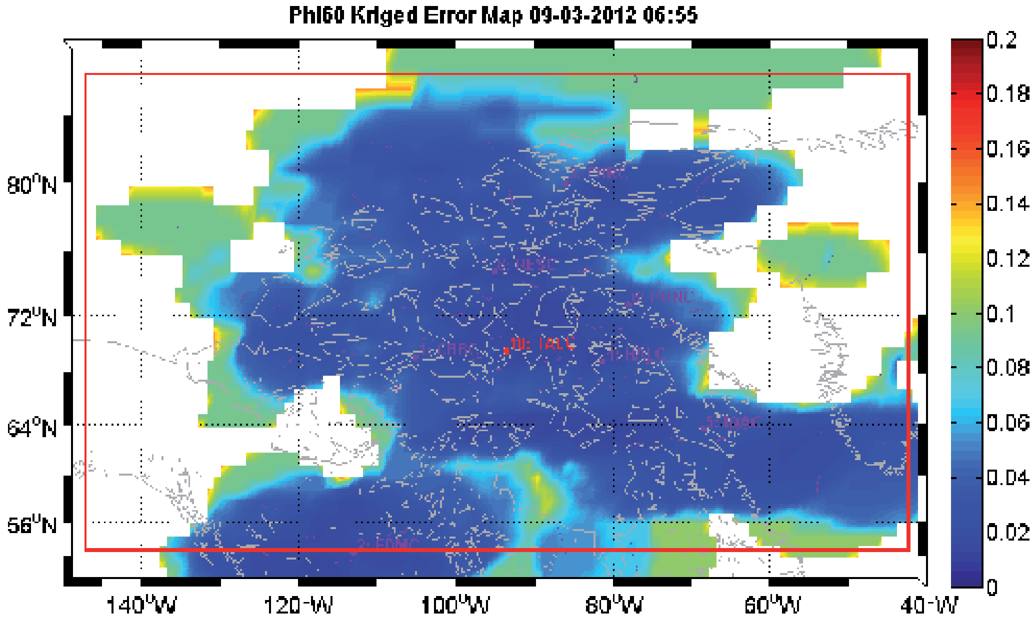

Figure 17. Phi60 Kriging Error map 9th of March 2012

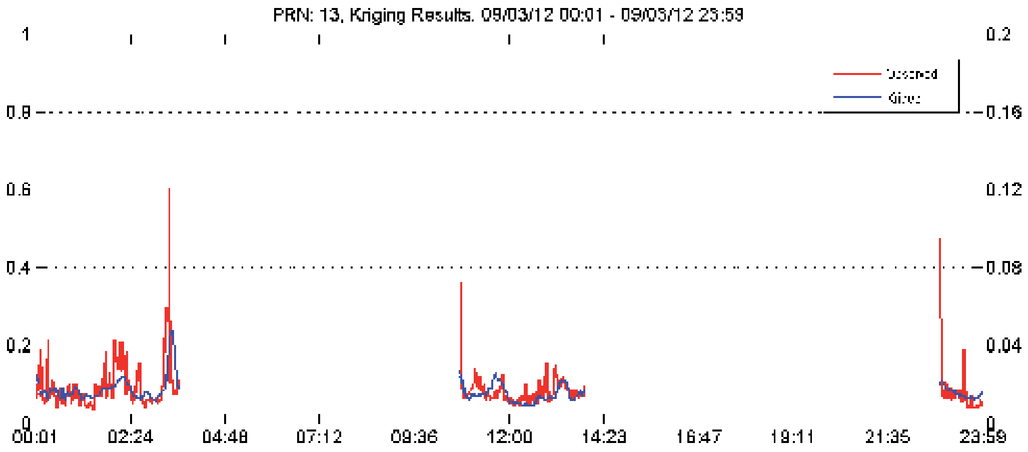

Figure 18. PRN 13 Kriging – Observed at station TALC

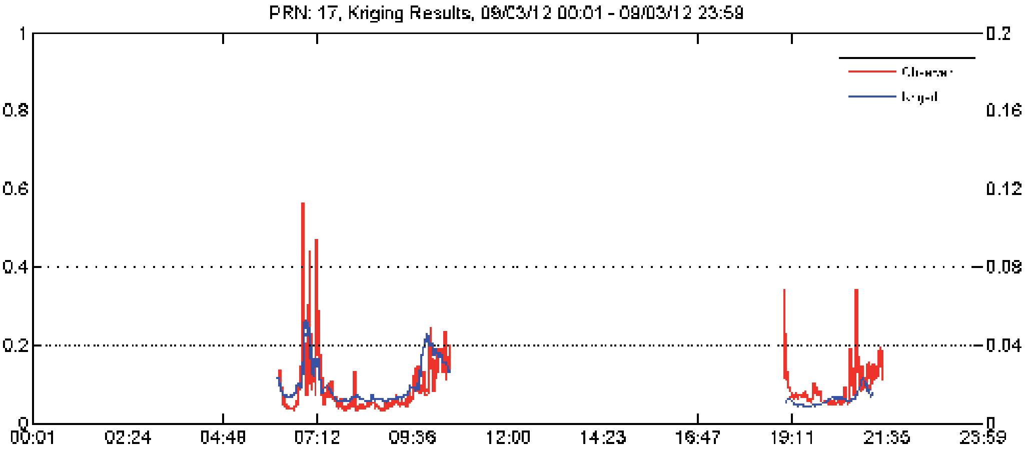

Figure 19. PRN 17 Kriging – Observed at station TALC

Acknowledgements

The research described in this paper focuses on a part of the research undertaken for the EU Marie Curie Actions project called "TRANSMIT" (Training Research and Applications Network to Support the Mitigation of Ionospheric Threats). The topic of the research is the development of tools to mitigate ionospheric scintillation effects in both real time and in post mission GNSS positioning computations. We would like to thank the European Commission for their support and making projects like "TRANSMIT" possible.

We would also like to thank the University of New Brunswick allowing us to use a comprehensive scintillation dataset from their CHAIN network (Canadian High Artic Ionospheric Network) [7].

Author details

Peter Kieft, Marcio Aquino and Alan Dodson

*Address all correspondence to: peter.kieft@nottingham.ac.uk marcio.aquino@nottingham.ac.uk alan.dodson@nottingham.ac.uk

Nottingham Geospatial Institute, University of Nottingham, Nottingham, United Kingdom

References

[1] Aquino M., Monico J. F. G., Dodson A.H., Marques H., De Franceschi G., Alfonsi L., Romano V., Andreotti M.. Improving the GNSS positioning stochastic model in the presence of ionospheric scintillation. *Journal of Geodesy*, 2009. 83 (2009): pp. 953–966.

[2] Basu S., 2003. Ionospheric scintillation: A tutorial [Internet]. 2003. Available from: cedarweb.hao.ucar.edu/workshop/tutorials/2003/basu03.pdf [Accessed: 30/05/2014]

[3] Basu S., MacKenzie E., Basu S.. Ionospheric constraints on vhf/uhf communications links during solar maximum and minimum periods. *Radio Science*, 1988. 23 (1988): pp. 363–378.

[4] Conker R. S., El-Arini M. B., Hegarty C. J., Hsiao T.. Modelling the effects of ionospheric scintillation on gps/sbas availability, in: ION (eds.). *Proceedings of the IAIN World Congress and the 56th Annual Meeting of The Institute of Navigation*. 2000. San Diego, USA. USA: ION. 2000. 563-576.

[5] Conker R. S., El-Arini M. B., Hegarty C. J., Hsiao T.. Modelling the effects of ionospheric scintillation on gps/satellite-based augmentation system availability. *Radio Science*, 2003. 38: 1001. doi: 10.1029/2000RS002604

[6] Fuentes M.. A high frequency kriging approach for non-stationary environmental processes. *Environmetrics* , 2001. 12 (2001): pp. 469-483. doi: 10.1002/env.473.

[7] Jayachandran P. T., Langley R.B., MacDougall J.W., Mushini S.C., Pokhotelov D., Hamza A.M., Mann I.R., Milling D.K., Kale Z.C., Chadwick R., Kelly T., Danskin D. W., Carrano C. S.. The Canadian high arctic ionospheric network (CHAIN). *Radio Science*, 2009. 44: RS0A03. doi: 10.1029/2008RS004046

[8] Kaplan E.D., Hegarty C.. *Understanding GPS: Principles and Applications*. 2nd ed. Boston, USA: Artech House. 2005. 726 p.

[9] Kintner P. M., Ledvina B. M., de Paula E. R.. GPS and ionospheric scintillations. *Space Weather*, 2007. 5: S09003. doi: 10.1029/2006SW000260

[10] Leick, A.. *GPS Satellite Surveying*. 3rd ed. Hoboken, USA: Wiley. 2004. 464 p.

[11] Sreeja, V., Aquino, M., Elmas, Z.G.. Impact of ionospheric scintillation on GNSS receiver tracking performance over Latin America: Introducing the concept of tracking jitter variance maps. *Space Weather*, 2011. 9

[12] VanDierendonck A., Klobuchar J., Hua Q.. Ionospheric scintillation monitoring using commercial single frequency c/a code receivers, in: *ION GPS*. 1993. Dayton, USA. USA: ION. 1993. 1333-1342.

[13] VanDierendock A.. GPS Receivers, in: Parkinson B.W., Spilker Jr. J.J. (eds.). *GPS Receivers in Global Positioning System: Theory and Applications, Vol 1*. 1st ed. USA: American Institute of Aeronautics and Astronautics. 1996. 329-408.

[14] Wackernagel H.. *Multivariate Geostatistics: An Introduction with applications*. 3rd ed. Berlin Heidelberg: Springer-Verlag. 2010. 387 p.

Challenges of Real-Time Monitoring of Ionospheric Perturbations and TEC Fluctuations with GPS Single Station

Marija Cokrlic

Additional information is available at the end of the chapter

http://dx.doi.org/10.5772/58780

1. Introduction

Ionosphere has a big influence on degradation of accuracy and reliability of the positioning with trans-ionospheric radio signals. Its influence is very critical. In the post processing mode, ionospheric characteristics can be determined very easily, but in near- and real-time it is a very challenging task. Determination of ionospheric characteristics requires permanent monitoring in real time, and nowcasting and forecasting of ionospheric indices. For now, we are familiar with the well known ionospheric indices:

- number of electrons along the signal propagation path: Total Electron Content (TEC);
- rapid and fast fluctuation of Radio Frequency (RF) signals' amplitude and phase ($S4$ and σ_{ϕ}) and
- rate of change of TEC (ROT).

In order to obtain information about the state of the ionosphere using single station GPS observations, we are developing and constantly upgrading our iono-tools module that is a part of the in-house academic software TUB-NavSolutions.

Previously, we presented some of the possibilities and methods to monitor ionospheric amplitude scintillation [1] and now we are dealing with TEC calculations, smoothing and levelling methods. As our algorithms and software are being tested, TEC estimation performance has been analysed in a simulated real-time mode. The achieved results are described here.

TEC values can be calculated from code-or carrier phase measurements. Usage of the carrier phases requires challenging ambiguity fixing, while *TEC* derived from code-phases are noisy.

Thus, for monitoring of the *TEC* in real-time the decision has been met to smooth code *TEC* using the carrier *TEC*. An approach, the so called levelling of *TEC* derived from the carrier phases using the code-phases, has been applied to overcome challenging fixing of carrier-phase ambiguity terms to integer numbers. Selected methods of smoothing of code *TEC*s (levelling of carrier-phases) are described and compared with *TEC* available online at the Center for Orbit Determination in Europe (CODE) in the IONosphere Map Exchange Format (IONEX). In this paper some results of the analysis of applicability and performance of the algorithms, using GPS observations from two selected days have been presented:

- 15th July 2012, day of the year 197 (DOY 2012:197) and
- 16th July 2012, day of the year 198 (DOY 2012:198).

Data that has been taken into analysis has been collected at the Kiruna station in the polar area.

To track intensity of Earth's geomagnetic activity and to detect geomagnetic storms, two indices have been chosen: Ap and Kp. It is worth to mention that even though geomagnetic and ionospheric storms are related, geomagnetic storms refer to disturbance of Earth's magnetic field, and ionospheric storm is a disturbance of the ionosphere [8].

2. Methodology

2.1. Total Electron Content estimation from GNSS single station measurements

Slant *TEC* has been estimated directly from GNSS dual frequency carrier- and code-phase in-situ measurements using the following equations:

$$TEC_{carrier} = \frac{1}{40.28}\frac{f_1^2 f_2^2}{f_2^2 - f_1^2}(\phi_2 - \phi_1) \tag{1}$$

$$TEC_{code} = \frac{1}{40.28}\frac{f_1^2 f_2^2}{f_2^2 - f_1^2}\left(P_1 - P_2 - c\frac{f_2^2 - f_1^2}{f_2^2}T_{gd}\right) \tag{2}$$

Where

- ϕ_1 and $\phi_2$are carrier-phase observations $[m]$,
- P_1 and P_2 are code-phase observations $[m]$,
- f_1 and f_2 are frequencies of L 1 and L 2 signals $[Hz]$,
- T_{gd} is transmitter's Estimated Group Delay between P_1 and P_2 measurements $[s]$,

- c is velocity of the $[m/s]$.

TEC derived from the carrier-phases are ambiguous and those ones derived from code-phases are very noisy. To take advantage that the ambiguous carrier-phases measurements have low noise and that the noisy code-phase measurements are not ambiguous, some smoothing and levelling methods have been applied.

2.2. TEC smoothing and levelling methods

TEC is calculated from both carrier- and code-phases using equations 1 and 2. After the both are calculated, levelling offset has been added according to the following formula:

$$TEC_{slant} = TEC_{carrier} + TEC_{offset} \tag{3}$$

Where value of the offset depends on the method has been applied.

2.2.1. Method I

Calculation of the levelling offset between code- and carrier-phases derived TEC along the whole arc according to [7].

$$TEC_{offset} = \frac{1}{N}\sum_{i=1}^{N} TEC_{code}(t_i) - TEC_{carrier}(t_i) \tag{4}$$

Where t_i indicates time period in which TEC has been observed and N is number of calculated TEC in the whole arc of satellite visibility.

2.2.2. Method II

Levelling approach suggested by Jakowski [5]. Here the offset is defined by the following formulas:

$$TEC_{offset} = TEC_{code} - TEC_{carrier} \tag{5}$$

$$TEC_{offset,\, i+1} = \frac{i}{1+i}\langle TEC_{offset}\rangle_i + \frac{1}{i+1} TEC_{offset,\, i+1} \tag{6}$$

2.2.3. Method III

Smoothing and filtering of code- with carrier-phases according to Hatch algorithm [3]. TEC derived from code-phases are being smoothed by previous TEC derived from carrier-phases observations.

$$\widehat{TEC_{code}(t_i)} = \frac{i}{N} + \frac{N-1}{N}\left[TE\hat{C}_{code}(t_i - 1) + \left(TEC_{carrier,i} - TEC_{code,i}\right)\right] \tag{7}$$

For real-time usage, when method *III* will be applied (Hatch filter), length of the filter must be reinitialized whenever cycle slip is detected. Detection of the cycle slips must be performed in all smoothing approaches.

2.3. Amplitude scintillation

For calculation of the amplitude scintillation, the $S4$ index was derived from signal power calculated from the I (in-phase) and Q (quadrature) components of bandpass signal (eq. 8):

$$s(t)=I(t)+jQ(t) \tag{8}$$

Power of the signal is now derived as:

$$P(t)=\frac{I^2+Q^2}{2} \tag{9}$$

The scintillation index has been calculated using following formula:

$$S4=\sqrt{\frac{\langle P^2(N)\rangle-\langle P(N)\rangle^2}{\langle P(N)\rangle^2}} \tag{10}$$

where

$$\langle P(N)\rangle=\frac{1}{N}\sum_{i=0}^{i=N} P(i) \tag{11}$$

and

$$\langle P^2(N)\rangle=\frac{1}{N}\sum_{i=0}^{i=N} P^2(i) \tag{12}$$

The argument i indicates the observation epoch number within the data time span, and N is the number of available observations.

According to the formula given by A.J. Van Dierendonck [2] $S4$ index has been calibrated by the influence of ambient (thermal) noise.

$$S4N_0=\sqrt{\frac{100}{SNR}\left[1+\frac{500}{19SNR}\right]} \tag{13}$$

Now, the final calculation of $S4$ index is done by:

$$S4_{calibrated}=\sqrt{S4^2-S4N_0^2} \tag{14}$$

2.4. Rate of change of Total Electron Content

In order to trace ionospheric irregularities [11] and to provide spatial variation of electron density [9], the rate of change of TEC (ROT) is introduced. The equation below (eq.13) describes estimation of the ROT parameter:

$$ROT = \frac{TEC^{t+i} - TEC^{t}}{(t+i) - t} = \frac{\left(\phi_1^{t+i} - \phi_2^{t+1}\right)\left(\frac{1}{40.28}\,\frac{f_1^2 f_2^2}{f_1^2 - f_2^2}\right) - \left(\phi_1^{t} - \phi_2^{t}\right)\left(\frac{1}{40.28}\,\frac{f_1^2 f_2^2}{f_1^2 - f_2^2}\right)}{(t+i) - t} \tag{15}$$

In our case we are calculating between epochs changes of TEC every one second. That gives us simplified equation of ROT without denominator because it is always equal to 1 sec (assuming there are no gaps).

3. Case study

Data processed for this analysis were collected at the Kiruna station in Sweden ($67.5026\,°N$, $20.2437\,°E$) with approximate position depicted in the Figure 1. In Kiruna there is a GNSS continuously operating station of the German Aerospace Center (DLR), division in Neustrelitz. The station is working for the Space Weather Application Center-Ionosphere (SWACI). It is configured for ionospheric scintillation monitoring and the observables (code- and carrier phases, and the I- and Q-amplitudes) are recorded with 50 Hz sampling rate.

Taken from Yahoo maps.

Figure 1. Position of Kiruna station in Sweden

Raw values of the observables collected at the station have been processed with university software being under development at Technische Universität Berlin (TUB) *TUB-NavSolutions*. The software module *iono-tools* is depicted in the Figure 2.

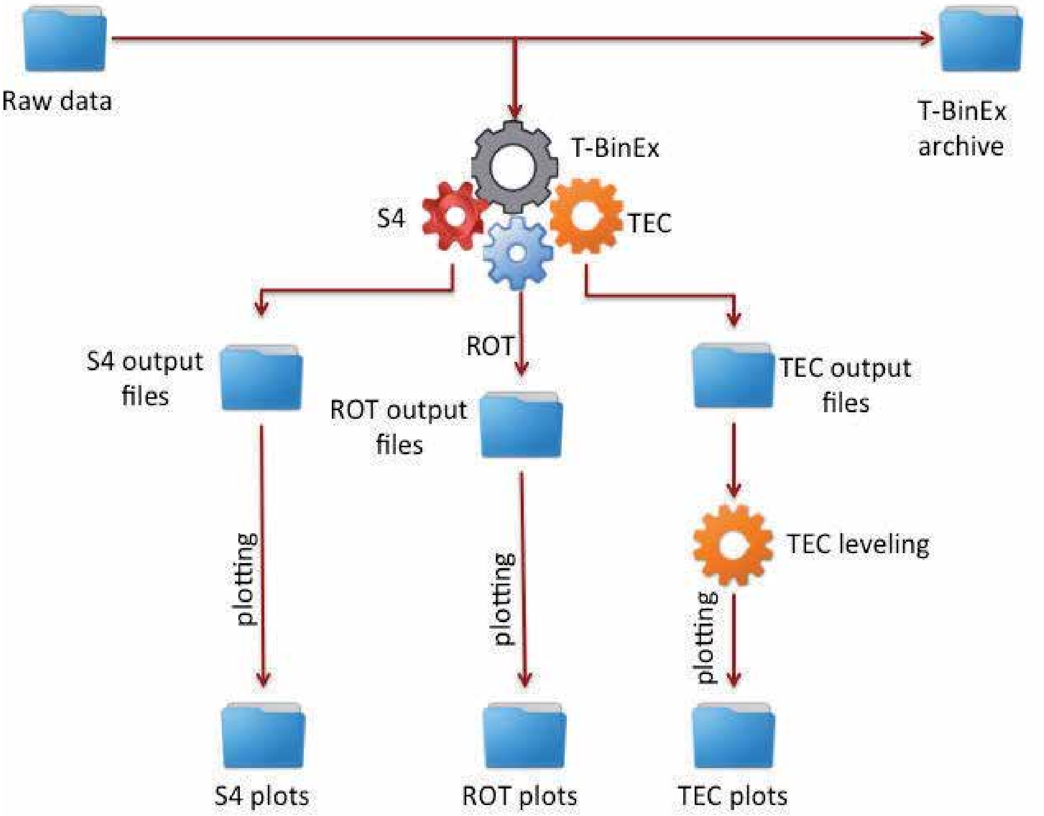

Figure 2. Basic architecture of *TUB-NavSolutions* software *iono-tools* module

Data taken into the analysis is from days with high geomagnetic activities. In the Figure 3. *Ap* and *Kp* indices are shown for only couple of days: 14-17. July 2012. In this paper we will focus on 15th and 16th July.

TEC values derived directly from the observations were compared with slant *TEC* derived from Global Ionospheric Maps (GIM) of the Center for Orbit Determination in Europe (CODE), Astronomical Institute of the University of Bern following Schaer [10].

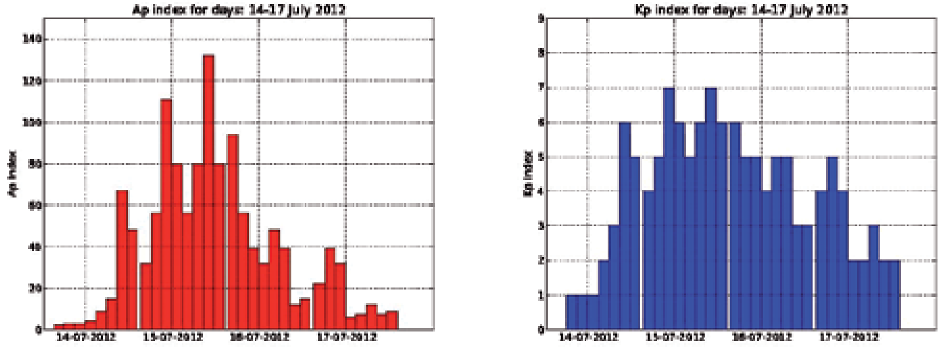

Data are taken from NOAA Space Weather Prediction Center.

Figure3. Daily averaged indices of geomagnetic activity

4. Results

Figure 4 and 5 show *TEC* for both days and for two selected satellites: PRN 09 and PRN 27. The light blue curve represents slant *TEC* values derived from CODE GIM and the magenta curve represents elevation angle. In the both Figures slant *TEC* derived from GIM (*TEC* from IONEX) is represented by a smooth curve. However, in the both Figures sudden and small peaks, in the all three smoothed time series of *TEC* are visible. These anomalies tell us that most probably some ionospheric disturbances appeared at that time. *TEC* derived from observations, smoothed and levelled with all three methods coincide with each other but all of them deviate from the GIM ones for more than 5 $[TECU]$.

In the Figure 4 interesting are two deviations both detected roughly between 9:00^h and 11:00^h UTC (marked with green circles). This is approximately the same time when *Ap* and *Kp* indices reached values that indicate a strong geomagnetic storm.

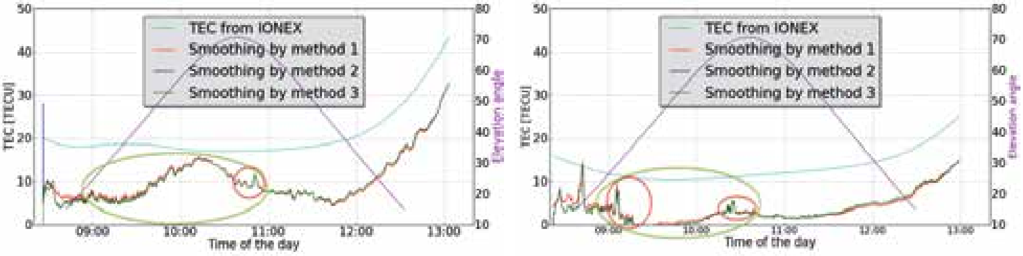

Figure 4. *TEC* calculated and interpolated for 15th and 16th July 2012 for satellite PRN 09

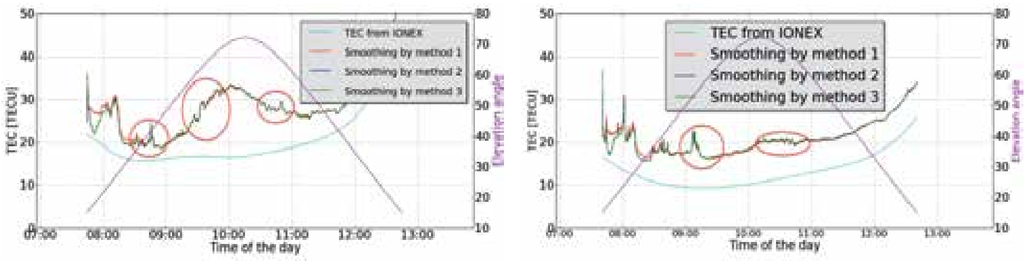

Figure 5. *TEC* calculated and interpolated for 15th and 16th July 2012 for satellite PRN 27

ROT values calculated from observations indicate disturbed ionospheric conditions for both days. In the both Figures, 6 and 7, we can notice sudden peaks and variations which confirm that at that time ionospheric perturbations took place.

If we compare *TEC* from the left panel of the Figure 4 with *ROT* from the left panel of the Figure 6 it is seen that larger oscillations appear in both time series at the same time. Special *warning* (based on strong *ROT* variations) comes a little bit before 11:00h.

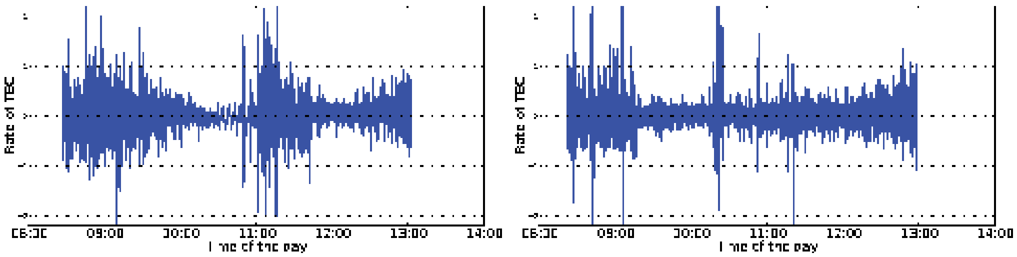

Figure 6. *ROT* for 15th and 16th July for satellite number PRN 09

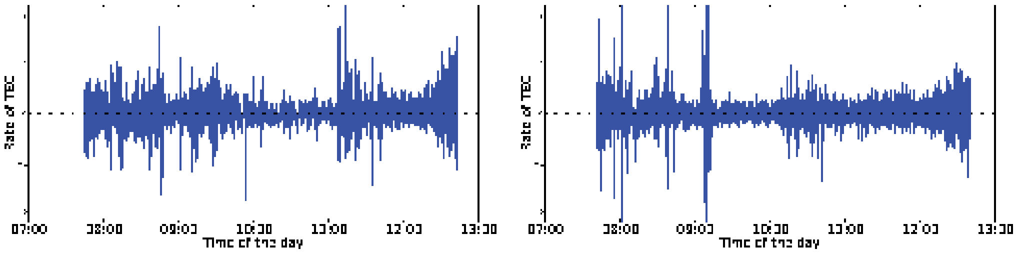

Figure 7. *ROT* for 15th and 16th July for satellite number PRN 27

Similar behaviour and coherence is visible also in other time series of *TEC* and *ROT* (marked with red circles in Figures 4 and 5)

- in the right panels of the Figures 4 and 6 a little bit after 9:00h and a little bit after 10:00h,

- in the left panels of the Figures 5 and 7 with big peaks a little bit before 9:00^h, around 9:30^h and before 11:00^h,
- in the right panels of the Figures 5 and 7 with sudden and big oscillation a little bit after 9:00^h and constant oscillations between 10:00^h and 11:00^h.

In the Figure 8 ionospheric amplitude scintillation parameter ($S4$) has been depicted. $S4$ values are displayed for each day and for all satellites in view. Even though ionosphere amplitude scintillation is less intense in polar regions, a few higher values (above 0.6) may be observed indicating ionospheric perturbations.

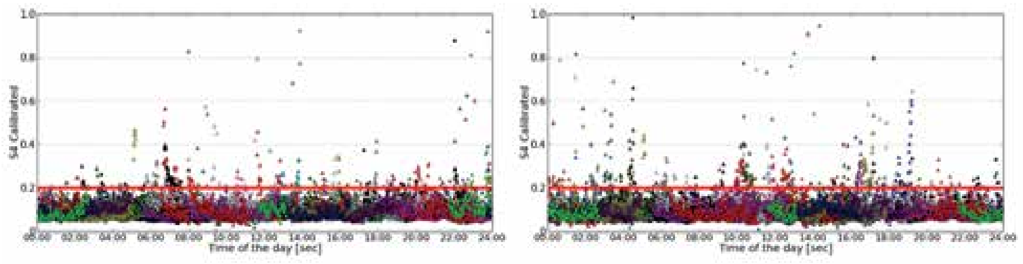

Figure 8. Amplitude scintillation index $S4$ for 15th and 16th July for all satellites

5. Discussions and conclusions

The data from only two selected days has been post processed. Both days, 15th and 16th July 2012, have been selected on the base of geomagnetic indices. There are clearly visible similarities between time series of TEC and ROT values derived from observations, on one side, and geomagnetic indices (Ap and Kp), on the other side. Variations in the time series of ROT are very similar to those in the time series of EC. Even small jumps (peaks), visible in TEC plots, can be assumed as correlated with ROT oscillations.

Some TEC smoothing and levelling methods have been tested here in order to select the most appropriate one for our real -and near-real time applications. All three tested methods give very similar results of the final TEC values. It has been found that the method II and III fulfil requirements for usage in real-time. In the Fig. 4 and 5 results from the two methods, II (green line) and III (blue line) are displayed. Both curves are overlapping. That is why we can have impression that blue curve does not exist, but looking for numerical values it is seen that they differ between each other on second place after decimal point only.

There are easy seen biases between TEC derived from our obervations and interpolated using CODE. A source of the biases is not identified yet because not enough data was available up to now. Investigation of it will be continued.

The above described draft results of investigations allow to assume that *TEC* and *ROT* variability can be used for detection of perturbed ionospheric conditions and probably for issue of warnings for real-time users.

Investigation of applicability of *TEC* and *ROT* for real-time warnings on ionospheric perturbations will be continued using GPS data collected at stations located in equatorial, mid-latitude and polar areas.

Acknowledgements

The research is funded by the FP7 People Programme through the Marie Curie Initial Training Network TRANSMIT-Training Research and Applications Network to Support the Mitigation of Ionospheric Threats.

We would like to thank Space Weather Application Center Ionosphere (SWACI) operated by German Aerospace Center (DLR) in Neustrelitz for the SWACI data sets.

Author details

Marija Cokrlic

Address all correspondence to: marija.cokrlic@tu-berlin.de

Department for Geodesy and Geoinformation Sciences, Technische Universität Berlin, Germany

References

[1] Cokrlic, M. & Galas, R. (2013), TUB software tools for monitoring ionospheric irregularities in a single station mode and first results, in ‘In Proceedings of 7th European Conference on Antennas and Propagations (EUCAP 2013)’, pp. 3562–3565.

[2] Dierendnock, A.J., Klobuchar, J. & Quyena, H. (1993), Ionospheric scintillation monitoring using commercial single frequency CA code receivers, in ‘In Proceedings on the 6th International Technical Meeting of the Satellite Division of the Institute of Navigation’, ION GPS-93, p. 333–344.

[3] Hatch, R. (1982), The synergism of GPS code and carrier measurements, in ‘In proceedings of the Third International Geodetic Symposium on Satellite Doppler Positioning’, pp. 1213–1231.

[4] Jakowski, N., Borries C. & Wilken, V. (2012), 'Introducing a disturbance ionosphere index', Radio Science 47. RS0L14.

[5] Jakowski, N., Mayer, C., Hoque, M. & Wilken, V. (2011), 'Total electron content models and their use in ionosphere monitoring', Radio Science 46.

[6] Ma, G. & Maruyama, T. (2006), 'A super bubble detected by dense GPS network at east asian longitudes', Geophysical research letters 33, 1–5.

[7] Moon, Y. (2004), Evaluation of 2-dimensional ionosphere models for national and regional GPS networks in Canada, Master's thesis, University if Calgary.

[8] Poole, I. (2002), 'Understanding solar indices', QSL pp. 38– 40.

[9] Basu S., Groves, K., Quinn, J. & P.Doherty (1999), 'A comparison of TEC fluctuations and scintillations at ascension island', Journal of Atmospheric and Solar-Terrestrial Physics (61), 1219–1226.

[10] Schaer, S., Gurtner, W. & Feltens, J. (1998), IONEX: Ionosphere Map Exchange Format Version 1.

[11] Tiwari, R., Bhattacharya, S., Purohit, P. & Gwal, A. (2009), 'Effect of TEC variation on GPS precise point at low latitude', The Open Atmospheric Science Journal (3), 1–12.

Chapter 8

The Reliability Evaluation of GNSS Observations in the Presence of Ionospheric Perturbations

Kinga Węzka

Additional information is available at the end of the chapter

http://dx.doi.org/10.5772/58779

1. Introduction

Global Navigation Satellite Systems (GNSS) observations are intrinsically uncertain and inaccurate. In fact, the influence of some phenomenon on the accuracy of the GNSS observations can be relatively easily reduced or removed. However, some other random and deterministic phenomena occurring in the GNSS signal propagation path, like ionospheric perturbations, are very difficult (or perhaps impossible) to predict, detect and model.

The ionospheric perturbations are described as fast and random variability of plasma density in the ionosphere. All of those irregularities can produce diffraction and refractions effects causing signal fading. Such power drops can affect the operations of GNSS receivers denying the signal acquisition or worsening the signal tracking, leading in some cases to a loss of lock. Therefore, they are especially harmful to real-time kinematic applications, with an autonomously working single-receiver. In such circumstances one of the most important requirements standing behind the autonomously working GNSS receiver is to ensure a high level of trust of correctness of the observations used by the positioning algorithm. In such applications verification and confirmation of a high-level reliability for the GNSS observations is a very critical issue. Due to that reason the quality monitoring of the observations affected by the ionospheric perturbations can play a crucial role to enhance reliability of positioning solution.

In presence of GNSS signal perturbations one of the most important requirements is effective integrity monitoring of GNSS observations. The user-level integrity monitoring scheme, the so-called Receiver Autonomous Integrity Monitoring (RAIM) should work independently of any external tools. The RAIM is a powerful technique to check consistency of positioning solution, can play strategic role in reliable positioning in the presence of any irregular perturbation of the GNSS observations. The main task of RAIM is to provide to the user up-to-date and valid warnings information when the system's performance exceeds a user specified tolerance.

In the paper the weighted least-squares-residuals (WLSR) method for reliability control of the GNSS observations is applied. In this method, the process of the Fault Detection and Exclusion (FDE) is performed by statistical tests. The algorithm assumes that the GNSS user estimate a single epoch (instantaneous) navigation solution by performing the Weighted Least-Squares (WLS) estimation. It has to be emphasized that the approach requires at least one redundant measurement. Selected GNSS data-sets from one continuously operated GNSS station located at high latitude, where ionospheric disturbances occur more frequently, have been used for the analysis and for evaluation of applicability of the proposed algorithm.

2. Receiver Autonomous Integrity Monitoring RAIM

In order to verify the integrity of the positioning solution, in the second half of 1980's, a concept of RAIM was formalized. Since that time a number of definitions of the receiver autonomous integrity were proposed. To start a discussion about RAIM one of the essential definitions should be quoted[1]: *"Integrity is that quality which relates to the trust which can be placed in the correctness of the information supplied by the total system. Integrity risk is the* probability *of an undetected failure of the specified accuracy. Integrity includes the ability of a system to provide timely warnings to the user when the system should not be used for the intended operation."*

The fundamental part of integrity monitoring and reliability assurance is application of a selected Fault Detection and Exclusion (FDE) algorithm. Here the least-squares-residuals method (LSR) [10,11] for reliability monitoring has been taken into consideration. The approach was improved by including individual weighting of the code pseudorange measurements [11]. The LSR is one of the most frequently used RAIM method classified as *snapshot scheme* in which only current observation epochs containing redundant number of measurements are processed. In opposite to this, in the *sequential scheme* measurements from the previous epochs are also taken into account (eg. Kalman filter).

2.1. Weighted Least-Squares (WLS) estimation

The main observables used in the GNSS positioning solution are distances between satellite s and receivers r, derived from signal TOA/TOF (Time of Arrival / Time of Flight). In these investigations only the code-phase observations have been used. The extended nonlinear equation for GPS code measurements r_r^s, expressed in meters, can be written as:

---

[1] Concept Paper 1 (WP/43), AWOP (All Weather Operations Panel) Working Group Meeting, Kobe, Japan, February/ March 1994, "Required navigation performance (RNP) - Considerations for the Approach, Landing and Departure Phases of the Flight".

$$P_r^s = \rho_r^s + c\left(\delta t_r - \delta t^s\right) + I_r^s + Z_r^s + c\left(HD_r - HD^s\right) + {}_r^s \tag{1}$$

where ρ_r^s is the geometrical distance between satellite s and receiver r. The other parameters are: δt_r and δt^s receiver and satellite clock corrections; HD_r and HD^s-code signal delays in the hardware of the receiver and satellite; I_r^s-ionospheric refraction; Z_r^s-tropospheric refraction; ${}_r^s$-observation noise. The nonlinear observations equations must be linearized around of approximate initial values of the coordinates x_0, and the receiver clock correction, using the Taylor series expansion, to solve for the parameters using the LS adjustment. Vector of the estimated parameters contains corrections Δx, Δy, Δz to the approximated position x_0 and the receiver's clock correction δt_r. The linearized observation model in the matrix notation for the code-phase observation can be written as:

$$\Delta\rho = A\Delta x + \Delta\varepsilon \tag{2}$$

Where $\Delta\rho$ is the misclosure vector, defined as the difference between "observed-calculated" (o-c) code measurements; A is the geometry or so-called, designed matrix; Δx are four unknowns parameters (three corrections to the coordinates and correction to the receiver clock); $\Delta\varepsilon$ is the vector containing measurement noise.

After the estimation process the user's coordinates are obtained by correcting approximated position x_0 using estimated incremental vector $\Delta\hat{x}$:

$$\hat{x} = x_0 + \Delta\hat{x} \tag{3}$$

Since $\Delta\rho$ has some unknown and random errors, the equation should be treated as a stochastic model. Then Δx can be estimated using the weighted least-squares approach. Required weight matrix Σ is assumed to be known, and estimation of x can be obtained from:

$$\Delta\hat{x} = \left(A^T\Sigma^{-1}A\right)^{-1}\Sigma^{-1}A^T\Delta\rho \tag{4}$$

where $A^T\Sigma^{-1}A$ is a non-singular (invertible matrix) variance-covariance matrix of estimated parameters.

Currently, in the stochastic approach many different observation weighting models have been used. One of the simplest and most commonly used is based on the satellite elevation angle. However, in the case of ionospheric perturbations, which are not directly dependent on the elevation angle (see Figure 3), applicability of this weighting approach can be useless. Due to that in this analysis one of the signal quality parameters which described all of the imperfections in the signal has been used. Signal Quality is usually represented as signal-to-noise ratio (SNR) or as carrier-to-noise ratio (CNR). Both of those parameters are essential to assess the performance of GPS receiver and they are directly related to the precision of code-phase and carrier-phase pseudorange observations [9]. SNR is obtained at the correlator output and is described as a ratio of the signal power S_{corr} to the noise power N_{corr} of the modulated signal. CNR is obtained at the receiving antenna and is described as a ratio of the signal power C_{ant} to the noise power N_{ant} of the modulated signal. Due to the fact that signal and noise power are amplified (between antenna and correlator output) by approximately the same factor we can assume that ratio of those parameters is also almost the same (equation 5).

$$CNR = \frac{C_{ant}}{N_{ant}} \approx \frac{S_{corr}}{N_{corr}} = SNR \tag{5}$$

The matrix Σ, being the weight matrix, describes the noise characteristics related to the measurements:

$$\Sigma = \begin{vmatrix} \sigma_1^2 & 0 & 0 \\ 0 & \ddots & 0 \\ 0 & 0 & \sigma_i^2 \end{vmatrix} \tag{6}$$

The diagonal components of the weight matrix (6) are the variances of the code measurement σ_i^2. This variance model (the so called *sigma* -) for weighting of the GPS observations has been proposed by [3] and is defined as:

$$\sigma_i^2 = a + b \bullet 10^{\frac{-C/N_0}{10}} \tag{7}$$

Where C / N_0 is the carrier-to-noise power density ratio expressed in *dBHz* unit. For the code-phase pseudorange observations the *SNR* can be used instead of C / N_0 as well. The SNR describes the ratio of the signal power and noise power in a given bandwidth, expressed in *dB* unit. The parameters *a* and *b* have to be chosen according to the local environment. In the paper [6,7] the authors proposed the following values of the parameters:

- for heavily degraded signal condition $a = 0.01 \left[\frac{m^2}{s^2}\right]$ and $b = 25 \left[\frac{m^2}{s^2} Hz\right]$;
- for lightly degraded signal condition $a = 10 \left[\frac{m^2}{s^2}\right]$and $b = 150 \left[\frac{m^2}{s^2} Hz\right]$.

RAIM FDE techniques have been developed for reliability monitoring based on statistical tests with the aim to detect and exclude faulty measurement. This process is used for checking consistency of the measurements. It is carried out by means of a statistical hypothesis test of the residuals of a least squares estimation of the GNSS position. Method presented in this paper, the so called weighted least-square-residual approach uses *weighted sum of square of the* *errors* (WSSE) as the test value. The WSSE can be explained as a quantity used in describing discrepancy between the data and an estimation model. It has to be emphasized that the approach requires at least one redundant observation. Faulty observations on the input to the navigation solution will be then excluded [14]. In the WLS method the estimated code-pseudorange residuals are:

$$\hat{v} = A\hat{x} - \Delta\rho = - R\Delta\rho \tag{8}$$

where, the so-called redundancy matrix R is:

$$R = C_{\hat{v}}\Sigma^{-1} \tag{9}$$

The trace of the R represents degree of freedom for the established model. $C_{\hat{v}}$ matrix in the equation (9) is the variance-covariance matrix of the estimated residuals:

$$C_{\hat{v}} = \Sigma - A\left(A^{T}\Sigma^{-1}A\right)^{-1}A^{T} \tag{10}$$

To obtain normally distributed $N(0,1)$ observations, the residuals $\hat{v}$, must be standardized:

$$Z_i = \left|\sqrt{\frac{\hat{v}_i}{\left(C_{\hat{v}}\right)_{ii}}}\right|, i = 1\ldots n \tag{11}$$

The FDE is based on statistical tests for outlier detection using null and alternative hypotheses. The presented scheme of FDE includes a global test for detection of presence of the unacceptable error, followed by a local test for exclusion of the faulty measurement.

Decision	**Situation**	
	H_0 is true *no blunder presents*	H_0 is false *blunder presents*
H_0 is reject *blunder detect*	Type I error: probability of false alarm α (significance level)	Correct decision: probability of rejecting a true blunder $(1 - \beta)$ (power of test)
H_0 is accept *no blunder detect*	Correct decision: probability of making a correct decision $(1 - \alpha)$ (confidence level)	Type II error: probability of missed detection β

Table 1. Statistical hypothesis testing with the errors classification

Two types of erroneous decision can occur [5] (Table I). The ***type I*** of erroneous decision occurs if the null hypothesis rejects the correct observation. Error of ***type II*** appears if the faulty observation is accepted. In the Table 1, the so-called *"significance level"* α denotes probability of committing of the ***type I*** errors and the $(1 - \alpha)$ is probability of making the correct decision and is also called *"confidence level"*. The probability of committing ***type II*** errors is denoted by β where $(1 - \beta)$ is the probability of rejecting a true blunder observation, also called *"power of the test"*.

The threshold values for the statistical tests

The threshold values for the global and the local tests must be predefined based on following parameters:

- α-is the false alarm probability of the global test
- α_0-is the false alarm probability of the local test,
- $\beta = \beta_0$-is the missed detection probability, should be this some for the local and the global test.

The above parameters α, β and α_0 are related by the following formula [1].

$$\lambda = (\lambda_0)^2 = \left(n_{1-\frac{\alpha_0}{2}} + n_{1-\beta}\right)^2 \tag{12}$$

$$\chi^2_{\beta,n-p,\lambda} = \chi^2_{1-\alpha,n-p} \tag{13}$$

Where λ is the non-centrality parameters of the non-centrally chi-square distribution χ^2. Thus, only two of them can be independently chosen. Furthermore, definition of values of the selected parameters is essential for consideration the following consequences:

- The large value α_0 implies a smaller critical value of the local test $n_{1-\frac{\alpha_0}{2}}$, causing exclusion of a higher number of correct observations.
- The large value of β_0 causes higher probability of missed detection, it means that more erroneous observation will be accepted as correct one.

Global Test-for the detection of faulty observation

Global test is used for evaluation if the set of GNSS observations include an erroneous observation. When the measurement errors are zero-mean normally distributed $N(0, \Sigma)$, the testing follows the central chi-square distribution χ^2. In such a case the test threshold value is defined by the inverse chi-square cumulative distribution function (CDF). This value is tested against the test parameters $\hat{v}^T \Sigma^{-1} \hat{v}$, the so-called *weighted sum of square error* **(WSSE)**. In the set of observations with distribution $N(0, \Sigma)$ the hypothesis is tested as:

$$
\begin{aligned}
H_0 &: \hat{v}^T \Sigma^{-1} \hat{v} \le \chi^2_{1-\alpha,n-p} \\
H_a &: \hat{v}^T \Sigma^{-1} \hat{v} > \chi^2_{1-\alpha,n-p}
\end{aligned}
\tag{14}
$$

The expression $(n - p)$ is degree of freedom, where n and p are number of observations and estimated parameters respectively. In a case when the result exceeds the threshold value $\chi^2_{1-\alpha,n-p}$, the null hypothesis H_0 is rejected and consequently alternative hypothesis is performed (see Fig.1). If H_0 is rejected and H_a is accepted, some inconsistency of the observations exists. In such a case the so called local test, assuming that only one blunder is present in the data set, should be applied.

Local Test-for the identification of faulty observation

A failed global test indicates that there is at least one erroneous observation. In such situation, the FDE algorithm starts execution of a local test to identify and reject that observation. The standardized residuals from the equation 10 are used to conduct the local test. Those residuals are compared with the α_0-quantile of the standard normal distribution $N(0, 1)$. The standardized residuals are normally distributed [15] with zero expectation if the $H_{0,i}$ is correct and with non-zero expectation value otherwise. The local test is based on the following hypothesis:

$$
\begin{aligned}
H_{0,i} &: |z_i| \le n_{1-\frac{\alpha_0}{2}} \\
H_{a,i} &: |z_i| > n_{1-\frac{\alpha_0}{2}}
\end{aligned}
\tag{15}
$$

where the probability α_0 was divided equally to the obtained right-tailed and left-tailed test. The null hypothesis $H_{0,i}$ denotes that i-th observation is not a blunder. Thus, when the $H_{0,i}$ is rejected then the alternative hypothesis $H_{a,i}$ is used to recognize if the threshold value is exceeded. The excluding process of the k-th erroneous observation is based on the following formulation [15]:

$$
H_{a,k} : Z_k \le Z_i \ \forall \ i, \ \wedge \ Z_k > n_{1-\frac{\alpha_0}{2}}
\tag{16}
$$

After exclusion of an erroneous observation and repetition of navigation solution, the statistical test should be repeated (Figure 1). As it was mentioned before, the process can be repeated until no more errors are detected or until the condition of redundant observation has stops being met.

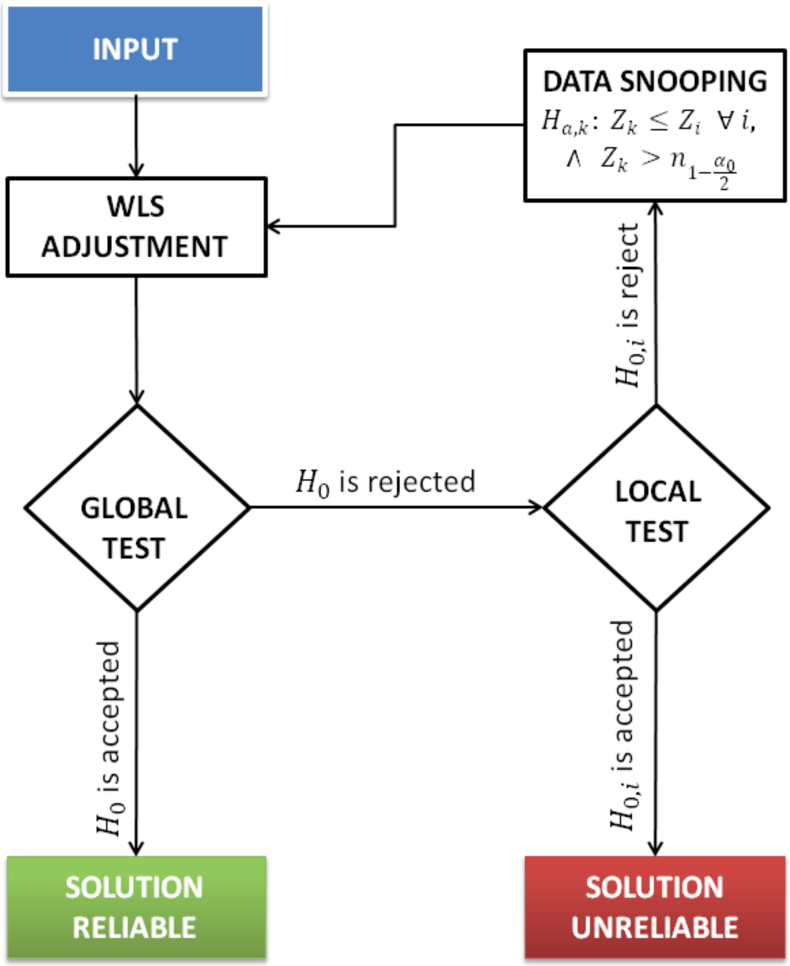

Figure 1. Fault Detection and Exclusion Scheme

3. Reliability tests with data collected in the presence of ionospheric perturbations

The investigations have been conducted using long time series of GNSS observations gathered at high latitudes 67.5 N LCKI (Kiruna/Sweden), see in the Fig. 2, where ionospheric perturbations occur more frequently and are stronger. The analysis were performed using high rate (1Hz) GPS data from the two selected days with low (2012 July, 05-Day of the Year-DOY: 187) and high (2012 July, 15-Day of the Year-DOY: 197) ionospheric perturbations. Some selected results of our investigations are presented in the figures below.

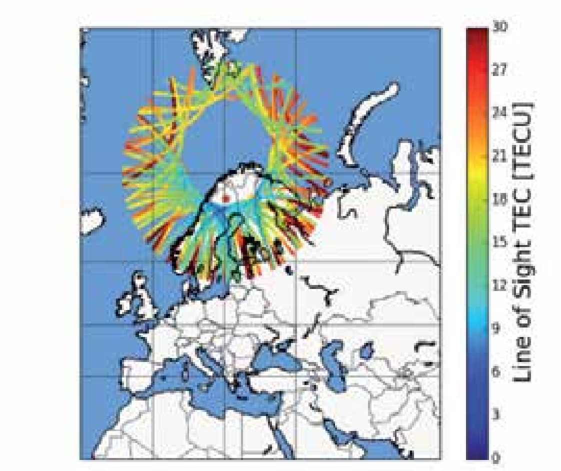

Figure 2. Localization of the GNSS receiver (LCKI, Kiruna/Sweden), visibility of satellites and sTEC (CODE/GIM from the Center for Orbit Determination in Europe, Astronomical Institute of the University of Bern). Slant TEC (in TECU unit) has been interpolated at the ionospheric pierce point (IPP) for each observed satellites. DOY:197

3.1. Influence of ionospheric perturbations onto quality of GNSS positioning

The ionospheric irregularities are correlated with the solar radiation and the Earth's geomagnetic field. Both of these phenomenon cause variability of electrons density in space and time. Since the ionospheric perturbations are directly associated with geomagnetic storms, for identification of those phenomena the planetary Kp-index has been used. This index represents irregular disturbances of the geomagnetic field caused by solar particle radiation [2]. The Figure 3 shows planetary Kp-index values during low-and high ionospheric perturbations.

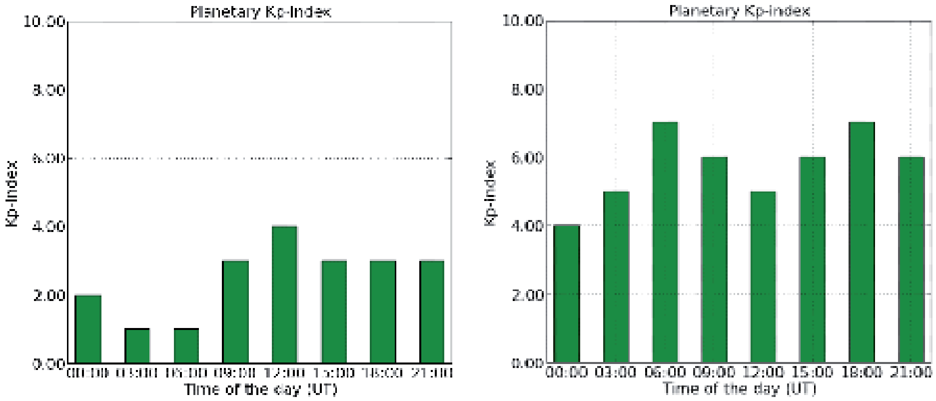

Figure 3. Planetary Kp-index: DOY187 (left) and DOY 197, (right) data LCKI – (Kiruna/Sweden), source: http://wdc.kugi.kyoto-u.ac.jp/kp/index.html)

Some other useful parameter used for monitoring the changes of the density of ions is continuous analysis of the time derivative of TEC [13] (ROT, rate of change of Total Electron Content). This parameter can be used for describing of direct correlation between ionospheric perturbations and GPS observations. The formula for ROT is written as:

$$ROT = \frac{TEC_t^s - TEC_{t-1}^s}{t_t - t_{t-1}} \tag{17}$$

where s is the visible satellite and t is the observation epoch. The TEC is derived from the dual frequency carrier phase measurements, and with usage of the ROT the "problem" of the carrier phase ambiguity fixing can be avoid.

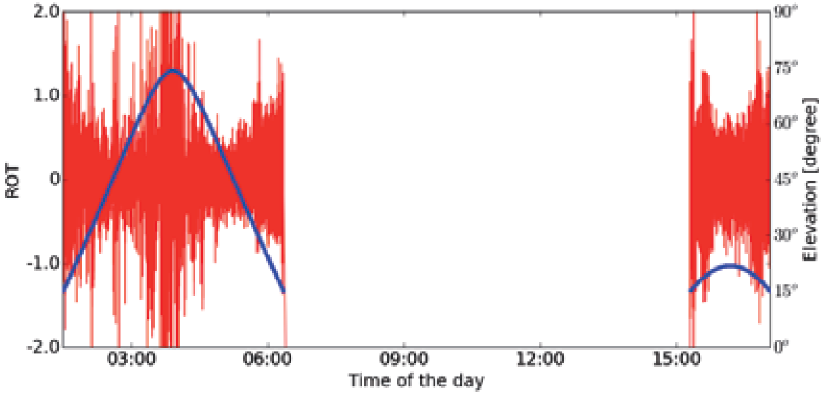

Figure 4. The relation between ROT and elevation angles presented for satellite PRN13 (DOY197), LCKI (Kiruna/ Sweden)

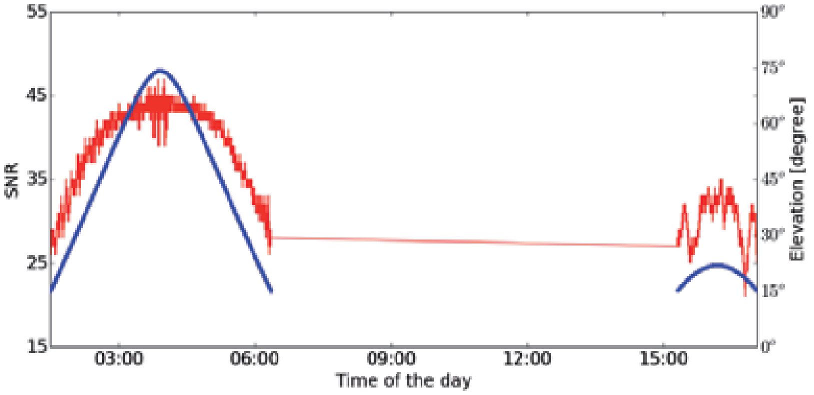

Figure 5. The relation between SNR (L2 frequency) and elevation angles presented for satellite PRN13 (DOY197), LCKI (Kiruna/Sweden)

In order to emphasize influences of ionospheric perturbation onto precision and accuracy of GNSS position displayed (see Figure 6), the residuals of GNSS coordinates are presented for the both selected days. This analysis shows some influences of the ionospheric disturbances on accuracy and precision of the GNSS positioning. The results obtained from the data recorded during strong ionospheric perturbations show higher degradation of precision and accuracy then the results obtained during low ionospheric perturbations. Some of the results are unacceptable by the applications where the high precision and reliability is required.

The effects of the ionospheric perturbations are also clearly seen in the Figure 7 where the presented carrier-phase residuals during high ionospheric perturbations are much bigger then carrier-phase residuals during the low ionospheric perturbations, Figure 8). The residuals "observed-calculated" (o-c) can be used to analyse observational noise level and to identify outliers in observations. Here the (o-c) values are used as an indicator describing the noise level of the carrier phase observations recorded under strong atmospheric disturbances.

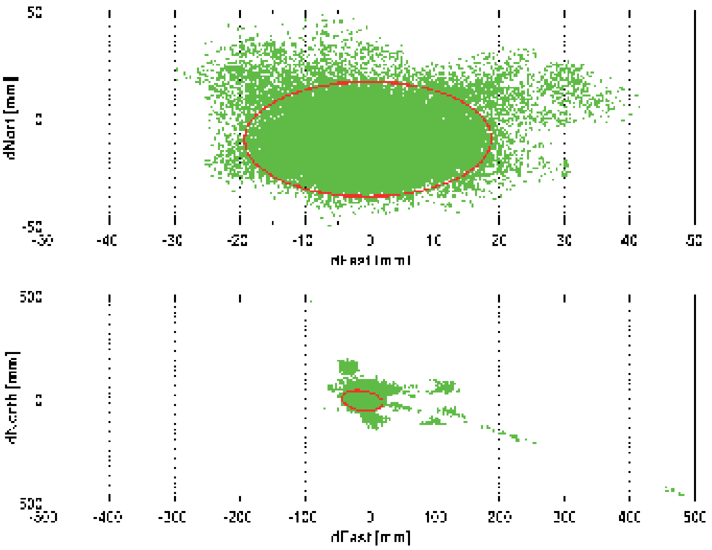

Figure 6. The confidence ellipse for the residuals of North and East coordinates, DOY:187 (upper figure) and DOY:197 (lower figure) (confidence level: 95%)-LCKI (Kiruna/Sweden)

An initial investigation was conducted in order to evaluate applicability of FDE method in order to improve performance of absolute positioning approaches in the presence of ionospheric perturbations. In this test the certainty levels for the reliability monitoring were predefined with the following values: the false alarm probability was set to $\alpha_0=10\%$ and the probability of missed detection was set to $\beta=20\%$.

In the Figure 9 solution of Single Point Positioning method are presented. This test has been performed using a set of simulated data. A simulated data approach has been used in order verify correctness of the implemented. The red points in the left graph (Figure 9) have been

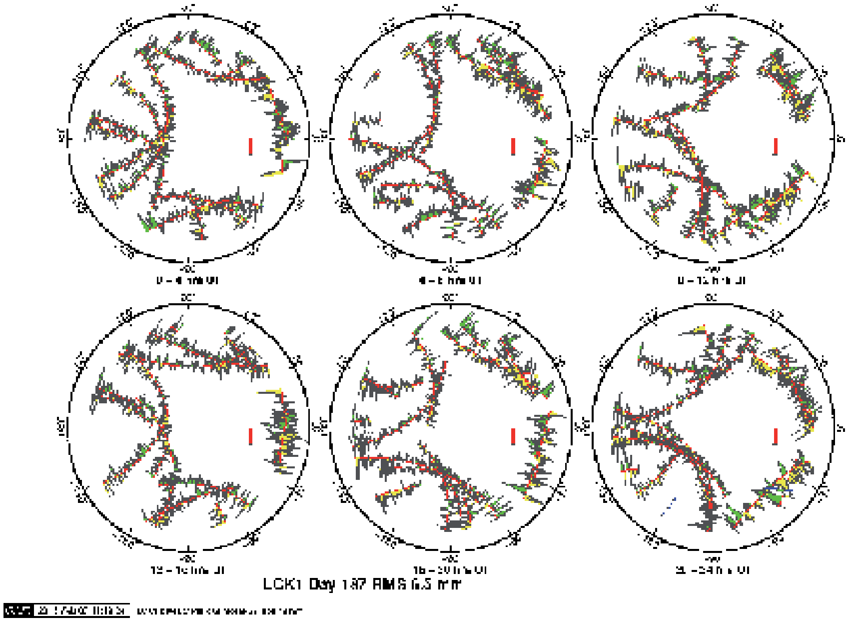

Figure 7. Carrier-phase residuals (o-c) per satellite DOY:187, LCKI (Kiruna/Sweden)

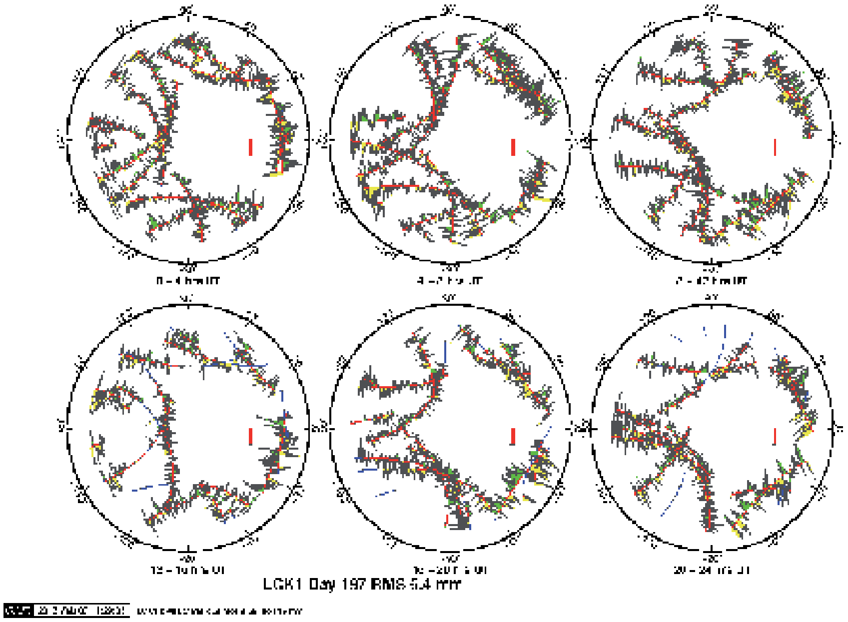

Figure 8. Carrier-phase residuals (o-c) per satellite DOY:197, LCKI (Kiruna/Sweden)

identified as unreliable solution. For those points inconsistency of GPS observations the have been detected. The right graph (Figure 9) shows solutions of the some set of GSP observations using the FDE. From this figure we can see that applicability of FDE gives ability to detect and to remove the erroneous observation and consequently to improve final solution.

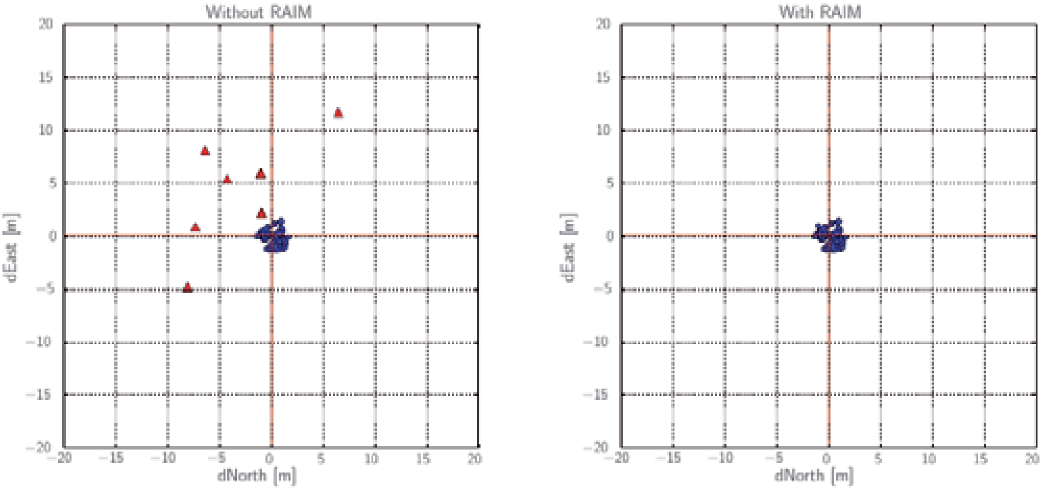

Figure 9. The Single Point Positioning solution without FDE (left) and with FDE (right)

4. Summary and conclusions

The paper considered integrity monitoring at the user-level for GNSS positioning applications. In order to improve performance of absolute point positioning algorithms, applicability of the fault detection and exclusion methods have been investigated. The suggested approach can be also used to support mitigation of ionospheric threats in GNSS real-time positioning solutions. Reliability testing of the fault detection and exclusion method has been performed with the weighted least-square residuals approach. Due to the strong influence of ionospheric perturbations onto the signal noise, the stochastic model has been defined using the weight matrix containing SNR (signal-to-noise ratio) values.

In this analysis only code-phase pseudo-ranges have been processed using a real-time single-epoch approach. It has been shown that the snapshot scheme allows unequivocal identification of blunder observations in a real-time "single epoch" standard point positioning approach and it can support mitigation of ionospheric perturbation influences. Due to strong influence of the geometry of the satellite constellation onto positioning quality, analysis of the DOP (dilution of precision) parameters will be taken into consideration as well. For the purpose of future analysis a stochastic model related to information about ionospheric perturbations will be developed and applied.

Acknowledgements

The research is funded by the FP7 People Programme through the Marie Curie Initial Training Network TRANSMIT-Training Research and Applications Network to Support the Mitigation of Ionospheric Threats.

In addition, acknowledgements are given to Space Weather Application Center Ionosphere (SWACI) operated by German Aerospace Center (DLR) in Neustrelitz for providing the SWACI data sets.

Author details

Kinga Węzka*

Address all correspondence to: kinga.wezka@tu-berlin.de

Technical University of Berlin, Department for Geodesy and Geoinformation Sciences, Berlin, Germany

References

[1] Baarda, W. A testing procedure for use in geodetic networks. Delft, Kanaalweg 4, Rijkscommissie voor Geodesie 2 (5), 1968.

[2] Bartels, J. The technique of scaling indices K and Q of geomagnetic activity. Annals of the International Geophysical Year 4, 215-226, 1957.

[3] Hartinger, H. & Brunner, F. Variances of GPS phase observations: The SIGMA model. GPS Solutions 2 (4), 35–43, 1999.

[4] Hewitson, S. & Wang, J. GNSS Receiver Autonomous Integrity Monitoring (RAIM) performance analysis. 2005.

[5] Kuang, S. Geodetic Network Analysis and Optimal Design: Concepts and Applications. Number ISBN-10: 1885863144, Ann Arbor Press Inc., Chelsea, Michigan, 1996.

[6] Kuusniemi, H. User-Level Reliability and Quality Monitoring in Satellite-Based Personal Navigation. PhD thesis, Institute of Digital and Computer Systems, Tampere University of Technology, Finland, Publication 544, 2005.

[7] Kuusniemi, H. & Lachapelle, G. GNSS signal reliability testing in urban and indoor environments. In Proceedings of NTM 2004 Conference (Session A2), San Diego, CA, January 26-28, The Institute of Navigation, 2004.

[8] Lachapelle, G. & Ryan, S. Statistical Reliability Measures for GPS. IMA Workshop on Mathematical challenges in GPS, University of Minnesota, 7 pages, 16-18 August 2000.

[9] Langley, R. B. GPS receiver system noise. GPS World, 1997.

[10] Parkinson, B. & Axelrad, P. Autonomous GPS integrity monitoring using the pseudorange residual. Journal of The Institute of Navigation 35 (2), 255–274, 1988.

[11] Parkinson, B. W. & Axelrad, P. A basis for the development of operational algorithms for simplified GPS integrity checking. In Institute of Navigation, Technical Meeting, 1st, Colorado Springs, CO, Sept. 21-25, 1987, Proceedings (A88-37376 15-04). Washington, DC, Institute of Navigation, pp. 269-276, 1987.

[12] Parkinson, B. W. & Spilker, J. J. Global Positioning System: Theory and Applications. Volume I-II, number ISBN-10: 1563471078, American Institute of Aeronautics and Astronautics, 1996.

[13] Pi, X., Mannucci, A. J., Lindqwister, U. J. & Ho, C. M. Monitoring of global ionospheric irregularities using the worldwide GPS network. Geophysical Research Letters 24: 2283–2286, 1997.

[14] Struza, M. A. Navigation system integrity monitoring using redundant measurements. Journal of The Institute of Navigation 35 (4), 1988.

[15] Tunissen, P. J. G. & Kleusberg, A. GPS for Geodesy (2nd edition). Number ISBN-3-540-63661-7, Springer, 1998.

[16] Walter, T. & Enge, P. Weighted RAIM for precision approach. 1995.

Chapter 9

A Filtering Method Developed to Improve GNSS Receiver Data Quality in the CALIBRA Project

Luca Spogli, Vincenzo Romano,
Giorgiana De Franceschi, Lucilla Alfonsi,
Eleftherios Plakidis, Claudio Cesaroni,
Marcio Aquino, Alan Dodson,
Joao Francisco Galera Monico and Bruno Vani

Additional information is available at the end of the chapter

http://dx.doi.org/10.5772/58778

1. Introduction

To study ionospheric scintillation on L-band radio signals, it is nowadays typical to acquire data with GNSS (Global Navigation Satellite System) receivers working at high frequency sampling rate (50-100 Hz) [1]. When dealing with such data, it is common to consider the contribution coming solely from observations at elevation angles, calculated from the receiver to the selected satellite, above an arbitrary threshold, typically 15-30°. Filtering out measurements made at low elevation angles helps keeping a high SNR (Signal to Noise Ratio) and eliminating non-ionospheric related effects, such as multipath [2].

The downside of that well consolidated method is a reduction of the field of view spanned by the GNSS receiver antenna, and, if it is the case, of the whole network. This is not crucial for dense networks or well covered areas, but it can be in the case of not well covered regions, for logistics (e.g. forests, deserts, etc.) and/or environmental reasons (e.g. oceans). The loss of information in many applications could be meaningful.

In this paper, we present a method to filter out spurious data based on an "outliers analysis" able to efficiently remove multipath affected measurements, reducing the data loss from 35-45% to 10-20%. It is based upon the Ground Based Scintillation Climatology (GBSC) ([3], [4]) and the station characterization based upon GBSC [5] is applied to the CIGALA[1]/ CALIBRA[2] network in Brazil. The research shown herein was carried out in the context of the CALIBRA (http://www.calibra-ionosphere.net) project and exploits the CIGALA/ CALIBRA network in Brazil, to which the method was applied, enlarging the field of view and, then, improving the capability of inferring the dynamics of the low latitude ionosphere.

2. Data and method

The CALIBRA project builds on the now ended CIGALA (http://cigala.galileoic.org/) project, and exploits a combined network of specialized receivers installed as part of the two projects, the so-called CIGALA/CALIBRA network, which is equipped with Septentrio PolaRxS receivers.

The PolaRxS is a multi-frequency, multi-constellation receiver capable of tracking simultaneously GPS L1CA, L1P, L2C, L2P, L5; GLONASS L1CA, L2CA; GALILEO E1, E5a, E5b, E5AltBoc; COMPASS B1, B2; SBAS L1 [6]. Sampling at 50 Hz, the receiver gives the following main output parameters:

1. σ_Φ phase scintillation index calculated over different time intervals (1, 3, 10, 30, 60 seconds);
2. S_4 amplitude scintillation index calculated over 60 seconds;
3. *TEC* (Total Electron Content) and *ROT* (Rate of TEC change) every 15 seconds,
4. spectral parameters: spectral slope of the phase Power Spectral Density (*p*) in the 0.1 to 25Hz range and the spectral strength of the phase Power Spectral Density (*T*) at 1 Hz (60 seconds);
5. Standard Deviation of the Code to Carrier Divergence (*CCSTDDEV* - 60 seconds);
6. *SNR* (60 seconds);
7. *locktime* (60 seconds).

All these quantities (except *TEC* and *ROT*) are calculated for all available signal frequencies transmitted by the satellites and along the slant path connecting receiver and satellite. *TEC* values are obtained by pseudorange measurements only. GPS-*TEC* measurement is based on the L2-P and L1-P pseudoranges; GLONASS-*TEC* is based on the L1-C/A and L2-C/A pseudoranges and Galileo-TEC is based on the L1BC and E5a. *ROT* is computed from the carrier phase measurements only, and hence is much more accurate than *TEC*.

The data used in this analysis was acquired by the CIGALA/CALIBRA network of PolaRxS receivers during the whole year in 2012. Table 1 summarizes all the CIGALA/CALIBRA stations available during the considered period with their corresponding identifier, location and geographic coordinates.

---

[1] CIGALA stands for Concept for Ionospheric-Scintillation Mitigation for Professional GNSS in Latin America.

[2] CALIBRA stands for Countering GNSS high Accuracy applications LImitation due to ionospheric disturbance in BRAzil.

Name	Location	Lat (°N)	Lon (°E)
MANA	Manaus	-3.12	-60.01
PALM	Palmas	-10.20	-48.31
POAL	Porto Alegre	-30.07	-51.12
PRU1	Presidente Prudente	-22.12	-51.41
PRU2	Presidente Prudente	-22.12	-51.41
SJCI	São José dos Campos	-23.21	-45.86
SJCU	São José dos Campos	-23.21	-45.96

Table 1. List of the CIGALA/CALIBRA network receivers used in the analysis.

Figure 1 shows the impact of applying a standard 20° elevation cutoff in terms of percentage of data coverage of the network, normalized to the total number of data points (GPS and GLONASS) available in 2012. Figure 1a shows the coverage obtained by applying no threshold on the elevation angle while figure 1b shows that obtained with a threshold of 20°. Both maps and the geomagnetic equator (red line) are projected at a height of 350 km, being representative of the ionospheric F2-layer peak height.

The cutoff reduces significantly the capability of the network in depicting the ionosphere northward of the geomagnetic equator and above the Atlantic Ocean, east of Brazil.

The filtering method based upon the outliers is then described: for each station of the network, the map in azimuth vs. elevation of the standard deviation of the *CCSTDEV* ($\sigma_{CCSTDDEV}$) is produced by using the GBSC technique. The bin size adopted is 5°x5° and observations on both GPS and GLONASS L1 frequency have been considered to maximize the number of observations in each bin. The CCSTDDEV is chosen as it is a good indicator of the multipath activity experienced by the receiver antenna [7] and its standard deviation ($\sigma_{CCSTDDEV}$) identifies the bin in which it experiences a large variability.

As an example, Figure 2a shows the map of $\sigma_{CCSTDDEV}$ obtained for the MANA station in 2012. Each value of $\sigma_{CCSTDDEV}$ is then used to create the corresponding histogram, shown in Figure 2b. The filtering method is based upon the identification of the outliers in such $\sigma_{CCSTDDEV}$ histogram. As stated in the general data analysis theory, most values of a distribution are expected in the inter quartile range (*IQR*) or located between the two hinges. Values lying outside 1.5 times the *IQR* are called "mild outliers" and values outside the boundaries of 3 times the *IQR* are termed "extreme outliers" [8]. The red line in Figure 2b indicates the cutoff for the mild outliers (1.5 *IQR*). The bins corresponding to values of $\sigma_{CCSTDDEV}$ greater than $<\sigma_{CCSTDDEV}>$+1.5 *IQR*, i.e. the mild outliers, are filtered out and new analyses can be performed.

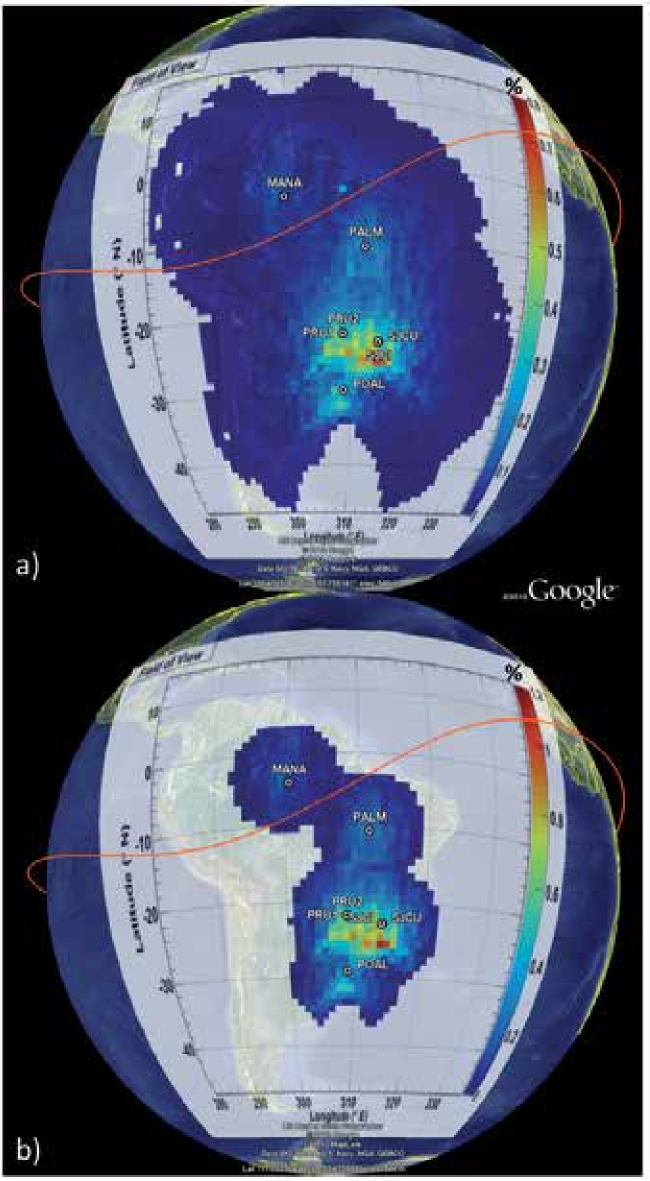

Figure 1. Percentage of data coverage of the CIGALA network considering the full dataset of 2012, obtained applying no threshold on the elevation angle (a) and with a threshold of 20° (b). Both maps and the geomagnetic equator (red line) are projected at 350 km of height.

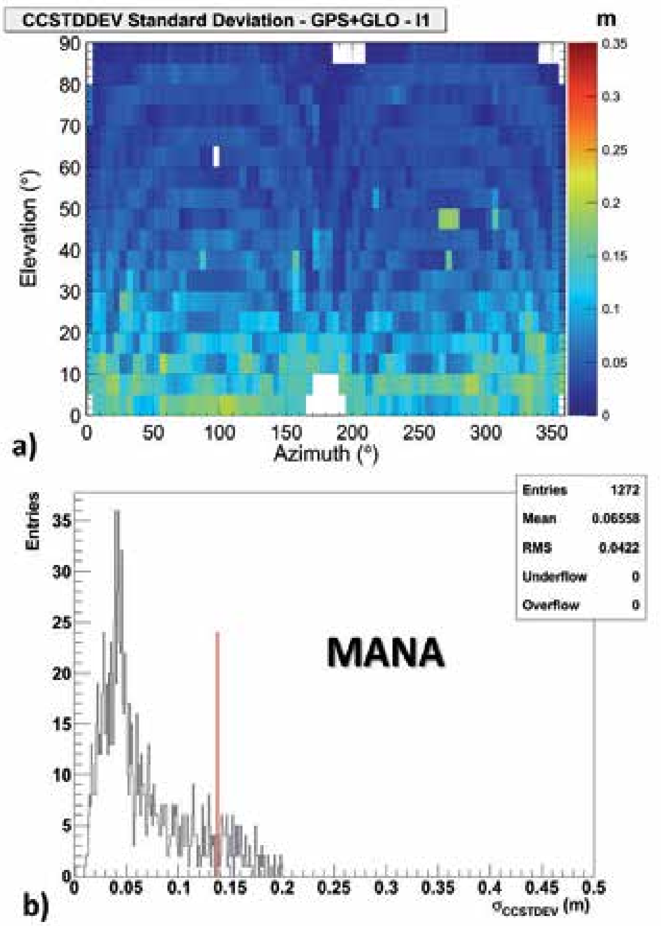

Figure 2. (a) Map of the $\sigma_{CCSTDDEV}$ in *azimuth* vs. *elevation* for MANA (GPS+GLONASS data on L1 frequency) for 2012. (b) Corresponding distribution of the $\sigma_{CCSTDDEV}$. The red line indicates the cut-off for mild outliers.

3. Results

The method is able to remove the contribution mostly from the low elevation angles, as expected, but to keep some “not noisy” bins. By using this technique the number of rejected observations ranges between 12% and 20%, reducing the data loss in comparison to the application of the standard elevation angle cut-off of 15-30°, which ranges between 35 and 45%. Similarly to Figure 1, the percentage of data coverage of the CIGALA/CALIBRA network after the filtering procedure is shown in Figure 3. From this figure and Figure 1(b) it is evident how this filtering allows to cover further ionospheric sectors of interest and to characterize there the pattern of ionospheric variability.

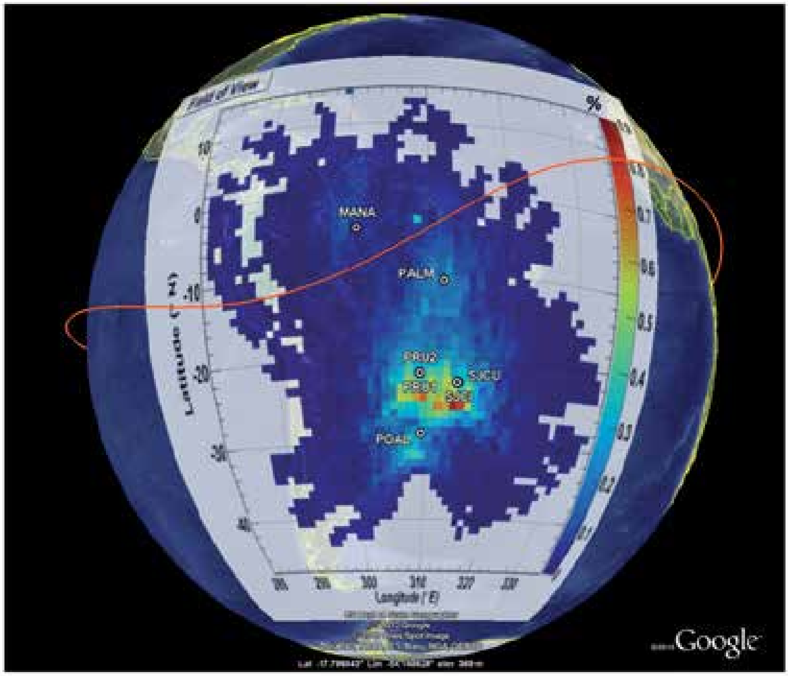

Figure 3. Percentage of data coverage of the CIGALA network receivers considering the full dataset of 2012 after the filtering procedure. The map and the geomagnetic equator (red line) are projected at a height of 350 km.

Figure 4 shows the map of the percentage of occurrence of the amplitude scintillation index S_4 [7] values above 0.25, in geographic coordinates. Such threshold of 0.25 allows the characterization of the areas of the ionosphere in which scintillation affects the GNSS signals in a moderate to strong manner. Only data acquired in the UT range between 22 and 04 UT has been considered, in order to focus on the post sunset hours in which most of the scintillation occurs (see, e.g., [9]). From this map (Figure 4), thanks to the enlargement of the field of view covered by the CIGALA/CALIBRA network introduced by the filtering algorithm, it is possible to see the enhancement of occurrence in correspondence with the northern crest of the Equatorial Ionospheric Anomaly (EIA) [10], mainly covered by the MANA observations. This enhancement is for geographic latitudes greater than 0°N and in a band nearly parallel to the geomagnetic equator (red line), where an occurrence peak of about 6% is reached. On the other hand, the southern crest of the EIA is well covered by the data and its effect in terms of amplitude scintillation occurrence is visible in the band of enhanced scintillation nearly parallel to the geomagnetic equator (red line) and reaching a peak value of about 16%. From these considerations, the most affected regions are those in the latitudinal range between 30°S and 10°N and in correspondence with longitudes between 300°E and 330°E, in particular over São Paulo and Tocantins States (due to the presence of the EIA southern crest) and northward of MANA (due to the presence of the EIA northern crest). The enhancement over POAL is also meaningful and possibly due to the presence of the particle precipitation occurring in the borders of the South Atlantic Magnetic Anomaly (SAMA) [11]. The SAMA is in fact another source of ionospheric turbulence leading to scintillation, as it disturbs the thermospheric circulation in the atmosphere and alters the rates of production and recombination of the ionized species, mainly under geomagnetic storms [12].

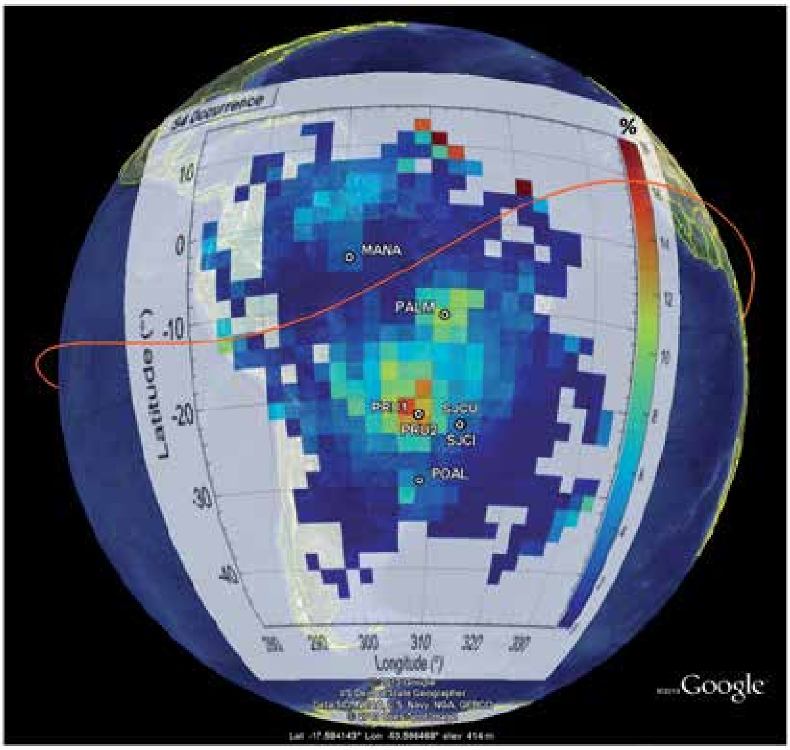

Figure 4. Map of S_4 percentage of occurrence above 0.25 in geographic coordinates (GPS+GLONASS, L1 frequency) in the UT range 22-04 UT.

4. Conclusion

We have shown how the development of a filtering method to remove spurious data based on an analysis of outliers is able to efficiently clean multipath and signal degradation from GNSS data. This approach limits the data loss to 10-20%, while the traditional cut off of 15°-30° on the elevation angle leads to losses of 35-45%. The reduction in data loss, averaged among all the station, is of a factor of about 2.4.

We applied the method to the 2012 data acquired by the CIGALA/CALIBRA network, increasing its capability to depict the ionospheric features. This method optimizes the capability of GNSS networks and helps in planning the installation of additional new receivers aiming to enlarge network coverage.

Acknowledgements

The CIGALA project (http://cigala.galileoic.org/) was funded under the EU Seventh Framework Program, and was carried out in the context of the Galileo FP7 R&D program. The CALIBRA project (http://www.calibra-ionosphere.net) was funded under the EU Seventh Framework Program, and was being carried out in the context of the Transport (including Aeronautics), Support to the European global satellite navigation system (Galileo) and EGNOS program. Both projects are supervised by the GSA.

VR contribution is included in the PhD research project: "Scintillation effects on GNSS: monitoring and data treatment development" carried out at the Nottingham Geospatial Institute of the University of Nottingham. In particular its contribution is in the method concept and algorithm development.

Two monitoring stations were provided by UNESP via FAPESP (Process no. 2006/04008-2). The authors also want to thank the following partner institutions in Brazil: IFTO (Instituto Federal do Tocantins), UFRGS (Universidade Federal do Rio Grande do Sul), INPE (Instituto Nacional de Pesquisas Espaciais), UNIVAP (Universidade do Vale do Paraiba), Petrobras (Petróleo Brasileiro S/A) and UEA/INPA (Universidade do Estado do Amazonas/Instituto Nacional de Pesquisas Ambientais).

Author details

Luca Spogli[1], Vincenzo Romano[1,2], Giorgiana De Franceschi[1], Lucilla Alfonsi[1],
Eleftherios Plakidis[1], Claudio Cesaroni[1], Marcio Aquino[2], Alan Dodson[2],
Joao Francisco Galera Monico[3] and Bruno Vani[3]

1 Istituto Nazionale di Geofisica e Vulcanologia, Rome, Italy

2 University of Nottingham, Nottingham, UK

3 Departamento de Cartografia, Universidade Estadual Paulista Júlio de Mesquita Filho, Brazil

References

[1] Kintner, P.M., T. Humphreys and J. Hinks (2009). GNSS and Ionospheric Scintillation – How to survive to the next solar maximum, InsideGNSS, July/August2009, 22-30.

[2] S. Skone and M. de Jong, The Impact of Geomagnetic Substorms on GPS receiver performance, Earth Planets Space, 52, 1067–1071, 2000.

[3] Spogli, L., Alfonsi, L., De Franceschi, G., Romano, V., Aquino, M.H.O., Dodson, A. Climatology of GPS ionospheric scintillations over high and mid-latitude European regions. Ann. Geophys. 27, 3429–3437,2009.

[4] Alfonsi, L., Spogli, L., De Franceschi, G., Romano, V., Aquino, M., Dodson, A., Mitchell, C.N. Bipolar climatology of GPS ionospheric scintillation at solar minimum. Radio Sci. 46, RS0D05, http://dx.doi.org/10.1029/2010RS004571, 2011.

[5] Romano, V., Spogli, L., Aquino, M., Dodson, A., Hancock, C., Forte, B., GNSS station characterisation for ionospheric scintillation applications, Advances in Space Research 52 (2013) 1237–1246.

[6] Bougard, B., Sleewaegen, J.-M., Spogli, L., Sreeja, V.V., Galera Monico, J.F., 2011. CIGALA: challenging the solar maximum in Brazil with PolaRxS. In: Proceeding of the ION GNSS 2011. Portland, Oregon.

[7] Van Dierendonck, A.J., Klobuchar, J., Hua, Q. Ionospheric scintillation monitoring using commercial single frequency C/A code receivers, in: ION GPS-93 Proceedings of the Sixth International Technical Meeting of the Satellite Division of the Institute of Navigation, Salt Lake City, USA, 22–24 September, 1333–1342, 1993.

[8] Barnett, V., Lewis, T., Outliers in Statistical Data. Wiley, 3rd Edition, 1995.

[9] Alfonsi, L., et al. GPS scintillation and TEC gradients at equatorial latitudes on April 2006. J. Adv. Space Res.(2010), doi:10.1016/j.asr.2010.04.020

[10] Kelley, M. C. (1989), The Earth's Ionosphere, pp. 121–143, Academic, San Diego, Calif.

[11] Spogli, L. et al., GPS scintillations and total electron content climatology in the southern low, middle and high latitude regions, ANNALS OF GEOPHYSICS, 56, 2, 2013, R0220; doi:10.4401/ag-6240

[12] Abdu, M.A., Batista, I.S., Carrasco, A.J., Brum, C.G.M., 2005. South Atlantic magnetic anomaly ionization: a review and a new focus on electrodynamic effects in the equatorial ionosphere. J. Atmos. Sol. Terr. Phys 67, 1643–1657.

B-Spline Model of Ionospheric Scintillation For – High Latitude Using *In-situ* Satellite Data

S. Priyadarshi and A. W. Wernik

Additional information is available at the end of the chapter

http://dx.doi.org/10.5772/58777

1. Introduction

Ionospheric scintillation is a popular phenomenon among space scientists and GNSS users. It has been widely discussed and studied in past but still difficult to model and predict on large scales. Ionospheric scintillations are caused by rapid random variations of the phase and amplitude of the radio waves passing through the ionosphere. As the signal propagation continues after passing through the region of irregularities in the ionosphere, phase and amplitude scintillation develops through interference of multiple scattered waves. After propagation to a receiver, the irregular phase may combine either constructively or destructively to increase or decrease the wave amplitude. Another possibility is that the cause of either increased or decreased phase velocity may be refractive when an electromagnetic wave enters a medium [8].

The first empirical model of scintillation was proposed by Fremouw and Rino in 1973 [6]. This model could estimate the scintillation index S_4 on VHF/UHF, under weak scatter conditions. Weak scatter condition is often violated near the equatorial anomaly and auroral regions. This model led the foundation of more advanced model "WBMOD". Aarons developed analytic model in 1985 [1] using 15-min peak to peak scintillation indices (not S_4) taken over 5 years at Huancayo, Peru using LES 6 satellite transmitted at 254 MHz. Next comes India model by Iyer and his group in 2006 [7]. They used cubic-B spline technique to develop an empirical model of magnetic quiet time scintillation occurrence at Indian equatorial and low latitudes. 250 MHz signal from FLEETSAT satellite was measured for 2 years at Trivandrum, near magnetic equator and Rajkot at the crest of equatorial anomaly. To describe the structure and extent of the radio scintillation generated by turbulence around and within the equatorial plumes a physical model has been developed by J. M. Retterer [10].

The first climatological model WBMOD has been developed by Northwest Research Associates, Inc. in which the user can specify his operating scenario. As the output the model returns: the phase scintillation spectral index p, the spectral strength parameter T, S_4, and phase scintillation index σ_ϕ. GISM has been described by Beniguel and Buonomo in year 1999 [4]. The model consists of two parts the NeQuick model and the scintillation model based on multiple phase screen algorithm. 2nd part of the model needs statistical information about irregularity as input. The algorithm is used to calculate the scintillation index at the receiver.

Basu and his group used first time satellite in situ data in scintillation modeling in 1976 [2]. They assumed a 3D power law irregularity spectrum with a constant spectral index of 4. They prepared another high latitude scintillation model in 1981, 1988 [3] using Atmospheric Explorer D data. Due to limited availability of data the model was suitable for northern winter under sunspot minimum condition.

Wernik et al. [12] used the Dynamics Explorer B data to estimate the irregularity spectral index and turbulence strength parameter, the factors that are required to calculate the scintillation index [11]. Their approach has been extended by Liu et al. [16] by introducing the finite outer scale.

Present model makes use of Dynamic Explorer 2 plasma density data covering period of August 1981 to February 1983. This period was near to maximum solar activity. In this model we are using the turbulence strength parameter C_s and the spectral index derived from Wernik et al. [12]. Simplest phase screen model described by Rino has been used to derive S_4 index. The parameters derived from Dynamic Explorer 2 satellite data are used with IRI model [5]. For comparing present model to the WAM model we produce maps in magnetic local time (MLT) and invariant latitude.

We present a spline model for the high latitude ionospheric scintillation using satellite in situ measurements made by the Dynamic Explorer 2 (DE 2) satellite. This analytical model is based on products of cubic B-splines and coefficients determined by least squares fit to the binned data. This product is constrained to make the fit periodic in 24 hours of geomagnetic local time, periodic in 360 degree of invariant longitude, in geomagnetic indices and solar radio flux. Discussion of our results clearly shows the seasonal and diurnal behavior of ionospheric parameters important in scintillation modeling for different geophysical and solar activity conditions. We also show that results obtained from our analytical model match observations obtained from in situ measurements. DE 2 satellite measurements give observations only along satellite orbit but our interpolation model fills the gaps between the satellite orbits.

2. Data preparation

The input data to our scintillation model are DE 2 retarding potential analyser (RPA) measurements of the ion density, equivalent by the charge neutrality to the electron density N_e. The altitude of its orbit was between about 300 and 1000 km (perigee: 309 km, apogee 1012 km, inclination: 89.99°, period: 98 min). The satellite was on a nearly polar orbit. The sampling frequency of RPA was 64 Hz, corresponding to every 120 m along the satellite orbit. These measurements were grouped over 8 s (512 samples) long segments [12].

The parameters derived from Dynamic Explorer 2 satellite (DE 2) data have been grouped separately into seasonal bins and for specific duration of case study (for studying geophysical events). These binned data have been appended from the few parameters obtained from IRI model and NASA's Goddard Space Flight Centre (http://omniweb.gsfc.nasa.gov/html/omni2_doc.html).

NASA's data server was used to get K_p index, F10.7 cm solar radio flux, Geo-magnetic field and sun spot number data. IRI model was used to append the binned data set with mean electron density, electron density peak height, and calculated irregularity layer thickness. The amplitude scintillation index S_4 was calculated using Rino's [11] weak scatter phase screen formula. In this calculation we took only those values of one dimensional spectral index p, which was less than 4.

3. B-spline model derivation

The reason of using DeBoor B-spline function [15] is one of the most famous property of B-spline functions that they has minimal support to a given degree of freedom, smoothness and domain partition. B-spline models are best because they provide similar results, even when using low-degree splines to the models produced using higher degree polynomials while avoiding instability at the edges of an interval (Runge's phenomenon).

Parameter's derived from DE 2 satellite data as a function of local time, day/season/month, geographic coordinates, K_p index and solar flux value F10.7, is expressed as simultaneous product of univariate normalized B-splines as given below

$$Parameter(t,\ d,\ geo.coord.,\ kp,\ F10.7)= \sum_{i=1}^{24}\sum_{j=1}^{365}\sum_{k=1}^{9}\sum_{l=1}^{6} a_{i,j,k,l}{}^{*}N_{i,4}(t)N_{j,2}(d)N_{k,2}(Kp)N_{l,2}(F10.7) \tag{1}$$

$$S_4(t,\ d,\ geo.coord.,\ kp,\ F10.7)= \sum_{i=1}^{24}\sum_{j=1}^{365}\sum_{k=1}^{9}\sum_{l=1}^{6} a_{i,j,k,l}{}^{*}N_{i,4}(t)N_{j,2}(d)N_{k,2}(Kp)N_{l,2}(F10.7) \tag{2}$$

where $a_{i,j,k,l}$ are monthly mean of amplitude scintillation index and/or parameters derived from RPA measurements for each interval of magnetic local time, invariant coordinate, K_p index and solar radio flux F10.7 cm. $N_{i,4}$ is a b-spline basis function of degree 4 and other b-spline basis function are of degree 2.

These all 4 B-spline basis functions are non-vanishing over limited intervals. They all add up to one at all magnetic local time, season, K_p index and F10.7 solar radio flux interval. For more details about properties of basis function one should refer to DeBoor [15]

We have used 3-hourly time nodes for magnetic local time. They vary between 0 to 23 hour as 3, 6, 9, 12, 15, 18, 21 and 24. For seasonal maps we have used 3-hourly magnetic local times and 10 day (the maps resolution is 3 h X 10 days) median of binned data. For K_p index 9 nodes were chosen which vary between 1 to 9. 6 individual nodes have been chosen for F10.7 cm radio flux value, they are 80, 130, 180, 230, 280 and 330 respectively.

The number and placement of magnetic local time nodes for each season and solar flux interval were individually chosen to account for large variability in amplitude scintillation index and other modeled parameters. It is tricky to cleverly observe rapid changes in amplitude scintillation index and parameters. Consequently more basis functions are needed to account for these rapid changes. Therefore, placement and number of magnetic local time nodes are different for different seasons and geophysical cases.

We could have used the higher density mesh of basis functions for all geophysical case studies. This gives freedom to the programmer and one can approach closer to the real observational results. Which simply means one should see the actual behavior of modeled parameter and cleverly chose the number and placement of more or less basis function in order to derive same parameter from the model.

The coefficient $a_{i,j,k,l}$ were determined by least square fit to the binned data and constrained to make the fit periodic in 24 hour and 360 geomagnetic longitude. The local time and diurnal B-spline functions are shown in Fig. 1. As we have already discussed for quiet geophysical conditions smaller number of basis functions are sufficient which should be

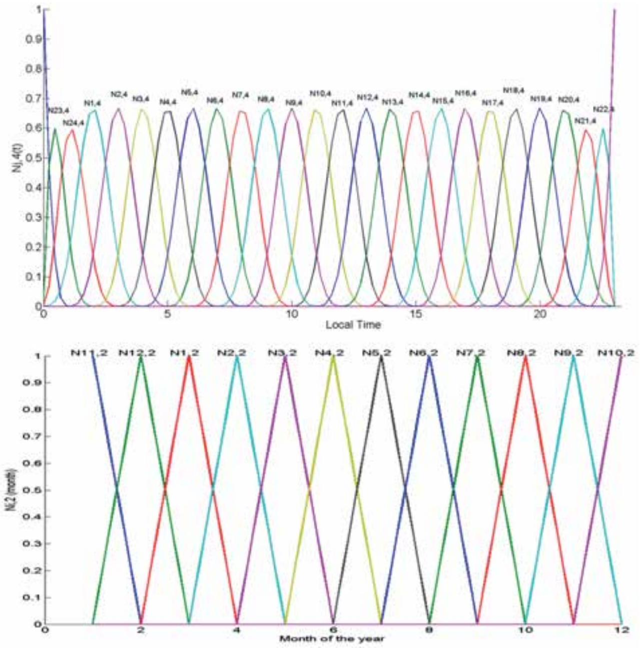

Figure 1. Basis function for the local time (upper figure) and month of the year (lower figure).

Considered as a quality of this consolidated model. This is because of less need of the modelling coefficients (e.g. basis functions) for modelling quiet geophysical condition (e.g., low solar flux). Using more B-spline function and their placement at right positions we can upgrade our model, which makes us enable of modelling disturbed geophysical conditions. This freedom outweighs our consolidated model. For comparing our model with observation we have prepared contour maps for real observation which use "contour" MatLab subroutine which uses linear interpolation method for plotting. Our modelled contours use B-spline interpolation method. From in situ measurements we derived the turbulence strength parameter C_s and the spectral index using the method discussed in WAM model. With the IRI model [5] the C_s parameter was rescaled to get its value at the height of the maximum electron density. The IRI model was also used to estimate the irregularity layer thickness. To convert the parameters derived from RPA measurements to the equivalent scintillation index one should rely on the scintillation theory [12].

4. Result and Discussion

From the weak scatter phase screen model introduced by C. L. Rino [11] amplitude scintillation index S_4 can be expressed as as

$$S_4^2 = \left(r_e\lambda\right)^2 L \csc E C_S Z^{p/2} \frac{\Gamma\left(1-p/4\right)}{\pi^{1/2}\Gamma\left(p/4+0.5\right)p} F\left(a,b\right) \tag{3}$$

where r_e is classical electron radius, λ is wavelength of the signal, L is the irregular layer thickness, θ is the zenith angle, C_s is turbulence strength parameter and Z is the Fresnel zone parameter and F is Fresnel filter factor.

The one dimensional spectral index p is an important parameter which determines the scintillation level [12]. Therefore, variation of spectral index with ionospheric changes becomes significantly important for studying the scintillation effect on trans-ionospheric communication links. Fig 2 shows the behaviour of spectral index in equinox for geomagnetic quiet conditions.

It is evident from the above figure that in quiet geomagnetic condition one dimensional spectral index intensifies near magnetic noon. For invariant latitude >70 degree, spectral index is more intense which in start of auroral zone. It seems expanding from auroral boundary to polar cusp region in night time. One can easily observe that in geomagnetic quiet condition modelled map is in good agreement with the one produced from real observation. Fig. 3 below shows the behaviour of spectral index for geomagnetic disturb days in equinox months.

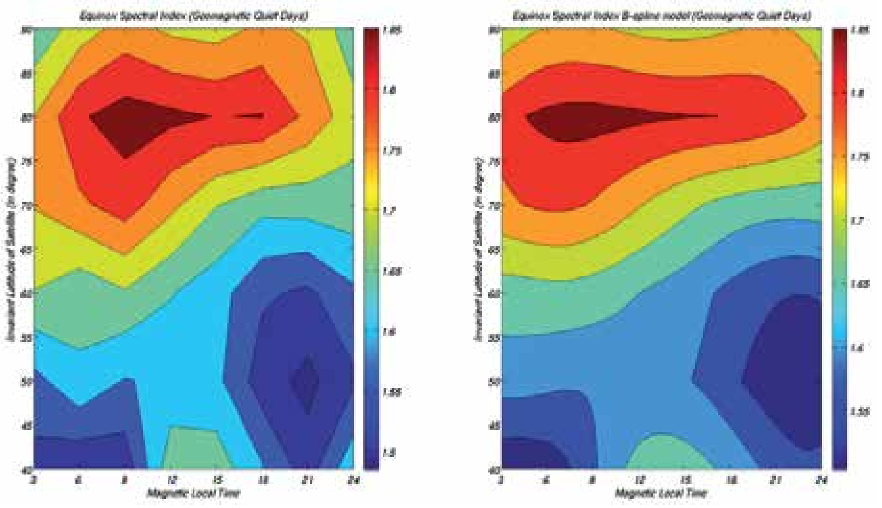

Figure 2. Spectral index for equinox for $K_p \leq 3$. Left contour is built from real data. Right picture is spectral index modelled using B-spline technique.

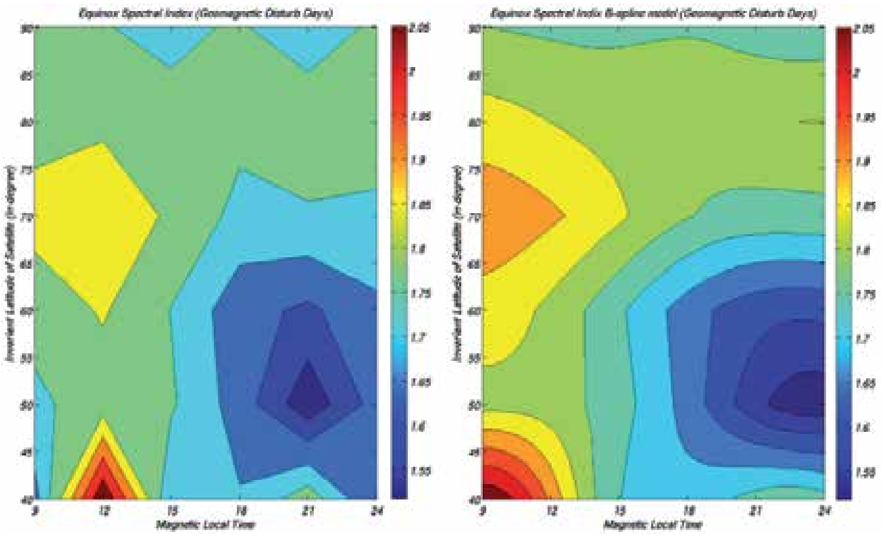

Figure 3. Spectral index for equinox for $K_p > 3$. Left contour is built from real data. Right one is spectral index modeled using B-spline technique.

It is evident from the figure that spectral index seems expanding from the auroral boundary towards the equator. The spectral index level is high in geomagnetic disturbed conditions of the equinox than that of the geomagnetic quiet days of the equinox months. Though the maxima is visible near the magnetic noon. Modelled results are in good agreement with the observations.

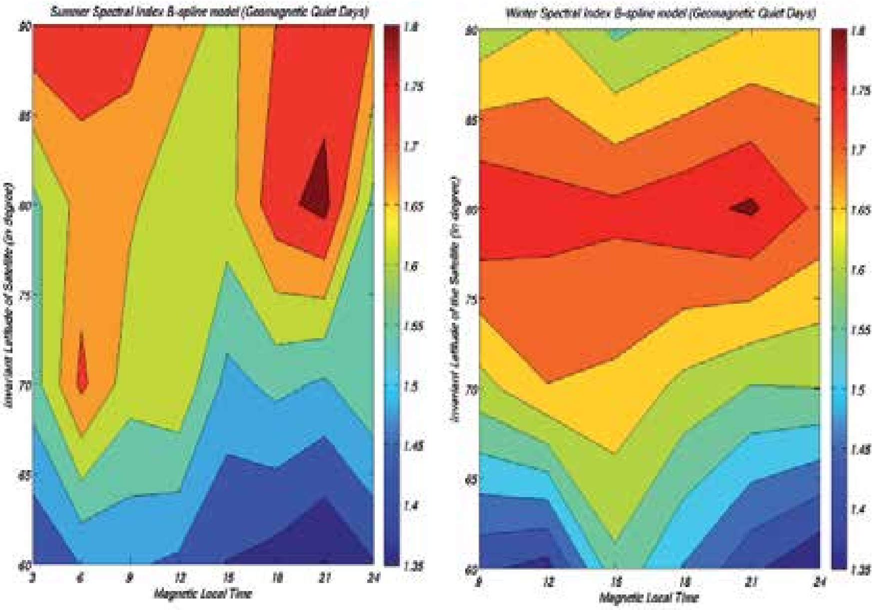

Figure 4. Spectral index for $K_p \leq 3$. Left contour is for summer. Right one is spectral index for winter. Both are modelled using B-spline technique.

Fig. 4 shows the modelled contours for winter and summer in quiet geomagnetic condition. During summer and low geomagnetic conditions largest mean value of spectral index is observed at high latitude (>70 degree invariant latitude). At low latitudes, in summer the mean spectral index is smaller but larger than that in winters. Fig. 5 represents geomagnetic disturbed behavior of spectral index for summer and winter. One can easily observe that in summer at high latitude greater than 70 degree spectral index is independent of geomagnetic effect. Nevertheless, spectral index at low latitudes (i.e. less than 70 degree) increases with geomagnetic activity both in summer and winter.

Seasonal behaviour of amplitude scintillation index and other ionospheric parameter have been modelled for geomagnetic quiet and disturb conditions. Fig. 6 shows the turbulence strength parameter for equinox when the $K_p \leq 3$. As we know invariant latitude is a parameter that describes where a particular magnetic field line touches the Earth. On the Earth's surface, the invariant latitude is equal to the geomagnetic latitude. Fig. 6 shows that C_s maximizes in auroral region near and after magnetic midnight. The left figure is created from the real observation and the right contour map is prepared using our B-spline model. As it is evident from the figure above, the model and observations are is good agreement. Fig. 7 below shows the variation of C_s with invariant latitude and magnetic local time for equinox month and in geomagnetic disturbed condition.

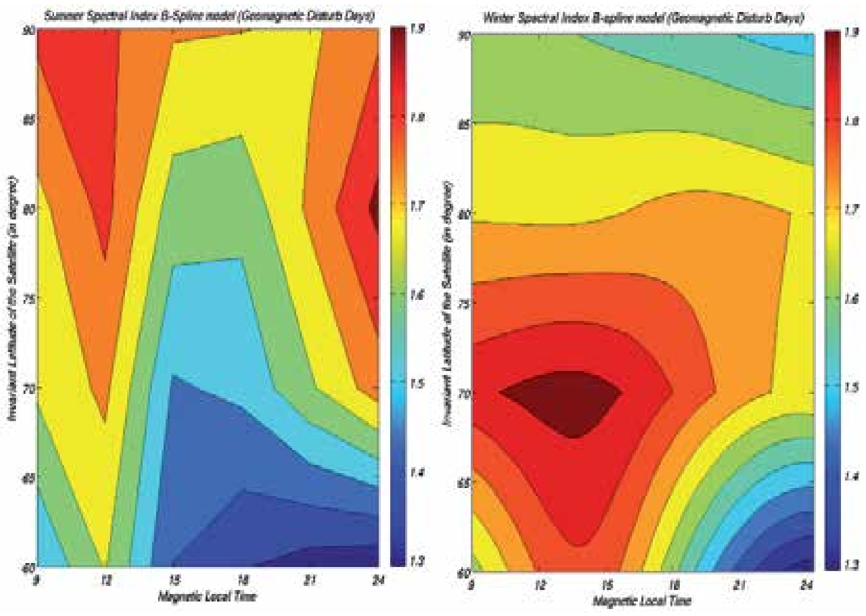

Figure 5. Spectral index for $K_p > 3$. Left contour is for summer. Right one is spectral index for winter. Both are modelled using B-spline technique.

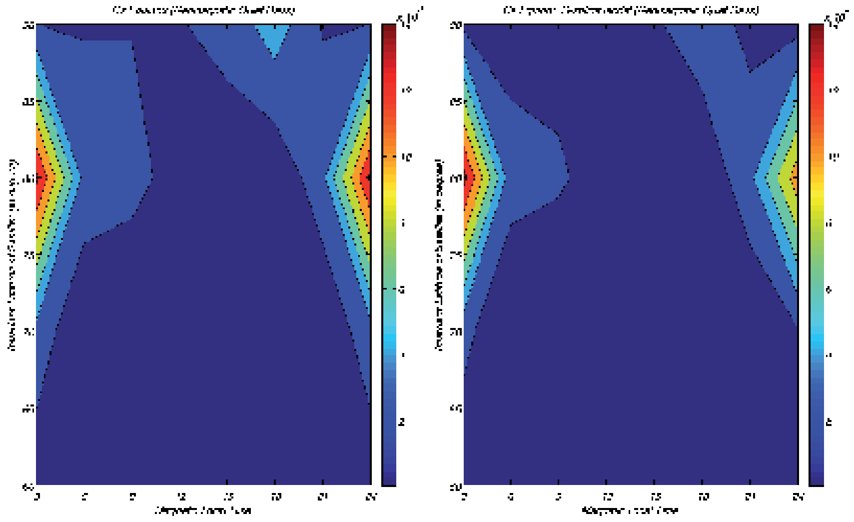

Figure 6. Turbulence strength parameter C_s of plasma density fluctuation for $k_p \leq 3$. Left map is from the real observation and right map is produced using B-spline model.

Invariant latitude >70 degree seems dependent of geomagnetic activity. Near magnetic noon a significant increase is visible at auroral boundary which is expanding to the polar cusp near the midnight.

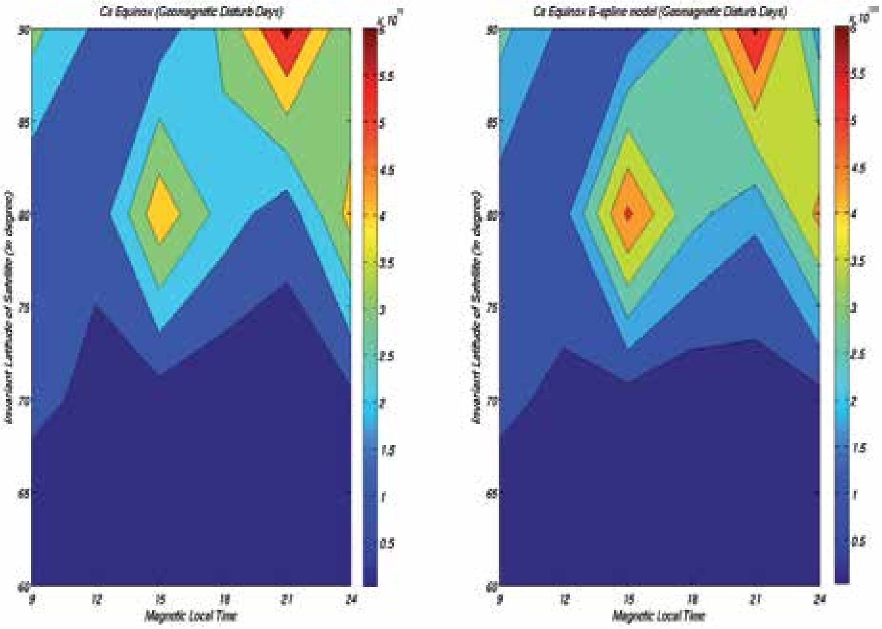

Figure 7. Turbulence strength parameter C_s of plasma density fluctuation for $K_p > 3$. Left contour is for summer derived from observation, right one is for winter which is modelled using B-spline technique.

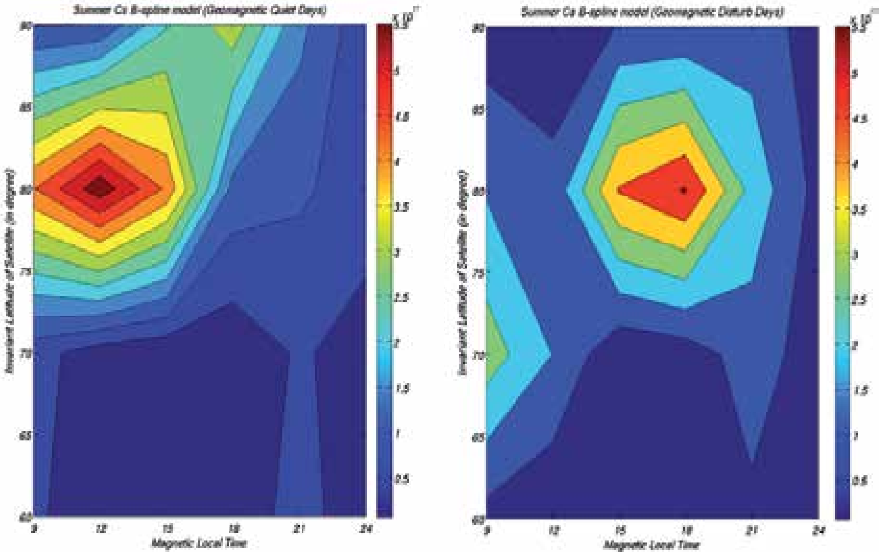

Figure 8. Turbulence strength parameter C_s of plasma density fluctuation. Left contour is for $K_p \leq 3$. Right one is spectral index for $K_p > 3$. Both are modelled using B-spline technique.

Fig. 8 above shows modelled turbulence strength parameter C_s for $K_p \leq 3$ and $K_p > 3$. In both the high and low magnetic conditions we observe a considerable enhancement in C_s for invariant latitude >70 degree. This maximum seems very much coherent with the maximum of spectral index near polar cusp region and noon sector of the polar cap. The only difference is the time of enhancement. For low magnetic activity condition maximum is near magnetic noon. But, for strong geomagnetic activity maxima is visible near magnetic dusk. Fig. 9 is modelled turbulence strength parameter for winter. Left contour is for weak magnetic activity while right one is for strong magnetic activity condition. The value of C_s is one order of magnitude higher than that in summer. Here our results are fully consistent with the WAM model results [12]. In winter C_s is independent of magnetic local time. In winter low latitude C_s is always smaller as compared to the high latitude C_s. During disturbed geomagnetic conditions a significant enhancement in C_s is visible in the dawn and dusk time for invariant latitude > 70 degree. Up to now our model is in excellent coherence with the observational results in both the magnetic weak as well as strong magnetic activity conditions.

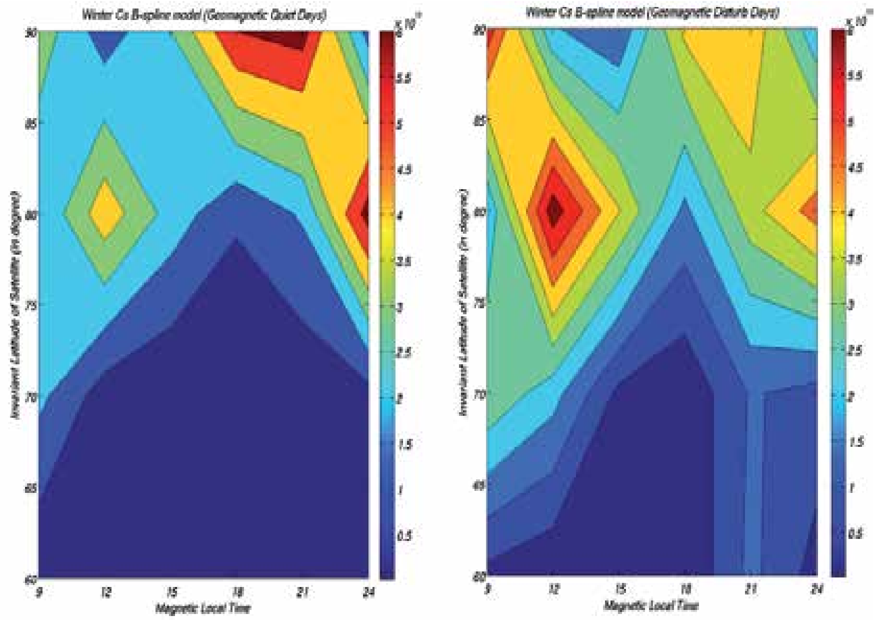

Figure 9. Turbulence strength parameter C_s of plasma density fluctuation. Left contour is for $K_p \leq 3$ and right one is for $K_p > 3$. Both are modelled using B-spline technique.

As we know from Rino's work on phase screen model, if we know turbulence strength parameter C_s and one dimensional spectral index p then it is possible to calculate equivalent amplitude scintillation index. While calculating equivalent amplitude scintillation index S_4 we have considered ionospheric irregularity to be isotropic for which Fresnel's filter factor F=1(see equation number 3). Fig. 10 shows the computed and modelled behaviour of amplitude scintillation index for equinox during magnetic weak condition.

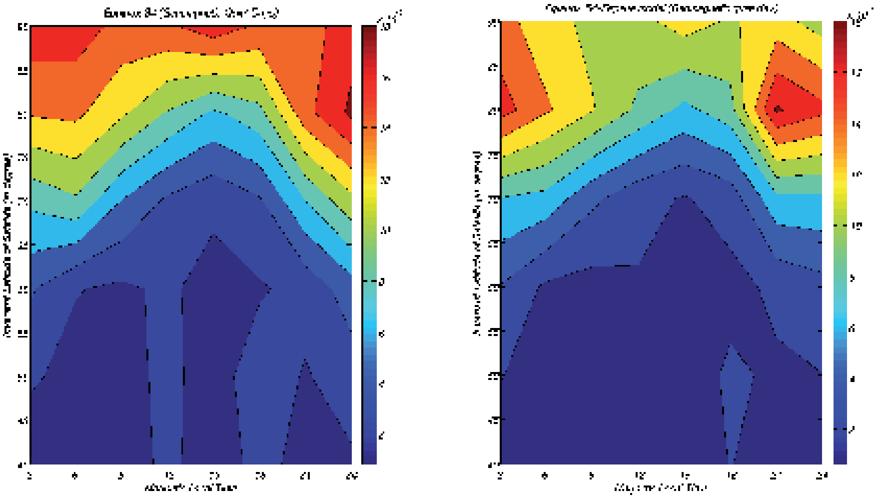

Figure 10. Amplitude scintillation index during equinox $K_p \leq 3$. Left contour is prepared from calculated S_4 but, right contour is modelled using B-spline technique.

For high invariant latitude maxima is visible near polar cusp. It is evident from the figure that scintillation index is varying with magnetic local time but, enhancement is more clear near mid-night. Modelled contour is in good agreement with the computed S_4 index map using DE 2 retarding potential (RPA) measurements.

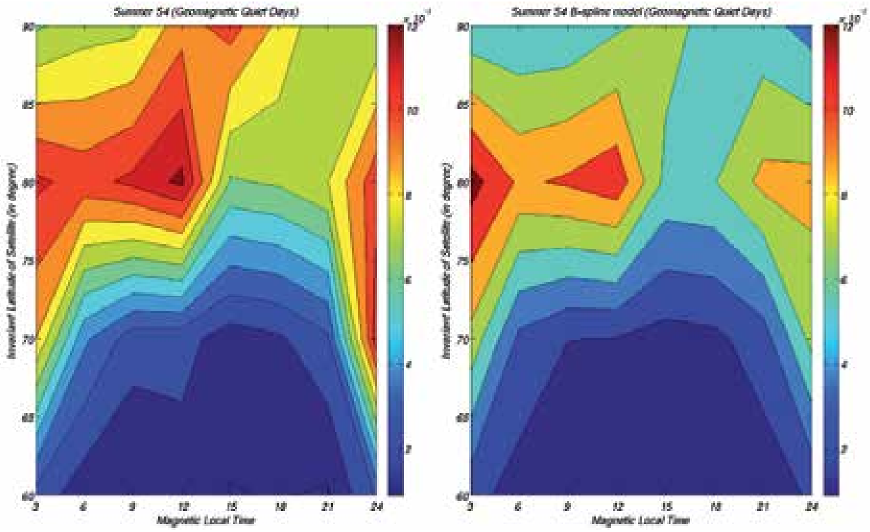

Figure 11. Amplitude scintillation index during summer Kp ≤ 3. Left contour is prepared from calculated S_4 but, right contour is modelled using B-spline technique.

Fig. 11, 12, 13 and 14 are contour maps for summer and winter months for high and low magnetic activity conditions. These maps show that in summer the scintillation is much weaker than that in winter. During summer and low magnetic activity, the strongest scintillation is noted around magnetic noon and midnight at latitudes corresponding to the polar cusp and auroral zone, respectively.

During winter and low magnetic activity, strongest scintillation is observed in the polar cap. The maps show that with increasing magnetic activity the regions of the most intense scintillation expand equatorward. In winter the expansion of the scintillation zone is less defined in the mid-night sector, and the polar cap scintillation intensity weakens. Spline model magnetic activity variations of the high latitude scintillation zone are consistent with those found in the scintillation and other ionospheric irregularity-sensitive measurements [12, 13 and references therein].

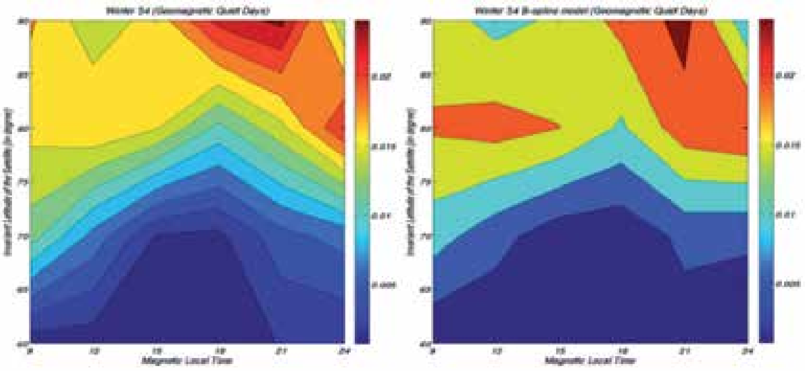

Figure 12. Amplitude scintillation index during winter $k_p \leq 3$. Left contour is prepared from calculated S_4 but, right contour is modelled using B-spline technique.

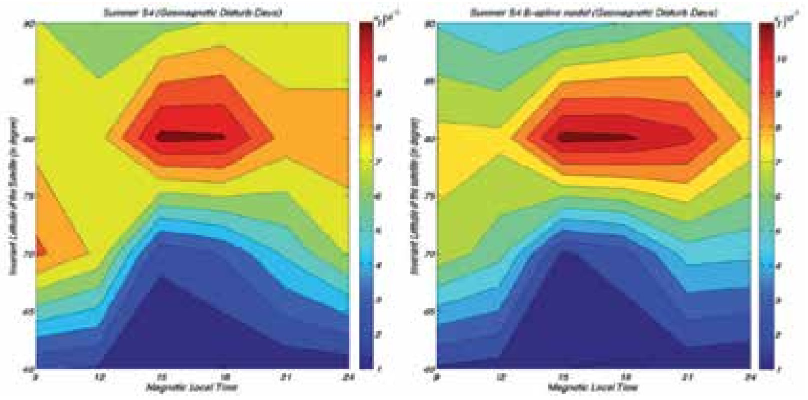

Figure 13. Amplitude scintillation index during summer $k_p > 3$. Left contour is prepared from calculated S_4 but, right contour is modelled using B-spline technique.

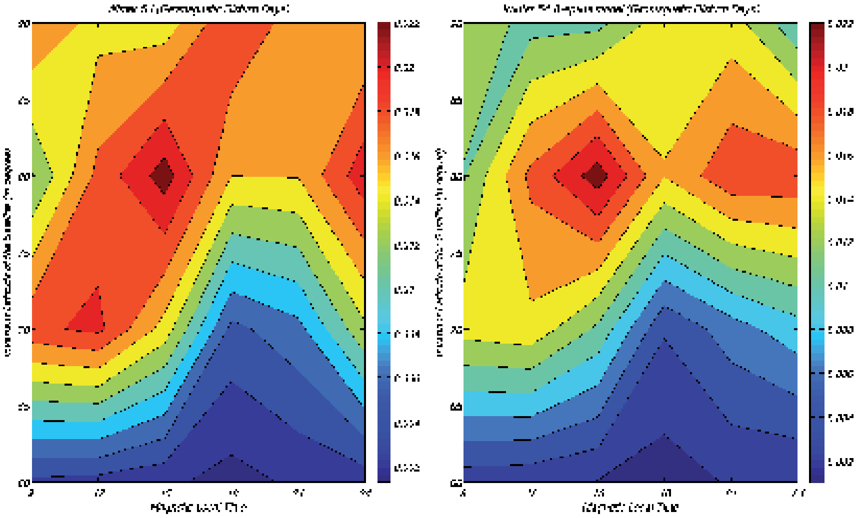

Figure 14. Amplitude scintillation index during winter $k_p > 3$. Left contour is prepared from calculated S_4 but, right contour is modelled using B-spline technique.

5. Summary and conclusion

Our scintillation model makes use of the DE 2 retarding potential analyzer plasma density data [14] covering the period from August 1981 to February 1983, near to the solar maximum activity. DE2 in-situ measurements of plasma density fluctuations provide direct information of structure and morphology of irregularity that are responsible for scintillation of radio waves on trans-ionospheric links.

Described model is for northern hemisphere high latitude ionosphere which uses DE 2 RPA measurements. For geomagnetic activity dependence of scintillation there is good agreement between model and measurements. Spline model are the best because they provide similar results, even when we use low-degree splines, to the models produced using higher degree polynomials while avoiding instability at the edges of an interval (Runge's phenomenon). This provides a reasonable realistic description of scintillation index and other ionospheric parameters.

Like any other model, our model also has certain limitations. Since it is an empirical model therefore we derive model from real observations. In any case our model will give suitable and convincing results for the geophysical condition which would be closely similar to the duration in which the data is recorded. Nevertheless, present model gives an average behavior of ionospheric parameters during different geophysical conditions. It can be compared with the observations performed in different solar activity condition and we strongly believe that the comparison would be convincing. DE 2 was working during moderate solar activity period when the sun spot number was between 80-140. Therefore our model is only valid for moderate solar activity conditions. We are using IRI model for the irregularity slab thickness and the height of peak electron density. IRI model often fails to give real behavior of ionospheric parameters for high latitude. There is possibility of erroneous calculation in our model similar to WAM model [12]. Third and most serious limitation of our model is placement and number of B-spline basis function. The number of data points for high geomagnetic activity condition is always less than that of weak geomagnetic condition. Sometimes it seems that in weak geomagnetic activity conditions the contour maps are smoother than that in high geomagnetic condition. This may also be considered as a limitation which can't be overcome since it is natural. As we have already discussed that for individual geophysical situations we choose different number of basis function and keep on experimenting with the placement of basis function in order to get more convincing results. It is always possible that some one can use different set of B-spline basis functions and could be able to produce better modelling than we did here. But, we take this limitation positively. It is because that we feel confident that there is always possibility of upgrading in our model.

Acknowledgements

This research work is undertaken in the scope of the TRANSMIT ITN (www.transmit-ionosphere.net), funded by the Research Executive Agency within the 7th Framework Program of the European Commission, People Program, Initial Training Network, Marie Curie Actions – GA No. 264476.

Author details

S. Priyadarshi and A. W. Wernik

*Address all correspondence to: spriyadarshi@cbk.waw.pl, aww@cbk.waw.pl

Space Research Centre (PAS), Warsaw, Poland

References

[1] Aarons J., Construction of a model of equatorial scintillation intensity, Radio Sci., 20, 397-402, 1985.

[2] Basu Su., Sa. Basu and B. K. Khan, Model of equatorial scintillation from in-situ measurements, Radio Sci., 11, 821-832, 1976.

[3] Basu Su., Sa. Basu, E. J. Weber and W. R. Coley, Case study of polar cap scintillation modeling using DE 2 irregularity measurements at 800 km, Radio Sci., 23, 545-553, 1988.

[4] Béniguel Y. and S. Buonomo, A multiple phase screen propagation model to estimate fluctuations of transmitted signals, Phys. Chem. Earth (C), 24, 333-338, 1999.

[5] Bilitza, D., International Reference Ionosphere-Status 1995/96, Adv. Space Res., 20(9), 1751–1754, 1997.

[6] Fremouw E. J. and C. L. Rino, An empirical model for average F–layer scintillation at VHF/UGF, Radio Sci., 8, 213-222, 1973.

[7] Iyer K. N., J. R. Souza, B. M. Pathan, M. A. Abdu, M. N. Jivani and H. P. Joshi, A model of equatorial and low latitude VHF scintillation in India, Indian J. Radio & Space Phys., 35, 98-104, 2006.

[8] Kintner P. M., Ledvina B.M. and Paula E. R. de., GPS and ionospheric scintillation, Space Weather, 5, S09003, doi:10.1029/2006SW000260, 2007.

[9] Priyadarshi S., Review of existing scintillation models, TRANSMIT NEWSLETTER, issue 1, November 2012.

[10] Retterer J. M., Forecasting low-latitude radio scintillation with 3-D ionospheric plume models: 2. Scintillation calculation, Journal of Geophysical Research, 115, A03307, doi:10.1029/2008JA013840, 2010.

[11] Rino C. L., A power law phase screen model for ionospheric scintillation, 1. Weak scatter, Radio Sci., 14, 1135-1145, 1979.

[12] Wernik A. W., L. Alfonsi, M. Materassi, Scintillation modeling using in situ data, Radio Sci., 42,RS1002, doi:10.1029/2006RS003512, 2007.

[13] Tsunoda, R. T., High-latitude F region irregularities: A review and synthesis, Rev. Geophys., 26, 719–760, 1988.

[14] Hanson, W. B., R. A. Heelis, R. A. Power, C. R. Lippincott, D. R. Zuccaro, B. J. Holt, L. H. Harmon, and S. Sanatani, The retarding potential analyzer for Dynamics Explorer-B, Space Sci. Instrum., 5, 503–510, 1981.

[15] DeBoor, C. A., A practical guide to splines, Appl. Math. Sci., 27, 1978.

[16] Lui, A. T. Y., Q.-G. Zong, C. Wang, and M. Dunlop, Electron Source Associated With Dipolarization at the Outer Boundary of the Radiation Belts: Non-storm Cases, J. Geophys. Res., 117, A10224, doi:10.1029/2012JA018084, 2012.

Chapter 11

Regional Ionosphere Mapping with Kriging and B-spline Methods

Oksana Grynyshyna-Poliuga,
Iwona Stanislawska and Anna Swiatek

Additional information is available at the end of the chapter

http://dx.doi.org/10.5772/58776

1. Introduction

The distribution of electrons in the ionosphere is of interest to scientists and also to engineers working on applications such as earth–space communication systems, which must transmit through the ionosphere, and skywave systems, which make use of ionospheric refraction. Electron content is commonly examined using total electron content (TEC) mapping. This mapping finds use in other applications such as studying the evolution of magnetic storms, which have, in the past, had profound effects on satellite communication systems and on other critical ground-based systems. Information on the electron content of the ionosphere can be collected using the global positioning system (GPS) and by examining the phase and amplitude changes which occur in paths between transmitting satellites and ground-based receivers. These data can then be processed in order to create maps of the ionospheric TEC.

As the number of paths between GPS ground stations and satellites is relatively low, producing TEC maps is an exercise in reconstruction from sparse data. Recent research has mainly focused on methods, such as tomography, that provide time-dependent volumetric reconstructions [1], [2]. However, when the data points are too sparsely distributed, these techniques are underconstrained and do not produce meaningful results. In ionospheric studies, problems relating to sparsity are particularly prevalent in historic data sets. For example, in 1992, there were only 25 receiver sites operated by the International GPS Service (IGS) in the U.S. [3], by 1996, there were over 75, and now, there are over 500. Therefore, while the issues due to undersampling have largely disappeared for TEC imaging systems utilizing modern GPS data, they still remain for older data and regularly arise in other geoscience applications [4], [5]. Consequently, interpolation methods still have an important role to play in ionospheric studies. The most commonly used interpolation technique for TEC-mapping studies are kriging and cubic B-spline. In addition, there are many other interpolation methods for geophysical data that have received little recent attention from the ionospheric imaging community.

2. Basic concepts on interpolation techniques

Interpolation methods can be divided into two categories, local and global, depending upon the locality of the points which are used to derive a given output point. Local techniques make use of a definition of locality to compute output values; only data which fall within a given point's local neighborhood are used to calculate output values. Global techniques use a weighted sum of all data to compute output values, and for large numbers of input points, an approximation is generally used. When a new datum is added to a globally interpolated field, the whole field must be recalculated, whereas for a locally interpolated field, only those positions within the neighborhood of the added datum need to be recalculated. These two points tend to favor the use of local techniques.

2.1. Cubic B-spline

This part introduces a procedure for multi-dimensional local ionospheric model. The model consists of a given reference part and an unknown correction part expanded in term of B-spline functions. This approach is used to compute regional models of Vertical Total Electron Content (VTEC) based on the International Reference Ionosphere (IRI 2012) and GPS observations from terrestrial Global Navigation Satellite System (GNSS) reference stations. The approach can be used for local and global modelling of different ionospheric parameters. In this paper, the focus lies on the three-dimensional local modelling of the VTEC depending on horizontal position ϕ,λ and on time t. The unknown VTEC is separated into a reference part $VTEC_{ref}$ taken from IRI 2012 and a correction part $\Delta VTEC$ which is modelled by a series expansion in tensor products of three systems of 1-D normalized endpoint-interpolating B-splines with and unknown coefficients $d_{k1,k2,k3}$ [9]. The basic observation equation reads

$$VTEC\left(\phi,\lambda,t\right)=VTEC_{ref}\left(\phi,\lambda,t\right)+\Delta VTEC\left(\phi,\lambda,t\right) \tag{1}$$

with

$$\Delta VTEC\left(\phi,\lambda,t\right)=\sum_{k_1=0}^{K_1-1}\sum_{k_2=0}^{K_2-2}\sum_{k_3=0}^{K_3-3}d_{k_1,k_2,k_3}\Phi_{k_1}^{J_1}\left(\phi\right)\Phi_{k_2}^{J_2}\left(\lambda\right)\Phi_{k_3}^{J_3}\left(t\right) \tag{2}$$

Each 1-D basis function system consists of $K=2^J+2$ single B-spline functions $\Phi_k^J(x)$ equally distributed on the unit interval for $J=3$. The number K of the functions depends on the level J of the spline.

2.2. Ordinary kriging

The kriging technique is a linear interpolator that belongs to the best linear unbiased estimator family estimators. Thus, the main purpose of the kriging technique is to estimate a certain unknown variable (Z^*) as a linear combination of the known values (Z_i):

$$Z^* = \sum_i \omega_i Z_i, \tag{3}$$

ω_i being the weights computed by the kriging equations (7), that are applied to each value $Z(x_i) = Z_i$.

In order to apply the ordinary kriging technique, it is necessary to assume that the random function Z_i belongs to the stationary random functions family, which means that the mean values and the standard deviation of Z_i have to be independent of the location. Moreover, the unbiased condition over the weights ($\sum_i \omega_i = 1$) is imposed. Then, the variance is minimized with the help of the Lagrange multipliers in order to impose the unbiased condition (8) for details:

$$L = \frac{1}{2} E\left[\left(Z^* - Z\right)^2\right] - \lambda\left(\sum_i \omega_i - 1\right), \tag{4}$$

$E[(Z^* - Z)^2]$ being the Z^* variance that can be expressed as a function of the semivariogram:

$$E\left[\left(Z^* - Z\right)^2\right] = 2\sum_i \omega_i \gamma_{i0} - \sum_i \sum_j \omega_i \omega_j \gamma_{ij}, \tag{5}$$

After differencing Eq. (5) with respect to λ and ω_i, and equating to 0, the ordinary kriging equations are obtained in compact form:

$$\sum_i \omega_i \gamma_{ij} + \lambda = \gamma_{i0}, \tag{6}$$

Therefore, in order to get the weights (ω_i), the following equation, that is expressed in matrix notation, has to be solved:

$\Omega = \Gamma^{-1} \Gamma_0,$

$$\Omega = \begin{pmatrix} \omega_1 \\ \omega_2 \\ \vdots \\ \omega_n \\ \lambda \end{pmatrix}, \Gamma = \begin{pmatrix} \gamma_{11} & \cdots & \gamma_{1n} & 1 \\ \gamma_{21} & \cdots & \gamma_{2n} & 1 \\ \vdots & \ddots & \vdots & \vdots \\ \gamma_{1n} & \cdots & \gamma_{nn} & 1 \\ 1 & \cdots & 1 & 0 \end{pmatrix}, \Gamma_0 = \begin{pmatrix} \gamma_{10} \\ \gamma_{20} \\ \vdots \\ \gamma_{n0} \\ 1 \end{pmatrix}. \tag{7}$$

Ω being the vector that contains the weights ω_i and the Lagrange multiplier λ. Γ is the matrix that contains the semivariogram estimations for the known values and locations, and Γ_0 is the vector that contains the semivariogram estimations for the unknown values but with known locations.

2.3. Semivariogram and covariance function

Previously to use the kriging technique it is necessary to determine the semivariogram (or alternatively two-times it, variogram). This is a function that describes the spatial correlation among the data used in the interpolation, which knowledge is important since it is used as the main input of the kriging algorithm (7). The semivariogram function is computed by means of doing the squared difference between pairs of observations at a semivariogram function is computed by means of doing the squared difference between pairs of observations at a fixed distance $d_l \pm \Delta d_l / 2$, as it is show in (1), see [8] for details:

$$\gamma^*(d_l) = \frac{1}{2m(d_l)} \sum_{i \neq j}^{m(d_l)} (Z_i - Z_j)^2, \tag{8}$$

γ^* being the experimental semivariogram, $m(d_l)$ the number of pairs of observations at a distance d_l, Z_i and Z_j are the observation values that correspond to points at x_i and x_j at a distance $| x_i - x_j | = d_l$.

Once the experimental semivariogram is computed, the next step is to adjust this experimental semivariogram to a theoretical one $\gamma(d_l)$, which must verify several mathematical conditions [8] in order to be applied in the kriging equations (7). It has to be noted that such theoretical semivariograms are classified in well-known semivariogram families, which try to take into account the most number of semivariogram types for families examples.

For the definition of the *covariance function* the stationarity of the first two moments (mean and covariance) of the random function is essential.

$$\begin{cases} E\left[Z(x)\right] = m \\ E\left[X(x) - m\right]\left[Z(x+h) - m =: C(h)\right] \end{cases} \tag{9}$$

Some properties of the covariance function are:

- The covariance function is bounded and its absolute value does not exceed the variance

$$|C(h)| \le C(0) = \mathrm{var}(Z(x)) \tag{10}$$

- Similar to the semivariogram, it is an even function

$$C(-h) = C(+h) \tag{11}$$

But unlike the semivariogram it can also take negative values.

- The covariance function divided by the variance is called the *correlation function*

$$\rho(h) = \frac{C(h)}{C(0)}, \tag{12}$$

which is bounded by

$$-1 \le \rho(h) \le 1 \tag{13}$$

- Furthermore, the semivariogram function can be deduced from a covariance function by

$$\gamma(h) = C(0) - C(h) \tag{14}$$

In general, the reverse is not true, because the semivariogram is not necessarily bounded. Thus, the hypothesis of second-order stationarity is less general than the intrinsic hypothesis (for the monovariate case) and unbounded semivariogram models do not have a covariance function counterpart.

- A covariance is a positive and negative definite functions.

2.4. Different semivariogram models

The use of a semivariogram in a Kriging procedure requires continuous semivariogram values for every distance $|h|$. Of course, this cannot be provided by the experimental semivariogram since only discrete measurements can be realized in practice. Fitting the experimental semivariogram by an appropriate semivariogram function helps to overcome this problem. Using a theoretical semivariogram also guarantees that the semivariance of any linear combination of sample values is positive. This is important for setting up a *Kriging system* where the values of an experimental semivariogram can lead to negative Kriging variances.

There are several reasons to favor the semivariogram instead of the covariance function. The semivariogram is a more general tool than the covariance. Another reason is more of practical interest: The semivariogram, unlike the covariance function, does not depend on the existence of a mean value. In practice, the mean is not known in most cases and has to be estimated out of the data, which also adds a bias. Therefore, the semivariogram is often preferred to the covariance function.

Using h to represent lag distance, a to represent (practical) range, and c to represent sill, the three most frequently used models (fig. 1) are:

Spherical: $g(h) = \begin{cases} c \cdot \left(1.5\left(\frac{h}{a}\right) - 0.5\left(\frac{h}{a}\right)^3\right) \\ c \end{cases}$

Exponential: $g(h) = c \cdot \left(1 - \exp\left(\frac{-3h}{a}\right)\right)$

Gaussian: $g(h) = c \cdot \left(1 - \exp\left(\frac{-3h^2}{a^2}\right)\right)$

These three models are shown below:

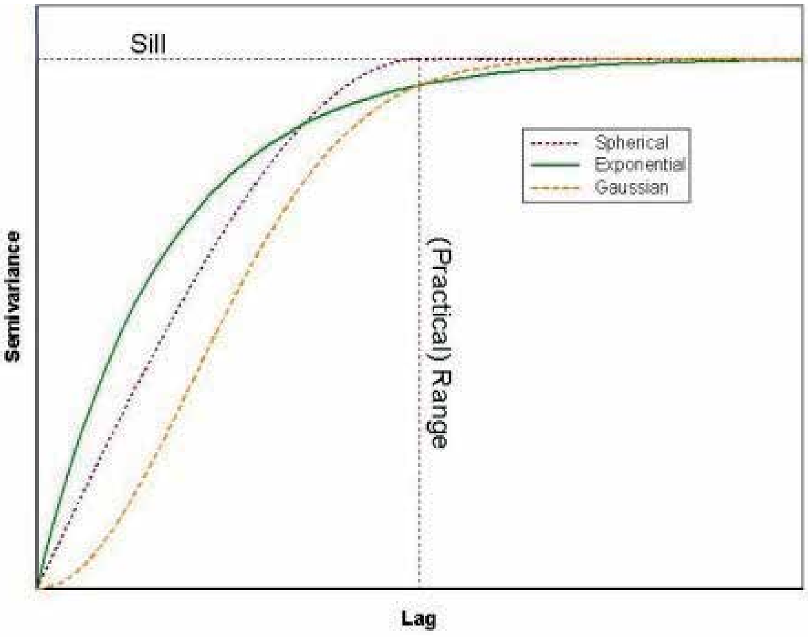

Figure 1. Spherical, Exponential and Gaussian semivariograms models

Most of semivariograms are defined through several parameters:

Sill: The semivariance value at which the semivariogram levels off. Also used to refer to the "amplitude" of a certain component of the semivariogram. For the plot above, "sill" could refer to the overall sill (1.0) or to the difference (0.8) between the overall sill and the nugget (0.2). Meaning depends on context.

Range: The lag distance at which the semivariogram (or semivariogram component) reaches the sill value. Presumably, autocorrelation is essentially zero beyond the range.

Nugget: In theory the semivariogram value at the origin (0 lag) should be zero. If it is significantly different from zero for lags very close to zero, then this semivariogram value is referred to as the nugget. The nugget represents variability at distances smaller than the typical sample spacing, including measurement error.

3. Results

3.1. VTEC maps

The September 28th Coronal Mass Ejection (CME) impacted Earth's magnetic field at 22:20 UT, September 30, 2012 sparking strong Geomagnetic storms at high latitudes. The Bz component of the interplanetary magnetic field (IMF) sharply deviated to -35 nT during the impact. Geomagnetic K-index reached Kp=7 levels on October 1st at 03:00 UT (fig.2) and NOAA/SWPC issued G3 (Strong) Geomagnetic Storm Level alert which is slightly higher than initially predicted.

In our research we used the GPS data of 18 EPN stations (tab.1) near to the EGNOS Ranging and Integrity Monitoring Stations (RIMS) network at the mid-latitude. After analyzing the geographic location of IPPs (fig.3) for all the observational epochs, a region located between 30° - 60° latitude and -40° - 45° longitude was selected to produce the local ionosphere maps each 15 minutes on a 2.5°x 2.5° grid using two interpolation methods (Kriging and cubic B-spline).

The TEC values obtained at IPPs were interpolated using kriging and the cubic B-spline model in order to create high-resolution regional maps of the ionosphere. The results, produced using the above methods, are compared and analyzed in the following section. Temporal evaluation of TEC distribution over study area on the first disturbed day (30 September) is presented in Fig. 4 via the series of TEC maps. When producing the maps we used 15 min averages of TEC data. This approach provides detailed analysis of the ionospheric response to the storm. A significant feature in latitudinal variations of the ionosphere was the presence of the trough. In Fig. 4, one can see that the trough first occurred east and after that was heading due west.

The ionosphere was modeled for the period of 18 hours (5:00 to 23:00 UT) during three days. The ionosphere maps obtained using Kriging and cubic B-spline methods present good

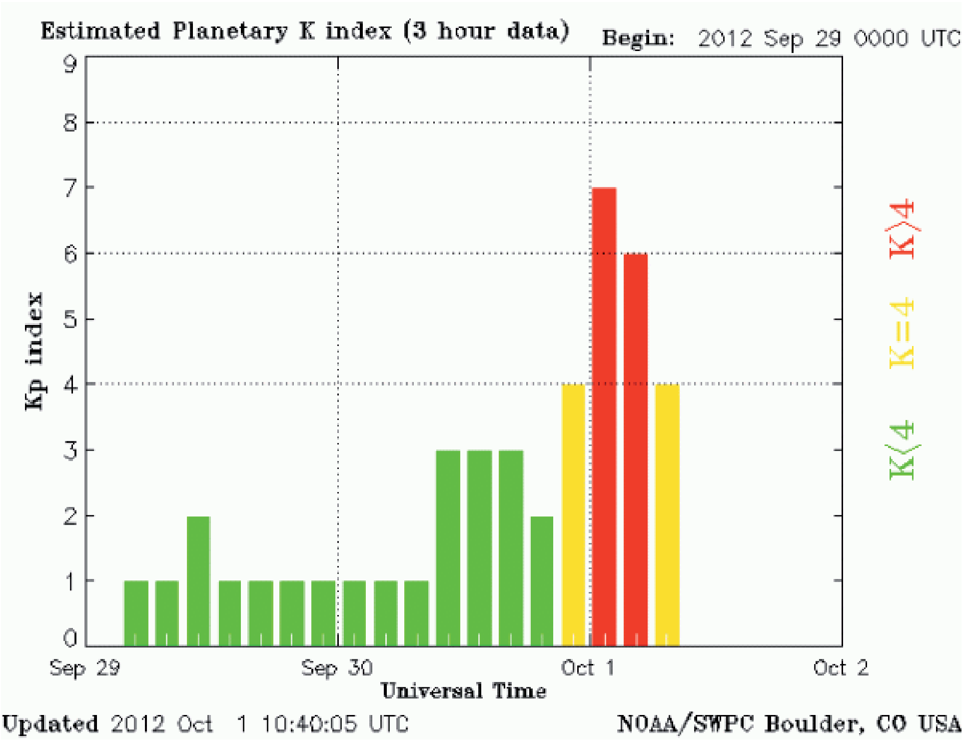

Figure 2. The values of Kp index during the experiment

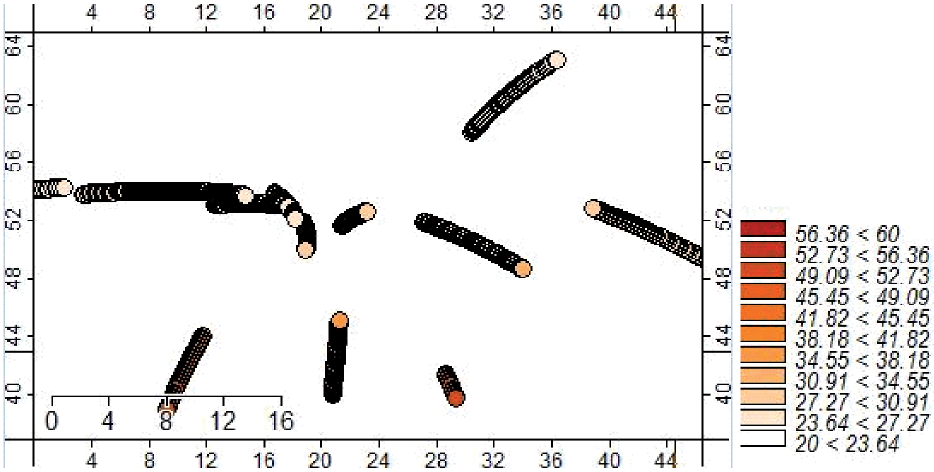

Figure 3. Example location of IPPs and their TEC values at 12:00-13:00 UT, September 30, 2012, when seven satellites were simultaneously observed.

agreement. The maximum TEC was observed around 12:00 UT during the first disturbed day (30 September). This might be explained by active geomagnetic conditions (see Fig. 2).

Station	Latitude (°N)	Longitude (°E)
Maartsbo, Sweden	60.6	17.3
Kirkkonummi, Finland	60.2	24.4
Suldrup, Denmark	56.8	9.7
Daresbury, UK	53.3	-2.6
Hailsham, UK	50.9	0.3
Potsdam, Germany	52.4	13.1
CBKA, Poland	52.2	21.1
Saint-Mande, France	48.8	2.4
Zimmerwald, Switzer.	46.9	7.5
Vigo, Spain	42.0	-8.8
Toulose, France	43.6	1.5
Santa Cruz, Portugal	39.4	-31.1
Cascais, Portugal	38.7	-9.4
Malaga, Spain	36.7	-4.4
Palma de Mallorca, Spain	39.5	2.6
Moto, Italy	36.9	15.0
Athens, Greece	38.0	23.9
Ankara, Turkey	39.9	32.8

Table 1. The coordinates of the selected stations

3.2. Semivariogram modelling for a single location

The main purpose of the GPS is to determine the position and velocity of a fixed or mobile object, placed over or near the earth surface, using the signals of the 32 satellites on earth orbit. GPS is a complex and expensive constellations of 32 satellites distributed in 6 orbital planes, at 20,200 km altitude, with an orbit inclination of 55 degrees and an approximately 12 hour period. The first step in interpolation using kriging is the formation of a semivariogram [6], [7].

As it has been mentioned before, one of the steps to solve the kriging equations is to compute an experimental semivariogram, in order to adjust a theoretical one. Thus, in principle, one semivariogram should be computed for each realization of the kriging equations (7). For any set of data we can compute the semivariance for each pair of points. These values can then be plotted against the lag distance as a scatter diagram, called the "semivariogram cloud" by Chauvet (1982) [10].

Figure 5 contains all of the information on the spatial relations in the data to lag. In principle, we could fit a model to it to represent the regional semivariogram, but in practice it is

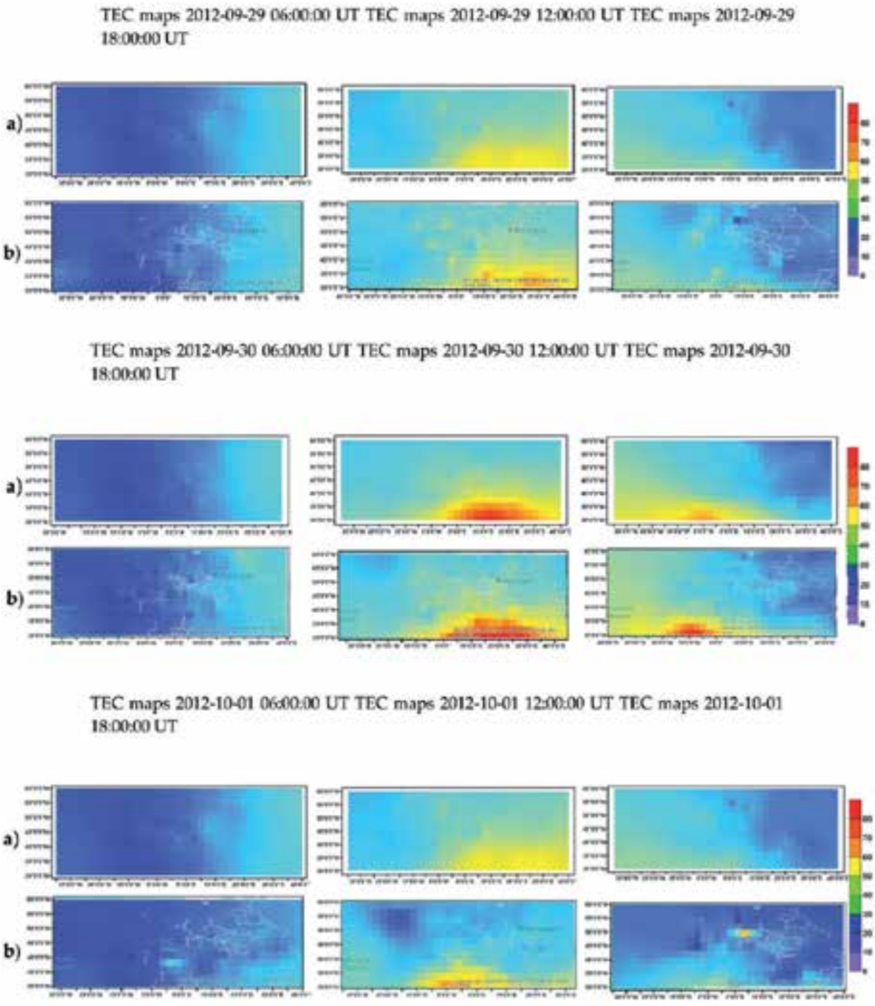

Figure 4. Ionospheric TEC maps created with Kriging (a) and cubic B-spline (b) interpolations methods

almost impossible to judge from it if there is any spatial correlation present, what form it might have, and how we could it. A more sensible approach is to average the semivariances for each of a few lags and examine the results [11]. Nevertheless, the semivariogram cloud shows the spread of values at the different lags, and it might enable us to detect outliers or anomalies. The tighter this distribution is, the stronger is the spatial continuity in the data.

In present work the semivariogram calculations were provided for different magnetic/ ionospheric conditions separately. Correlation distance determined from the semivariogram for disturbed conditions is about 10 degrees. Survey data in two dimensions are often unevenly distributed. Each pair of observations is separated by a potentially unique lag in both distance

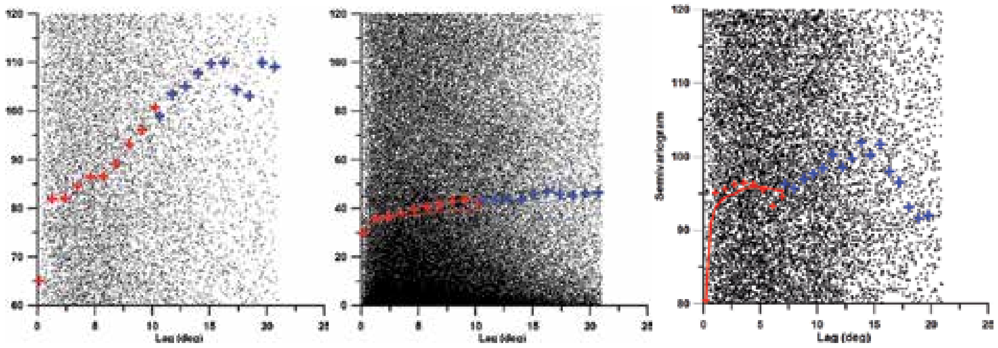

Figure 5. An example of semivariograms for disturbed conditions with logarithmic presentation. Crosses are averaged data, lines – fitted data, red – full data set, and blue crosses – data created artificially

and direction. To obtain averages containing directional information we must group the separations by direction as well as by distance. We choose a lag interval, the multiples of which will form a regular progression of nominal lag distances as in the one-dimensional case. We then choose a range in distance, usually equal to the lag interval. We also choose a set of direction and a range in direction. When all comparisons have been made the experimental semivariogram will consist of the set of averages for the nominal lags in both distance and direction. We can extend further by computing the average experimental semivariogram over all directions.

The semivariogram is sensitive to outliers and to extreme values in general. If the extreme is near the margin of the region then it will contribute to fewer comparisons than if it is near the centre. The end point on a regular transect, for example, contributes to the average just once for each lag, whereas points near the middle contribute many times. If data are unevenly scattered then the relative contributions of extreme values are even less predictable. The result is that the experimental semivariogram is not inflated equally over its range, and this can add to its erratic appearance.

4. Conclusions

This work demonstrates the concept and practical examples of mapping of regional ionosphere, based on GPS observations from permanent stations near to the EGNOS Ranging and Integrity Monitoring Stations (RIMS) network. Interpolation/prediction techniques, such as kriging (KR) and the cubic B-spline, which are suitable for handling multi-scale phenomena and unevenly distributed data, were used to create total electron content (TEC) maps. Their computational efficiency (especially the B-spline) and the ability to handle undersampled data (especially kriging) are particularly attractive. The data sets have been collect into strong geomagnetic storm at September 2012. TEC maps have a spatial resolution of 2.5° and 2.5° in latitude and longitude, respectively, and a 15-minutes temporal resolution. The time series of the TEC maps can be used to derive average monthly maps describing major ionospheric trends as a function of time, season, and spatial location.

Acknowledgements

This research work is undertaken in the scope of the TRANSMIT ITN (www.transmit-ionosphere.net), funded by the Research Executive Agency within the 7th Framework Program of the European Commission, People Program, Initial Training Network, Marie Curie Actions – GA No. 264476.

Author details

Oksana Grynyshyna-Poliuga, Iwona Stanislawska and Anna Swiatek

*Address all correspondence to: ogp@cbk.waw.pl, stanis@cbk.waw.pl, ana@cbk.waw.pl

Space Research Centre Polish Academy of Science, Warsaw, Poland

References

[1] C. N. Mitchell and P. S. J. Spencer, "A three-dimensional time-dependent algorithm for ionospheric imaging using GPS," Ann. Geophys., vol. 46, no. 4, pp. 687–696, 2003.

[2] J. M. Pallares, G. Ruffini, and L. Ruffini, "Ionospheric tomography using GNSS reflections," IEEE Trans. Geosci. Remote Sens., vol. 43, no. 2, pp. 321–326, Feb. 2005.

[3] E. Brockmann and W. Gurtner, "Combination of GPS solutions for densification of the European network: Concepts and results derived from 5 European associated analysis centers of the IGS," in Proc. EUREF Workshop, Ankara, Turkey, May 1996.

[4] M. Liao, T. Wang, L. Lu, W. Zhouzhou, and D. Li, "Reconstruction of DEMS from ERS-1/2 TANDEM data in mountainous area facilitated by SRTM data," IEEE Trans. Geosci. Remote Sens., vol. 45, no. 7, pp. 2325–2335, Jul. 2007.

[5] M. Gianinetto and P. Villa, "Rapid response flood assessment using minimum noise fraction and composed spline interpolation," IEEE Trans. Geosci. Remote Sens., vol. 45, no. 10, pp. 3204–3211, Oct. 2007.

[6] N. A. C. Cressie, Statistics for Spatial Data. Hoboken, NJ: Wiley, 1991.

[7] H. Omre, "The variogram and its estimation," in Geostatistics for Natural Resources Characterization. Amsterdam, The Netherlands: Reidel, 1984, pt. 1, pp. 107–125.

[8] Cressie, N.A.C., 1993. Statistics for Spatial Data, revised ed. Wiley, New York, EUA.

[9] Schmidt M, Dettmering D, Mößmer M, Wang Y, Zhang J (2011) Comparison of spherical harmonic and B-spline model for VTEC. Radio Sci 46:RSOD11. doi: 10.1029/2010RS004609

[10] P. Chauvet, (1982). The Variogram Cloud. In Proceedings of the 17th APCOM Symposium. Colorado School of Mines, Golden, CO, pages 757-764.

[11] R. Webster, M.A. Oliver: Geostatistics for Environmental Scientists. Wiley, Chichester, 2001. Hardbound, 271 pp., ISBN 0471965537.

Statistical Case Studies of High and Low Latitude Ionospheric Scintillations

Đorđe Stevanović

Additional information is available at the end of the chapter

http://dx.doi.org/10.5772/58775

1. Introduction

Ionospheric scintillations are fluctuations in amplitude and phase of the radio wave signal passing through the ionosphere on its path to the receiver, caused by small scale irregularities in the electron density structure [1]. Occurrence of scintillation depends on various factors, such as: solar activity, geomagnetic conditions, geo-location of the receiver, time of day, angle of signal arrival, ionospheric structure geometry and many others [1-6]. Causing signals disturbances and distortion, scintillation can significantly affect the GNSS accuracy and cause severe problems to commercial navigation systems. Scintillating signals can be classified by the intensity of fluctuations into categories of weak and strong scintillations. High and low magnetic latitudes represent the most affected regions by ionospheric irregular structures in F and E ionospheric layers. While phase scintillations are more pronounced in the sub-polar and polar regions, amplitude scintillations are significantly stronger and more pronounced in near equatorial regions [7-10].

In last five decades, statistical studies of the ionospheric scintillating radio signals brought different approaches and solutions. Some of these solutions are widely adopted and used in scintillation modelling and forecasting ionospheric dynamics, as joint Gaussian distribution of complex radio wave signal. This solution gives applicable results for weak scintillating signals [3], but in case of strong scintillations there is not an easy way to derive satisfactory results, leading to a need for further investigations [8]. While phase scintillations mainly follow the Gaussian distribution and do not represent a problem in ionospheric modelling, more complicated case is with amplitude scintillations. Revolution in ionospheric modelling and developing of the ionospheric scintillation theory has been made during '70s and ‘80s, covered mostly in papers by Rino and Fremouw [11-16]. During this period various researches had been performed providing different information on a probability distribution function (PDF) used as amplitude scintillation descriptor [11-12, 17]. Last two decades brought few intriguing studies [18-21] performed on statistics of scintillating signal leading to a need for more detailed and precise description of radio scintillation signal's amplitude and phase PDFs for strong fluctuations.

The focus of this paper is on the statistical analysis of ionospheric scintillation in high and low latitude during strong and moderate geomagnetic activity. Gaussian and Nakagami-m PDFs of scintillating signals have been examined using real measured data and compared with theoretically derived PDFs. Further testing had been done on different data intervals, necessary for correct higher order statistical analysis, avoiding errors influence. The analysis results are presented with higher order moments, dependent on various parameters (scintillation indices, geo-location and solar/magnetic activity). Implementation of higher order moments, skewness and kurtosis, could give additional information about the ionospheric irregularities influence on the propagating signal and relation to the time delay of the signal.

2. Analysed data and methods

The data used in analysis have been measured by NovAtel GPS Ionospheric Scintillation/TEC Monitor (GISTM), model GSV4004B, one of three monitoring receivers installed at the Polish Polar Station in the region of the Hornsund Bay in southern Spitsbergen (approximately 77° N, 15.55° E). The second data source was derived using a Septentrio's PolaRxS Ionospheric Scintillation Monitoring (ISM) receiver located at Presidente Prudente (approximately-21.99° N, 308.59° E), Brazil, set during Concept for Ionospheric Scintillation Mitigation for Professional GNSS in Latin America (CIGALA) project. The geographical locations of both stations are indicated in the Fig. 1. The locations of the receivers made possible study of the ionospheric scintillations in the most affected regions characterized by very intense and complex behaviour of plasma - polar and auroral latitudes, due to interaction of the solar wind and interplanetary magnetic field with the Earth's magnetic field, and low latitudes, due to equatorial anomaly and electrojets. Parameters of interest in performed data analysis are signal amplitude and phase during quiet and active geomagnetic periods, recorded during measurement campaigns.

Both receivers collect raw amplitude and phase output data with a 50 Hz sampling rate, which are post-processed by removing trend and outliers, most probably caused by instrumental error. Mean and standard deviation method was used to identify and remove data outliers, defined as all data points taking absolute value greater than three standard deviations about the mean value. Following the widely used procedure proposed by Van Dierendonck [13] for detrending signal amplitude and phase, the raw data were detrended with the high pass sixth-order Butterworth filter with the cutoff frequency at 0.1 Hz. As additional conditions, study contained only measurements made at elevation angles greater than 15°, to avoid errors induced by most intense multipath, and with continuous satellite contact or a time of lock greater than 180 seconds. Computed ionospheric indices used in tracking fluctuations of amplitude and phase are S_4, defined as the standard deviation of the received signal amplitude during 60 seconds of measurement, normalized to the average signal amplitude, and σ_φ, defined as the standard deviation of the detrended carrier phase evaluated over 60 seconds.

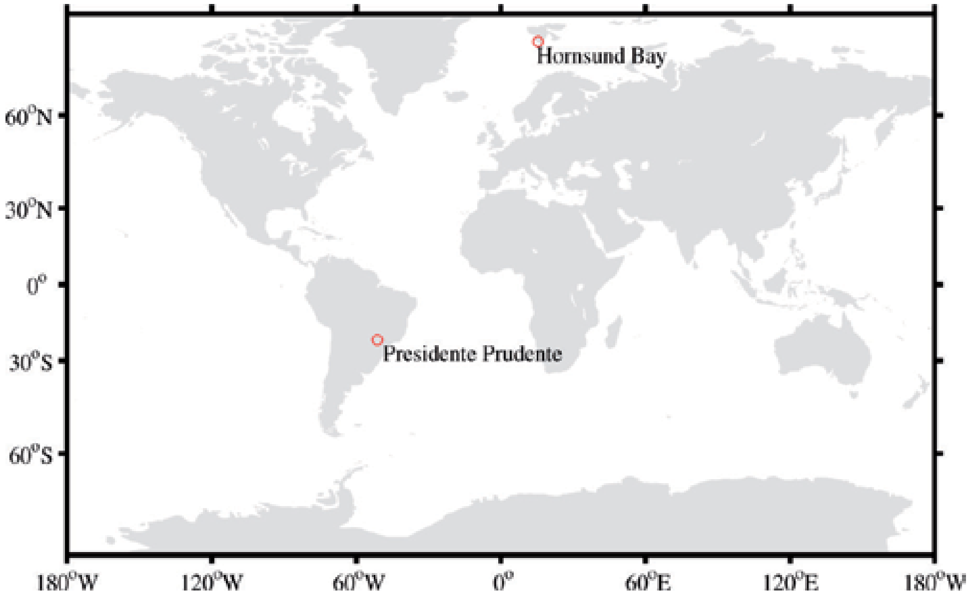

Figure 1. Geographical locations of receivers used in analysis – receiver set in high latitudes at Hornsund Bay, Spitsbergen and in low latitudes at Presidente Prudente, Brazil.

Two case studies on statistical analysis of the scintillating signals were undertaken during strongest geomagnetic storm in 2010, on 5-6th April, at Hornsund Bay, Spitsbergen, and moderate geomagnetic condition during 1st November 2011, at Presidente Prudente, Brazil. Geomagnetic disturbance index Kp is used as indicator of magnetospheric and ionospheric influence to the H component of geomagnetic field, which is in close relation with the generation of ionospheric irregularities producing scintillations. Contributing parameters, as provisional 1 hour disturbance storm time (Dst) and 1 minute auroral electrojet (AE) indices are used in further data selection and in gaining detail information on all latitude magnetic activity. Data for all geomagnetic condition parameters were retrieved from the web archive of World Data Centre for Geomagnetism, Kyoto (wdc.kugi.kyoto-u.ac.jp). From Fig. 2 it is possible to notice that in case of 5-6th April 2010 level of Kp index reaching a maximum value of 8, while Dst and AE reached values of-81 and 2291 nT, respectively. While in case of low latitude data Kp index achieved not so high level with maximum value of 5, whereas Dst and AE come to-72 and 1261 nT, respectively.

Analysis covered processing of 1, 3 and 12 hours data intervals for each of the tracked satellite PRNs, in order to test higher order moments on optimal amount of data mandatory for correct results. First analysis tests, not included in the paper, took data intervals of 3 and 12 hours, but due to averaging of large dataset, information from data points with pronounced scintillations had been lost and in all cases resulted to a close Gaussian PDF. Data analyses included

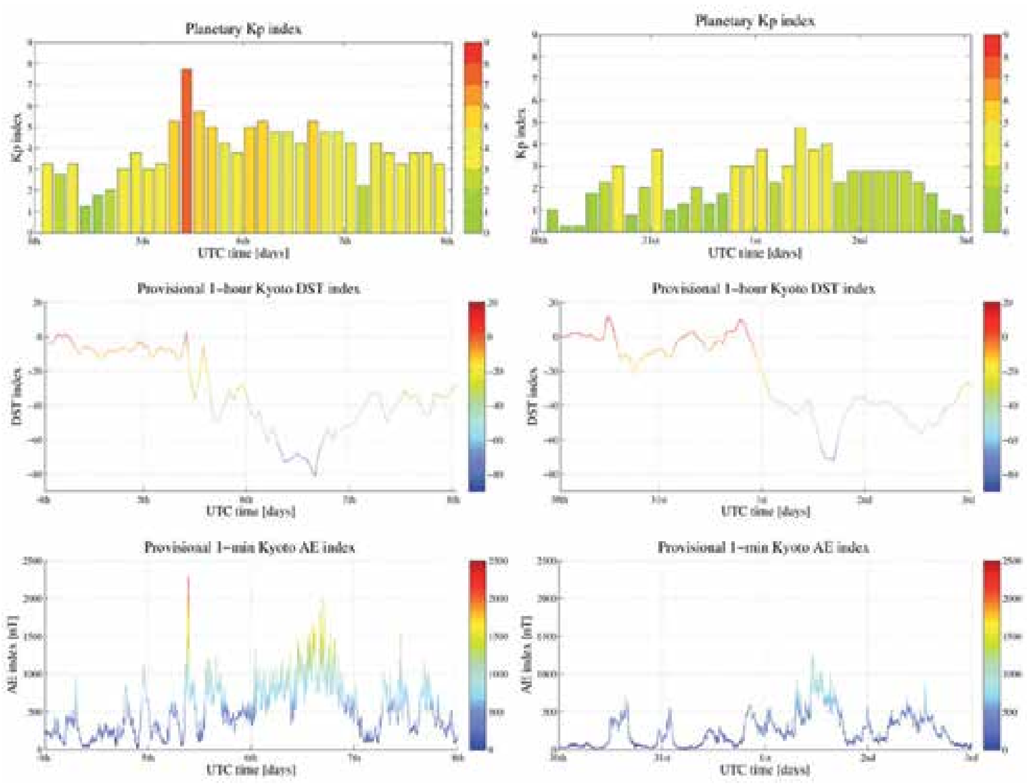

Figure 2. Fluctuations in geomagnetic Kp, Dst and AE indices during strong geomagnetic storm on 5-6thApril 2010 (right side graphs) and for moderate geomagnetic conditions on 1st November 2011 (left side graphs), showing initial and recovery phase of the storm.

Gaussian, and Nakagami-m PDF of scintillating signals and its dependences on higher order moments. Nakagami-m distribution is known as mostly used in the statistical analysis for description of behaviour of strong ionospheric scintillation influence on the signal amplitude. Skewness is calculated as follows (third moment about the mean divided by sample variance powered by 1.5):

$$skewness = \frac{\frac{1}{n}\sum_{i=1}^{n}(x_i - X)^3}{\left[\sqrt{\frac{1}{n}\sum_{i=1}^{n}(x_i - X)^2}\right]^3}\ , \tag{1}$$

and kurtosis as fourth moment about the mean divided by squared sample variance and normalized by 3:

$$kurtosis = \frac{\frac{1}{n}\sum_{i=1}^{n}(x_i - X)^4}{\left[\sqrt{\frac{1}{n}\sum_{i=1}^{n}(x_i - X)^2}\right]^2} - \frac{3}{2}\ , \tag{2}$$

n is number of values in a sample, x_i represents i-th value in the sample and X is sample mean value.

Choice of the PDFs in analyse is mainly relied on scientific and historical aspect [8, 14-20]. Nakagami-m distribution is known as mostly accepted solution in modelling of signal intensity, while Gaussian distribution is well known and widely used in statistical descriptive tool in science. In case of examination of signal intensity PDF, Gaussian distribution is used as reference distribution to measured data and Nakagami-m distribution. Gaussian distribution with zero mean, showed as acceptable, simple and effective solution for representation of the signal phase PDF for weak and moderate scintillations, is defined as

$$P(I) = \frac{1}{\sigma\sqrt{2\pi}} \exp\left(-\frac{(I - \mu)^2}{2\sigma^2}\right), \tag{3}$$

where I is signal amplitude, σ is a standard deviation and $\mu$is mean value. Gaussian distribution have found use across the various scientific fields, due to simplicity of use, good approximation of variety of natural phenomena and well clarified theory behind.

Nakagami-m distribution, widely used in characterisation of ionospheric scintillation of signal intensity, radio links and wireless fading channels, is given by formula [9]:

$$P(I) = \frac{m^m I^{m-\frac{1}{2}}}{\Gamma(m)\langle I\rangle^m} exp\left(-\frac{mI}{\langle I\rangle}\right), \tag{4}$$

I represent single value of the signal amplitude calculated per 60 seconds, function shape parameter m is equal to $1/S_4^2$, $\Gamma(.)$ is Gamma function and <. > represents time average value of the signal amplitude. Spread parameter in Nakagami function, marked as $<I>$, is equal to signal amplitude mean value, which is set to 1. Nakagami distribution represents good approximation in describing multipath scattering with different groups of reflected wave [23].

Theoretical distribution of higher order moments, used in comparison with distribution of measured data, is calculated from the formula:

$$\int_0^\infty P(I) I^n dI, \tag{5}$$

where $P(I)$ is Nakagami PDF, I is signal amplitude and n=[1..4] is the order of the calculated statistical moment. From 3.381(4) formula of Gradshteyn and Ryzhik [23], integral was simplified to analytical problem.

3. Results

In order to obtain the information about probability distribution of scintillating signal, statistical analysis was performed by using higher order moments of signals phase and amplitude. Analysis was performed in two steps, first one included testing calculated higher order moments for received phase and amplitude for several time intervals (1, 3 and 12 hours), and the second step included comparison of the PDF of measured data with PDFs obtained from theory. Initial test cases included data set lengths of 3 and 12 hours of measurements, fulfilling the condition that amount of data points should be large enough for correct calculations of higher order moments. In these cases analysis showed good agreement with Gaussian distribution function, but only due to averaging over whole data set and losing valuable information about strong amplitude and phase fluctuations. This fact was confirmed with analysis of data samples of 1 hour length, which are shown in this paper. Additional condition is introduced, after detrending and removing outlier from measured data, only samples with more than 80% of usable data was taken in further processing.

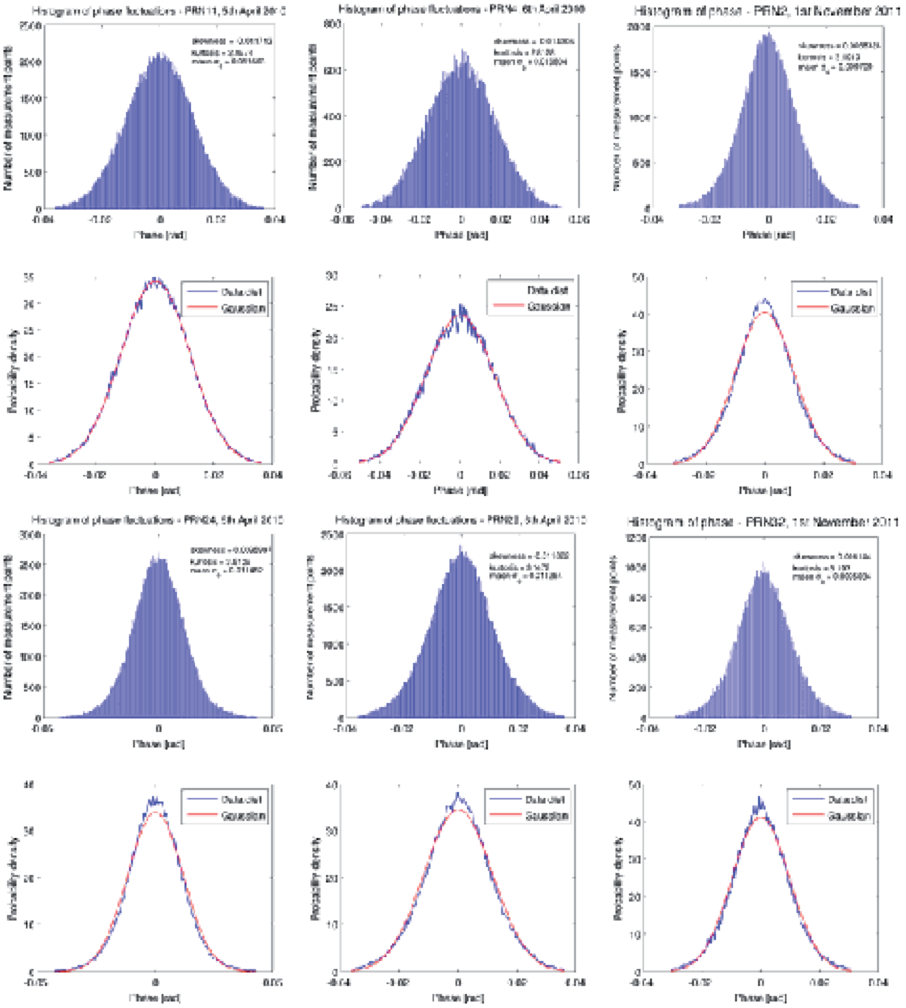

Figure 3. Histograms of phase fluctuations made for one hour of observation, left and middle columns of graphs are for high latitudes measurements made on 5-6th April 2010, and right column of graphs for low latitude measurements made on 1st November 2011. Graphs in 2nd and 4th row represent PDF of measured data with fitted Gaussian distribution function.

Results of signal phase analysis for measurements in all three cases are shown in Fig. 3, with randomly chosen satellites PRN11, 4 and 2 (from left to right in figure) from group of cases with good alignment with Nakagami PDF in case of amplitude distribution, and PRN24, 29 and 32 from group showing deviant characteristic. Most of analyzed samples showed good agreement with Gaussian distribution, but as it could be seen from the last row of plots in some cases (large skewness and/or kurtosis), phase distribution deviated from Gaussian PDF.

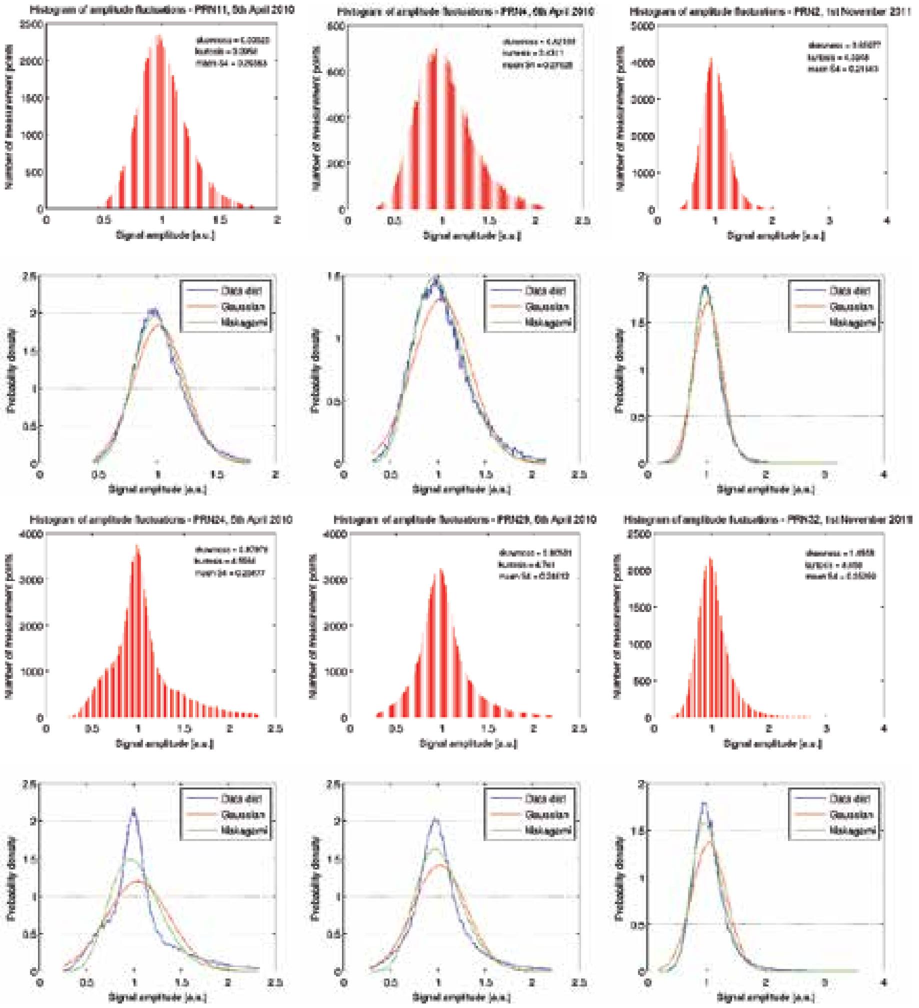

Figure 4. Histograms of amplitude fluctuations made for one hour of observation, left and middle columns of graphs are for high latitudes measurements made on 5-6th April 2010, and right column of graphs for low latitude measurements made on 1st November 2011. Graphs in 2nd and 4th row represent PDF of measured data with fitted Gaussian and Nakagami distribution function.

Results of analysis for amplitude scintillation are displayed in Fig. 4. Presented are PDFs of measured amplitude data with fitted theoretical Gaussian and Nakagami distributions. As in

Fig. 3 first two lines illustrates good agreement between experimental PDF and Nakagami fitted distribution. The agreement is more pronounced between 10:00 and 19:00 of local time, while the second case, showing deviations from Nakagami distribution, appears more in evening and early morning hours, especially in case of low latitudes. More detail analysis on larger data set is required for any further conclusions made on statistics of PDF deviation appearance and possible links to geo-physical parameters controlling these phenomena.

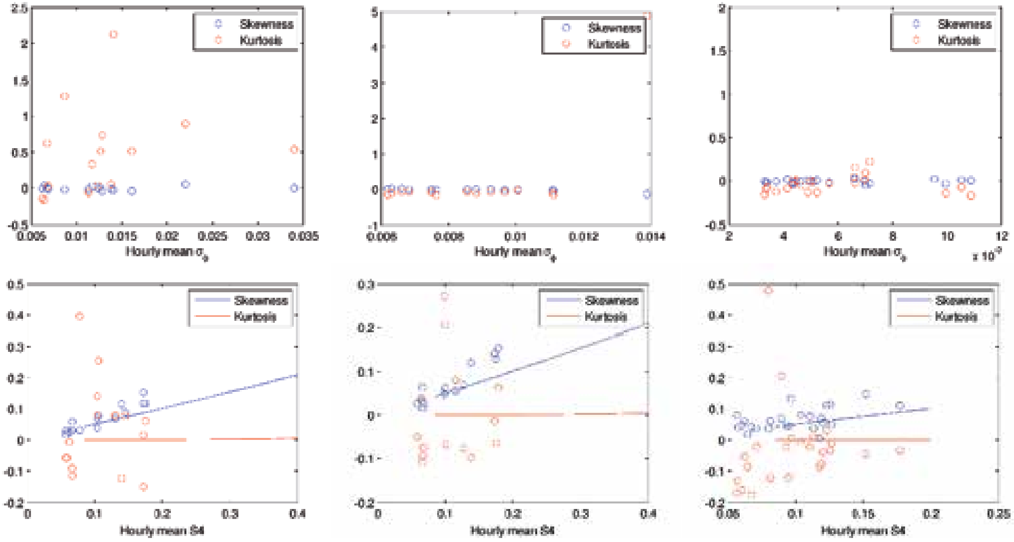

Figure 5. Representation of hourly mean higher order moments dependence of scintillation indices σ_φ(first row) and S_4(second row) for 5th, 6th April 2010 and 1st November 2011 watched from left to right side. Solid lines in the bottom graphs represent fitted theoretically derived skewness (blue) and kurtosis (red) from Nakagami distribution function for signal amplitude, which could be calculated only for values $S_4 \geq 0.09$.

Fig. 5 depicts hourly values of higher order moments dependence on mean values of σ_φ and S4. All the σ_φ and S4 values are calculated every minute from randomly chosen PRN with full data set, which means that in specific hour PRN was visible all the time and measurements were performed without loose of lock. In graphs showing dependence from σ_φ, skewness (blue y-axis and marks) and kurtosis (red y-axis and marks) are mainly taking values around zero, proving good agreement with Gaussian distribution. Only in case of 5th April 2010, it is possible to notice significant deviation from kurtosis, which occurs most possibly due to instrumental error. Bottom graphs displays higher order moments of amplitude, where skewness of measured data (circular markers) follows fitted distribution of moments (solid red line-skewness, and blue line-kurtosis) for smaller values of S4, while higher S4 skewness characteristic of measured data start rising much faster than theoretical one. Kurtosis controverts theoretical distribution, because of very sparse and chaotic behaviour, which could mean that Nakagami PDF is not ideal solution for representing amplitude distribution.

4. Conclusions

Paper presents results of a GPS signal measurements statistical analysis at high and low latitudes. Focus was on the probability distribution of phase and amplitude under disturbed geomagnetic conditions for moderate and strong scintillations. Results show, as expected, a good agreement between the measured scintillating signal phase distribution and Gaussian distribution. More interesting case is for the signal amplitude, where a systematic increase of skewness and kurtosis with the S_4 values has been observed. In the case of weak scintillation (small S_4) the probability distribution of amplitude is close to the Gaussian, while for strong scintillations (large S_4) the skewness and kurtosis indicate considerable departure from the Nakagami distribution. This might be indicative of the non-Gaussian distribution of ionospheric electron density fluctuations [19]. Dispersion in case of kurtosis could be due to the natural spread, but further experiments are required.

Future research should consider more probability function models and χ^2 goodness-of-fit tests for checking the precision of the distribution functions fit to the measured data. Also, more data sources, especially in low latitudes, and comparisons with in-situ measurements and other ground instruments measurements would be valuable reference in development of final model of scintillation signal distribution.

Acknowledgements

This work was undertaken in the scope of the TRANSMIT ITN (www.transmit-ionosphere.net), funded by the Research Executive Agency within the 7th Framework Program of the European Commission, People Program, Initial Training Network, Marie Curie Actions--GA No. 264476. The author would like to thank for GPS ground data from Presidente Prudente, Brazil, obtained through the CIGALA and CALIBRA project facility, and geomagnetic indices data provided by World Data Centre for Geomagnetism, Kyoto. The author is grateful to Prof. Andrzej W. Wernik from Space Research Centre for helpful discussions and comments.

Author details

Đorđe Stevanović

Space Research Centre Polish Academy of Science (SRC PAS), Warsaw, Poland

References

[1] A. W. Wernik, J. A. Secan, and E. J. Fremouw. Ionospheric irregularities and scintillations. *Adv. in Space Research*, 2003. 31(4): pp. 971-981.

[2] J. Arrons. Global Morphology of Ionospheric Scintillations. *Proceedings of the IEEE*, 1982. 70 (4): pp. 360-378.

[3] K. C. Yeh and C. H. Liu. Radio Wave Scintillations in the Ionosphere. *Proceedings of the IEEE*, 1982. 70 (4): pp. 324-360.

[4] A. W. Wernik, L. Alfonsi, and M. Materassi. Ionospheric irregularities, scintillation and its effect on systems. *Acta Geophysica Polonica*, 2004. 52 (2): pp. 237-249.

[5] P. M. Kintner, B. M. Ledvina, and E. R. de Paula. GPS and ionospheric scintillations. *Space weather*, 2007. 5(9).

[6] S. Basu, K. M. Groves, S. Basu, and P. J. Sultan. Specification and forecasting of scintillations in communication/navigation links: Current status and future plans. *J. Atmos. Sol. Terr. Phys.*, 2002. 64: pp. 1745-1754.

[7] B. Deng, J. Huang, W. Liu, J. Xu, and L. Huang. GPS scintillation and TEC depletion near the northern crest of equatorial anomaly over South China. *Advances in Space Research*, 2013. 51: pp. 356-365.

[8] C. N. Mitchell, L. Alfonsi, G. De Franceschi, M. Lester, V. Romano, and A. W. Wernik. GPS TEC and scintillation measurements from the polar ionosphere during the October 2003 storm. *Geophysics Research Letters*, 2005. 32 (L12S03)

[9] S. Skone, F. Man, F. Ghafoori, and R. Tiwari. Investigation of Scintillation Characteristics for High Latitude Phenomena, in: *Proceedings of GNSS08*. The Institute of Navigation. Savannah, GA. The Institute of Navigation. 2008.

[10] C. L. Rino. Ionospheric Scintillation Theory-A Mini-Review. *IEEE Transactions on antennas and propagation*, 1976. pp. 912-915.

[11] C. L. Rino and E. I. Fremouw. Statistics for ionospherically diffracted VHF/UHF signal. *Radio Science*, 1973. 8(3): pp. 223-233.

[12] C. L. Rino, R. C. Livingston, and H. E. Whitney. Some new results on the statistics of radio wave scintillation, 1. Empirical evidence for Gaussian statistics. *Journal of Geophysical Research*, 1976. 81(13): pp. 2051-2057.

[13] E. J. Fremouw, R. L. Leadabrand, R. C. Livingston, M. D. Cousins, C. L. Rino, B. C. Fair, and R. A. Long. Early results from the DNA Wideband satellite experiment-Complex-signal scintillation. *Radio Science*, 1978. 13(1): pp. 167-187.

[14] C. L. Rino. A power law phase screen model for ionospheric scintillation: 1. Weak scatter. *Radio Science*, 1979. 14(6): pp. 1135-1145.

[15] C. L. Rino. On the application of phase screen models to the interpretation of ionospheric scintillation data. *Radio Science*, 1982. 17(4): pp. 855-867.

[16] E. J. Fremouw and J. A. Secan. Modelling and scientific application of scintillation results. *Radio Science*, 1984. 19(3): pp. 687-694

[17] E. J. Fremouw, R. C. Livingston, and D. A. Miller. On the statistics of scintillating signals. *J. Atmospheric Phys.*, 1980. 42: pp. 717-731.

[18] A. W. Wernik and K. C. Yeh. Chaotic behaviour of ionospheric scintillation: modeling and observations. *Radio Science*, 1994. 29(1): pp. 135-144.

[19] A. W. Wernik and M. Grzesiak. Scintillation Caused by the Ionosphere With non-Gaussian Statistics of Irregularities. *Radio Science*, 2011. 46 (RS6011)

[20] T. E. Humphreys, M. L. Psiaki, J. C. Hinks, and P. M. Kintner Jr. Simulating ionosphere-induced scintillation for testing GPS receiver phase tracking loops. *IEEE J. Sel. Top. Signal. Process*, 2009. 3: pp. 707-715.

[21] A. O. Morales, E. R. De Paula, W. J. Perrella, and F. S. Rodrigues. On the distribution of GPS signal amplitudes during low-latitude ionospheric scintillation. *GPS Solutions*, 2013. 17: pp. 499-510.

[22] A. J. Van Dierendonck, J. Klobuchar, and Q. Hua. Ionospheric Scintillation Monitoring Using Commercial Single Frequency C/A Code Receivers, in: *Proceeding ION ITM*. Salt Lake City, UT: 1993.

[23] I. S. Gradshteyn and I. M. Ryzhik. *Table of Integrals, S*eries and Products. Academic Press 2007.

Performance Analysis of Empirical Ionosphere Models by Comparison with CODE Vertical TEC Maps

Pavel Najman and Tomislav Kos

Additional information is available at the end of the chapter

http://dx.doi.org/10.5772/58774

1. Introduction

Nowadays, the Global Navigation Satellite System (GNSS) is commonly used for positioning, navigation and timing. The GNSS based services are used in many areas such as maritime, aviation, agriculture, public transportation and geodesy. The GNSS receiver computes its position by trilateration using ranges between satellites and the receiver, where the ranges are calculated from measurements of time-of-arrival of satellite radio signals [1]. However, the signals do not propagate ideally. Many factors can change signals' propagation speed or trajectory and they can consequently cause incorrect determination of the receiver position.

One of the factors which affect GNSS signal propagation is the ionosphere. The ionosphere causes delay of radio signals, and if not mitigated, it can be the largest source of error (ionospheric error) in GNSS positioning and navigation [2]. There are several possibilities to compensate for the ionospheric effect. First technique is to use multi-frequency satellite-receiver communication which takes advantages of dispersive nature of the ionosphere. This approach called ionosphere-free combination can remove about 99 % of the ionospheric error [3]. In case the receiver uses only one frequency it can use a Satellite Based Augmentation Systems (SBAS) such as the Wide Area Augmentation System (WAAS) or European Geostationary Navigation Overlay Service (EGNOS). These systems determine condition of nearby ionosphere from a network of reference stations and send the information to the user via a geostationary satellite [4]. If the SBAS service is not available or it is not supported by the receiver, an ionospheric model can be used to estimate the ionospheric error. Ionospheric models are also used for satellite and receiver inter-frequency bias estimation and Total Electron Content (TEC) calibration [5].

There are several empirical ionospheric models. Well known empirical models included in our study are the Klobuchar model, International Reference Ionosphere (IRI) and NeQuick. In addition, we evaluated accuracy of a relatively new model developed at DLR (Deutsches Zentrum für Luft-und Raumfahrt), the Neustrelitz TEC Model (NTCM) [6]. As each of the models applies different modeling approach and was developed with different background data, we assume that their TEC modeling performance differ and the use of one model in particular condition would be better than use of another.

Some of the recent analysis evaluated TEC modeling performance of the Klobuchar model and the NeQuick 2 by comparison of modeled TEC with GNSS measurements [7], [8]. In our study, we evaluated performance of four empirical ionospheric models comparing them with Global Ionospheric Maps (GIMs) produced at the Center for Orbit Determination in Europe (CODE), using a similar approach as in [9] for the Klobuchar model and the NeQuick 2. This approach has the advantage that all TEC data are in the zenith direction, therefore, we can avoid conversion between slant and vertical TEC which can produce additional error [10]. On the other hand, GIMs do not contain direct measurements and we have to consider their data accuracy.

To estimate TEC mismodeling for each model, we compared modeled TEC data with CODE GIMs over three years (2010, 2011 and 2012). Such data were produced at the CODE using measurements from about 200 GPS/GLONASS stations. The evaluation will show variation in models' TEC modeling performance with respect to time of day, season, location and space weather condition. In addition, it will show in which cases the CODE GIMs' inaccuracy prevents performance evaluation.

2. The ionosphere

The ionosphere is the part of the atmosphere with large amount of charged particles (ions and electrons). A typical vertical profile of ionospheric electron density (Figure 1) is divided into the several layers according to the different ionization and recombination principles [11]. The ionospheric structure significantly varies with geographical location, local time and with changes in solar-terrestrial environment.

We can divide ionospheric variations into two groups. The first group includes variations with periodic behavior that can be distinguished from empirical data. These variations are: daily variation, seasonal variation, dependence on the geomagnetic field and climatological dependence on space weather. These phenomena can be analytically described and modeled by empirical ionospheric models.

The second group of ionospheric variations includes sudden ionospheric disturbances (SID) or small rapid changes in the electron density causing scintillation. Even though these phenomena are often observed, they do not show any behavior pattern to the magnitude or period of occurrence [12]. As these variations belong to ionospheric weather rather than to climatology they are not modeled by empirical ionospheric models.

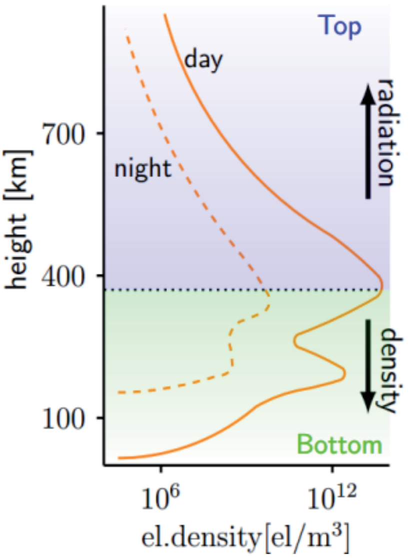

Figure 1. A typical vertical electron density profile of the ionosphere. The electron density profile during day and night is represented by full and dashed line, respectively. The dotted line shows the average height of the daily electron density maximum. The picture was made by the authors according to [13].

Radio signal which propagates through the ionosphere experiences changes of its propagation speed and trajectory. These changes depend on the signal carrier frequency and electron density of the ionosphere [14]. The ratio between the group propagation velocity v and the speed of light in vacuum c can be described as refractive index n_{ion}:

$$n_{ion} = \frac{c}{v} \tag{1}$$

The refractive index of the ionosphere n_{ion} can be derived from the Appleton-Hartree formula. Usually, we considering only the first two terms of the n_{ion} equation as the rest contributes to the ionospheric error by less than 1% [15]. The group refractive index then leads to

$$n_{ion} = 1 + \frac{40.3\ N_e}{f^{\,2}} \tag{2}$$

where N_e is the electron density and f is the signal carrier frequency. If we write the ionospheric propagation time as integration of the propagation speed over the propagation path and include (2) we get

$$\tau_{ion} = \int_S \frac{1}{v_{ion}} \mathrm{d}S = \int_S \frac{n_{ion}}{c} \mathrm{d}S \tag{3}$$

Figure 2.Ionospheric propagation delay can be converted to the equivalent distance by multiplication with the speed of electromagnetic wave in vacuum: $\rho = c \cdot \tau$. Ionospheric group delay can then be written as

$$\Delta \rho_{ion} = \frac{40.3}{f^2} \int_S N_e dS \tag{4}$$

The integration of the electron density along the path is usually referred to as *Total Electron Content (TEC):*

$$TEC = \int_S N_e \mathrm{d}S \tag{5}$$

which is the total number of electrons in a tube of 1 m^2 cross-section along the GNSS signal path through the ionosphere. If we know the frequency of the signal, the value of TEC allows us to compute the propagation delay introduced by the ionosphere, which is an error for our point of view. All ionospheric models considered in this study can provide TEC values.

There are two commonly used types of TEC values: vertical and slant TEC. Vertical total electron content (vTEC) at a certain geographical point stands for TEC in the direction of the zenith. TEC between a satellite and a receiver is usually referred to as the slant TEC (sTEC). This notation signifies that the TEC is at a different angle then the zenith. TEC is usually given in TEC Units (TECU) where 1 TECU=10^{16} electrons/m^2.

3. Ionospheric models

3.1. Klobuchar model

The Klobuchar model was developed by John A. Klobuchar at the Air Force Geophysics Laboratory, U.S. The algorithm is used to correct ionospheric time-delay in GPS for single frequency communication. The model was developed in 1975 keeping in mind limited computation memory and capability of receivers, therefore, the model algorithm is very fast and has minimum complexity.

One of the main criteria of the algorithm design was to fit best the daily period with the largest TEC values, i.e. afternoon period. The Klobuchar model approximates daytime variation of ionospheric time delay as a half period of cosine function with maximum at 14 hours local time. The amplitude and period of the cosine are each calculated with 4 coefficients transmitted by GPS navigation message. The night time ionospheric delay is set as a constant value of 5 ns (Figure 2.) [16].

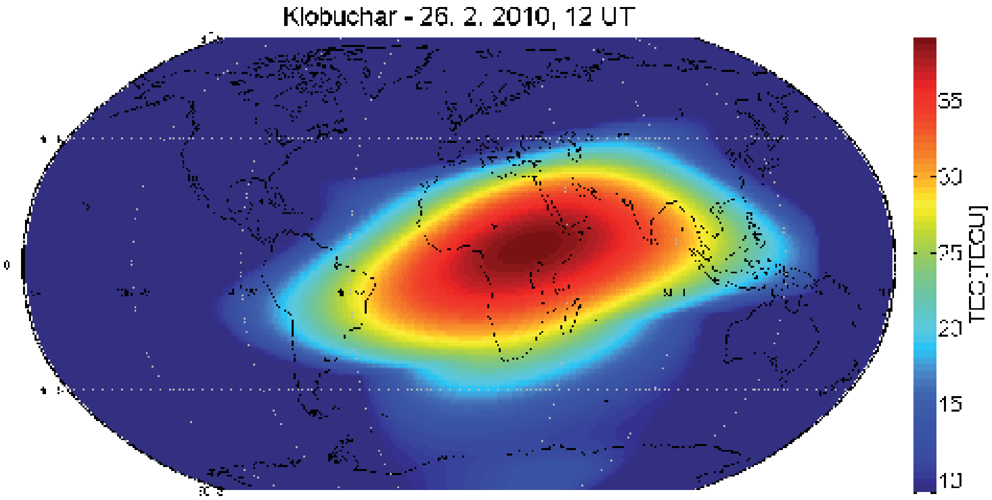

Figure 2. Global ionospheric map of 26th February 2010, 12 UT modeled by the Klobuchar model.

3.2. IRI2012

The first version of the International Reference Ionosphere was developed as a joint project of Committee on Space Research (COSPAR) and Union of Radio Science (URSI) in 1978. Since then, the model has been continuously improving.

The IRI is able to compute vertical electron density profile and vTEC as well as other ionospheric parameters such as ion densities and ion temperatures. The IRI divides the ionosphere into six sub-regions where each of them is described by several parameters. The model also uses lists of f_oF2 and $M(3000)F2$ parameters (f_oF2 is critical frequency of the ionospheric layer F2 which is usually the layer with N_e maximum, $M(3000)F2$ is ratio between maximum usable frequency for ionospheric radio link over the distance of 3000 km using layer F2 and f_oF2, more information can be found in [17]). The integration height for TEC computation is limited to 2000 km [18].

To calculate vertical el. density profile of the ionosphere, user can choose one from several models for each region. In this work, we used standard IRI setting. The IRI uses both space weather and geomagnetic indices, i.e. Solar Radio Flux ($F_{10.7}$) index, International Sunspot Number (R_i) and magnetospheric Ap index which describes variations in the Earth's geomagnetic field.

Comparing to the Klobuchar model, the ionosphere structure modeled by the IRI is more complex including also the equatorial anomaly (Figure 3). Equatorial anomaly is the area with higher TEC distanced about 20° north and south from the equator. Source code of current IRI version is available on model's webpage (http://irimodel.org/).

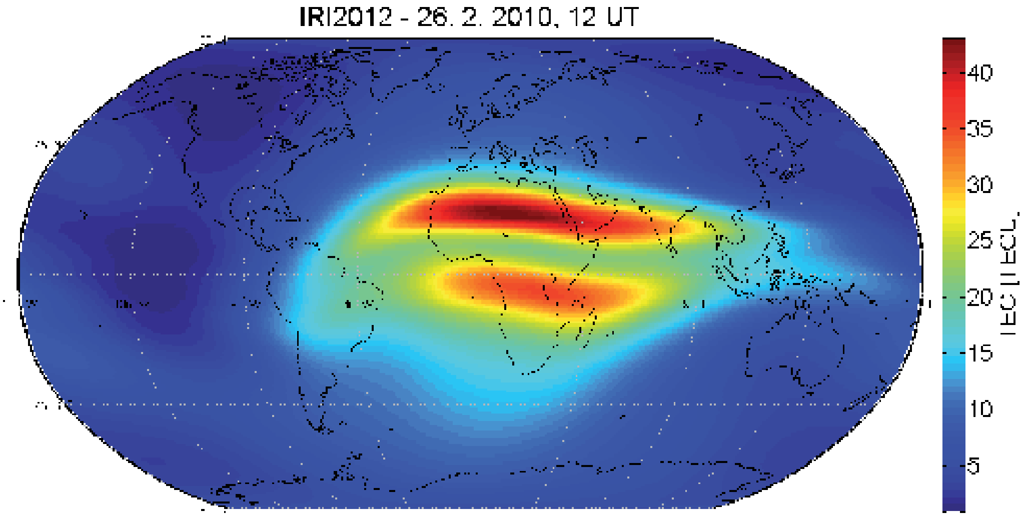

Figure 3. Global ionospheric map of 26th February 2010, 12 UT modeled by the IRI2012.

3.3. NeQuick 2

The NeQuick is an empirical model based on the model introduced by Di Giovanni and Radicella in 1990. Its modified version is used in the GNSS Galileo to aid single-frequency positioning [19]. The model has been also included into the ITU-R recommendation as a suitable method for TEC modeling. In addition, the IRI model uses NeQuick algorithm as a default option for the upper ionosphere computation.

The NeQuick is able to calculate electron density at any given location in the ionosphere. Therefore, it can provide TEC and electron density profile between any two given points [20]. For the analyses, we used the NeQuick version 2 which we obtain at the International Centre for Theoretical Physics in Trieste, Italy. The model is driven by monthly-mean solar radio flux.

NeQuick is a complex electron density model. As well as in case of the IRI, we can distinguish equatorial anomaly on the NeQuick GIM (Figure 4).

3.4. NTCM

Recently, a new global ionospheric model NTCM was developed at the Institute of Communications and Navigation, DLR in Neustrelitz, Germany. The model can provide values of vTEC at any given time and location. The core of the model consists of 12 coefficients which can be autonomously used for full solar cycle. The driver of the NTCM is the $F_{10.7}$ index. The model does not use any integration of electron density profile, therefore, it is very simple and fast [5]. The model analytically describes daily variation, seasonal variation, equatorial altitude anomaly and solar flux dependency as harmonic functions. All the formulas of the model algorithm can be found in [6].

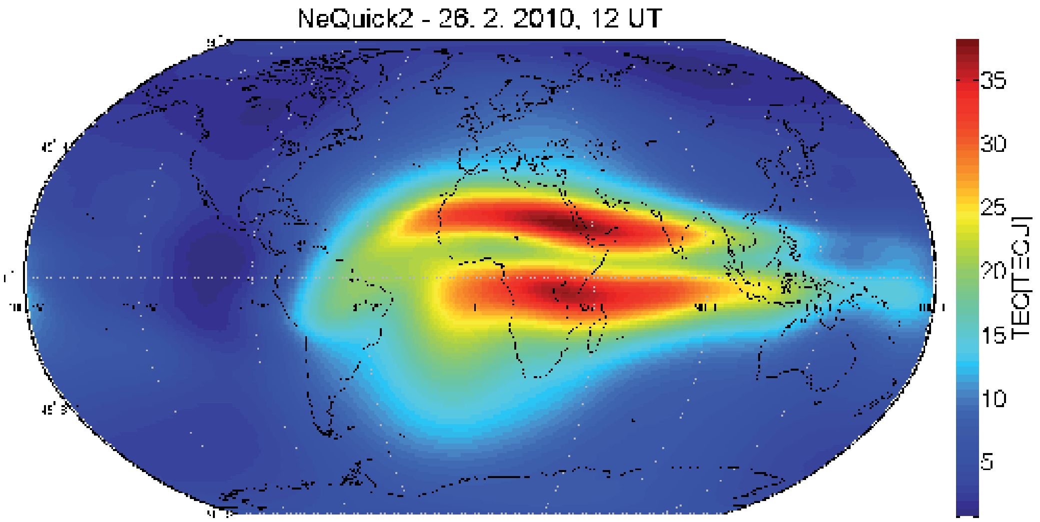

Figure 4. Global ionospheric map of 26th February 2010, 12 UT modeled by the NeQuick 2 model.

The NTCM, as well as the Klobuchar, is a TEC model. The GIM structure is rather simple and more similar to the Klobuchar one than to the GIMs produces with the electron density models IRI and NeQuick (Figure 5).

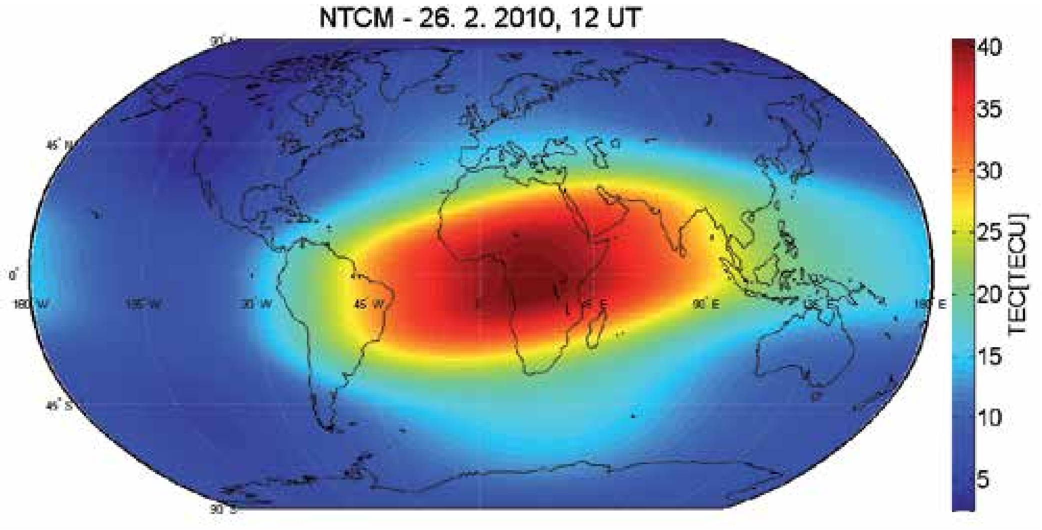

Figure 5. Global ionospheric map of 26th February 2010, 12 UT modeled by the NCTM model.

4. Data and methodology

All the ionospheric models discussed here are climatological. For our comparison, we chose CODE as a form of climatological reference rather than real measurements which can be affected by local ionosphere weather.

4.1. CODE

The Center for Orbit Determination in Europe at the Astronomical Institute at University of Berne, Switzerland provides GIMs on daily bases from 1995. The maps are available in the IONosphere map EX change format (IONEX) from 1997. CODE GIMs cover area from 87.5° northern to 87.5° southern latitude and from 180° western to 180° eastern longitude. The grid point step is 2.5° in latitude and 5° in longitude. GIMs are produced with 2 hours interval and the maps are generated using data from about 200 GPS/GLONASS sites of the IGS (International GNSS Service) and other institutions. Each map grid point contains a vTEC value calculated from measurements from the GNSS sites [21].

The accuracy of the CODE vTEC values depends on the local density of the GNSS reference network. The reference stations are not equally distributed over the whole world and CODE has higher level of inaccuracy at places with lack of reference stations, typically over oceans. Along vTEC values, CODE IONEX files contain also RMS maps (Figure 6) which give value of RMS error for each GIM grid point.

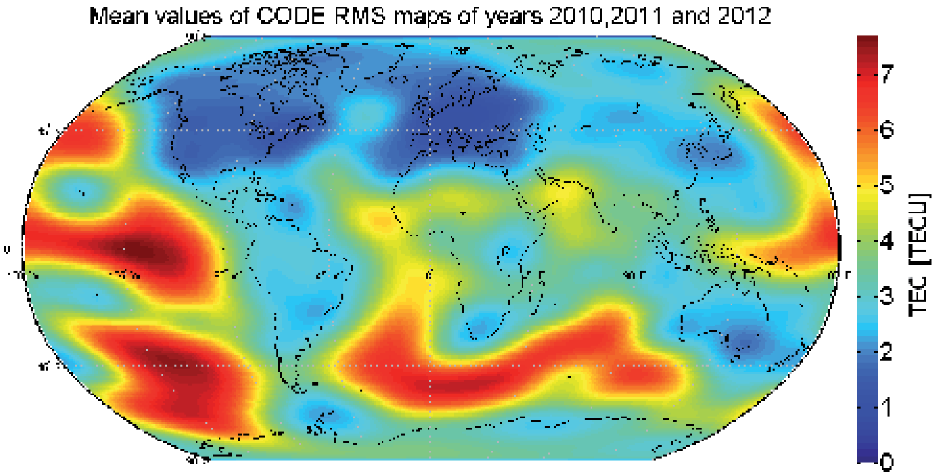

Figure 6. Averaged map of all the RMS error values of CODE maps during years 2010, 2011, and 2012.

4.2. Dataset

As the goal is a climatological study a lot of data are required. In this study, we processed data from years 2010, 2011, and 2012. Considering 12 maps per day and 2012 as a leap year, we made comparisons with 13,152 CODE maps. As each map has 71x73 (±87.5 latitude with 2.5° step, ±180 longitude with 5° step) values, we processed 68,166,816 CODE values in total.

First, we created similar GIM databases as the CODE one with all 4 models so that, for each CODE map, we created 1 map for each ionospheric model (4 maps per 1 CODE map). The modeled maps have the same grid points as CODE maps and each grid point contains corresponding modeled vTEC value.

As the next step, we divided data into groups. First division was according to the universal time (UT). For example, maps for 12 UT were compared only with each other and not with maps for different UT. As the CODE time resolution is 2 hours, this division created 12 data groups. Secondly, we divided data according to months in order to analyze effect of seasonal variation. This division created 12 month sub-groups for each of the 12 UT data groups.

The last division criterion was solar activity. Solar radio flux $F_{10.7}$ and international sunspot number R_i are considered to be two primary long-term solar indices. The $F_{10.7}$ is often used as a proxy for R_i making these two indices interchangeable, however, a recent study showed that there is a disagreement during the last decade [22]. We chose $F_{10.7}$ over the R_i as we assume that the index derived from measurements on Earth surface corresponds more to the ionospheric behavior rather than index derived from measurements of a solar phenomena (sun spots). The Figure 7 shows the observed solar radio flux variation for years 2010, 2011, and 2012. The data for the 1st of January 2011 and 2012 were missing and were filled as linear interpolation of values of adjacent days.

Considering 3 years of data, each group has approximately 91 days (e.g. March group has 93 days as 3 years mean 3 Marches (3x31=93)). To keep the number of days within one $F_{10.7}$ group high enough we decided to divide the groups into only 4 $F_{10.7}$ sub-groups. Applying this division, each sub-group should have approximately 23 days where every sub-group includes only days within particular $F_{10.7}$ range. We divided the dataset in order to keep the amount of days in groups as balances as possible, which led to non uniform distribution of F10.7 intervals (Figure 7). Even so, some groups have significantly less or more days then ideal 23 days (Table 1).

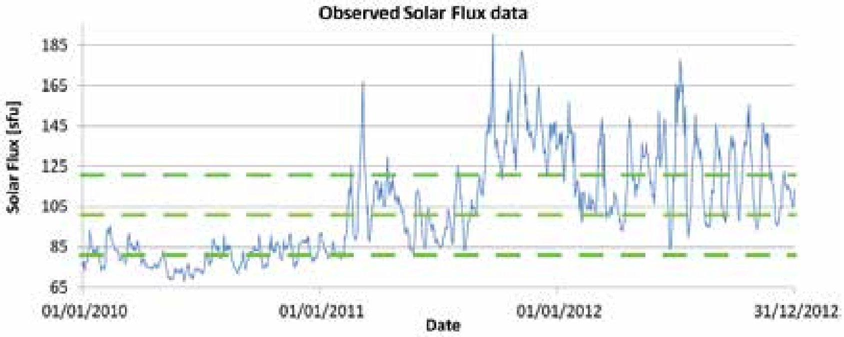

Figure 7. Variation of observed $F_{10.7}$ for years 2010, 2011, and 2012. The green lines divide the $F_{10.7}$ into ranges.

$F_{10.7}$ range [sfu]	Number of days per group												mean
	Month												
	1.	2.	3.	4.	5.	6.	7.	8.	9.	10.	11.	12.	
0 – 82	32	13	11	30	32	30	19	20	14	13	13	12	19.9
83 – 100	30	37	28	9	17	27	40	30	19	20	23	25	25.4
101 – 122	6	34	38	43	30	15	12	30	20	17	10	26	23.4
> 122	25	1	18	8	14	18	22	13	37	43	44	30	22.8

Table 1. Number of analyzed days in specified data groups according to $F_{10.7}$ range and month. The last column shows mean number of days per $F_{10.7}$ range.

4.3. Comparison method

We estimated the TEC mismodeling of all models comparing the modeled ionospheric maps with the reference CODE maps for each data group. We calculated the mismodeling as mean absolute difference between model's and CODE's TEC_{diff} for each map grid point as

$$\overline{TEC_{diff}}_{m1} = \frac{1}{N} \sum_{n=1}^{N} |vTEC_{Ref_n} - vTEC_{m1,n}|, \tag{6}$$

where $vTEC_{Ref}$ is the reference CODE vTEC value and $vTEC_{m1}$ is the corresponding vTEC value modeled by the model *m1*. The number *N* stands for the number of analyzed maps and depends on particular data group. For example, for the month January and $F_{10.7}$ range of 83 – 100 sfu the *N* is 30 (Table 1). We computed the mean absolute difference for each UT separately.

As it was mentioned, the accuracy of CODE data varies and should be considered. We calculated mean CODE RMS error RMS_{code} for each grid point of each data sub-group as

$$\overline{RMS_{code}} = \frac{1}{N} \sum_{n=1}^{N} RMS_{code_n}, \tag{7}$$

where the *N* is again the number of analyzed maps for each data group.

The decision of the most accurate model was made for each map grid point of each data group. Referring to Figure 8, in case the TEC_{diff} for all models for particular grid point was higher than the corresponding RMS_{code}, the model with the lowest TEC_{diff} is marked as decisively the best model of the grid point. Also, in case only one model has TEC_{diff} below corresponding RMS_{code} this model is marked as decisively the best model. In case two or more models have TEC_{diff} lower than corresponding RMS_{code}, the model with lowest TEC_{diff} is still identified as the best in average but not decisively with respect to the other models within the RMS_{code} threshold, because the CODE accuracy for that particular grid point is not high enough.

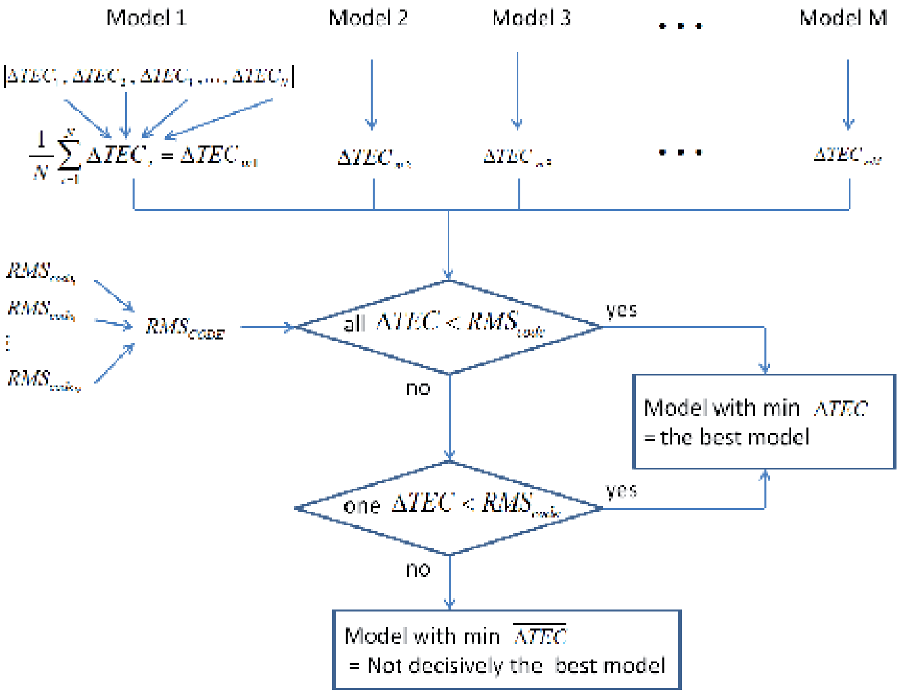

Figure 8. Block scheme of decision making of the best model for one grid point.

5. Results

Results for each field of Table 1 are represented in form of grid maps. As there are 48 groups and each of them has 12 UT-sub-groups we do not show all the results but only two examples. It should be noted that all the shown maps display interpolated data (1° x 1°) but the original grid resolution is 2.5° in latitude and 5° in longitude.

The first example (Figure 9) shows results for October, 14 UT and $F_{10.7}$ range of 101 – 122 sfu. Figure 9a shows TEC_{diff} calculated by the best models for particular areas. The average value of TEC_{diff} is 3.7608 TECU and 63 % of the values are lower than the average. Higher values of TEC_{diff} are mostly at the area of equatorial anomaly. The spatial distribution of the best models over the globe is shown in Figure 9b. This maps shows which model has the lowest TEC_{diff} to CODE for particular location. If we apply the criterion of the RMS_{code} (Figure 9c) we can identify the regions for which the insufficient accuracy of CODE data prevents identification of the decisively best model (marked with gray-white stripes, Figure 9d). In these areas two or more models have their TEC_{diff} lower then RMS_{code}. The Figure 9e additionally shows regions where only two models have TEC_{diff} lower then RMS_{code}. The areas are marked with stripes with colors of the particular models.

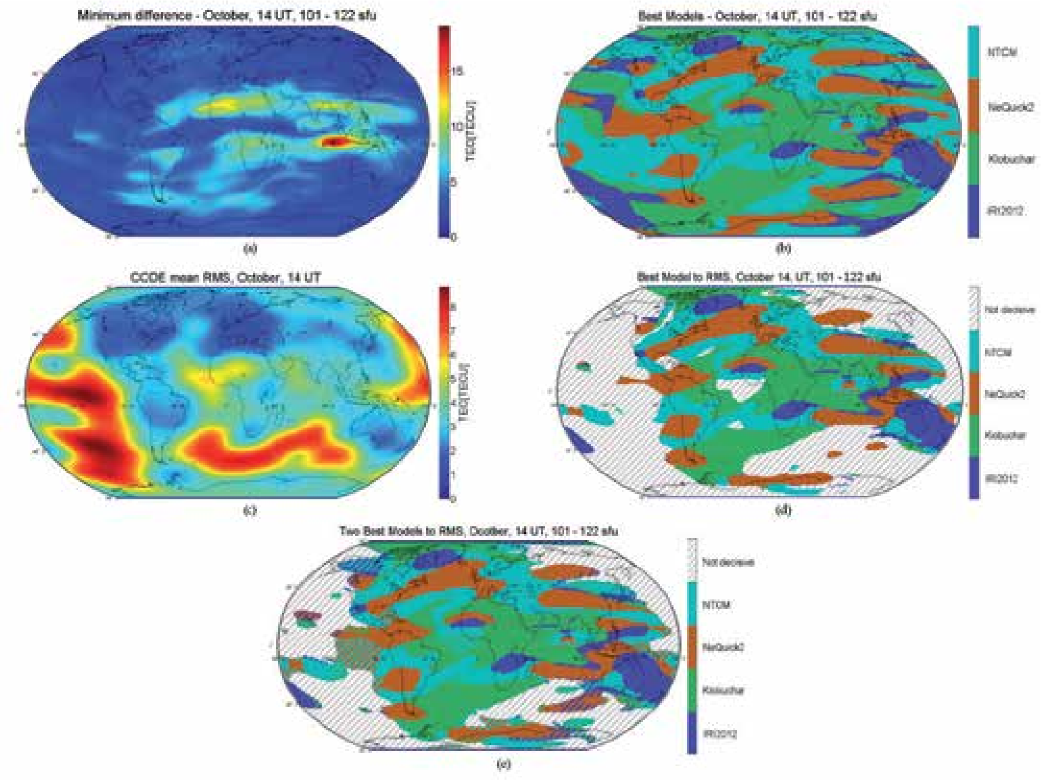

Figure 9. Global maps for October, 14 UT and $F_{10.7}$ range of 101 – 122 sfu. The top left map shows values of mean difference between the TEC values of selected best models and CODE TEC (a). The top right map shows the best models distribution over the globe (b). The third map shows mean RMS error of CODE data for this data group (c) and on four map we marked regions for which it is not possible to decide of the most accurate (gray-white stripes, d). The last map shows the areas where two models have TEC_{diff} lower then CODE RMS error (e).

The second example of results is for January, 02 UT for 0 – 82 sfu data group (Figure 10). As it was expected, the TEC_{diff} values are lower during the periods with low solar radio flux. The average value of TEC_{diff} is 1.755 TECU and 59 % of the values are lower than the average (Figure 10a). The best models distribution can be seen in Figure 10b and the map considering the mean RMS error criterion in Figure 10c. The amount of the gray-white areas indicates that for this data group two or more models have their TEC_{diff} lower then RMS_{code} in majority of cases. Additionally, Figure 10d shows that for about half of the globe three or all four models have their TEC_{diff} lower then RMS_{code} (gray-white areas).

The results can be also expressed in form of a graph for particular location. Both Figure 11 and 12 show performance of the models for the location: 60° northern latitude and 15° eastern longitude. Results for October, 14 UT and 101 – 122 sfu is shown in Figures 11 and results for January, 02 UT and 0 – 82 sfu in Figure 12. The graph for October shows that in all cases there is no more than one model with TEC_{diff} lower than RMS_{code} so that the best model was

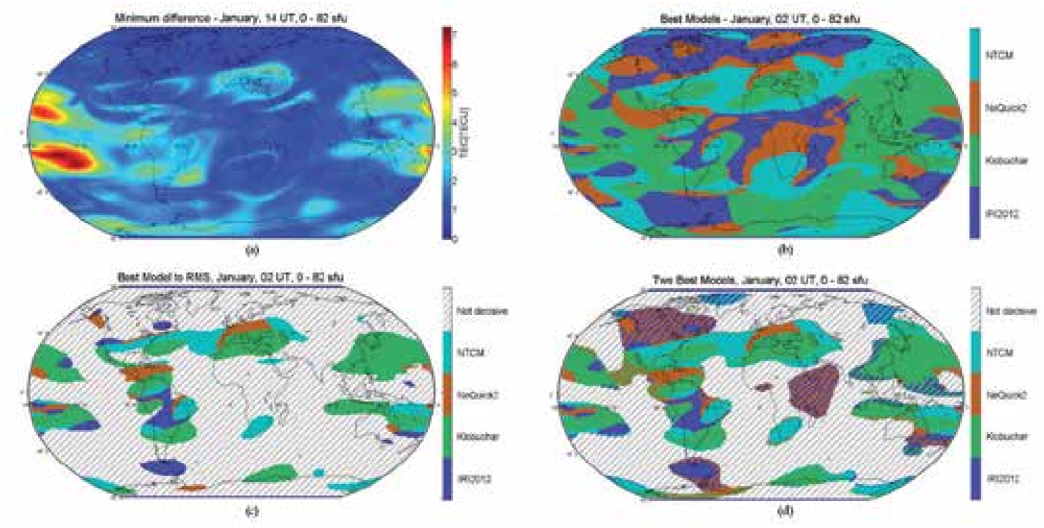

Figure 10. Global maps for January, 02 UT and $F_{10.7}$ range of 0 – 82 sfu. The top left map shows values of mean difference between the TEC values of selected best models and CODE TEC (a). The top right map shows the best models distribution over the globe (b). At the third map we marked the regions for which it is not possible to decide of the best model (gray-white stripes, c). The last map shows the areas where two of four models have TEC_{diff} lower then CODE RMS values (d).

decisively identified for the whole day. On the other hand, for January, it was not possible to identify the best model decisively during the morning and evening and night as for these periods more models have TEC_{diff} lower then RMS_{code}.

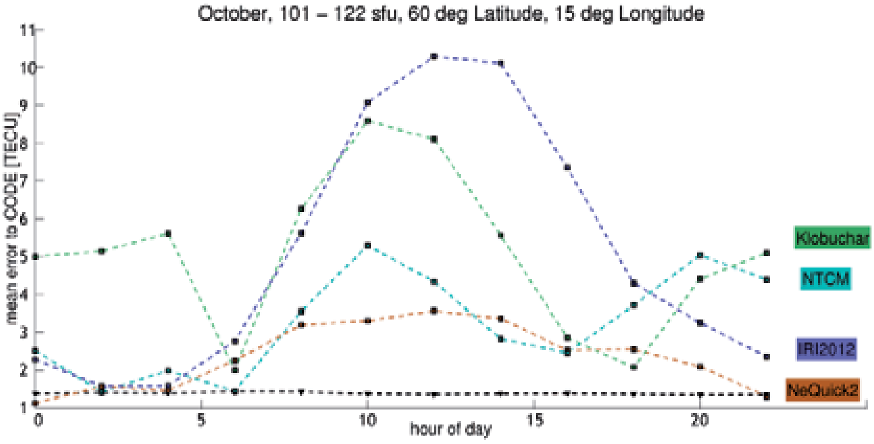

Figure 11. Variation of the mean difference between model and CODE TEC values for October 14 UT and $F_{10.7}$ range of 101 – 122 sfu. The black dashed line signifies the mean CODE RMS error.

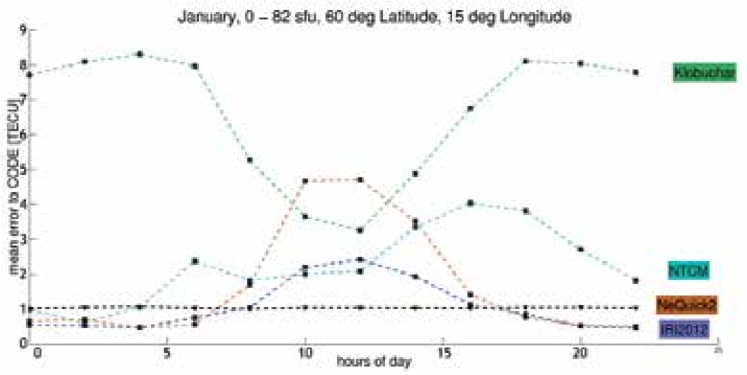

Figure 12. Variation of the mean difference between model and CODE TEC values for January, 02 UT and $F_{10.7}$ range of 0 – 82 sfu. The black dashed line signifies the CODE RMS error value.

If we summarize results for all data groups we can show how much were models identified as the best with respect to different areas (Table 2). The EU region was chosen between 65° – 30° northern latitude and 10° western to 50° eastern longitude and the USA between 55° – 0° northern latitude and 130° – 50° western longitude. Similar results but with respect to $F_{10.7}$ ranges are shown in Table 3. Table 4 summarizes the amount of cases for which the analysis was able to decisively determine the best model with respect to both $F_{10.7}$ and different regions.

Model	Portion cases [%]		
	Region		
	All data [%]	Decisive EU [%]	Decisive USA [%]
IRI2012	19.1	14.9	16.3
Klobuchar	32.9	44.0	41.1
NeQuick2	18.9	13.7	11.9
NTCM	29.1	27.4	30.7

Table 2. Amount of cases the models were decisively identified as the best one for different regions considering all data.

Region	Portion of cases [%]			
	$F_{10.7}$ range [sfu]			
	0 – 82	83 – 100	101 – 122	> 122
IRI2012	11.3	12.2	19.0	18.3
Klobuchar	49.7	45.5	37.8	37.3
NeQuick2	14.0	16.9	18.6	11.5
NTCM	25.0	25.4	24.6	32.9

Table 3. Amount of cases the models were identified as the best one according to the solar flux ranges.

Region	**Portion of cases [%]**			
	$F_{10.7}$ Range [sfu]			
	0 – 82	83 – 100	101 – 122	> 122
Whole globe	28.9	41.0	51.7	59.7
EU region	77.8	88.8	89.3	92.2
USA region	56.0	69.0	73.2	81.1

Table 4. Amount of cases for which the analysis was able to decisively identify the best model.

6. Discussion

One of the constrains of this research is the small amount of solar radio flux sub-groups. In our case, the same model is marked as the best one for particular location and time for both $F_{10.7}$ of 83 sfu and 100 sfu. A finer solar flux scale would be more adequate. We used wide solar flux ranges to keep amount of days in data groups high enough. However, there are still 4 groups with number of days lower then 10 (one group with only 1 day) which we consider to be insufficient. Future research can overcome this issue by including more years into the analysis, preferably a whole solar cycle.

Considering Table 2 and 3, the Klobuchar and NTCM were marked as the best models in more cases than the IRI and NeQuick. Such results are not in agreement with results from [6] and [7] where Klobuchar always performs worse than the NeQuick. However, in our case, both the IRI and NeQuick are driven by averaged indices while NTCM and Klobuchar by daily indices. This provides the advantage for NTCM and Klobuchar of ability to respond on any rapid day-to-day variation of the ionosphere. In the studies [6] and [7] the NeQuick is driven by Ionization level, while we used monthly mean $F_{10.7}$. It can be expected that applying Ionization level would significantly change our results, this will be done in future.

Good performance of the Klobuchar model in our test is surprise and it will be better investigated in the future work using larger database of reference data, different indices to drive the models and comparing results for different reference data sources.

The Table 4 shows that we were able to decisively identify the best model for most of the cases in the EU and USA region, especially during the middle and high solar activity. This is caused by the fact that during the periods with higher solar activity the difference between modeled TEC and the CODE's TEC rises while CODE RMS error stays roughly the same. In particular for these cases the information about the best model can be very important to minimize the potential impact of the ionosphere mismodeling in single frequency positioning. However, to verify this assumption the results should be tested on real TEC measurements.

7. Conclusion

We compared TEC data modeled by empirical ionospheric models: IRI2012, Klobuchar, NeQuick2 and NTCM to the CODE TEC data. We analyzed CODE GIMs for every two hours for years 2010, 2011 and 2012. The results show that the CODE RMS error values are low enough to identify the decisively best model in most cases above Europe and North America, especially during the days with higher solar radio flux. The ability to decisively recognize the best model decreases for lower solar radio flux values. For these periods more models have mean absolute TEC deference lower than corresponding mean CODE RMS error. The study shows that the Klobuchar and NTCM were marked as the best model in more cases than NeQuick 2 and IRI 2012. However, the performance of all models varies according to the time, location and solar flux which indicates that there is not one model which performs the best under all conditions. In addition, there is still a significant portion of cases for which the best model could not be identified decisively.

In the future work, we plan to analyze data for more years, improve the solar radio flux resolution and include the Galileo version of the NeQuick into our analysis. We also plan to perform the analysis on the different reference databases and test the results on real TEC measurements.

Acknowledgements

Pavel Najman's research work is undertaken in the scope of the TRANSMIT ITN, funded by the Research Executive Agency within the 7th Framework Program of the European Commission, People Program, Initial Training Network, Marie Curie Actions-GA no 264476.

We would like to thank to Astronomical Institute of the University of Bern for freely available CODE maps. We would also like to thank to Bruno Nava and Sandro M. Radicella for the NeQuick 2 source code.

Author details

Pavel Najman* and Tomislav Kos

*Address all correspondence to: pavel.najman@fer.hr

Faculty of Electrical Engineering and Computing, University of Zagreb, Zagreb, Croatia

References

[1] P. Daly. Navstar GPS and GLONASS : global satellite navigation systems. *Electronics & Communication Engineering Journal*, 1993. (December): pp. 349-357.

[2] B. Hofmann-Wellenhof, H. Lichtenegger, E. Wasle . *GNSS - Global Navigation Satellite Systems: GPS, GLONASS, Galileo and More*. Wien: Springer-Verlag Wien. 2008. 517 p.

[3] S. Bassiri, G. A. Hajj . Higher-Order Ionospheric Effects on the GPS Observable and Means of Modeling Them. *Advances in the Astronautical Sciences*, 1993. 82(2): pp. 1-14.

[4] EU Satellite Navigation Programme Management. EGNOS - Safety of Life Service Definition Document Luxembourg: European Commision. 2013. 50 p.

[5] N. Jakowski, C. Mayer, M. M. Hoque and V. Wilken . Total electron content models and their use in ionosphere monitoring. *Radio Science*, 2011. 46(6). doi: 10.1029/2010RS004620

[6] N. Jakowski, M. M. Hoque, and C. Mayer. A new global TEC model for estimating transionospheric radio wave propagation errors. *Journal of Geodesy*, 2007. 81(9): pp. 966-974.

[7] S. M. Radicella, B. Nava, and P. Coisson. Ionospheric models for GNSS single frequency range delay corrections. *Fisica de la Tierra*, 2008. 20: pp. 27-39.

[8] A. Angrisano, S. Gaglione, C. Gioia, M. Massaro, U. Robustelli, and R. Santamaria. Ionospheric models comparison for single-frequency GNSS positioning, in:*European Navigation Conference 2011*. 2011. 92-106.

[9] A. M. A. Farah. Comparison Of GPS/Galileo Single Frequency Ionospheric Models With Vertical Tec Maps. *Artificial Satellites*, 2008. 43(2): pp. 75-90. doi: 10.2478/v10018-009-0008-5

[10] B. Nava, S. M. Radicella, R. Leitinger, and P. Coïsson. Use of total electron content data to analyze ionosphere electron density gradients. *Advances in Space Research*, 2007. 39(8): pp. 1292-1297. doi: 10.1016/j.asr.2007.01.041

[11] J. K. Hargreaves. *The solar-terrestrial environment*. 2nd ed. Cambridge: Cambridge University Press. 1992. 420 p.

[12] Z. Deng, S. Schön, H. Zhang, M. Bender, and J. Wickert. Medium-scale traveling ionospheric disturbances (MSTID) modeling using a dense German GPS network. *Advances in Space Research*, 2013. 51(6): pp. 1001-1007. doi: 10.1016/j.asr.2012.07.022

[13] Lancaster University - Departement of Physics. The Ionosphere: an Introduction [Internet]. Available from: http://spears.lancs.ac.uk/ionosphere_intro/ [Accessed: 13.1.2014]

[14] M. Hernández-Pajares, J. M. Juan, and J. Sanz. Precise Ionospheric Determination and its Application to Real-Time GPS Ambiguity Resolution, in:*Proceedings of Institute of Navigation ION-GPS*. Nashville: 1989.

[15] M. M. Hoque and N. Jakowski. Higher order ionospheric propagation effects on GPS radio occultation signals. *Advances in Space Research*, 2010. 46(2): pp. 162-173. doi: 10.1016/j.asr.2010.02.013

[16] J. A. Klobuchar. Ionospheric Time-Delay Algorithm for Single- Frequency GPS Users. *IEEE Transactions on Antennas and propagation*, 1987. AES-23(3): pp. 325-331.

[17] B. Zolesi and L. R. Cander. *Ionospheric Prediction and Forecasting*. Berlin: Springer Berlin Heidelberg. 2014. 240 p. doi: 10.1007/978-3-642-38430-1

[18] D. Bilitza and B. W. Reinisch. International Reference Ionosphere 2007: Improvements and new parameters. *Advances in Space Research*, 2008. 42(4): pp. 599-609. doi: 10.1016/j.asr.2007.07.048

[19] A. Aragón-Ángel, R. Orús, M. Amarillo, M. Hernández-Pajares, J. Juan, and J. Sanz. Preliminary NeQuick assessment for future single frequency users of GALILEO, in: *Proceedings of the 6th Geomatic Week*, Barcelona: 2005.

[20] B. Nava, P. Coïsson, and S. M. Radicella. A new version of the NeQuick ionosphere electron density model. *Journal of Atmospheric and Solar-Terrestrial Physics*, 2008. 70(15): pp. 1856-1862. doi: 10.1016/j.jastp.2008.01.015

[21] R. Dach, E. Brockmann, S. Schaer, G. Beutler, M. Meindl, L. Prange et al.. GNSS processing at CODE: status report. *Journal of Geodesy*, 2009. 83(3-4): pp. 353-365. doi: 10.1007/s00190-008-0281-2

[22] F. Clette and L. Lefèvre. Are the sunspots really vanishing?. *Journal of Space Weather and Space Climate*, 2012. 2: A06. doi: 10.1051/swsc/2012007

Comparison between the NeQuick Model and VTEC Estimation by GPS Measurements over Egypt

A. M. Mahrous, O. A. AbuElezz, A. M. Abdallah and
R. Fleury

Additional information is available at the end of the chapter

http://dx.doi.org/10.5772/58773

1. Introduction

The most important measured feature in the ionosphere is the Total Electron Content (TEC) which is significant for the operation of the ground and space-based systems involving radio wave signal propagation. At the middle and lower ionosphere, the electron density exhibits a strong seasonal variation due to the change in the solar zenith angle and the solar radiation flux through the whole year. At the upper ionosphere and the F2 layer, the electron density is mostly affected by the plasma transport process, diffusion, electric fields and neutral wind motions. The most important seasonal feature is that NmF2 in winter is greater than NmF2 in summer. This phenomenon is called the seasonal anomaly.

This study uses the TEC-data obtained from two dual-frequency GPS receivers at Helwan and Alexandria, in Egypt. The receiver type, geographic and magnetic coordinates of these stations are shown in Table 1. Helwan station belongs to the Scintillation Network and Decision Aid (SCINDA) system which is a network of ground-based receivers that monitor the ionosphere at UHF and L-band [1]. The receiver tracks the constellation of visible GPS satellites but with a minimum 20° elevation cut off angle in order to minimize the multipath effect. For ALEX2 station, it is located at Centre d'Etudes Alexandrines and provides GPS observations with 30 seconds.

The NeQuick [2] is an ionospheric electron density model developed at the Aeronomy and Radio propagation Laboratory of The Abdus Salam International Centre for Theoretical Physics (ICTP), Trieste, Italy, and at the Institute for Geophysics, Astrophysics and Meteorology (IGAM) of the University of Graz, Austria. It is based on the original profiler proposed by

Di Giovanni and Radicella, 1990 [3]. It allows calculating the electron concentration at any given location in the ionosphere and thus the Total Electron Content (TEC) along any ground-to-satellite ray-path by means of numerical integration. The basic inputs are: position, time and solar flux (or sunspot number) and the output is the electron concentration at the given location in space and time.

The NeQuick model divides the ionosphere into two regions [4]: the bottomside, up to the F 2-layer peak, consists of a sum of five semi-Epstein layers [5] and the topside is described by means of an only sixth semi-Epstein layer with a height-dependent thickness parameter.

In this paper, we present a preliminary comparison between GPS-TEC measurements and the NeQuick modelling results over Egypt. Using a combination of the above datasets together with NeQuick calculations, we conduct a statistical annual analysis about the ionospheric behaviors during the enhancing phase of the current solar cycle 24, showing the average behavior and solar activity dependence of GPS and NeQuick-derived TEC.

Observatory station	**Symbol**	**Geographic coordinates**		**Geomagnetic coordinates**		**Receiver type**
Helwan	HELW	29.86 °N	31.32 °E	26.91 °N	108.72 °E	GSV 4004B
Alexandria	ALEX2	31.19 °N	29.91 °E	28.46 °N	107.75 °E	LEICA GRX1200GGPRO

Table 1. A list of the ground-based GPS sites used in this study.

2. Analytical Formulation

According to the theory of radio wave propagation in ionosphere, the ionospheric delay (Δtion) is proportional to the Total Electron Content (TEC) along the signal path and inversely to the squared frequency (*f*) used [6].

$$\Delta t_{ion} = \frac{40.3}{f^{2}} TEC \tag{1}$$

Each of the 31 operational GPS satellites is broadcasting information on two frequency carrier signals L1=1.57542 GHz and L2=1.2276 GHz. Due to the dispersive nature of the ionosphere, the two radio signals are delayed while their phases are advanced. The receivers provide two different range measurements (known as Pseudorange, P1, P2), and two different phase measurements (φ1, φ1) corresponding to the two signals. The Differential Pseudorange (DPR) and the Differential Carrier Phase (DCP) are given (in TECU) as follows;

$$\mathrm{DPR} = \mathrm{A}\ \left(\mathrm{P2\text{-}P1}\right) \tag{2}$$

$$\mathrm{DCP} = \mathrm{B}\ \left[\varphi 1\ -\ \left(f1 / f2\right)\ \varphi 1\right] \tag{3}$$

The constants A and B have been determined such that the computed TEC has units of TECU (1 TECU=1016 el/m2) and are given by:

$$\mathrm{A} = 2.854\ \mathrm{TECU} / \mathrm{ns} \tag{4}$$

$$\mathrm{B} = 1.812\ \mathrm{TECU} / \mathrm{L1\ cycle} \tag{5}$$

By combining use of pseudorange and carrier phase, a higher precision of TEC estimation can be implemented.

$$\mathrm{TEC_R} = \mathrm{DCP} + < \mathrm{DPR\ \text{-}\ DCP} > \mathrm{ARC} \tag{6}$$

The notation < >ARC in eq. (6) indicates an average taken over a phase connected arc (between successive cycle slips). The relative total electron content ($\mathrm{TEC_R}$) provides an absolute estimate of total electron content prior to "calibration" by subtraction of the receiver and satellite differential biases.

$$\mathrm{TEC} = \mathrm{TEC_R} - \mathrm{A}\ \left(\ \mathrm{BR} - \mathrm{BS}\ \right) \tag{7}$$

where BR is the receiver differential code bias and BS is the satellite differential code bias. We use estimating for the satellite biases provided by the Center for Orbit Determination in Europe (CODE). These biases are available by FTP download as 30 days average with the mean satellite differential biases removed [8]. For ALEX2 station, the receiver bias contains a contribution from the satellite biases, but this is of no consequence in the calibration since both contributions are removed in the end. Another method for estimating the receiver bias is used at HELW station. The inter-frequency bias associated with a particular receiver is estimated late at night (between 03:00 and 06:00 LT) when the ionosphere is minimally structured, using an iterative approach that minimizes the variance of verticalized TEC measured along the different satellite links. The nightly estimated receiver bias is shown to be insensitive to the assumed centroid height used in the single-layer approximation of the ionosphere. A 14 day running average of the bias is used to minimize the effect of this variability on the calibrated TEC [6].

The verticalized TEC is estimated as follows:

$$VTEC = [\mathrm{TECR}\ -\ \mathrm{A}\ (\ \mathrm{BR}\ -\ \mathrm{BS}\ )] / \mathrm{M}(h_{pp},\ \varepsilon) \tag{8}$$

where $\mathrm{M}(h_{pp},\ \varepsilon)$ is the single layer mapping function of the ionosphere, defined as

$$\mathrm{M}(h_{pp},\ \varepsilon) = \sec\ \left\{\sin^{-1}\left[R_E \cos\varepsilon / \left(R_E + h_{pp}\right)\right]\right\} \tag{9}$$

where R_E is the Earth radius, ε is the GPS satellite elevation angle and $h_{pp}$is the height of ionospheric piercing point. This height may be determined using an ionospheric model, or held fixed at a value representative of typical conditions. In this work 350 Km has been used.

NeQuick calculates the ionospheric electron density profile by relying on three anchor points: E, F1 and F2 which represents the peaks of the different layers of the ionosphere. The electron density at any location is computed based on the characteristic parameters (peak electron density, peak height) of these anchor points. To describe the electron density of the ionosphere above 90 km and up to the peak of the F2 layer, the NeQuick uses a modified DGR (Di Giovanni-Radicella) profile formulation which includes five semi-Epstein layers [5] with modelled thickness parameters (B) [4]. Three profile anchor points are used; namely the E layer peak, the F1 peak and the F2 peak that are modelled in terms of the ionosonde parameters foE, foF1, foF2 and M(3000)F2. The NeQuick model computes the electron density by one to three Epstein layers. The shape of an Epstein layer is given by the following function [7]:

$$N_{\mathrm{Epstein}}(h,\ h_{\max},\ N_{\max},\ B) = \frac{4\mathrm{Nmax}}{\left(1 + \exp\left(\frac{h\ -\ \mathrm{hmax}}{B}\right)\right)^2} \exp\left(\frac{h\ -\ \mathrm{hmax}}{B}\right) \tag{10}$$

where Nmax is the layer peak electron density, hmax is the layer peak height and B is the layer thickness parameter.

In the median GPS calculations, the geomagnetic Kp and Ap indices were used in-order to eliminate the geomagnetic active days plus one day after and before. In the present study we run the model using the monthly smoothed sunspot number R12 for each hour for the coordinates of HELW and ALX2 stations. We therefore obtain a simulated VTEC values which are compared to the corresponding derived median VTEC-GPS measurements.

3. Results and discussion

A monthly plots and annual maps for VTEC were created for both GPS-receiver stations. These measurements were compared with the simulated results from NeQuick model to test the validation through several seasons (table 2). The GPS-VTEC values are taken each hour and the median for each month was founded. All the measurements and calculations were taken during the enhancing phase of the current solar cycle along 201, 2011, 2013 and 2014 years.

Season	Months
Winter	Dec ,Jan, and Feb.
Vernal Equinox	March, April, and May.
Summer	June, Jul, and Aug.
Autumnal Equinox	Oct., Nov. and Dec

Table 2. Seasonal classifications

The following figures 1, 3, 5 and 7 displays the monthly variations of the measured VTEC (continuous red line) and simulated (dashed blue line) data for HELW and ALEX2 stations during the years 2010, 2011, 2012 and 2013, respectively. Figures 2, 4, 6 and 8 shows a contour maps for the VTEC derived from GPS-RINEX files and NeQuick modeling at HELW and ALEX2 stations during the years 2010, 2011, 2012 and 2013, respectively.

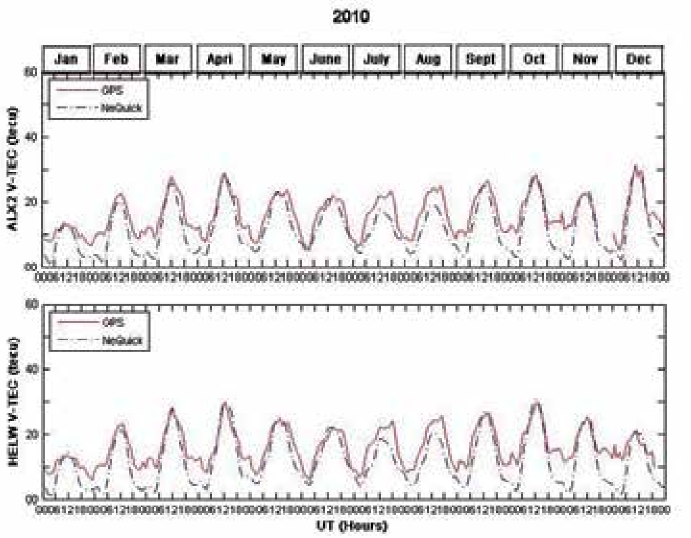

Figure 1. The monthly variations of the measured GPS-VTEC measured-(continuous red line) and the NeQuick simulated ones (dashed blue line) data taken from ALEX2 and HELW stations during the year 2010.

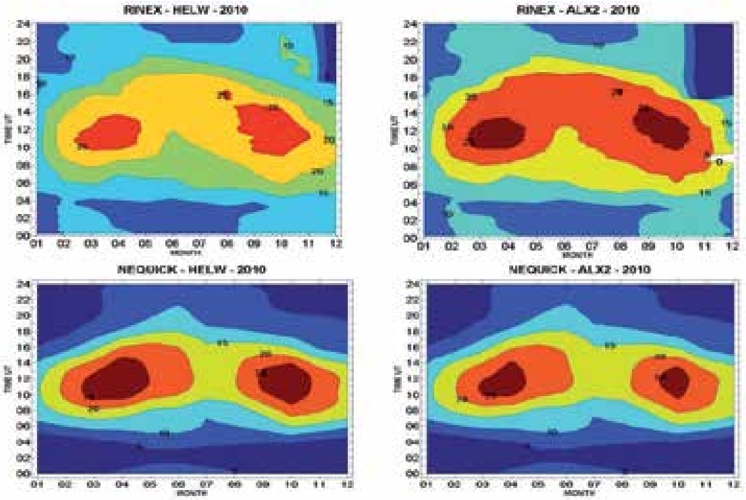

Figure 2. Contour map of VTEC measured and simulated data during the year 2010 at HELW and ALEX2 stations.

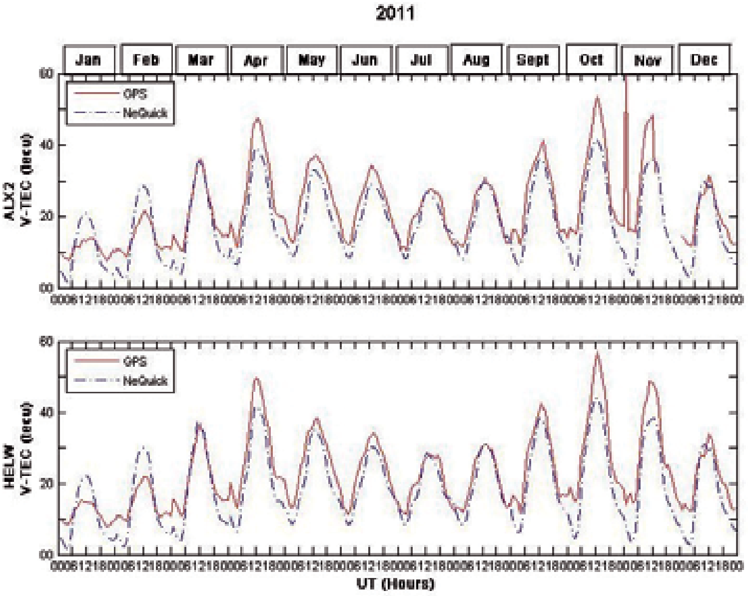

Figure 3. The monthly variations of the measured GPS-VTEC measured-(continuous red line) and the NeQuick simulated ones (dashed blue line) data taken from ALEX2 and HELW stations during the year 2011.

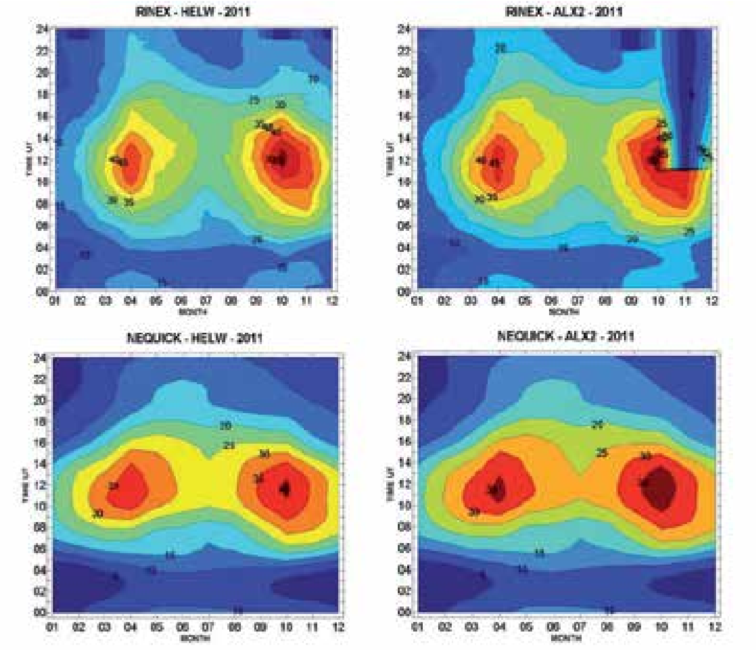

Figure 4. Contour map of VTEC measured and simulated data during the year 2011 at HELW and ALEX2 stations.

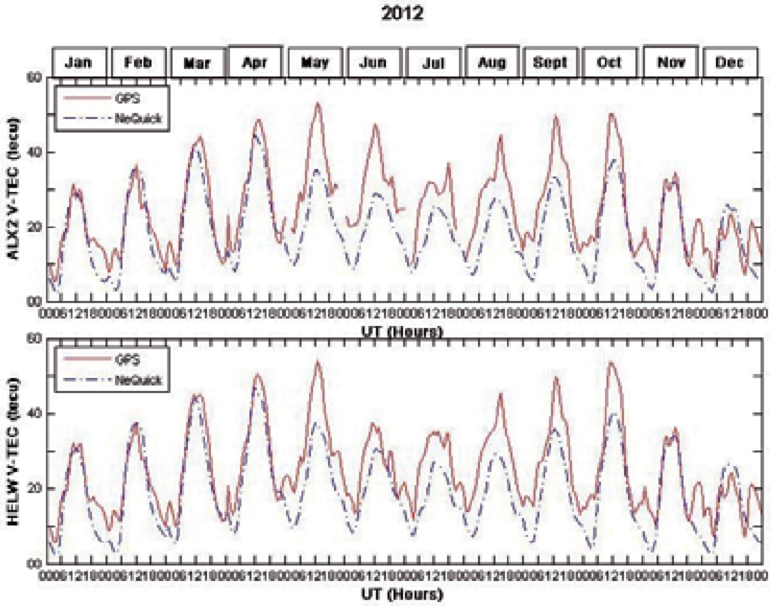

Figure 5. The monthly variations of the measured GPS-VTEC measured-(continuous red line) and the NeQuick simulated ones (dashed blue line) data taken from ALEX2 and HELW stations during the year 2012.

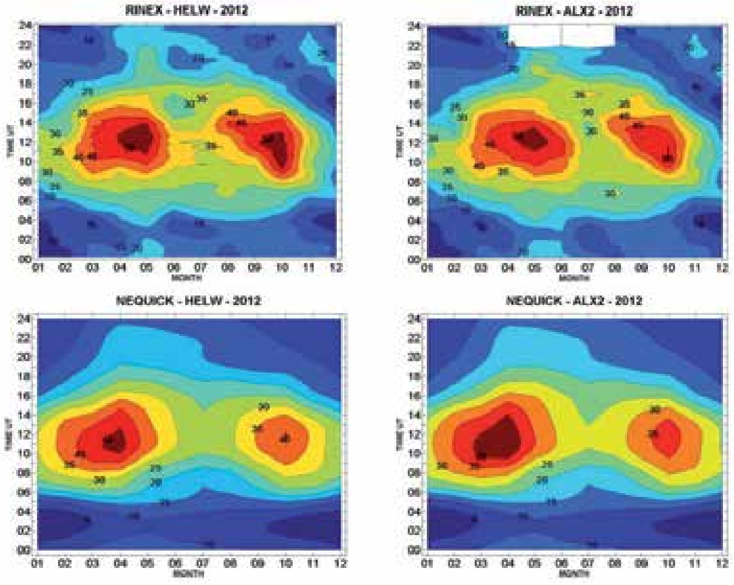

Figure 6. Contour map of VTEC measured and simulated data during the year 2012 at HELW and ALEX2 stations.

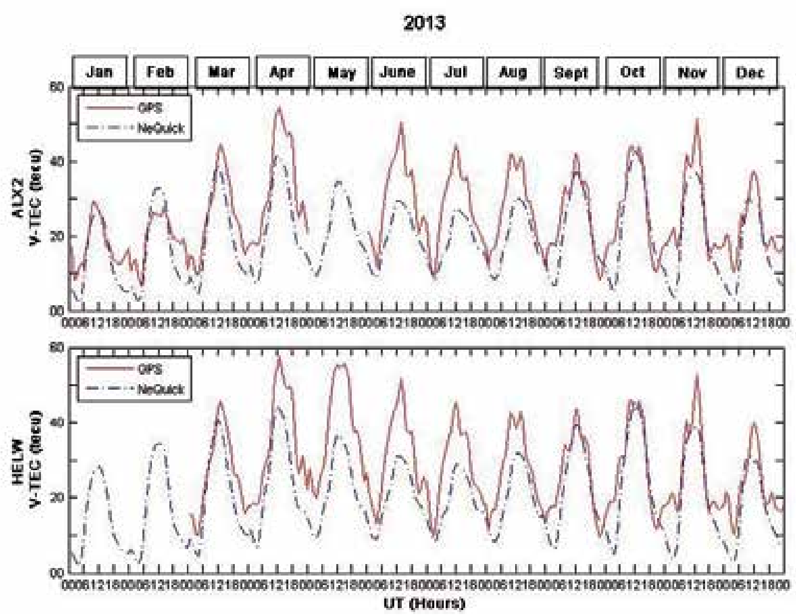

Figure 7. The monthly variations of the measured GPS-VTEC measured-(continuous red line) and the NeQuick simulated ones (dashed blue line) data taken from ALEX2 and HELW stations during the year 2013.

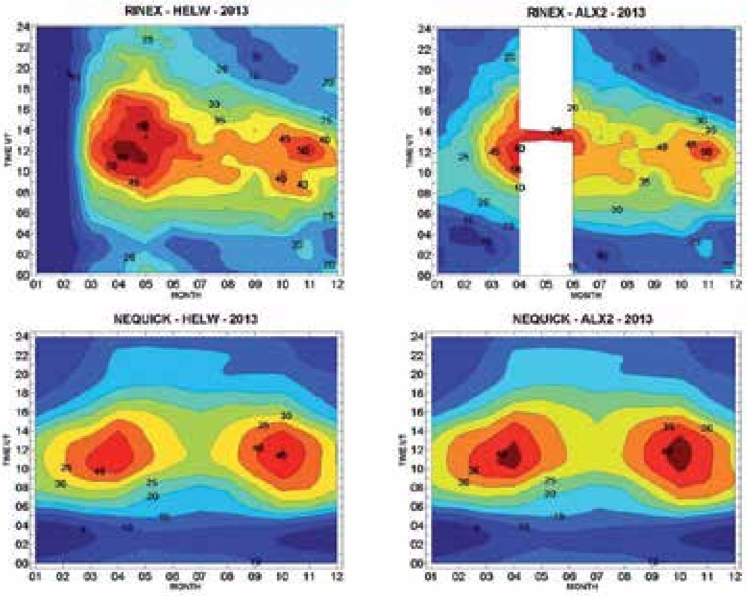

Figure 8. Contour map of VTEC measured and simulated data during the year 2013 at HELW and ALEX2 stations.

By comparing the experimental results derived from HELW and ALEX2 stations, there is harmony between their deviation values. This can be attributed to the small difference in latitude and practically at the same local time.

However, the experimental VTEC values at HELW may experience a small increasing than ALEX2. This is because the geomagnetic latitudes at HELW may be considered near to the northern crest of the equatorial anomaly. From the comparison figures, both the measured GPS-VTEC values and the simulated NeQuick ones show two daytime peaks appear mainly at the beginning of the two Equinox seasons. Tracking the difference between the measured and simulated VTEC through the monthly plots and the contour maps, an obvious increasing in the deviation appears as moving toward the maximum of the solar cycle.

The TEC values during the solar minimum year, 2010, show the best matching between the experimental and simulated results (Fig.1). The contour maps in Fig. 2 also confirm the above results as the values of the two equinox peaks are comparable. Fig. 3 shows the TEC monthly plots for 2011 which is higher than that in the previous year. A weighted difference appears between the measured and simulated TEC values at HELW and ALEX2, especially at the equinox months. The corresponding contour maps in Fig. 4 shows that the difference between the measured and simulates VTEC rises as moving to higher levels in the solar cycle. In 2012 (Fig. 5), the VTEC-GPS data is weightily overshooting the NeQuick simulated results at the whole of day in the summer and autumn with an average deviation of about 10 TECU. The measured GPS-TEC data shows 50 TECU peak at both vernal and autumn equinoxes at the noontime (Fig. 6). The NeQuick simulated results shows also TEC peaks but lower in value at the equinox and autumn. Fig. 7 displays the monthly variations of the GPS-VTEC which is almost higher than the simulated NeQuick results during the winter daytime. The higher deviation at the summer is greater than that in the previous years. Also, the peaks appeared in the NeQuick simulated results (Fig. 8) show high values in the vernal equinox and autumn respectively during the daytime at HELW and ALEX2 stations. These values being less than the GPS measured ones.

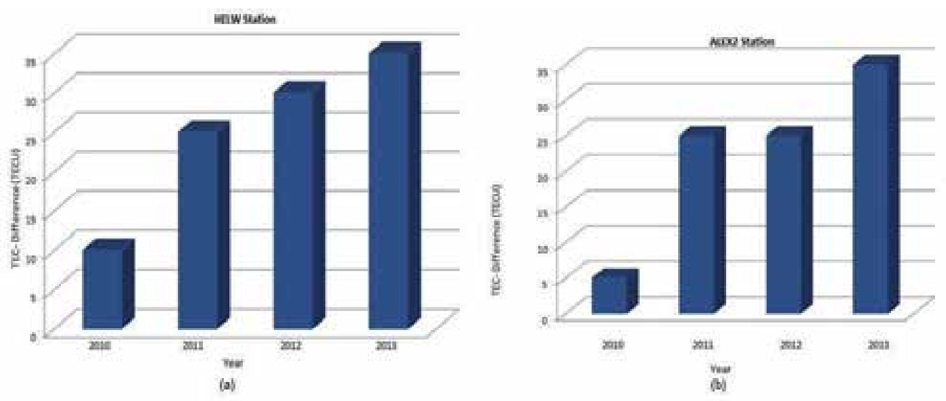

Figure 9. Average difference in TEC values between the GPS-measured and NeQuick-simulated electron density from 2010 to 2013 at (a) HELW and (b) ALEX2 stations.

There is always a difference between the experimental VTEC measurements and the simulated NeQuick ones. This difference being minimum during low solar activity, 2010, and then begin to ascending increase in a convenient way with the enhanced solar activity (Figure 9).

4. Conclusion

This paper provides a method to investigate the monthly/annual TEC variations in the low-mid latitude ionosphere and explore the sensitivity of NeQuick modeling TEC during solar activity variation. The NeQuick results show a good representation during the daytime at low solar activity (2010) in contrary with the nighttime. The observed behaviour of the ionospheric TEC manifest that the annual TEC contour maps show a remarkable seasonal variation. The TEC values on both GPS-receivers yield their maxima during the vernal and autumnal months. The TEC seasonal changes results from changes in the ratio of the concentration of atomic oxygen and molecular nitrogen (O/N2) in the F-region. In the equinoctial months, solar radiation is absorbed mainly by atomic oxygen. This is the reason for high values of TEC in the equinoxes [9]. The low values of TEC are observed in winter whereas high values are observed in equinox and summer.

It can be seen that both the two GPS observations yield similar tendencies in both TEC values and occurrence time. However, there is still a quite difference in TEC values at the two stations. This may be attributed to the different observing instruments employed.

The TEC behavior is practically the same at the two GPS stations due to the small difference in latitude between the two stations. But, the difference between the experimental and modeled values at HELW station shows higher values than the difference at ALEX2. Also, the maximum variation appears in the equinox and the minimum occurs in the summer.

In general, an obvious increasing difference between the experimental and modeled TEC values was appeared during the enhancing phase of the solar cycle which has a notable effect on the results.

Acknowledgements

The authors like to thank TRANSMIT (TRAINING RESEARCH AND APPLICATIONS NETWORK TO SUPPORT THE MITIGATION OF IONOSPHERIC THREATS) project,www.transmit-ionosphere.net, for allowing the opportunity to present this work at 3^{ed} TRANSMIT Workshop 2014, organised by the Politecnico di Torino, Torino, Italy.

http://dx.doi.org/10.5772/58773

Author details

A. M. Mahrous[1], O. A. AbuElezz[1], A. M. Abdallah[1] and R. Fleury[2]

1 Space Weather and Monitoring Centre, Faculty of Science, Helwan University, Cairo, Egypt

2 Ecole Nationale Suptrieure des TClCcommunications de Bretagne, Brest, France

References

[1] K. Groves, S. Basu, E. Weber, M. Smitham, H. Kuenzler, C. Valladares, R. Sheehan, E. MacKenzie, J. Secan, P. Ning, W. McNeil, D. Moonan, and M. Kendra, Equatorial scintillation and systems support, Radio Sci. , 32, 2047, 1997.

[2] R. Leitinger, B. Nava, G. Hochegger, S. M. Radicella,. Ionospheric profiles using data grids. Physics and Chemistry of the Earth (C) 26 (5), 293–301, 2001.

[3] G. Di Giovanni and S. M. Radicella, An analytical model of the electron density pro_le in the ionosphere. Advances in Space Research. 10(11), pp. 27-30, 1990.

[4] B. Nava, P. Coïsson and S. M. Radicella, A new version of the NeQuickionosphere electron density model, Journal of Atmospheric and Solar-Terrestrial Physics, Volume70, Issue 15, December 2008, p. 1856-1862, 2008.

[5] K. Rawer, Replacement of the present sub-peak plasma density profile by a unique expression. Advances in Space Research 2 (10), 183–190, 1982.

[6] C. S. Carrano, and K. Groves, The GPS Segment of the AFRL-SCINDA Global Network and the Challenges of Real-Time TEC Estimation in the Equatorial Ionosphere, Proceedings of the 2006 National Technical Meeting of The Institute of Navigation, Monterey, CA, January 2006, pp. 1036-1047, 2006.

[7] S. M. Radicella, M. L. Zhang, The improved DGR analytical model of electron density height profile and total electron content in the ionosphere. Ann. Geofis, p. 35-41, 1995.

[8] S. Schaer and W. Gurtner, IONEX: The ionosphere map exchange format version 1. Proceedings of the IGS AC Workshop, IGS, Darmstadt, Germany, 1998.

[9] H. Ishbeth and C S G K. Setty, The F-layer at sunrise, J Atmos Terr Phys (UK), 20 pp 263-276, 1961.

Multiresolution Tomography of Ionospheric Electron Density

T. Panicciari, N.D. Smith, F. Da Dalt, C.N. Mitchell and
G.S. Bust

Additional information is available at the end of the chapter

http://dx.doi.org/10.5772/58772

1. Introduction

The ionosphere is an ionized medium which affects the electromagnetic signal that travels through it. The state of the ionosphere is studied in terms of Total Electron Content (TEC). This is a measurable observation, that in our case, is obtained from an estimation of the delay of the signal transmitted from a satellite and received at a ground station [1,2]. Computerized Ionospheric Tomography (CIT) uses a collection of observations to estimate the state of the ionosphere. CIT is also denoted as an inverse problem.

A 2D imaging of the ionosphere based on medical imaging was formerly proposed by Austen et al. [3], where a satellite in polar-orbit was used to collect TEC observations from a chain of ground receivers. There are substantial differences between medical and ionospheric scenarios mainly due to the geometry of the problem. CIT has, in fact, limitations such as limited angle observations and uneven/sparse distribution of the ground stations [4, 5] that make the solution unstable and difficult to solve. However, the capability of the method was demonstrated by Mitchell et al. [6] where, along a quasi-2D plane, features in the electron density were revealed at mid and auroral latitudes. Other research groups have successfully developed their CIT algorithms which are reviewed in Bust and Mitchell [7].

Geometric limitations cause the reconstruction to be underdetermined, especially where data are not available (e.g. in the oceans gaps). In general, a proper regularization is needed to compensate for where no data is available in order to reduce artefacts and noise within the results. Most of the algorithms are based on Tikhonov regularization [8], but another recent approach, new for CIT, is based on sparse regularization [9]. An implementation of this is given by the Fast Iterative Shrinkage-Thresholding Algorithm (FISTA) [10, 11]. A description of the sparse regularization for CIT will be described in a forthcoming paper. This technique is used to overcome the limitation in the horizontal representation of ionospheric structures due to the uneven and sparse distribution of the ground receivers using simulated data.

An experiment is demonstrated here, using real data, where the advantages of sparse regularization using wavelets are illustrated over a standard implementation using spherical harmonics. TRANSIT data from the data set in [12] is also used. This data set consists of three Coherent Ionospheric Doppler Receivers (CIDRs), developed at Applied Research Laboratories at the University of Texas (Austin) and capable of observing the signal from TRANSIT system. Some results are presented comparing the Incoherent Scatter Radar (ISR) located in Sondrestrom (Greenland) and the CHAMP satellite. CHAMP data are from the Digital Ion Drift-Meter (DIDM) instrument provided by Air Force Research Laboratory (AFRL, Hanscom).

Section II illustrates the problem and solutions using two different regularization techniques. The data used for the reconstruction and comparison are described in Section III. Results and conclusions are presented in Section IV and Section V.

2. Method

TEC observations z are collected from ground receivers. They are in the form of Slant Total Electron Content (STEC) and are described according to the following equation (forward problem)

$$z=An+c \tag{1}$$

where$z$ is the vector containing the uncalibrated observations of STEC, $\mathbf{A}$ is the projection matrix of geometry that maps the electron density n into the observations z. The vector n is described through the matrix of basis functions $\mathbf{K}$ and basis function coefficients x

$$n=Kx \tag{2}$$

The matrix $\mathbf{K}$ defines the basis functions that we need in order to define the vertical and horizontal variation of the electron content. For the purpose of this paper we will focus on the horizontal basis functions, while vertical basis functions are described by Empirical Orthonormal Functions (EOFs) [13, 14].

The c term of (1) takes into account the fact that z is uncalibrated. Therefore the observations are affected by some biases c. They are solved together with z, to find the solution of the inverse problem of (1).

We solved the inverse problem of (1) by using two different regularizations:

- Tikhonov regularization. In this case, all the coefficients are used to estimate the state of the ionosphere. The method seeks to minimize the energy of the coefficients in some sense. Spherical harmonic basis functions are used in this case.
- Sparse regularization. The solution is solved with the Fast Iterative Soft-Thresholding Algorithm (FISTA) [10, 11]. It is particularly tailored for wavelet basis functions due to their ability to compact the information. The method seeks to minimize the number of basis functions needed to represent the structures in the ionosphere fittingly.

Both regularizations can guarantee a unique solution under certain conditions [15].

3. Data

Two different case studies are proposed using as comparison the Incoherent Scatter Radar (ISR) located in Sondrestrom (Greenland) and CHAMP satellite. Those case studies are representative of perturbed (kp=6) and quiet ionosphere (kp=2).

The first case study (kp=6) is based on a chain of TRANSIT receivers across Greenland together with GPS receivers. They recorded data during the day of the 30th September 2000, where data were collected within a time window of 9 minutes, with a sample rate of 30 seconds.

Fig. 1 shows the receivers, TRANSIT (red) and GPS (blue), used for the reconstruction together with the ray coverage. The TRANSIT satellite (ID18362) pass (purple) is also shown. The location of the ISR is illustrated with a black circle, and the scan path is indicated with a black solid line. For the present experiment only two of three TRANSIT receivers were available.

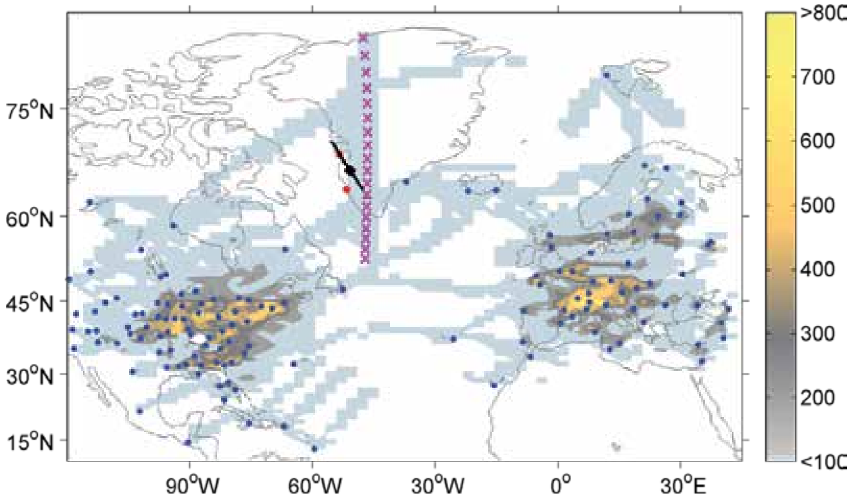

Figure 1. Number of rays and GPS ground stations (blue), TRANSIT ground stations (red), TRANSIT satellite pass (purple) and radar scan path (black).

The second case study (kp=2) used GPS receivers only for the day of 7th October 2002. Data sample rate was 30 seconds within a time window of 9 minutes. Fig. 2 shows the data coverage, GPS receivers (blue) and the southward CHAMP satellite pass (cyan).

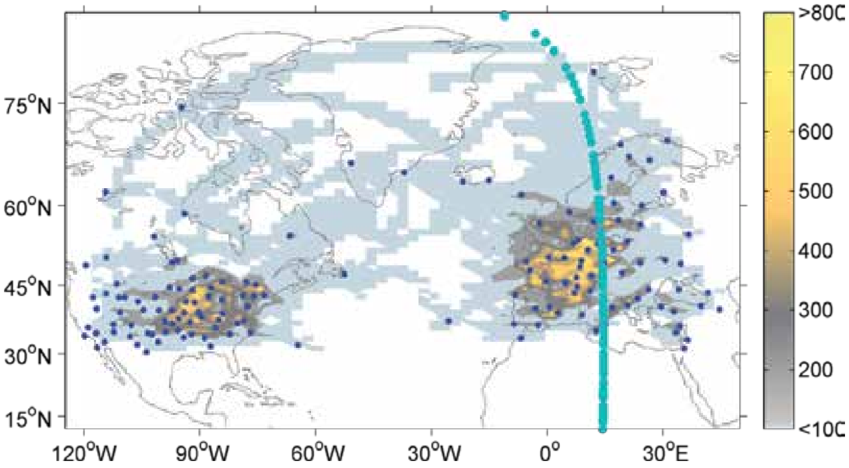

Figure 2. Number of rays and GPS ground stations (blue) and CHAMP satellite pass (cyan).

4. Results

A grid of dimension 64x64x22 voxels was selected in longitude, latitude and altitude. It corresponds to a maximum resolution of about 1x2 degrees in latitude and longitude and 50km in altitude.

EOFs from Chapman profiles [16] were used to constrain the vertical profile to be physically meaningful. In contrast, Discrete Meyer (DM) wavelets and Spherical Harmonic (SH) basis functions were used to describe the horizontal variation of ionospheric structures. We compared the results obtained with discrete Meyer (DH) and Spherical Harmonic (SH) basis functions at two different resolutions (by selecting subsets of horizontal basis functions). An ISR scan was also used as validation.

Fig. 3 shows the reconstruction obtained with SH (left) and DM (right) for two different resolutions. Values are in 1016 electrons/m2.

The low resolution reconstruction is shown in Fig. 3a and 3b for SH and DM, respectively. They both show a reasonable reconstruction with structures that appear smooth and with little detail but DM has some edge effects.

Fig. 3c and 3d show the reconstruction for SH and DM at higher resolution. The number of coefficients is significantly increased and SH needs a stronger regularization. The stronger regularization damps many coefficients down and the reconstruction loses its smoothness

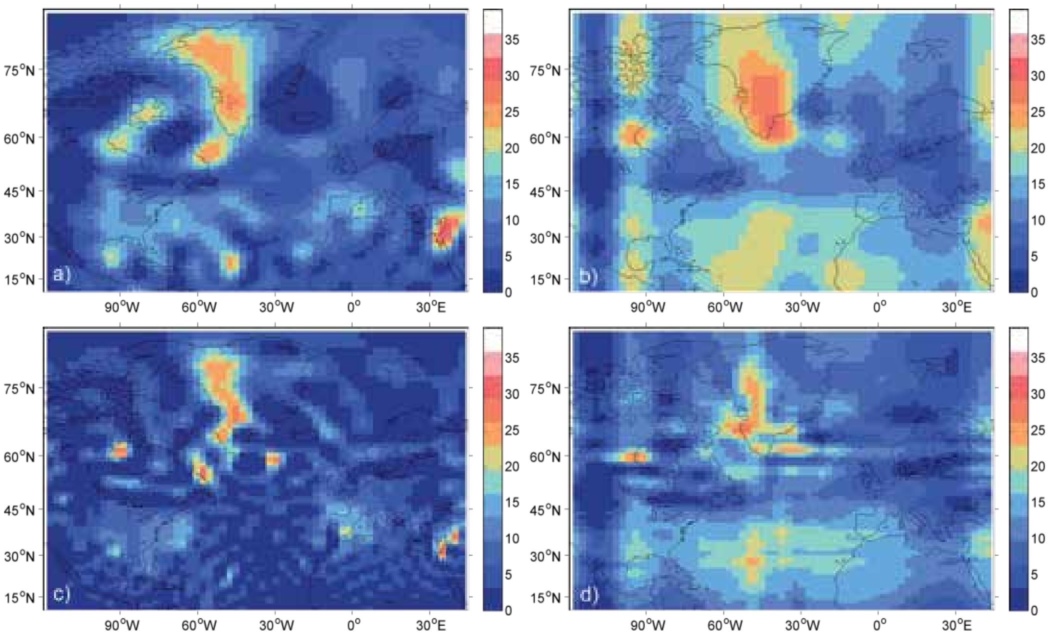

Figure 3. Low resolution reconstruction for: a) spherical harmonics; b) discrete Meyer; and high resolution reconstruction for: c) spherical harmonics; d) discrete Meyer. TEC values are in 10^{16} electrons/m^2.

(Fig. 3c) in comparison to the low resolution one (Fig. 3a). A ring oscillation phenomenon is also present due to the high number of basis functions to be estimated. This does not happen for DM. There are some lengthened structures (Fig. 3d) when using DM (between Greenland and Norway), which are mainly due to the particular data coverage (Fig. 1). Furthermore, DM reconstructs a structure located at 62°N 47°W (South of Greenland, Fig 3d), which is not present when using SH. In general, better performances can be obtained with a higher number of ground stations. The correctness of the results cannot be easily verified using real data due to the limited number of instruments that can be used for validation. The reliability of the methods described here will be illustrated in a forthcoming paper based on simulated data.

The sparse regularization aims to reconstruct the state of the ionosphere with the minimum number of basis functions. This makes the inversion stable, maintaining most of the information that was available at low resolution but better defining the edges of the reconstruction. This can be shown by comparing the reconstruction with the ISR scan that was available during the same time interval.

Fig. 4 shows a southward longitudinal ISR scan starting at 03:21:20UT on 30th September 2000. The scan has a duration of less than 4 minutes and values are shown in 1011 particles/m3. An enhancement can be seen towards the North while a depletion is evident in the South. In particular, a trough is present at the latitude of 64 degree.

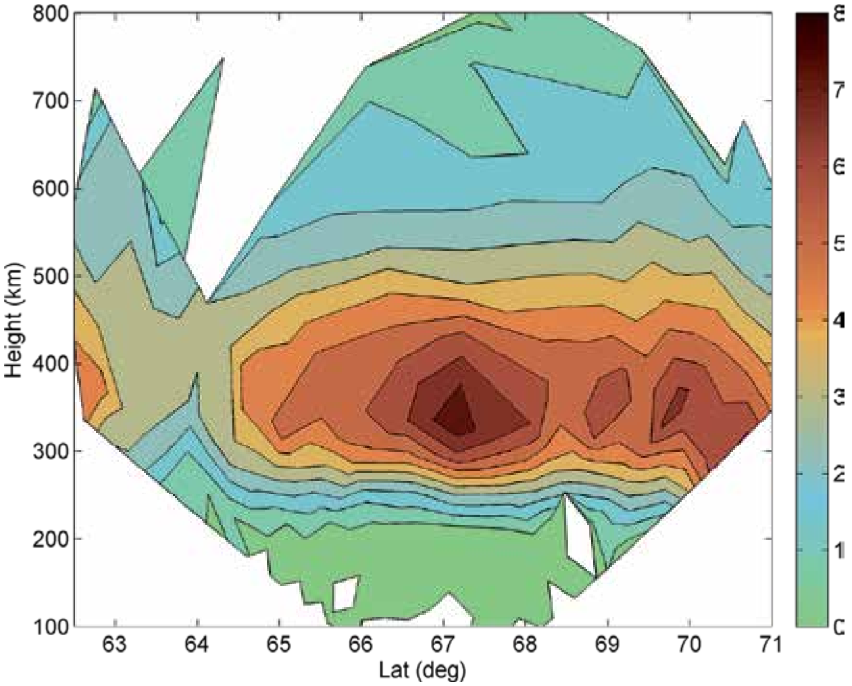

Figure 4. Southward longitudinal Incoherent Scatter (IS) radar scan starting at 03:21:20UT on 30th September 2000. Values of electron density are in 10^{11} particles/m^3.

Fig. 5a-5d show the electron density (10^{11} particles/m^3) of the reconstruction along the radar scan path for SH (left) and DM (right), and for low (top) and high resolution (bottom). The radar scan plane is aligned with the geomagnetic field lines and is tilted by about 27 degrees in the anticlockwise direction with respect to the reconstruction plane. The latter is instead aligned to the geographic coordinate system.

At low resolution SH produces a smooth profile (Fig. 5a), as DM similarly does (Fig. 5b). At higher resolution the depletion starts to be better defined and visible for SH (Fig. 5c). Both SH (Fig. 5c) and DM (Fig. 5d) show the same trough as well as a southward enhancement as indicated in the radar (Fig. 4); although the trough edges are more well-defined for DM (Fig. 5d). This is in agreement with the structure reconstructed in Fig. 3d using DM at 62°N 47°W.

Fig. 6a-b show a horizontal electron density profile from CHAMP (red) and from reconstruction (blue) during the day of the 7th October 2002. The CIT profile was extracted at the CHAMP altitude. A pale yellow background identifies latitudes where there is data coverage and it is over-imposed on a grey background that defines the CHAMP samples that were not in the time window used for the reconstruction. A dark grey is generated when the two backgrounds are overlapping.

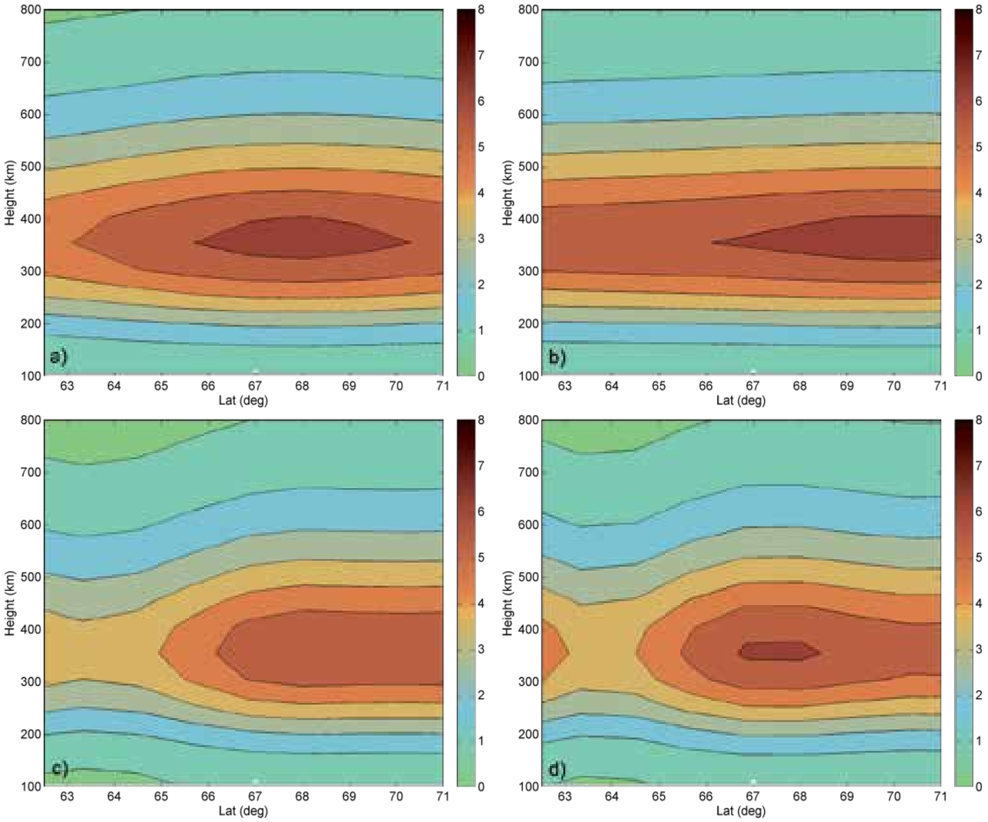

Figure 5. Cross sections from low resolution tomographic reconstructions for: a) spherical harmonics; b) discrete Meyer; and from high resolution tomographic reconstructions for: c) spherical harmonics; d) discrete Meyer. Values of electron density are in 10^{11} particles/m^3.

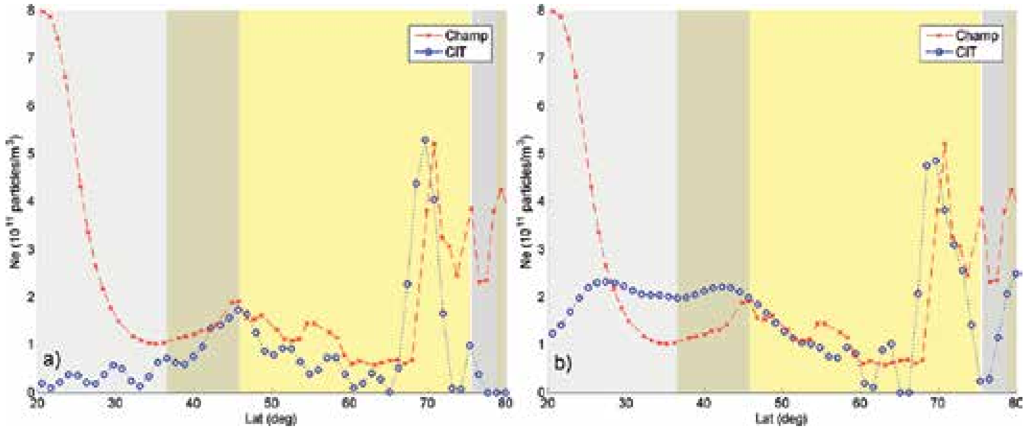

Figure 6. comparison of electron density from CHAMP (red) and CIT (blue) at high resolution using: a)spherical hamonics; b) discrete Meyer.

SH and DM reconstruct well the enhancement at about 70 degrees. It is noticeable the ring oscillation phenomenon for SH (Fig. 6a) while, for DM (Fig. 6b) that phenomenon is not present. DM seems also to estimate better the slope around 50 degrees. It is remarkable the different behaviour where data are not available. SH (Fig. 6a) decreases rapidly towards zero while DM reproduces a smooth enhancement before decreasing to zero. This is mainly due to the contribution of a large scale basis function that is used to represent the smooth part of the ionosphere. In that region the number of rays is small and not enough for resolving smaller features with smaller wavelets. SH (Fig. 6a) shows also the effect of a stronger regularization. The basis function coefficients are damped down and this causes an underestimation of the electron density.

5. Conclusions

Sparse regularization allows minimizing the number of basis functions that are needed for the reconstruction. Therefore, the algorithm estimates only the coefficients of a smaller subset of the entire set of basis functions; which in an underdetermined problem like in the Computerized Ionospheric Tomography (CIT) becomes of particular attractiveness. The reconstructions illustrated demonstrate sparse regularization as a valid alternative to Tikhonov regularization. Furthermore, sparse regularization seemed to preserve the information when the total number of coefficients to estimate increases. The results also show that the structure reconstructed at 62°N 47°W (South of Greenland) with sparse regularization is in good agreement with the radar scan. The same structure is not present with SH. This confirms wavelets and sparse regularization as a promising approach to detect different-scale structures of the ionosphere.

Better wavelet constructions may lead to further improvements in the reconstruction. In addition, the previous knowledge of the scales of structures that we could expect at different locations might likely help in the case of non-uniform or a small number of observations, to produce a smoother ionospheric reconstruction.

Acknowledgements

The authors acknowledge David Cooke (AF Research Lab) for CHAMP data, UNAVCO and IGS for GPS data. TRANSIT data were originally collected as part of a NSF project (ATM# 9813864) and ISR observations were supported by the NSF Cooperative Agreement AGS-0836152.

This research activity was supported by a Marie Curie initial training network (TRANSMIT) within the 7th European Community Framework Programme under Marie Curie Actions.

Author details

T. Panicciari[1], N.D. Smith[1], F. Da Dalt[1], C.N. Mitchell[1] and G.S. Bust[2]

1 Dept. of Electronic and Electrical Engineering, University of Bath, UK

2 Applied Physics Laboratory, Johns Hopkins University, USA

References

[1] Davies K.. *Ionospheric radio*. London: Peter Peregrinus. 1996. 600 p. doi: 10.1049/PBEW031E

[2] Mannucci A.J., Iijima B.A., Lindqwister U.J., Pi X., Sparks L., and Wilson B.D.. GPS and Ionosphere, in:W. Ross Stone (eds.). *Review of Radio Science 1996–1999*. Oxford: Wiley-IEEE Press. 1999. 625-665.

[3] Austen, J. R., Franke, S. J., Liu, C. H., Yeh, K. C. Application of Computerized Tomography Techniques to Ionospheric Research, in:*Proceedings of the Beacon Satellite Symposium 1986*. Finland. University of Oulu. 25-35.

[4] Yeh, K.C., Raymund, T.D.. Limitations of ionospheric imaging by tomography. *Radio Science*, 1991. 26(6): pp. 1361-1380. doi: 10.1029/91RS01873

[5] Na, H., Lee, H.. Analysis of fundamental resolution limit of ionospheric tomography, in:*Acoustics, Speech, and Signal Processing*. 23-26 Mar. San Francisco, CA. IEEE. 1992. 97-100. doi: 10.1109/ICASSP.1992.226267

[6] Mitchell, C.N., Jones, D.G., Kersley, L., Pryse, S. E., Walker, I.K.. Imaging of field-aligned structures in the auroral ionosphere. *Annales geophysicae*, 1995. 13: pp. 1311-1319. doi: 0992-7689

[7] Bust, G. S., Mitchell, C. N.. History, current state, and future directions of ionospheric imaging. *Reviews of Geophysics*, 2008. 46(1)doi: 10.1029/2006RG000212

[8] Tikhonov, A. N., Arsenin, V. Y.. *Solutions of ill-posed problems*. Winston. 1977. 258 p. doi: 0470991240

[9] Donoho, D.L.. For most large underdetermined systems of linear equations the minimal $\ell 1$-norm solution is also the sparsest solution. *Communications on pure and applied mathematics*, 2006. 59(6): pp. 797-826. doi: 10.1002/cpa.20132

[10] Beck, A., Teboulle, M.. A fast iterative shrinkage-thresholding algorithm for linear inverse problems. *SIAM Journal on Imaging Sciences*, 2009. 2(1): pp. 183-202. doi: 10.1137/080716542

[11] Daubechies, I., Defrise, M., De Mol, C.. An iterative thresholding algorithm for linear inverse problems with a sparsity constraint. *Communications on pure and applied mathematics*, 2004. 57(11): pp. 1413-1457. doi: 10.1002/cpa.20042

[12] Watermann, J., Bust, G.S., Thayer, J.P., Neubert, T., Coker, C.. Mapping plasma structures in the high-latitude ionosphere using beacon satellite, incoherent scatter radar and ground-based magnetometer observations. *Annals of Geophysics*, 2002. 45(1): pp. 177-189. doi: 10.4401/ag-3488

[13] Fremouw, E.J., Secan, J.A., Howe, B.M.. Application of stochastic inverse theory to ionospheric tomography. *Radio Sci.*, 1992. 27(5): pp. 721-732. doi: 10.1029/92RS00515

[14] Sutton, E., Na, H.. High resolution ionospheric tomography through orthogonal decomposition, in:*IEEE International Conference on Image Processing*. 13-16 Nov 1994. Austin, TX. Los Alamitos: IEEE Computer Society Press. 1994. 148-152. doi: 10.1109/ICIP.1994.413549

[15] Mallat, S.. *A wavelet tour of signal processing: the sparse way*. 3rd ed. Burlington, MA: Academic press. 2008. 832 p.

[16] Hargreaves, J.K., Gadsden, M.. *The Solar-Terrestrial Environment: An Introduction to Geospace - the Science of the Terrestrial Upper Atmosphere, Ionosphere, and Magnetosphere*. New York: Cambridge University Press. 1995. 284 p. doi: 10.1017/CBO9780511628924

ANIMo — A New Ionospheric Model. Ionospheric Modeling for Ionospheric Imaging and Forecasting Purposes

F. Da Dalt, C. Benton, T. Panicciari, N. D. Smith and
C. N. Mitchell

Additional information is available at the end of the chapter

http://dx.doi.org/10.5772/58771

1. Introduction

Ionospheric tomography is a powerful technique for studying and monitoring the upper atmosphere and its dynamics. This is extremely relevant to attempts made to reduce vulnerabilities of Global Navigation Satellite System (GNSS) signal propagation due to the presence of ionospheric charged particles. The concentration of the latter can be measured by considering time and phase delays of GNSS signals. By integrating the measured density values, it is possible to calculate the Total Electron Content (TEC) along a specific signal path. Ionospheric tomography uses GNSS TEC observations in order to compose three dimensional reconstructions of the ionosphere through an operation called inversion. In contrast to other applications (e.g. medical or industrial), ionospheric tomography cannot rely on a designed scanning instrument. Satellites and receivers do not entirely surround the ionosphere, therefore providing an incomplete scan-geometry. Furthermore, GPS ground-receivers are distributed unevenly on the earth’s surface which translates to poor data coverage, resulting in a lack of necessary information. MIDAS (Multi-Instrument Data Analysis System) [1, 2] is an ionospheric tomography software package developed at the University of Bath by the INVERT group. In order to overcome the limitations due to poor data coverage, MIDAS is assisted by external information. To date, empirical models are utilized to support the inversion in MIDAS algorithms, especially in relation to the missing vertical information. The idea behind this project is to implement a purely physics-based ionospheric model into MIDAS; ANIMo was built for this intent, which may be applied in different modes. ANIMo can simply be used to substitute erroneous reconstructions or to aid the inversion by adding

---

sensible vertical information. Besides, ANIMo, together with TEC observations, is expected to be the background model in a DA scheme within MIDAS. The goal is not only to improve ionospheric tomography reconstructions but also to perform short-term forecasting.

Section 2 illustrates ANIMo features and its anatomy. Sections 3 and 4 are dedicated to ANIMo validation and sensitivity tests and their results respectively. Conclusions are presented in Section 5.

2. ANIMo

2.1. Requirements and assumptions

ANIMo is a physics-based ionospheric model. This characteristic is very important for reaching the aforementioned goals. The advantages of using a first-principle model are various. Firstly, it is preferable to avoid using empirical models in a DA approach, especially when forecasting. Secondly, the usage of a physical model will permit to have more control and awareness on the analysis produced by the DA scheme. This includes, for example, the possibility of simulating specific unsettled conditions and studying their evolution. Further, specific requirements for this model are robustness and stability. These features keep the model reliable also in extreme conditions. In general, the model assumes that the chemical processes of the ion species O^+, NO^+ and O_2^+ and the transportation process of the ambipolar diffusion are sufficient to describe the electron density evolution in mid latitude regions. In order to maintain the mentioned requirements and reach a certain level of accuracy, ANIMo was intentionally developed to avoid complexity by taking into account these principal ionospheric processes.

2.2. Description

ANIMo is a global model – it solves a three dimensional grid of latitude, longitude and altitude, and is mainly used for mid-latitude regions. It solves the continuity equation only for the ion species $O^+$for a given vertical profile:

$$\frac{\partial[O^+]}{\partial t} = Q - L\left([O^+]\right) - \frac{\partial\left([O^+]v\right)}{\partial z} \tag{1}$$

The production rate Q is calculated by considering the geometry of solar radiation and the relative Extreme Ultraviolet spectra provided by the EUVAC model from Richards, Fennelly and Torr [3, 4]. Together with lists of data from Fennelly and Torr [5], EUVAC supplies absorption and ionization cross section values. The chemical rates used for the calculation of the loss term L are provided by the work of Torr and Torr [6]. The latter and the EUVAC model are also used to self-consistently calculate the density values of the minor species $NO^+$and O_2^+. The transportation term, $\partial\left([O^+]v\right)/\partial z$, considers mainly the vertical ambipolar diffusion. A continuous downward flux of particles is included as the topside boundary condition. The value of this flux can vary, but it is generally around 1 x 10^{11} $m^{-2}s^{-1}$. The standard value of the ion-neutral (O^+-O) collision frequency given by Salah [7] is used in the calculation of the vertical diffusion velocity. During day-time the velocity is corrected to provide a day-time maintenance adjustment. The neutral densities are given by the MSIS model [8], in particular, by one of its latest versions NRLMSISE-00 [9]. The ion and electron temperatures are provided by the International Reference Ionosphere (IRI) model [10], whose latest available (IRI 2012) version is also used. The model assumes that the sum of the major ion densities (O^+, NO^+ and O_2^+) is equal to the electron density. Its outcomes are therefore ion and electron densities profiles included between 80 and 600 km altitude.

The closest existing model to ANIMo is the FLIP (Field Line Interhemispheric Plasma) by Richards et al. [11]. The similarity is to be searched mainly in the modelling of the chemical dynamics.

3. Validation

The validity of the model was tested against different instruments and other ionospheric models. In this document four validation tests are presented. For all of them, the simulation was set in order to reproduce the vertical profile above the location of the Millstone Hill Haystack Observatory (Lat. 42° Long. 288°) from an altitude of 80 to 600 km in 10 km steps. This allowed comparison of the model with measurements from the local Incoherent Scatter Radar (ISR) and ionosonde. Furthermore, the location was chosen in the past for the intercomparison of physical models by the Ionospheric-Thermospheric community [12]. A geomagnetic unperturbed period with medium-low solar intensity was chosen for all experiments. Table 1 reports details about the selected case studies.

Case study	Validation test parameters (Input parameters)		
	Dates	**Ap**	**F10.7**
Winter	29-30/12/2011	9 - 7	142.3 - 136.4
Spring	09-11/03/2010	2 - 9 - 10	76.8 - 79.3 - 83.1
Summer	23-25/06/2011	18 - 11 - 6	99.5 - 99.4 - 96.7
Autumn	07-08/09/2010	10 - 11	77.3 - 75.6

Table 1. Details about the presented case studies for the validation test. They correspond, together with the selected location (geographic latitude and longitude), to the used input parameters. ANIMo is able to retrieve Ap and F10.7 parameters automatically.

Figures 1-5 show the evolution of the modelled profiles by ANIMo (blue solid line in Figures 2-5) for a few days, where the outcomes were saved every half-hour. In particular, Figure 1 shows the evolution of the whole electron density profile over the selected time. In Figures 2-5, IRI 2012 (green solid) simulations, Millstone Hill ISR (red solid) and ionosondes (black solid) measurements are also plotted. The latters (Fig. 2-5) show the comparison in terms of electron density at the peak (NmF2) and peak altitude (hmF2). The choice of the comparison criteria was determined by two factors. First, it is vital that the model performs well for the above terms in order to support ionospheric tomography imaging. Secondly, this is good practice in ionospheric models comparison [12]. ANIMo (solid blue) in general behaves well. It is able to reproduce day-night variations, and as illustrated collectively by the graphs, it also senses seasonal ones. The summer and autumn tests (Fig. 4, 5) show that ANIMo slightly underestimates the electron density at the peak height. Regarding the peak altitude, it tends to overestimate during night-time. Both biases can be corrected by modifying top-side boundary conditions and day-time maintenance adjustments.

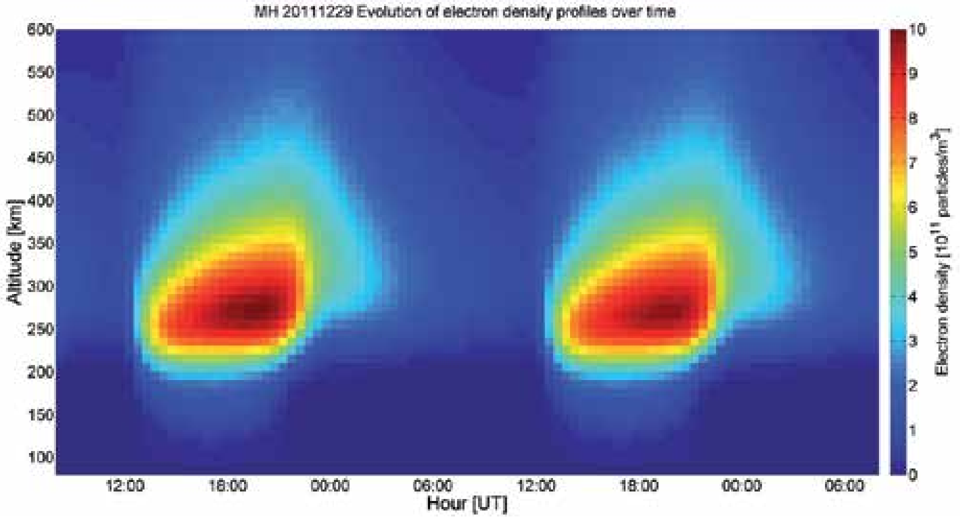

Figure 1. The plot shows the evolution of the electron density profile produced by ANIMo for the winter case.

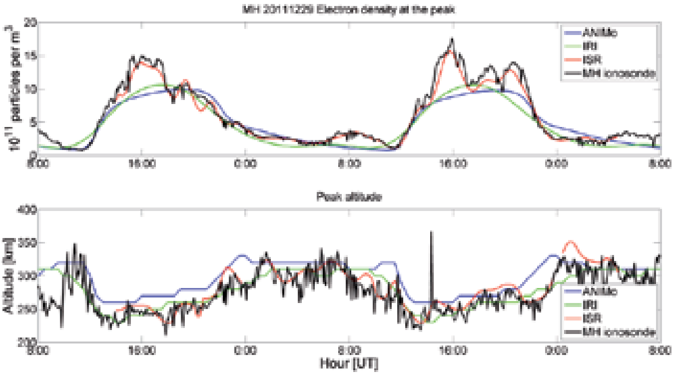

Figure 2. Validity test (winter case). The graphs show, respectively, the comparisons of electron densities at the peak and peak heights produced by ANIMo, modelled by IRI 2012 and measured by Millstone Hill ISR and ionosonde.

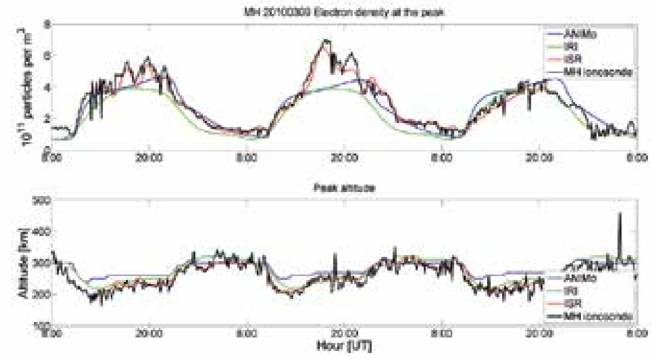

Figure 3. Validity test (spring case). The graphs show, respectively, the comparisons of electron densities at the peak and peak heights produced by ANIMo, modelled by IRI 2012 and measured by Millstone Hill ISR and ionosonde.

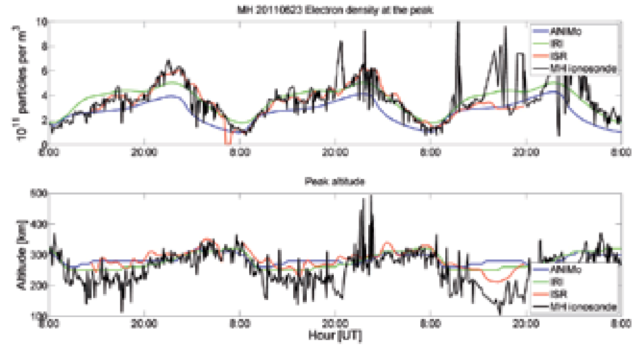

Figure 4. Validity test (summer case). The graphs show, respectively, the comparisons of electron densities at the peak and peak heights produced by ANIMo, modelled by IRI 2012 and measured by Millstone Hill ISR and ionosonde.

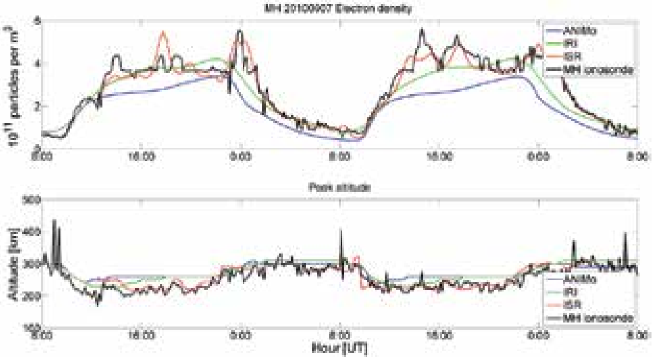

Figure 5. Validity test (autumn case). The graphs show, respectively, the comparisons of electron densities at the peak and peak heights produced by ANIMo, modelled by IRI 2012 and measured by Millstone Hill ISR and ionosonde.

4. Temperature sensitivity

The aim of this sensitivity test was to check the robustness of ANIMo by modifying input arguments and checking their effects on its outcomes. In particular, this paragraph reports a selection from a series of tests conducted by tuning the temperature input parameter. The chosen case study is that of winter, already presented in the validation test. Figure 6 shows the comparison between outcomes obtained by using different temperature input values. As aforementioned, ANIMo normally uses temperature values produced by IRI 2012, the relative outcome of which is reported in the graph with a solid blue line. The model was also fed with temperature measurements from the Millstone Hill ISR (black solid) and artificial profiles defined by keeping the temperature constant in altitude and time at 1000 K (gold dashed), 2000 K (orange dashed) and 3000 K (red dashed). The test demonstrates the importance of ion and electron temperatures as input in modeling the electron density of the ionosphere. Furthermore, it shows that ANIMo is a robust model in terms of temperature modification, where for robustness is intended the ability of coping with large changes of external forcing parameters. IRI and ISR driven outcomes are very similar. Regarding the remaining simulations, increasing the selected input value translates to a gradual alteration of the model results. As expected, the higher the temperature, the smaller the electron density and bigger the peak altitude. This is due to the fact that the temperature affects the recombination rates and diffusion velocities of the model. In particular, if the recombination rate increases there will not only be a general decrease in electron and ion densities but also a lift of the peak altitude that is not replenished enough by the photoionization. In addition to this, the collision frequency is bigger in a hotter environment. This, plus the diminished charged particle density slows down the diffusion that tends to move ions and electrons to lower positions of the profile.

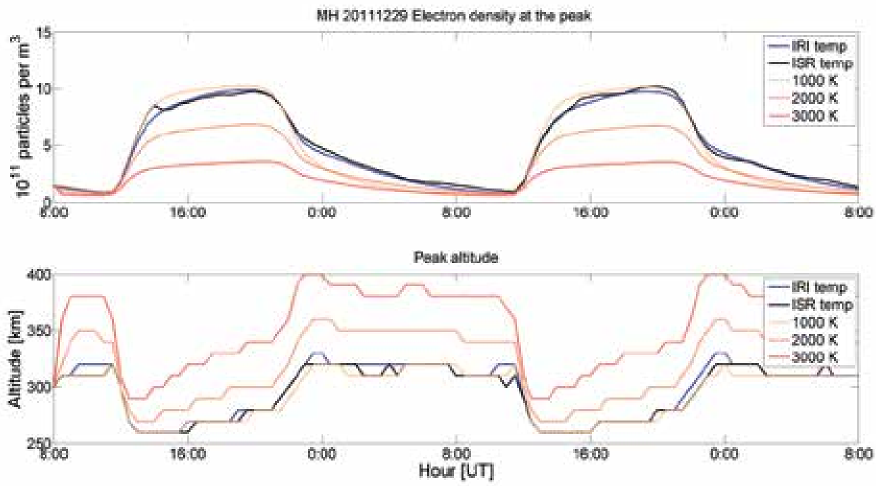

Figure 6. Sensitivity test (winter case). The graphs show, respectively, the comparisons of electron densities at the peak and peak heights produced by modifying ANIMo temperature input parameters.

5. Conclusions

The preliminary results of the validation and sensitivity tests presented in this document are very promising. The validation demonstrated that ANIMo is capable of reproducing different features of the ionosphere in a reasonable manner, considering the physics that had been taken into account. This was confirmed by previous comparisons with the Utah State University Time Dependent Ionospheric Model (USU TDIM) [13]. However, further validation tests and minor adjustments are required. Further, the temperature sensitivity test shows that ANIMo is robust and stable. At this phase of its development, ANIMo is exhibiting the characteristics required for supporting ionospheric tomography imaging. The next step will see the implementation of ANIMo in a DA scheme which will develop MIDAS algorithms into a full physics forecasting system.

Acknowledgements

Special thanks go to:

Jan J. Sojka (Centre for Atmospheric and Space Sciences, Utah State University).

Gary S. Bust (Johns Hopkins University Applied Physics Laboratory).

Anthea Coster (MIT Haystack Observatory).

Chris Budd (Dept. of Mathematical Sciences University of Bath)

Radar observations and analysis at Millstone Hill are supported under Cooperative Agreement with the Massachusetts Institute of Technology by the US National Science Foundation.

Ionosonde observations are taken from the Space Physics Interactive Data Resource (SPIDR) [14].

This research activity was supported by a Marie Curie initial training network (TRANSMIT) within the 7th European Community Framework Programme.

Author details

F. Da Dalt, C. Benton, T. Panicciari, N. D. Smith and C. N. Mitchell

*Address all correspondence to: F.Da.Dalt@bath.ac.uk

Dept. of Electrical and Electronic Engineering, University of Bath, UK

References

[1] C. N. Mitchell, P. S. J. Spencer. A three-dimensional time-dipendent algorithm for inospheric imaging using GPS. *Annals of Geophysics*, 2003. 46(4): pp. 687-696. doi: 10.4401/ag-4373

[2] P. S. J. Spencer, and C. N. Mitchell. Imaging of fast moving electron-density structures in the polar cap. *Annals of Geophysics*, 2007. 50(3): pp. 427-434. doi: 10.4401/ag-3074

[3] P. Richards, J. Fennelly, and D. Torr. EUVAC: A solar EUV flux model for aeronomic calculations. *Journal of Gephysical Research*, 1994. 99(A5): pp. 8981-8992. doi: 10.1029/94JA00518

[4] P. Richards, J. Fennelly, and D. Torr. Correction to "EUVAC: A solar EUV flux model for aeronomic calculations". *Journal of Geophysical Research*, 1994. 99(A7): pp. 13283. doi: 10.1029/94JA01446

[5] J. Fennelly, and D. Torr. Photoionization and photoabsorption cross sections of O, N2, O2, and N for aeronomic calculations. *Atomic Data and Nuclear data tables*, 1992. 51(2): pp. 321-363. doi: 10.1016/0092-640X(92)90004-2

[6] D. Torr, and M. R. Torr. Chemistry of the thermosphere and ionsophere. *Journal of Atmospheric and Terrestrial Physics*, 1979. 41(7-8): pp. 797-893. doi: 10.1016/0021-9169(79)90126-0

[7] J. E. Salah. Interim standard for the ion-neutral atomic oxygen collision frequency. *Geophysical research letters*, 1993. 20(15): pp. 1543-1546. doi: 10.1029/93GL01699

[8] A. E. Hedin. MSIS-86 thermospheric model. *Journal of Geophysical Research*, 1987. 92(A5): pp. 4649-4662. doi: 10.1029/JA092iA05p04649

[9] J. Picone, A. Hedin, D. P. Drob, and A. Aikin. NRLMSISE-00 empirical model of the atmosphere: Statistical comparisons and scientific issues. *Journal of Geophysical Research*, 2002. 107(A12): pp. SIA 15-1-SIA 15-2. doi: 10.1029/2002JA009430

[10] D. Bilitza. *International Reference Ionosphere 1990, NSSDC 90-22*. World Data Center-A for Rockets & Satellites ed. Greenbelt, Maryland, USA: 1990.

[11] P. Richards, D. Torr, M. Hagan, and M. Buonsanto. A new algorithm for improved ionospheric electron density modeling. *Geophysical resarch letters*, 1995. 22(11): pp. 1385-1388. doi: 10.1029/95GL01351

[12] D. Anderson, M. Buonsanto, M. Codrescu, D. Decker, C. Fesen, T. Fuller-Rowell, B. Reinisch, P. Richards, R. Roble, and R. W. Schunk. Intercomparison of physical models and observations of the ionosphere. *Journal of Geophysical Research: Space Physics (1978-2012)*, 1998. 103(A2): pp. 2179-2192. doi: 10.1029/97JA02872

[13] J. Sojka, M. David, and R. W. Schunk. TDIM Comparison with Bath-Model for Summer and Winter 2011 [Personal communication]. 2013.

[14] M. Zhizhin, E. Kihn, R. Redmon, D. Medvedev, and D. Mishin. Space Physics Interactive Data Resource-SPIDR. *Earth Science Informatics*, 2008. 1(2): pp. 79-91. doi: 10.1007/s12145-008-0012-5

Chapter 17

Implementation of Ionospheric Asymmetry Index in TRANSMIT Prototype

M.M. Shaikh, R. Notarpietro and Bruno Nava

Additional information is available at the end of the chapter

http://dx.doi.org/10.5772/58551

1. Introduction

Radio occultation (RO) [4] missions such as GPS/MET, CHAMP (pilot projects) [3, 17, 18], COSMIC and MetOP [1, 11, 19, 20] have been designed to sound the Earth's neutral atmosphere and ionosphere via radio links between a GPS and GPS receiver on-board Low Earth Orbit (LEO) satellites. The U.S. GPS/MET experiment was the first mission, which successfully applied RO technique to the Earth atmosphere monitoring using GPS signals. Since then, RO technique has become a powerful tool to study the ionosphere [7, 10]. In neutral atmosphere, using RO technique, the bending of the signal is extracted and inverted into refractivity profiles through the Abel inversion [5, 8, 17]. In the ionosphere, where bending is negligible, carrier phase measurement and corresponding limb-TEC (LTEC in what follows) observations are used to extract electron density profiles, Ne(h), defined along the tangent points of ray paths (also known as 'ray perigees') between LEO and GPS (see fig. 1). The retrieval algorithm considers the time-series of LTEC below LEO orbit (between points A1 and A2 in fig. 1) observed from the same GPS satellite during an occultation event. Therefore the LTEC above LEO orbit (TEC from GPS-to-B or GPS-to-A2 in fig. 1) have to be removed before starting the inversion procedure [14] in order to take the contribution of LTEC from upper atmosphere out from the total LTEC (TEC from GPS to LEO). With the data from both pilot missions (GPS/MET, CHAMP), it was only possible to perform LTEC measurements at the highest point of LEO orbit (point B in fig. 1) so that the LTEC above LEO had to be modelled or considered constant all over the occultation [14]. With modern interpolation techniques applied in post processing of current RO missions (such as COSMIC), such above LEO orbit LTEC can be precisely estimated and removed before applying the data inversion techniques. A widely used data inversion technique used to obtain vertical electron density profile in the ionosphere is the 'Onion-peeling' inversion algorithm [9].

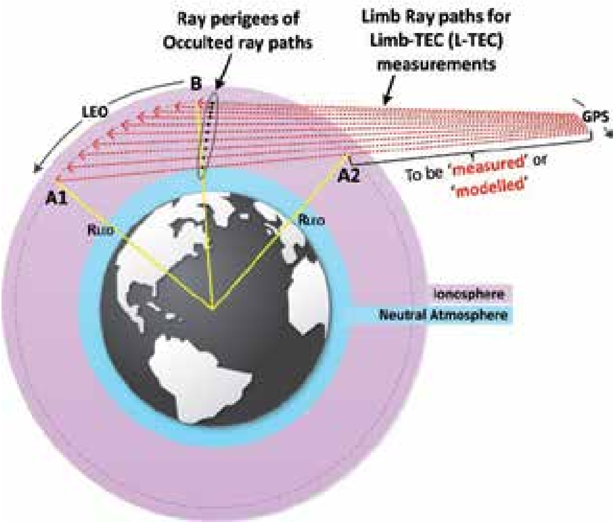

Figure 1. Limb TEC (LTEC) measurement in the ionosphere using radio occultation technique. A1 and A2 are points defined at opposite sides of LEO orbits around ray perigees (black dots). TEC calculated between A1 and A2 is defined as 'internal orbit LTEC'.

Onion-peeling algorithm is based on the assumption of spherical symmetry of Ne distribution in the ionosphere (Ne depends only on height). It is a very effective tool for RO data inversion in case of small horizontal gradients present in the ionosphere (particularly during undisturbed geomagnetic periods). But, for disturbed geomagnetic conditions, for example under the equatorial anomaly region, large electron density gradients may be experienced which could lead to the failure of Onion-peeling algorithm producing erroneous Ne(h) profiles as output. In the present work, a simulation study has been performed to assess the effects of the spherical symmetry assumption on the inverted electron density profiles using Onion-peeling. In order to produce synthetic background ionosphere data, we used two climatological models, NeQuick [13] and IRI [2], and a data analysis system known as 'Multi-Instrument Data Analysis System (MIDAS)' [12]. MIDAS use tomographic techniques to combine observation from many sources simultaneously in a single inversion, with the minimum of a priori assumptions about the form of the ionospheric electron concentration distribution. In this work, MIDAS has been used in two modes, i.e. with standard form and with RO data assimilation. In its standard form, MIDAS doesn't use RO data as a source of ionospheric data. For the latter mode, ionospheric RO data from COSMIC mission for 26th September 2011 has been used for the assimilation. We only performed our analysis for the geomagnetic storm observed on 26th September 2011 over mid-latitudes.

In the next sections, we have presented how we assessed the problem of asymmetry in the ionosphere and its implementation in TRANSMIT prototype. In section 2, we have briefly introduced the Onion-peeling algorithm and its implementation in our work. In section 3, a discussion on the simulation results are presented. In section 4, an overview of TRANSMIT prototype with the description of processor 3C (Ionospheric asymmetry) is presented. In section 5, we have summarized the work by drawing the main conclusions and discussing prospects for the future work.

2. Formulation of the problem

In this work, we have applied the standard Onion-peeling algorithm to invert simulated RO data under a constraint of using ideal geometries: by considering only internal orbit ray paths (ray paths below the LEO orbit), fixed occultation planes and vertically distributed ray perigees positions. This is considered in contrast to what is shown in fig. 1 which shows an illustration of real RO event in which ray perigee positions are not vertically distributed. This happens because LEO and GPS satellites circulate in totally different orbits and independent of each other. LEO satellites, in most cases, have orbit altitudes well below 1000 km and GPS satellites have orbit altitudes approximately 20, 000 km from Earth's surface. In a real RO event, this creates a scenario where the azimuth of the occultation plane changes with almost each ray exchanged between LEO and GPS (there are several hundred rays exchanged in a single RO event). Consequently, position of ray perigee (the tangent point of ray exchanged between LEO and GPS) is independently computed for each ray. Therefore, it is not possible to have vertically distributed ray perigee positions in a real RO event. However, in this work, rationale behind the use of this so called 'ideal geometry' is to focus the dependency of retrieval errors on the inversion approach only and avoiding to take into account inaccuracies due to geometry. The possibility to use external data, like vertical TEC maps [6] to improve the solution has therefore not been considered in the present work. In our analysis, we considered a LEO satellite with orbit altitude of 800 km from Earth's surface. The background ionosphere is computed using NeQuick, IRI and MIDAS (with and without RO data assimilation).

2.1. RO data inversion using onion-peeling technique

For a given occultation event, the LTEC related to the internal orbit ray path 'i' can be computed considering a set of spherical shells (identified by peel 'j') like 'onion shells' [9], characterized by a constant electron density (the radius of each shell is the impact parameter of the ray). Analytically, the LTEC associated to the ith ray can be defined as:

$$L\ TEC_i = 2 \sum_{j=1,\,N}^{i} 2L_{ij} Ne_j \tag{1}$$

where,

'L_{ij}' is the length of the segment 'i' related to the electron density characterizing shell 'j'

'Ne_j' is the electron density charactering shell 'j'

'$LTEC_i$' is the limb-TEC value related to the 'ith' ray path crossing all the shells

'N' is total number of shells

Considering this definition, the LTEC may be easily inverted to extract the Ne characterizing each shell ‘Ne_j’, starting from the most external ray path. The matrix (Eq. (1)) describing the linear system of equations is triangular, and therefore it can be solved from top to bottom for LTEC inversion to extract the Ne(h) profile.

2.2. Onion-peeling derived errors

Following are the definitions of the errors and observables we have used to evaluate the impact of ionospheric asymmetry on Onion-peeling inversion. The retrieved electron density profiles are then compared with the collocated NeQuick, IRI and MIDAS (with and without RO data assimilation) ‘true’ vertical Ne(h) profiles in terms of difference on VTEC and difference on the NmF2 values. These indicators can be defined as:

$$\Delta VTEC = \int_{h_*}^{h_{LEO}} Ne_{Onion-peeling}\, dh - \int_{h_*}^{h_{LEO}} Ne_{NeQuick}\, dh \qquad (2)$$

$$\Delta NmF2 = | NmF2_{Onion-peeling} - NmF2_{NeQuick} | \qquad (3)$$

In [15], we defined the asymmetry level index of the ionosphere considering the degree of dissimilarity of electron density distribution along the two-halves of a given below LEO orbit ray path (as defined in section I) crossing the ionosphere from LEO satellite height down to a 100 km. In the present work, we have applied the asymmetry level index by using three different electron density distribution obtained from NeQuick, IRI and MIDAS (with and without RO data assimilation) and presented a comparative analysis of the results together with its implementation in the TRANSMIT prototype.

3. Simulation results

In this work, we have only performed our analysis over mid-latitudes where a geomagnetic storm effects were observed from UT 18:00 on 26th September 2011 to early hours of 27 September 2011. NeQuick and IRI were used with the solar flux input taken automatically by the model. For MIDAS, results are presented using both standard output and RO data assimilated output. Ionospheric RO data from COSMIC mission collected during 26 September 2011 storm (from UT 12:00 to UT 24:00) over mid-latitudes (Latitude range: 20°N-84°N/ Longitude range: 116°W – 64°E) has been used for the assimilation. Approximately, data from 80 RO events of COSMIC mission have been assimilated. We divided our analysis in two subsets, Quiet-time (from UT 13:00 to UT 14:00) before the start of geomagnetic storm and Storm-time (from UT 19:00 to UT 20:00) on 26 September, 2011.

3.1. Quiet-time analysis

Fig. 2(a) shows two comparative plots of asymmetry values evaluated using NeQuick, IRI and MIDAS (with and without RO data assimilation) for UT 13:00 and UT 14:00. Fig. 2(b)

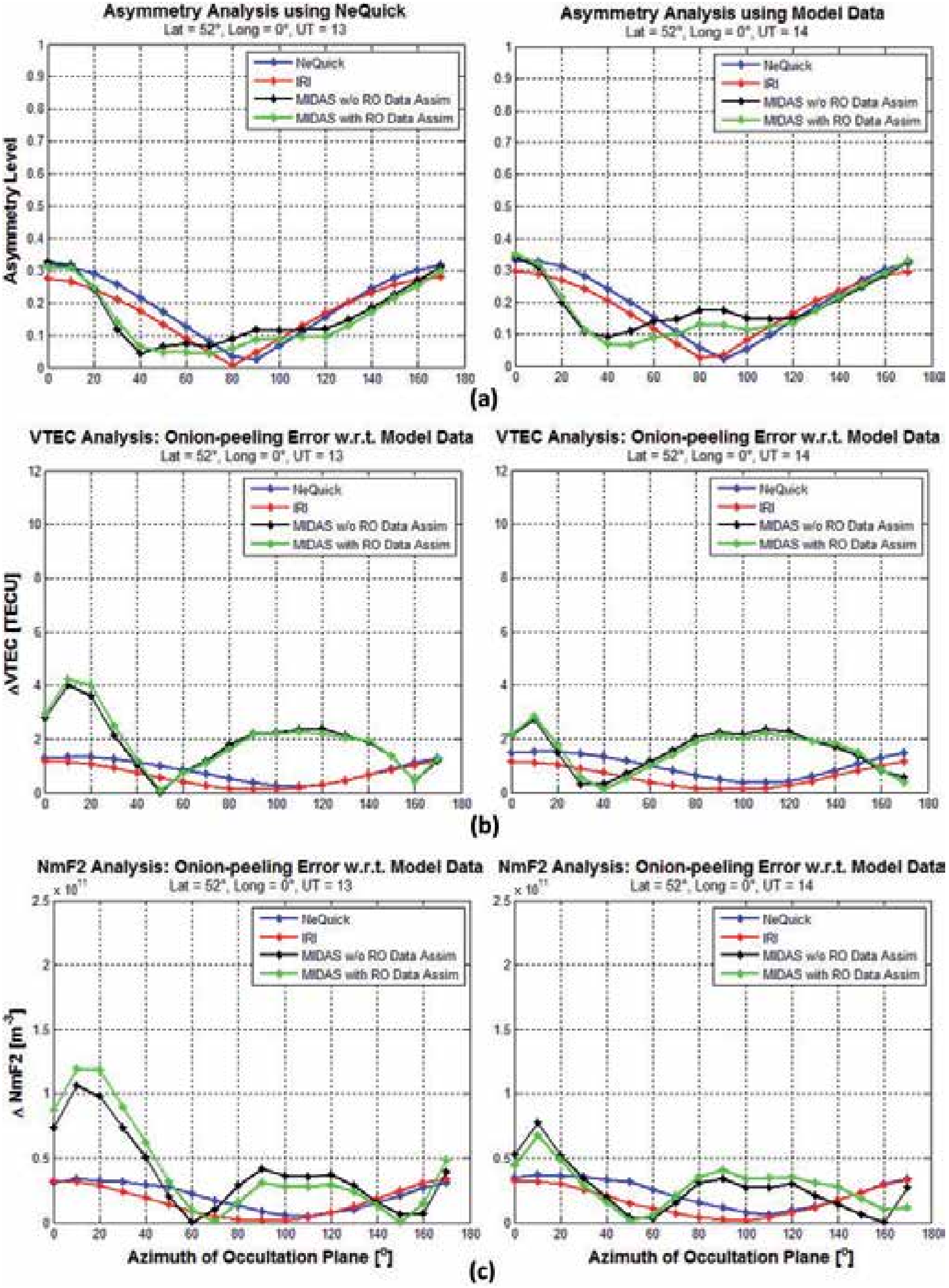

Figure 2. Quiet-Time results for UT 19:00 and 20:00. (a) Asymmetry comparison (b) ΔVTEC comparison (c) ΔNmF2 comparison

and 2(c) show the derived Onion-peeling inversion errors (ΔVTEC and ΔNmF2) for the same UTs, respectively. Comparing the plots, it is evident that an overall good correlation exist between evaluated asymmetry and the associated inversion errors (ΔVTEC and ΔNmF2) as function of the azimuth of occultation plane for NeQuick, IRI, and MIDAS (with and without RO data assimilation). Considering the quiet geomagnetic conditions, asymmetry evaluation is low for all three background ionosphere as expected (maximum asymmetry index values are less than 0.4). These low values can also be observed from the plots of inversion errors. Although the derived error values shown in 2(b) and 2(c) are not exactly correlated with the evaluated asymmetry for all azimuth of occultation plane, we still can find good agreement between the overall behavior of the asymmetry with the inversion errors. In fact, there is a very good agreement between them for certain range of the azimuth of occultation plane in parts. Moreover, asymmetry values together with the inversion error values are all low in numbers which is a good indication that the evaluation has been carried out during a quiet geomagnetic period. Use of MIDAS with or without RO data assimilation didn't produce much different results in quiet-time as all values of asymmetry together with their derived inversion errors are very close to each other in both cases.

3.2. Storm-time analysis

Fig. 3 shows plots from the storm time subset. Correlation between the asymmetry values and their associated errors is evident for all electron density distributions, separately. Comparing the plots at the same UTs, it is evident that an even better correlation exists between the evaluated asymmetry and the Onion-peeling derived errors (ΔVTEC and ΔNmF2) as a function of azimuth of the occultation plane. Unlike quiet-time subset, MIDAS (with and without RO data assimilation) results show very different behavior from NeQuick and IRI. This shows a clear difference between a climatological model (NeQuick and IRI) and a data assimilated model (MIDAS). There seems to be no evidence of an active storm from NeQuick and IRI results (asymmetry range is almost similar to quiet time subset). Whereas, in MIDAS case we can easily observe large values of asymmetry and associated errors from Az=120° to 150° which provides evidence of an active storm. A higher level of correlation between the results shows that the asymmetry algorithm works very well for highly geomagnetic disturbed periods. In contrast to the quiet-time analysis, the use of RO data assimilation can be better observed in storm-time. Specifically, for UT 19:00, the difference of MIDAS as a 'ground truth' ionosphere with and without RO assimilation is clearly evident.

4. TRANSMIT prototype

The main deliverable of TRANSMIT project is a prototype which is being developed as a coordinated input from all level 1 partners. After discussions with the industry partners, it was concluded that that Precise Point Positioning (PPP) results would be the main output of the

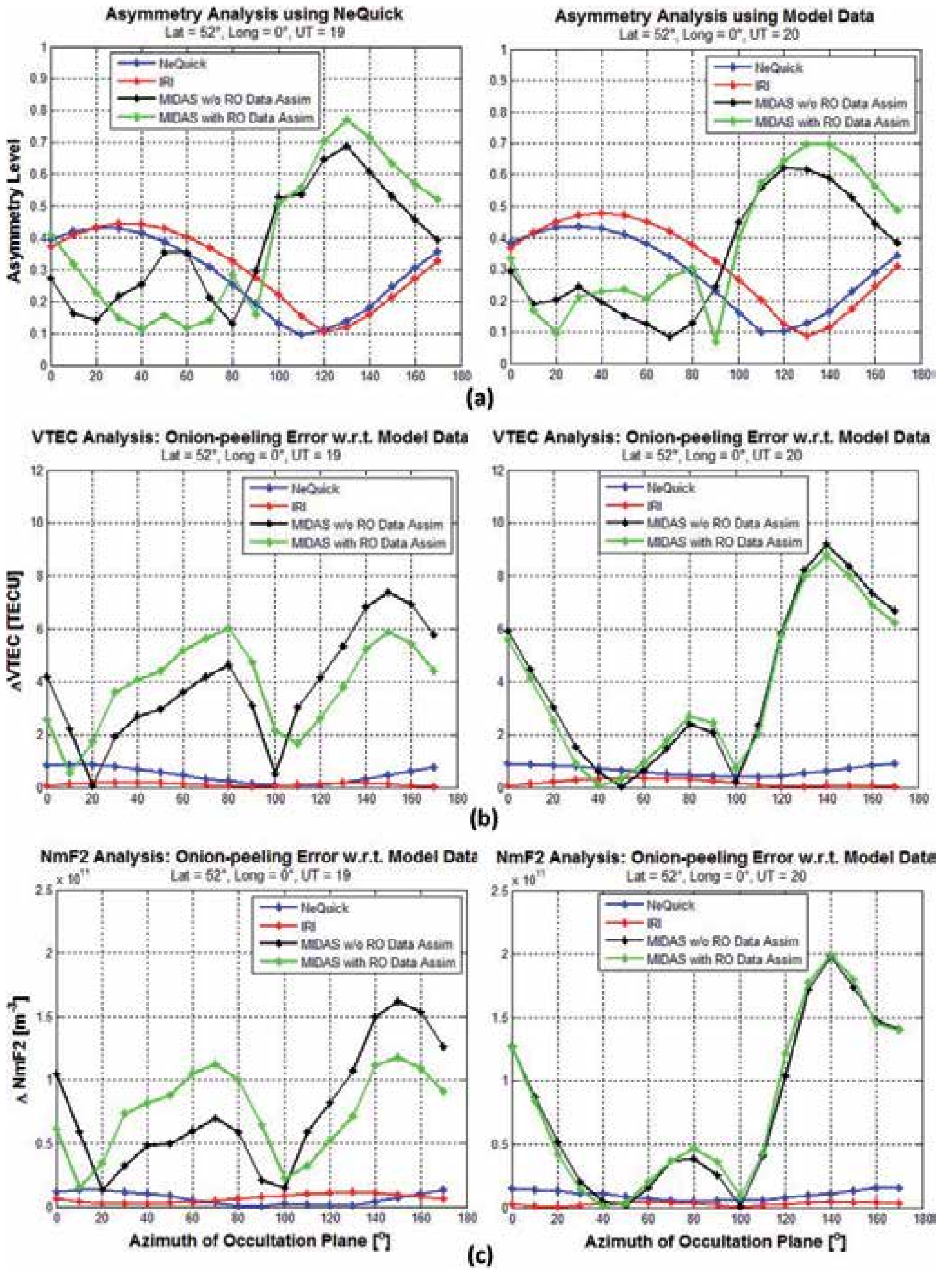

Figure 3. Storm-Time results for UT 19:00 and 20:00. (a) Asymmetry comparison (b) ΔVTEC comparison (c) ΔNmF2 comparison

prototype. Both Single Frequency PPP and Double Frequency PPP are being considered as prototype outputs. To achieve this, 3 main processors were identified as follows:

i. Processor1: S4 and TEC prediction

ii. Processor 2a: PPP mitigation

iii. Processor 2b: Improved tracking,

iv. Processor 3a: Improved MIDAS TEC

v. Processor 3b: Ionospheric models

vi. Processor 3c: Ionospheric Asymmetry

4.1. Prototype operation

Fig. 4 shows a complete flow/block diagram of the TRANSMIT prototype. Main data flow operations through the prototype has been marked in red as 1 to 6. A brief description of each operation is given below:

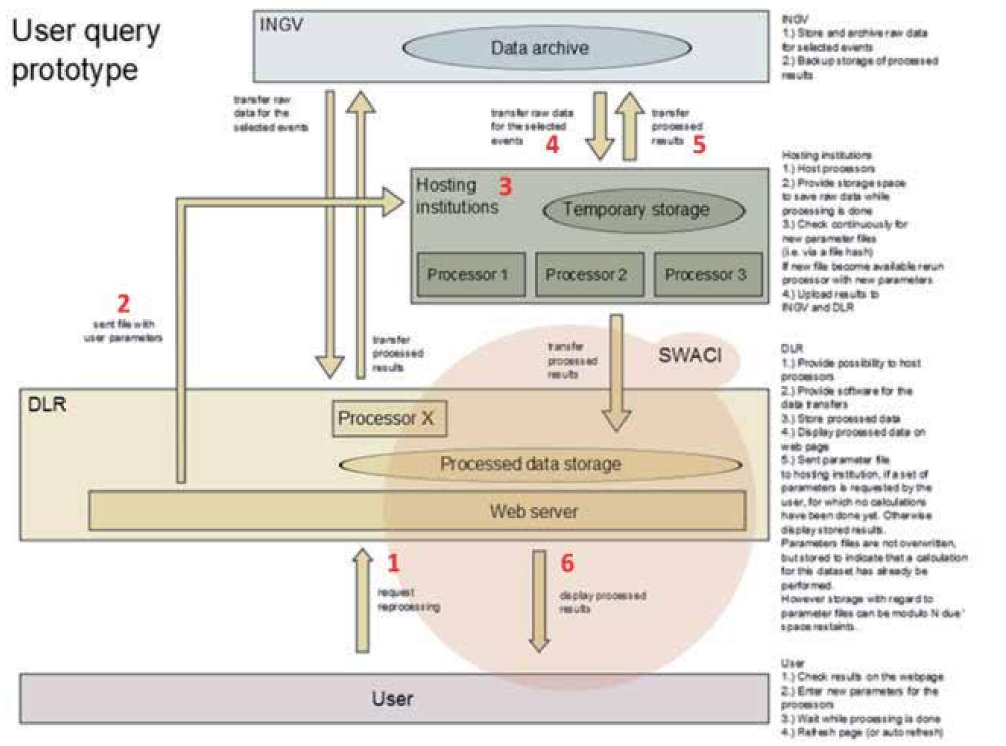

Figure 4. Prototype data flow diagram

1. User request (a form with selection of subprocessor and case study should be available)
2. The user parameter file is generated and sent to POLITO
3. Automatically the processor 3C.subprocessor starts and asks for input (through INGV interface – see point 4)
4. The 3C.subprocessor send output to INGV and SWACI (through INGV and SWACI interfaces)
5. SWACI displays the output for the user (in the form of "surfable" maps as explained)

4.2. Processor 3C: Ionospheric asymmetry

Processor 3C will deal with the ionospheric asymmetry evaluation. A complete block diagram of the processor 3C with data inputs and outputs for each block is shown in fig. 5. For each identified case study, processor 3C will exploit high correlation between asymmetry and associated errors on retrieved electron density profiles. This will be done for real RO events' data taken from COSMIC mission. The processor will produce global asymmetry maps (not shown to the users) using different background ionosphere (provided by model data computed using NeQuick, IRI and MIDAS) for quasi-horizontal TEC observations. By querying these global maps of asymmetry, for each identified case study, processor 3C will compute the expected level of asymmetry present in the ionosphere in the geographical location of the selected RO event. Then, on the basis of the computed asymmetry, the RO event will be displayed in specified color (red, yellow or green) on a 2D map (as shown for output 1 in fig. 4). The color will be an indicator of the expected quality of RO product (considering standard Onion-peeling inversion), as shown in fig. 5. The second output (output 2 in fig. 4) will be a comparison between two RO data inversion techniques; one is the 'standard Onion-peeling' and the other is 'model-aided inversion algorithm' (we are currently working on). For model-aided data inversion, we will provide electron density profiles by taken real geometry from COSMIC mission and considering different model data as background ionosphere. Based on functionality, we have divided processor 3C in three sub-processors 3C.1, 3C.2 and 3C.3 (as shown in fig. 5). A brief description of all sub-processors are as follows:

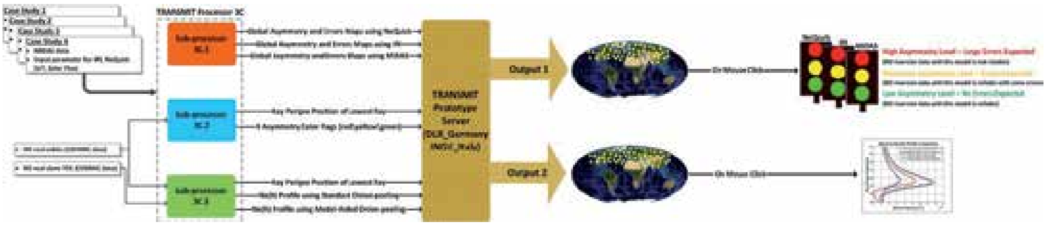

Figure 5. Processor 3C block diagram (see Appendix for larger view)

4.2.1. Sub-processor 3C.1: Global maps of asymmetry index

This part of processor 3C will generate global asymmetry maps for the selected case study. Ideal radio occultation (RO) geometries are taken into account. 18 global maps for each background ionosphere will be generated. Main features of sub-processor 3C.1 are as follows:

a. Global asymmetry maps will be generated considering ideal RO geometries and three different background ionosphere computed using NeQuick, IRI and MIDAS; for each 10° azimuth of occultation plane. The asymmetry level will only be computed for one trajectory of the RO event (the one at 100 km). Users will not be able to see any of these asymmetry maps. These maps will only be used in the processing of output1 and output2 (as shown in fig. 5).

4.2.2. Sub-processor 3C.2: Electron density profile retrieval (standard techniques) effectiveness

The main goal is to show the effectiveness of RO inversion data if the standard onion-peeling algorithm would be used. This will be done by giving a color code (green, yellow, red) to each RO event which will be based on the asymmetry evaluation for that event. The asymmetry for each RO event will be evaluated using processor 3C.1.Main features of sub-processor 3C.2 are as follows:

a. Using real orbits of RO events available in the area defined by the case study, and the global maps of asymmetry computed by sub-processor 3C.1, processor 3C.2 will evaluate the expected level of asymmetry present in the ionosphere in the geographical location of the selected RO event. Then, on the basis of the evaluated asymmetry, the RO event will be displayed in specified color (red, yellow or green) on a 2D map (as shown for output 1 in fig. 5). The color will be an indicator of the expected quality of RO product (considering standard Onion-peeling inversion.

b. Two electron density profile obtained considering standard retrieval algorithms will be shown. One for the best case (lowest asymmetry level among all events) and the other for the worse case (highest asymmetry level among all events).

4.2.3. Sub-processor 3C.3: Onion-peeling model aided Electron density profile retrieval

For each occultation event available in the area defined by the case study, a comparative plot will show the inverted electron density (Ne) profiles obtained using standard Onion-peeling algorithm and the model-aided inversion algorithm (in the latter case three Ne profiles will be available based on each background ionosphere evaluated using NeQuick, IRI and MIDAS). Main features of sub-processor 3C.3 are as follows:

a. Two images of specified format containing Ne profiles of two selected events will be shown. Events with lowest and highest asymmetry will be selected (as done in sub-processor 3C.2). Comparative results related to standard and advanced retrievals will be shown as follows:

b. One electron density profile obtained using standard Onion-peeling inversion

c. Three electron density profiles obtained using model-aided inversion (one for each background ionosphere; NeQuick, IRI and MIDAS).

5. Conclusion & future work

In this work, we have shown the implementation of asymmetry index using three different background ionosphere computed using NeQuick, IRI and MIDAS (with and without RO data assimilation). Previously [16], while implementing the asymmetry index only with climatological models (NeQuick and IRI), it was observed that with a climatological model, it is possible to estimate asymmetry indices only for an ionosphere in 'nominal conditions'. Indeed a climatological model cannot be used to evaluate ionospheric asymmetry for ionospheric conditions in real/near-real time as it does not support data assimilation. In this work, after completing a thorough analysis, we have observed that, in a normal solar activity condition, the climatological model may work as good as a data assimilated model in calculating ionospheric asymmetry. However, during an active solar storm, a data assimilated electron density model can outperform the climatological model and produce much improved results. We have observed a clear difference in results evaluated in two different geophysical conditions. In the storm-time case, we found asymmetry and its associated RO inversion errors much higher than in the quiet-time case. This shows a clear advantage of using data assimilated model as 'ground truth' in ionospheric asymmetry evaluation.

In sections 3.1 and 3.2, we presented the simulation results without highlighting how the use of MIDAS may impact the evaluation of ionospheric asymmetry. As these are our first results with only one case study using MIDAS, it would be difficult to determine exactly how much beneficial it would be to use MIDAS with RO data assimilation as it requires more computation and a higher set of input data. However, it may be concluded from the results of this study that, in case of quiet geomagnetic periods, asymmetry evaluation using MIDAS with or without RO data assimilation may not be of much difference. keeping in view of processor 3C of the TRANSMIT prototype, we are currently studying more case studies in order to analyze which mode of MIDAS would be preferable as source of background ionosphere.

In the scenario of TRANSMIT prototype implementation, we are going to evaluate global asymmetry maps (not shown to the users) with their associated inversion error (ΔVTEC and ΔNmF2) plots with background ionosphere computed using NeQuick, IRI and MIDAS. By querying these global maps of asymmetry, and for a given geometry of a real RO event, the information provided will be the prediction of the expected level of asymmetry present in the ionosphere and its potential impact on Radio Occultation inverted products using estimates of ΔNmF2 and ΔVTEC. An improved inversion technique is currently being developed which may be helpful to reduce the error in RO inversion products by tactfully removing the ionospheric symmetry hypothesis from the standard inversion techniques. This will drive the output2 of processor 3C in future.

Appendices

Block Diagram of Processor 3C (Supplement of figure 5)

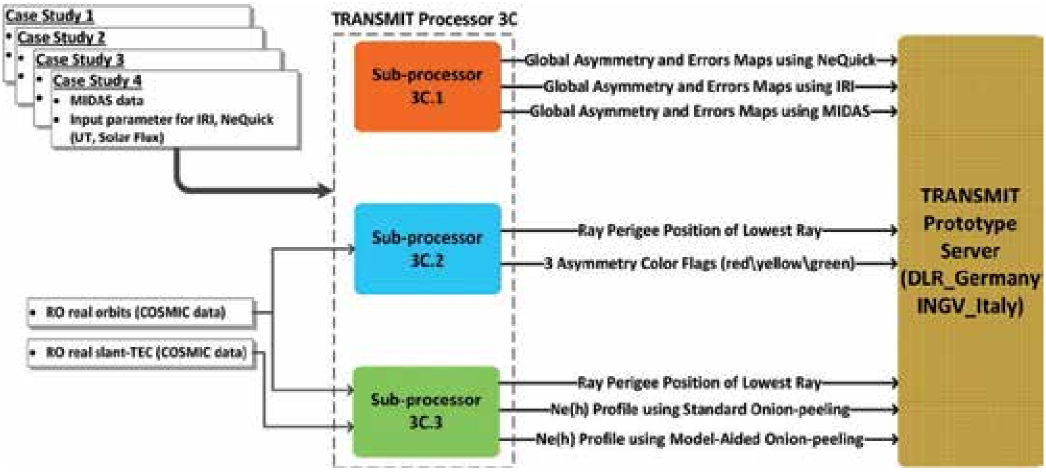

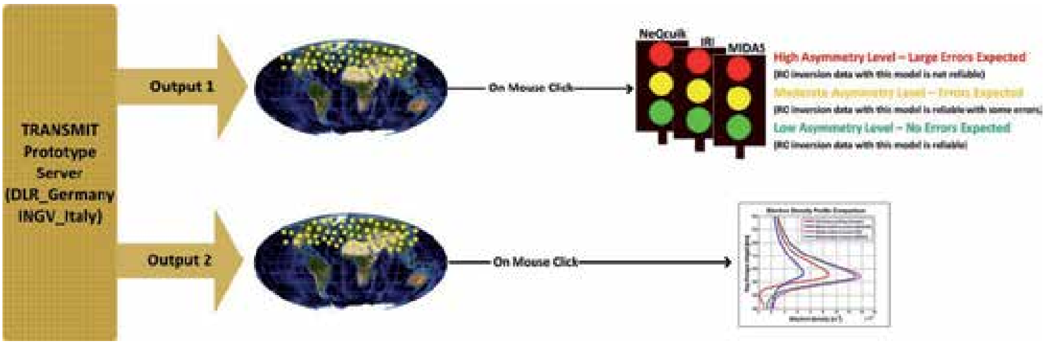

Acknowledgements

This research work is undertaken under the framework of the TRANSMIT ITN www.transmit-ionosphere.net), funded by the Research Executive Agency within the 7th Framework Program of the European Commission, People Program, Initial Training Network, Marie Curie Actions-GA no. 264476.

Author details

M.M. Shaikh[1], R. Notarpietro[1] and Bruno Nava[2]

1 Department of Electronics and Telecommunications, Politecnico of Turin, Turin, Italy

2 The Abdus Salam International Centre for Theoretical Physics, Trieste, Italy

References

[1] Anthes R. A., Ector, D., Hunt D. C., Kuo Y-H., Rocken C., Schreiner W. S., Sokolovskiy S. V., Syndergaard S., Wee T-K., Zeng Z. P., Bernhardt A., Dymond K. F., Chen Y., Liu H., Manning K., Randel W. J., Trenberth K. E., Cucurull L., Healy S.B., Ho S-P., McCormick C.T., Meehan K., Thompson D.C. & Yen N.L. (2008). The COSMIC/FORMOSAT-3 Mission: Early Results. Bulletin of the American Meteorological Society, Vol. 89, pp. 313-333, doi: 10.1175/BAMS-89-3-313.

[2] Bilitza D., B.W. Reinisch (2008). International Reference Ionosphere 2007: Improvements and new parameters, Advances in Space Research 42 (2008) 599–609.

[3] Gorbunov, M.E. (2001). Analysis and validation of GPS/MET radio occultation data, Journal of Geophysical Research, vol. 106, No. D15, pages 17, 161-17, 169.

[4] Hajj G.A., Kursinski E. R., Romans L.J., Bertiger W.I., Leroy S.S. (2001). A technical description of atmospheric sounding by GPS occultation, Journal of Atmospheric and Solar-Terrestrial Physics.

[5] Healy S.B., Haase J., Lesne O. (2002). Abel transform inversion of radio occultation measurements made with a receiver inside the Earth's atmosphere, Annales Geophysicae (2002) 20: 1253–1256 c European Geophysical Society.

[6] Hernandez-Pajares M., Juan J. M., Sanz J. (2000). Improving the Abel inversion by adding ground GPS data to LEO radio occultation in ionosphere sounding, Geophysical research letters, vol. 27, no. 16, pages 2473-2476.

[7] Kulikov I., A. J. Mannucci, X. Pi, C. Raymond, G. A. Hajj (2011). Electron density retrieval from occulting GNSS signals using a gradient-aided inversion technique, Advances in Space Research, 47(2), 289-295, doi:10.1016/j.asr.2010.07.002.

[8] Kursinsky E.R. (1997). Observing Earth's atmosphere with Radio Occultation measurements using the Global Positioning System, Hournal of Geophysical Research, Vol. 102, No. D19, Pages 23, 429-23, 465.

[9] Leitinger R., H.P.Ladreiter, G.Kirchengast (1997). Ionosphere tomography with data from satellite reception of GNSS signals and ground reception of NNSS signals, Radio Sci., 32(4), 1657-1669.

[10] Liu J. Y., C. Y. Lin, C. H. Lin, H. F. Tsai, S. C. Solomon, Y. Y. Sun, I. T. Lee, W. S. Schreiner, and Y. H. Kuo (2010). Artificial plasma cave in the low-latitude ionosphere results from the radio occultation inversion of the FORMOSAT-3/COSMIC, J. Geophys. Res., 115(A7), A07319, doi:10.1029/2009JA015079.

[11] Luntama J-P., Kirchengast G., Borsche M., Foelsche U., Steiner A., Healy S., Von Engeln A, O'Clerigh E. & Marquardt C. (2008). Prospects of the EPS GRAS Mission For Operational Atmospheric Applications. Bulletin of the American Meteorological Society. Vol. 89, pp. 1863-1875, doi: 10.1175/2008BAMS2399.1.

[12] Mitchell, C.N., Spencer, P. (2003). A three-dimensional time-dependent algorithm for ionospheric imaging using GPS, Annals of Geophysics, vol. 46, no. 4, pp. 678–696.

[13] Nava B., Coisson P., Radicella S.M. (2008). A new version of the NeQuick ionosphere electron density model, Journal of Atmospheric and Solar-Terrestrial Physics 70 (2008) 1856-1862.

[14] Schreiner W.S., Sokolovskiy S.V., Rocken C. (1999). Analysis and validation of GPS/MET radio occultation data in the ionospher, Radio Science, Volume 34, Number 4, Pages 949-966.

[15] Shaikh, M.M., Notarpietro, R., Nava, B. (2013). The Impact of Spherical Symmetry Assumption on Radio Occultation Data Inversion in the Ionosphere: An Assessment Study, Advances in Space Research, doi: http://dx.doi.org/10.1016/j.asr.2013.10.025.

[16] Shaikh M. M., Notarpietro R. (2013). Evaluation of the Impact of Ionospheric Asymmetry on GNSS Radio Occultation Inversion Products using NeQuick and IRI, Proceedings of International Conference on Localization and GNSS (ICL-GNSS), ISBN: 978-1-4799-0484-6.

[17] Ware R.H., Exner M., Feng D., Gorbunov M., Hardy K.R., Herman B., Kuo Y.H., Meehan T.K., Melbourne W.G., Rocken C., Schreiner W., Sokolovskiy S.V., Solheim F., Zou X., Anthes R., Businger S. & Trenberth K. (1996). GPS Sounding of the Atmosphere from Low Earth Orbit: Preliminary Results, Bull. Am. Meteorol. Soc., Vol. 77, pp. 19-40.

[18] Reigber, Ch., H. Luhr, and P. Schwintzer (2000). CHAMP mission status and perspectives, Suppl. to EOS, Transactions, AGU, 81, 48, F307.

[19] Dieter K., Marc Cohen, Yves Buhler, Peter Schlüssel, Rosemary Munro, Axelvon Engeln, EoinÓ Clérigh, Hans Bonekamp, Jörg Ackermann, Johannes Schmetz and Juha-Pekka Luntama (2007). An Introduction to the EUMETSAT Polar system, Bull. Amer. Meteor. Soc., 88, 1085–1096. doi: http://dx.doi.org/10.1175/BAMS-88-7-1085.

[20] Anthes, R.A., Rocken, C., and Kuo, Y.-H. (2000). Applications of COSMIC to meteorology and climate, Special issue of Terrestrial, Atmospheric and Oceanic Sciences, 11, 115-156.

Edited by Riccardo Notarpietro, Fabio Dovis, Giorgiana De Franceschi and Marcio Aquino

TRANSMIT (Training Research and Applications Network to Support the Mitigation of Ionospheric Threats) is an initiative funded by the European Commission through a Marie Curie Initial Training Network. It provided a coordinated program of academic and industrial training, focused on atmospheric phenomena that can significantly impair a wide range of systems and applications that are at the core of several activities embedded in our daily life. TRANSMIT deals with the harmful effects of the ionosphere on these systems. Main aim of the project has been to develop a web based prototype demonstrator aiming to showcase the project research outcomes in a user friendly manner, through a series of model outputs and tools that could serve as the blueprint for a future service to assist users and industry to mitigate the effects of ionospheric threats to GNSS.

This book is concerned with the TRANSMIT 2014 Workshop Appraisal of Scientific and Technological Output that took place in Torino (Italy) on February 2014, where a full update on the status of the prototype development and the next steps leading to its full implementation were provided

ISBN 978-953-51-5050-3

Photo by korionov / iStock

IntechOpen